Combinatorial Investigation of Nanolaminate Ternary Carbide Thin Films

A Thesis
Submitted to the Faculty
of
Drexel University
by
Theodore H. Scabarozi Jr.
in partial fulfillment of the
requirements for the degree
of
Doctor of Philosophy
December 2009

Dedication

To my wife Lori and son Maxwell.

Acknowledgements

I would like to acknowledge all the people who have supported, assisted, and collaborated with me during my four years of Ph.D. studies at Drexel University.

First and most important, I would like to thank my thesis supervisor, Professor Michel W. Barsoum, for his patience, motivation, and confidence in me. Without him and his renewed interest in MAX phase materials my graduate studies would never have been a reality.

I am thankful to the National Science Foundation for providing my Ph.D. funding under grants DMR-0503711 and DMR-0821406.

I am grateful to my thesis committee members, Professors Richard Knight and Caroline Schauer at Drexel University, and Professors Sam Lofand and Jeff Hettinger from Rowan University for their guidance and support as well as their fruitful and enlightening discussions. Their encouragement has been a driving force throughout the course of my research.

I would like to acknowledge the members of the MAX phase research group Drs. Peter Finkel, Shahram Amini, Sandip Basu, Aiguo Zhou, Surojit Gupta, Eva Jud Sierra, and also Alex Moseson, Nina Lane, Charles Spencer, Ismail Albayrak, Babak Anasori, and John Lloyd for their assistance and valuable conversations on research.

I would like to acknowledge the members of Department of Materials Science and Engineering, Judith Trachtman, Keiko Nakazawa, Yenneeka Long, Andrew Marx, Professors Jonathon Spanier, Roger Doherty, and Christopher Li for their assistance and teachings during my studies.

I would like to acknowledge the members of the Materials Characterization Facility at Drexel University, Dee Breger, Jim Suttie, Ed Basgall, and Zhorro Nikolov for their assistance with my research.

I am grateful to Rowan University students: William Tambussi, Stephen Clipper, Juan Roche, Andrew Rosenfeld, Christina Gennaoui, Travis Flemming, Katelyn Wittenberger, Katie Sullivan, Patrick Hann, Bryce Adamson, Dan Piwowar, Christian Steinmetz, Erik Pfeiffer, Jimmy Applegate, Sherman Benjamin, and Robert Nolte for their diligent work in the lab, while enduring my demanding work ethic.

I am grateful to Rowan University Staff members, Jon Foglein, Rich Norton, and Dr. Chary for their assistance and discussions with my research. I am especially grateful to Carl Lunk who kept the thin film lab and characterization equipment in operation despite of all the unforeseen problems.

I would like to acknowledge collaborators Per Eklund, Jenny Frodelius, Jens Emmerlich, Hans Högberg, and Lars Hultman from Linköping University and Ulf Jansson and Ola Wilhelmsson from Uppsala University for their insightful and enlightening discussions on thin film physics and especially to those who invited me to attend Flyers games during their visit to Drexel University.

Last, but not least, I am extremely grateful for all the support, motivation, and encouragement I received from my family and friends throughout the course of my Ph.D. studies. Without them I would not have accomplished such an important and significant achievement.

Table of Contents

List of Tables

List of Figures

Abstract

Combinatorial Investigation of Nanolaminate Ternary Carbide Thin Films
Theodore H. Scabarozi Jr.
Supervisor: M.W. Barsoum, Ph.D.

MAX phases have shown a combination of metal- and ceramic-like properties making them candidates in aerospace and other high-performance applications currently dominated by superalloys. The MAX phases follow the general formula $M_{n+1}AX_n$, where M is an early transition metal, A is an A-group element, X is C and/or N, and $n = 1$ to 3. The hexagonal structure consists of edge sharing M_6X octahedra interleaved with A-group element layers. This layered structure, referred to as nanolaminate, leads to the unique and interesting properties. With more than fifty MAX phases already identified, an almost unlimited number of solid solution possibilities exist. Combinatorial methods provide a technique which allows for a large number of thin film samples to be generated with minimal time and expense. In this research, investigations of thin film MAX phase ternary carbides synthesized by magnetron sputtering in the temperature range of RT-1000 °C are reported. The ultimate goal was to synthesize MAX phase thin film solid solutions by a combinatorial method in an attempt to identify enhanced properties.

The M_2AC MAX phases that formed in the following systems, Ti-Nb-Al-C, V-Cr-Al-C, V-Cr-Ge-C, were examined. In all solutions, only mixing of the M elements was investigated. All textured films grew epitaxially (*c*-axis) on *c*-sapphire substrates or deposited binary carbide buffer layers. The lowest synthesis temperature resulting in textured growth was for V_2AlC at 600 °C, however; formation of nanocrystalline Cr_2AlC was observed at 550 °C as indicated by Raman spectroscopy. High temperature X-ray

diffraction of amorphous Cr-Al-C and Cr-Ge-C films showed textured growth of the MAX phase occurred around 650 °C, and 725 °C, respectively. All combinatorial studies were performed at 850 °C with $(Ti_{1-x}Nb_x)_2AlC$ films grown on TiC buffer layers while $(V_{1-x}Cr_x)_2AlC$ and $(V_{1-x}Cr_x)_2GeC$ grown directly on sapphire. Complete solubility across the entire range of x was observed for all systems. Additionally, new thin film phases of V_3AlC_2, V_4AlC_3, $Nb_5Al_3C_x$, $Cr_5Ge_3C_x$, $(Ti_{1-x}Nb_x)_3AlC_2$, $(Ti_{1-x}Nb_x)_4AlC_3$, and $(V_{1-x}Cr_x)_4AlC_3$ were discovered.

The M-element impacts many different properties of MAX phase films. The surface of most films were rough, some containing large hexagonal crystals. Yet, this work has demonstrated that the surface roughness can be tuned using elemental substitutions on the M-sites. While friction testing found all films to have relatively low coefficients of friction (<0.12), this too was found to be influenced by the M-element. Raman spectroscopy of $(Ti_{1-x}Nb_x)_2AlC$ films indicates possible stiffening around $x = 0.75$ explicitly demonstrating the role of the M-element in this solid solution. All films were good electrical conductors with metal-like conduction down to 2K with magnitude and temperature dependence of the resistance tunable through composition. The Hall coefficient and magnetoresistance were also controlled by M-element substitution. While dramatic changes have not been observed, it is clear that the application of combinatorial methods has improved the understanding of the role of the M-element in determining the properties of MAX phases improving the ability to use the materials for thin film applications and beyond.

Chapter 1: Materials Science

Materials science and engineering is an interdisciplinary field relating the structure and properties of matter and its applications to various areas of science and engineering. The foundation of materials science involves relating the desired properties and relative performance of a material in a certain application to the structure of the atoms and phases in that material through characterization. The major determinants of the structure of a material and thus of its properties are its constituent chemical elements and the way in which it has been processed into its final form. These characteristics, taken together and related through the laws of thermodynamics, govern a material's microstructure and its properties. This science investigates the relationship between the structure of materials at atomic or molecular scales and their macroscopic properties. The most recent research has focused on nanotechnology.

1.1. Bulk Metals and Ceramics

Metals occupy the bulk of the periodic table, while non-metallic elements can only be found on the right-hand-side of the Periodic Table. A metal is a chemical element, compound, or alloy characterized by being a good conductor of both electricity and heat and forms cations and ionic bonds with non-metals. In a metal, atoms readily lose electrons to form positive ions. The ions are surrounded by delocalized electrons which are responsible for the conductivity. The material is bound together by electrostatic interactions between the ions and the electron cloud, resulting in a metallic bond. Most elemental metals fall into the category of base metals defined as those which oxidize or corrode relatively easily. Noble metals such as gold, silver, and platinum are resistant to oxidation or corrosion.

Most elemental metals are either too soft, brittle or chemically reactive for practical use. Combining metals in different ratios forms alloys, which in turn modifies the properties of the metals to produce desirable characteristics. The purpose of creating alloys is to make them less brittle, harder, resistant to corrosion/oxidation, or enhance color and luster. The study of metal alloys represents a significant part of materials science. Of all the metallic alloys in use today, the alloys of iron (steel, stainless steel, cast iron, tool steel, alloy steels) make up the largest proportion. Iron alloyed with various proportions of carbon gives low, medium, and high carbon steels. For the steels, the hardness and tensile strength of the steel are directly related to the amount of carbon present, with increasing carbon levels also leading to lower ductility and toughness. The addition of silicon and graphitization will produce cast irons (although some cast irons are made precisely with no graphitization). The addition of chromium, nickel and molybdenum to carbon steels (more than 10 wt. %) results in stainless steels.

Other significant metallic alloys are those of aluminum, titanium, copper and magnesium. Copper alloys have been utilized for a long time, the most common being brass and bronze. Alloys of aluminum, titanium, and magnesium are known for their high strength-to-weight ratios, relatively low densities, and ductility and machinability. These materials are ideal for applications where enhanced properties are more important than bulk cost, such as in the aerospace industry (turbines, space vehicles), nuclear power plants, surgical implants, and automotive engineering applications.

A ceramic material is a compound of metallic and nonmetallic elements where the interatomic bonding is predominately ionic. Ceramics are typically strong in compression, weak in shearing and tension, thermally and electrically insulating, chemically inert, thermal shock resistant, brittle, and hard. Ceramics generally can withstand very high temperatures such as temperatures that range from 1,000 °C to 1,600 °C (1,800 °F to 3,000 °F). Ceramic materials can be divided into six categories; glasses, clays, refractories, abrasives, cements, and advanced or technical ceramics. Ceramics can be crystalline or non-crystalline (amorphous).

Traditional ceramic raw materials, including clay minerals such as kaolinite, have been utilized for centuries. Glasses represent one of the most commonly used ceramics, examples include borosilicate (ovenware), soda-lime (bottles), fiberglass (home insulation), and optical flint (eye glass lenses). Refractory ceramics are used for high-temperature applications where they do not melt, decompose, and remain unreactive with the material and environment. Typical examples are furnace bricks, silica (SiO_2), periclase (MgO), and alumina (Al_2O_3). Cement ceramics consist of cement, plaster-of-Paris, and lime, which when mixed with water subsequently set and harden. The final material is a strongly bonded material that can be molded into almost any shape. Portland cement is the most common in this category. The modern ceramic materials, which are classified as advanced ceramics, include silicon carbide, silicon nitride, and tungsten carbide. Both are valued for their abrasion resistance, and hence find use in applications such as the wear plates of crushing equipment in mining operations. Advanced ceramics are also used in the medicinal, electrical, and electronics (semiconductor) industries.

Other than metals and ceramics, polymers are also an important part of materials science. Polymers are the raw materials (the resins) used to make what are commonly called plastics. Plastics are really the final product, created after one or more polymers or additives have been added to a resin during processing, which is then shaped into a final form. Polymers which have been around, and which are in current widespread use, include polyethylene, polypropylene, PVC, polystyrene, nylons, polyesters, acrylics, polyurethanes, and polycarbonates. Plastics are generally classified as commodity, specialty, and engineering plastics.

1.2. Thin Films

Thin films are used for numerous applications including decorative or color enhancement, protective coatings (oxidation, corrosion, chemical, thermal), microelectronics, optical coatings, magnetic media, and hard tribological coatings for tools. A thin film can be defined as a coating of material typically less than 1 μm (10,000 Å) which exhibits a large surface-to-volume ratio. It is this large ratio that leads to the unique and enhanced properties seen in thin films and not in the bulk material. There are many techniques used for creating thin films, each having advantages and disadvantages. One of the oldest is cathodic-arc deposition discovered by Joseph Priestley in the mid-1700s.[1]

As mentioned previously an important application for thin films is in the tooling industry. Early coatings included binary carbide and nitride materials such as TiC and TiN. These films greatly enhanced the lifetime and operating temperature of high-speed tools like mill bits. Continued research has found solid solutions and alloying also enhance the desired properties. The most recent discoveries are that of TiAlCN or nanocrystalline (nc-) binaries embedded in an amorphous (a-) matrix, for example nc-TiN/a-SiN.[2, 3] Vepřek reported extremely high hardness values for these nanocomposites well above 50 GPa.[4] These types of materials are a continued effort to make ‘superhard’ material like cubic BN and diamond, whose hardness approaches 100 GPa.

The interest in thin film materials is twofold. First, single crystals are valuable for determining the physical properties of materials. Comparison of the electronic transport results of single-crystal epitaxial films to those of its bulk counterpart can investigate anisotropy in the material.[5] Second, thin-film coatings are desired for numerous engineering applications such as carbide and nitride coatings for increased wear resistance. Table 1.1 lists various film properties and associated applications.

Table 1.1 Thin film properties and applications.

Thin film Property	Typical Applications
Optical	Reflective/antireflective coatings
	Interference filters
	Decorative (color/luster)
	Memory discs (CDs/DVDs)
	Waveguides
Electrical	Insulation
	Conduction
	Semiconductor devices
	Piezoelectric drivers
Magnetic	Memory storage
Chemical	Barriers to diffusion or alloying
	Oxidation or corrosion protection
	Gas/liquid sensors
Mechanical	Tribological (wear-resistant) coatings
	Hardness
	Adhesion
	Micromechanics
Thermal	Barrier layers
	Heat sinks

Chapter 2: MAX Phase Materials

This chapter will discuss the MAX phase materials and their properties.

2.1. Introduction

In the nineteen sixties Nowotny and co-workers first synthesized powders of a family of ternary carbides and nitrides.[6-8] These compounds have since been termed MAX phases, following the general formula $M_{n+1}AX_n$, where M is an early transition metal, A is an A-group element, X is C and/or N, and $n = 1$ to 3.[9-13] The compounds have a hexagonal structure consisting of layers of the A-group element interleaved with $M_{n+1}X_n$ layers having the rock-salt structure, as schematically represented in Fig. 2.1. Note that the MAX structure is very anisotropic with c/a ratios ranging from 3.48 to 7.82, where Ti_2SC represents the former and Ti_4AlN_3 the latter. A current list of the more than

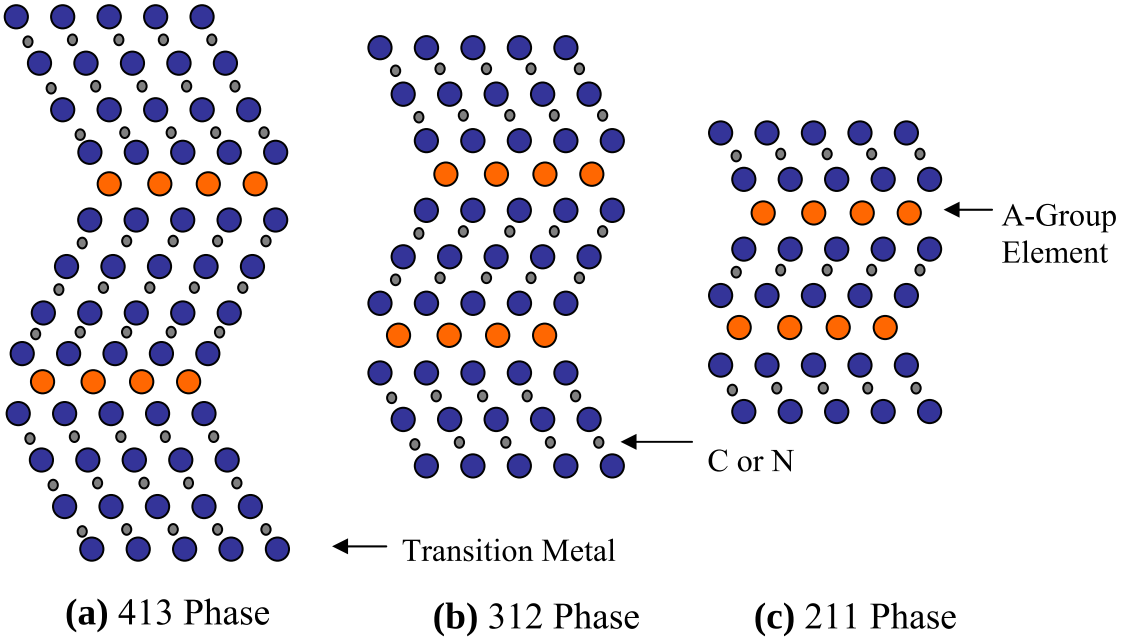

Figure 2.1 Schematic representation of the structure of the MAX phases. Blue circles represent the M element, orange represents the A-group element, and gray represents C and/or N.

Table 2.1 Summary of $M_{n+1}AX_n$ ternary compounds. Most of these phases were discovered by Nowotny and coworkers in the nineteen sixties.[6-8] As can be seen, the 211 family is the largest of the MAX phases, with titanium forming the most compounds out of the M-group elements. Relatively, only a few MAX phases have been synthesized in thin films. Highlighted materials have been synthesized in thin film form by various groups worldwide.

211						312	413
Cr_2AlC	Hf_2SnC	Nb_2SC	Ti_2GaN	V_2AlC	Zr_2InN	Ta_3AlC_2	Ta_4AlC_3
Cr_2GaC	Hf_2SnN	Nb_2SnC	Ti_2GeC	V_2AsC	Zr_2PbC	Ti_3AlC_2	Ti_4AlN_3
Cr_2GaN	Mo_2GaC	Ta_2AlC	Ti_2InC	V_2GaC	Zr_2SC	Ti_3GeC_2	Ti_4GeC_3
Cr_2GeC	Nb_2AlC	Ta_2GaC	Ti_2InN	V_2GaN	Zr_2SnC	Ti_3SiC_2	Ti_4SiC_3
Hf_2InC	Nb_2AsC	Ti_2AlC	Ti_2PbC	V_2GeC		Ti_3SnC_2	Nb_4AlC_3
Hf_2InN	Nb_2GaC	Ti_2AlN	Ti_2SC	V_2GeN			V_4AlC_3
Hf_2PbC	Nb_2InC	Ti_2CdC	Ti_2SnC	V_2PC			
Hf_2SC	Nb_2PC	Ti_2GaC	Ti_2TlC	Zr_2InC			

50 known MAX phases is given in Table 2.1. The majority of materials (more than 40) can be represented by the general chemical formula M_2AX or 211; there are five known M_3AX_2 (312) and six known M_4AX_3 (413) compounds. However, there are literally an infinite number of solid solutions possible, with only a few already characterized.[7, 14-28]

2.2. Properties

Most of the work accomplished to this point has focused on the mechanical and elastic properties of the bulk materials with only a few materials having been characterized electrically in spite of their interesting electronic properties.[9, 24, 27, 29-33] Listed below are several of the reasons these solids are an interesting class of materials:

1) They are excellent conductors of electricity and heat; the electrical and thermal conductivities of Ti_3SiC_2 are more than double those of Ti metal.[9]

2) At $< 4 \times 10^{-3}$, the friction coefficient of the basal planes is extremely low. Low friction is maintained even after the samples have been left in air for six months.[34]
3) They retain many of their properties and are thermally stable to very high temperatures (>1700 °C).[12, 35]
4) They generally have small Seebeck and Hall coefficients.[9, 27]
5) They are the only polycrystalline solids that deform by kink and shear band formation, together with delaminations of the grains.[35-38]
6) One of the most characteristic properties of the MAX phases is the ease with which they can be machined, which is not typical for ceramics or carbides and nitrides.
7) They are generally elastically stiff (at 320 GPa the stiffness of Ti_3SiC_2 is almost 3 times that of Ti metal, with the *same* density, 4.5 g/cm^3).[9]
8) They are the only solids that exhibit fully reversible dislocation-based deformations.[39]
9) With Vickers hardness values in the range 2-5 GPa range, these compounds are relatively soft compared to other early transition metal carbides and nitrides.[9]
10) These solids are exceptionally thermal shock resistant and damage tolerant.[10, 12, 40-42]
11) Some are quasi-ductile at room temperature.[10]

The first four listings have increased interest when considering thin films. The first two make them excellent candidates for electrical contacts. Groups at Linköping and Uppsala

Universities in Sweden are currently working in collaboration with industry exploring this application. The third interesting property of thermal stability is attractive in the aerospace and energy generation fields. Even the best superalloys have temperature limits; MAX-phase coatings can provide additional protection to the more expensive base materials.

Chapter 3: Thin Film Synthesis and Growth

3.1. Film Growth

The following sections discuss the growth of films from nucleation to crystal orientation.

3.1.1. Nucleation and Kinetics

Surface kinetics explains how an atom behaves upon impingement with a surface. Figure 3.1 shows the various adsorption processes an atom may experience upon contact with a substrate.[43] When an atom first lands on a surface, if there is enough activation energy typically due to heating the substrate, the atom now termed adatom, will begin to diffuse on the surface (physisorption). The adatom will diffuse over the surface until a lower energy potential (bonding site) is contacted (chemisorption). These bonding sites are typically defects, kinks, or steps where weak bonding between the adatom and substrate occur. Because the adatom is only weakly bonded to the substrate,

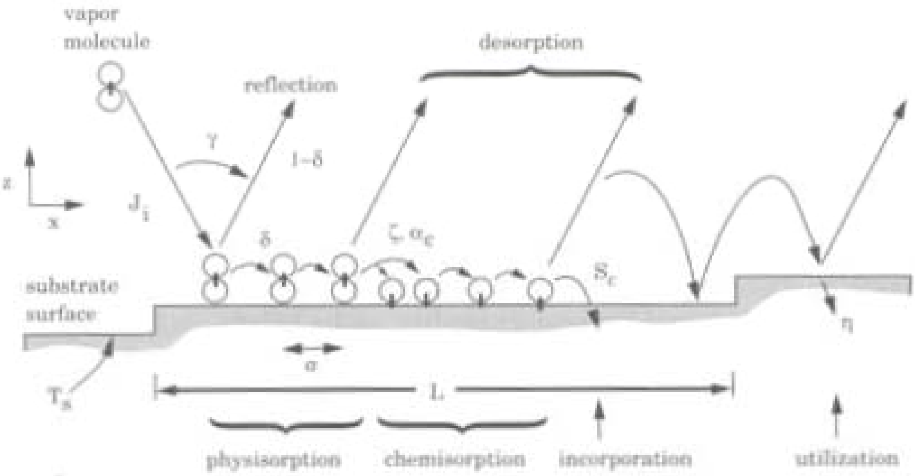

Figure 3.1 Adsorption processes for an impinging molecule upon a substrate.[43]

the dangling bonds create a less favorable higher energy system. Upon additional bonding of adatoms during the incorporation phase the system energy decreases and the species is considered utilized. It is possible for the impinging molecule to contain enough energy such that it actually reflects off the surface. Additionally, if the adatom gains enough energy (either thermally or via an applied electrical bias) during diffusion prior to bonding with another adatom or surface defect it may desorb from the substrate. The frequency of desorption, ν_{des}, is:

$$\nu_{des} = \nu_s \exp\left(-\frac{\Delta G_{des}}{kT}\right) \tag{3.1}$$

where ν_s is the surface vibration frequency, ΔG_{des} the free energy of the desorbing atom, *k* Boltzmann constant, and T is temperature. The residence time, τ_0, is how long the adatom will remain on the surface before desorbing if no additional bonding occurs expressed as:

$$\tau_0 = \frac{1}{\nu_{des}} = \frac{1}{\nu_s} \exp\left(\frac{\Delta G_{des}}{kT}\right) \tag{3.2}$$

During the residence time an adatom will move from one surface site to the next at a diffusion frequency, ν_{diff}, defined as:

$$\nu_{diff} = \nu_s \exp\left(-\frac{\Delta G_j}{kT}\right) \tag{3.3}$$

where ΔG_j is the energy required to jump to a neighboring site. This appears similar to the desorption frequency, however, it should be noted that ΔG_{des} is larger than ΔG_j because the former breaks a bond whereas the latter does not change the number of bonds. Finally, the surface diffusivity, D_s, is defined as:

$$D_s = \lambda^2 \nu_{diff} = \lambda^2 \nu_s \exp\left(-\frac{\Delta G_j}{kT}\right) \tag{3.4}$$

where λ is the jump distance. Unlike in bulk diffusion, no vacancy needs to be created, a surface has sites available. Figure 3.2 graphically shows the energy of an adatom during its diffusion on the surface from Ref. [43]. Weak surface bonding occurs during the physisorption phase, followed by a decrease in energy when bonding occurs referred to as chemisorption. After chemisorption the atom is considered incorporated into the film requiring significant energy to diffuse through the material.

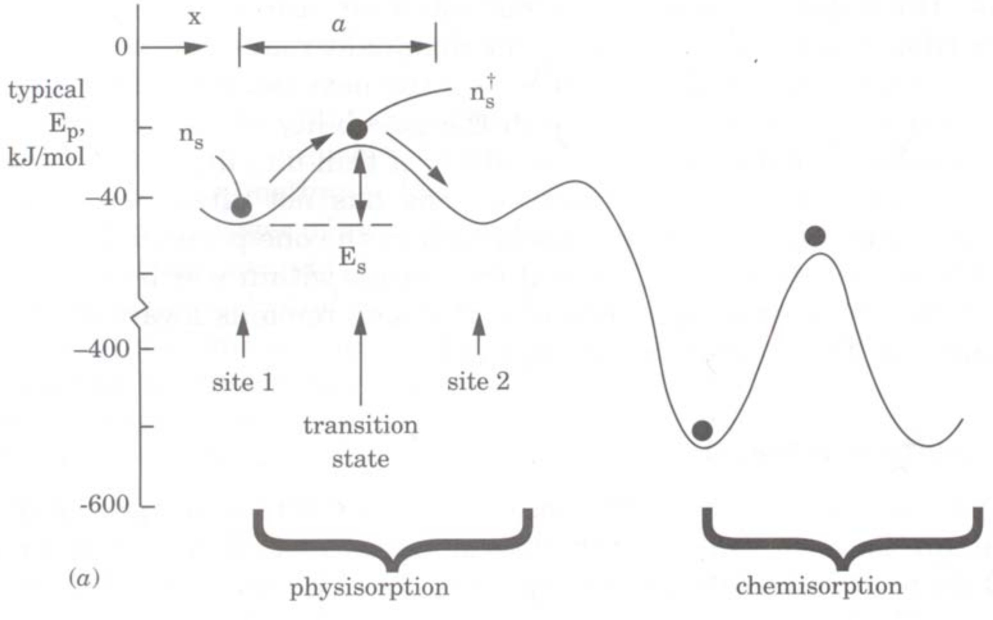

Figure 3.2 Illustration of adatom energy during surface diffusion.[43]

3.1.2. Growth Mechanisms

There are three growth modes in thin films, shown schematically in Figure 3.3.[44] The first is Volmer-Weber island growth. In this case the impinging atoms will prefer to bond to each other, forming three dimensional islands. This can be attributed to low substrate wetting and more typical low substrate temperature where there is insufficient activation energy for surface diffusion to occur.

The second growth mechanism is Frank-Van der Merwe layer by layer.[44] In this case growth occurs in monolayers attributed to good substrate wetting and fast surface diffusion, again directly related to a higher substrate temperature. Only after a layer has completely grown will the next begin.

The third mechanism and most common in film growth is a combination of island and layer-by-layer referred to as Stranski-Krastanov.[44] Here the film usually starts out as island growth resulting in a continued upward growth as opposed to a completed layer formation followed by new nucleation on top of that. This is very sensitive to the substrate temperature, as mentioned previously, determining whether upward or outward growth dominates. The larger island clusters grow with some surface diffusing atoms known as adatoms diffusing around. The perimeter of the large islands offers a high binding energy site for growth. However, some adatoms bond separately of these large islands; these will likely attracted more adatoms forming another island cluster.

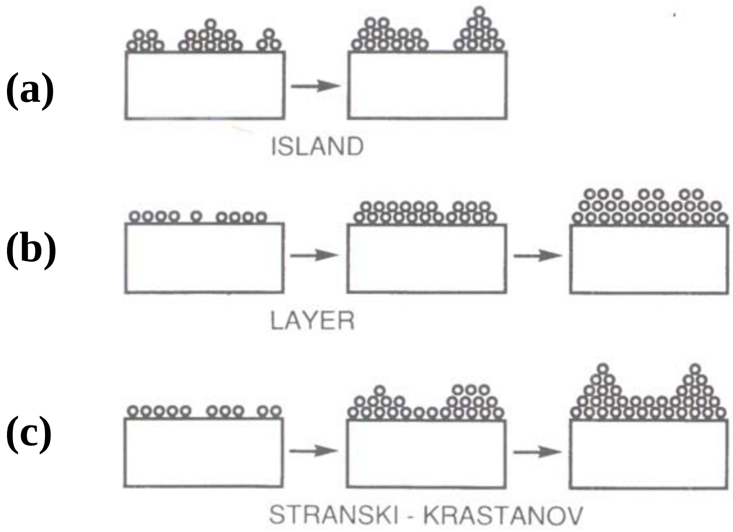

Figure 3.3 Illustration of a) Volmer-Weber (island), b) Frank-Van der Merwe (layer), and c) Stranski-Krastanov (mixed) thin film growth modes.[44]

3.1.3. Film Orientation

Following nucleation the film begins to grow. The next important understanding is how the film will grow. As mentioned previously, the most prominent factor in film synthesis is thermal energy. By controlling this one can control the type of film orientation: amorphous, polycrystalline, textured, or epitaxial. An amorphous material has no long range ordering of the atoms; glass is an amorphous solid. Polycrystalline materials are solids composed of many crystallites of varying size and orientation, the orientation is random within the material. Textured and epitaxial materials exhibit a preferred orientation of the crystals that can be a result of the substrate or the lowest free energy orientation of the material.

In order to understand how thermal energy affects orientation a model needs to be constructed. Figure 3.4 represents a schematic of a structure zone model (SZM) for evaporated films as a function homologous temperature defined as T_S/T_M, where T_S is the

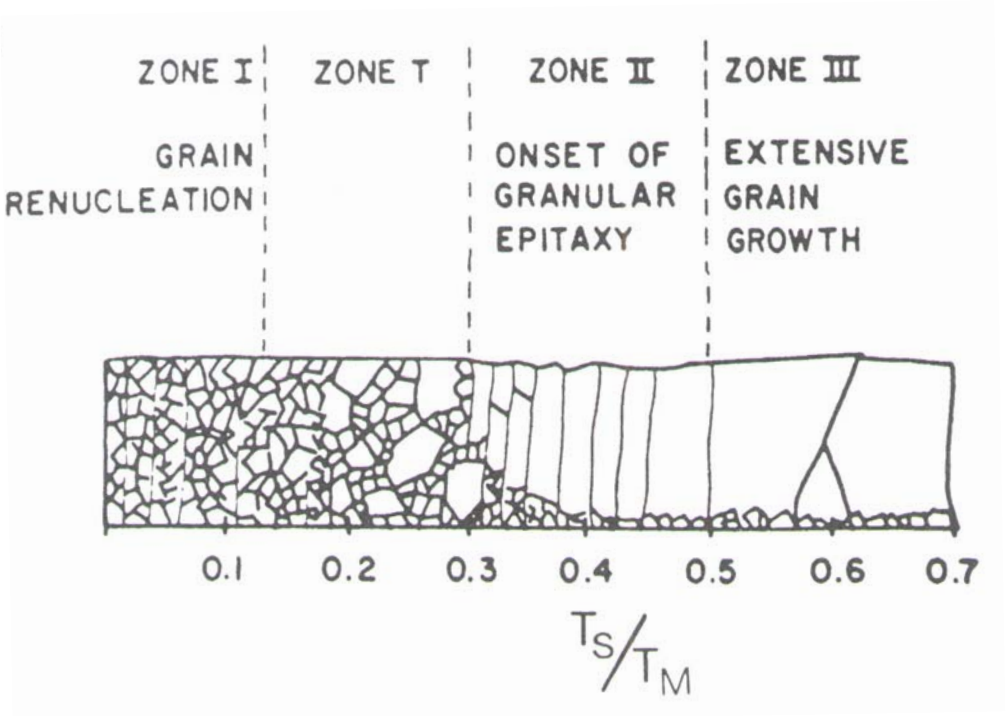

Figure 3.4 Schematic of a structure zone model for evaporated films. [44]

substrate temperature and T_M the melting temperature of the material.[44] While the method of synthesis in this thesis is magnetron sputtering instead of melting, the evaporated SZM serves as a good example, the only difference being that Zones II and III are combined into a single zone for magnetron sputtering. Additionally, SZMs are not rigid but depend upon material deposited and complexity of the phases to be synthesized. Zone I represents low-temperature deposition where the adatom lacks the energy to diffuse any significant amount. Orientation is amorphous or nanocrystalline. Zone T is a 'transition' zone where enough thermal energy is provided to allow the adatom to diffuse along the surface. The density increases along with grain size with random or polycrystalline orientation beginning. Zone II represents a region of moderate deposition temperature, where both bulk and surface diffusion occur. Films are dense with medium textured grains present. The last, Zone III, represents high-temperature deposition where bulk and surface diffusion strongly affect phase synthesis. Extensive grain growth occurs, resulting in dense films where textured or epitaxial orientation is preferred. Significantly above Zone III, viz. $T_S/T_M \sim 1$, film growth decreases dramatically as desorption becomes a prominent process.

As mentioned previously, there are four types of film orientation, three of which are schematically represented in Figure 3.5. The first, from Zone I, is amorphous or nanocrystalline, here there exist no order or phase formation, only weak Van-der-Waals bonding taking place. Once enough energy is provided (Zone T), phase synthesis can occur allowing for polycrystalline or random growth to occur (Fig. 3.5a). Increasing temperature in Zone II results in the preferred or textured orientation shown in Figure 3.5b. Here the grains grow either in a lower-free-energy orientation, as is typical in binary carbides such as TiC which prefer the (111) orientation regardless of substrate orientation or form a relation with the substrate orientation. In Figure 3.5b, the film exhibits an out-of-plane texturing (light arrows); however, the in-plane orientation, denoted by bold

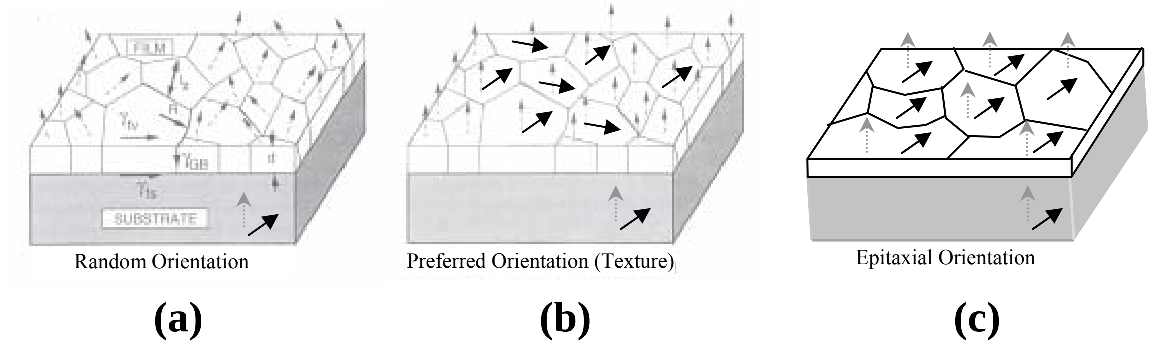

Figure 3.5 Schematics of a) polycrystalline film orientation, b) preferred orientation (textured), and c) epitaxial orientation. Light and bold arrows represent out-of-plane and in-plane directions.[44]

arrows, is not the same, in this case there exists two different orientations. Epitaxy is a special case, where there must exist a relation between both the in-plane and out-of-plane orientations of the substrate and film. Figure 3.5c shows an epitaxial relationship between film and substrate; where both in- and out-of-plane orientations match. It should be noted that the in-plane orientation of the film does not have to match the substrate, but all grains in the film must have the same orientation.

3.2. Thin Film Deposition

The following section will introduce and describe the technique used to synthesize thin films within this thesis, magnetron sputtering. It is first necessary to mention other techniques used to create thin films. There are two categories of film deposition: physical vapor deposition (PVD) and chemical vapor deposition (CVD).

PVD comprises techniques in which the depositing species are deposited via a physical route. These include: thermal evaporation, cathodic arc, laser ablation, molecular beam epitaxy, and sputtering which will be described in the following section. Thermal evaporation relies on melting the material to be deposited. It is a low cost deposition technique that is limited to materials with low melting points (<1200 °C), the depositing species have very low energy, and a significant amount of impurities are present. Cathodic arc utilizes a high power electric arc impinged upon the target to vaporize the material. The technique is useful for covering large areas, but suffers from large particles (~ μm in size) in depositions. Laser ablation uses high power laser light to melt, evaporate, and ionize the material to deposit. The depositing species have high energy reducing substrate temperature, but the process has a small deposition area and can contain large particles similar in cathodic arc. Molecular beam epitaxy (MBE) is a special technique which is capable of depositing monolayers of a material. This technique requires an ultra-high vacuum to produce high quality epitaxial films and superstructures.

CVD consists of techniques that rely on chemical reactions to occur in order to form films. In general, all techniques pass a reactive gas across the substrate that is at an elevated temperature where a reaction occurs either on the substrate or with another gas leading to the resulting deposited film. The depositing species energy in most CVD techniques is low, thus requiring a higher substrate temperature than those found in PVD techniques. Atmospheric vapor CVD is performed at ambient atmosphere, most commonly used in mass production. The technique is fast and covers large areas, but suffers from significant contamination. Low-pressure CVD is similar to atmospheric; however, it is performed under a vacuum, reducing the amount of impurities introduced into the film. Plasma enhanced CVD utilizes a plasma during deposition to increase the energy of the depositing species, which can result in lower substrate temperatures required. Metal organic CVD uses volatile metal organic compounds to form films, typically used in the semiconductor industry. The last technique rather new is organic CVD which has been developed for the organic light emitting diode (OLED) industry.

3.2.1. Introduction: Magnetron Sputtering

Sputtering is a type of physical vapor deposition. Deposition is performed in a high-vacuum chamber (< 10^{-6} Torr, 10^{-4} Pa). The sputtering process can be likened to a cannon ball shot at a wall. The sputtering gas, typically a noble gas such as Ar, is introduced to the chamber to a pressure of 3-100 mTorr (0.4-13 Pa). A large negative potential is applied to the target material which ionizes the Ar atoms. The ionzied gas atom (the ‘cannon ball’) then bombards the target (the ‘wall’) knocking loose a target atom (Fig. 3.6a). The atoms deposit on the substrate (and surrounding area) creating a thin film.

Similar to sputtering, magnetron sputtering includes the use of magnets behind the target. The magnets enhance the sputtering yield by trapping electrons released during the ionization process in the magnetic field lines. Figure 3.6b shows a schematic cross-section of a magnetron. The trapped electrons recombine with ionized gas atoms which allows the neutral gas atom to be ionized again, creating a region of high plasma density. Sputtered atoms typically have a few eV of kinetic energy associated with them. This allows for synthesis to occur at lower substrate temperatures as compared to lower-energy techniques such as thermal evaporation. A bias, which is an applied negative potential to the substrate, can increase the energy of the depositing species typically decreasing the synthesis temperature; however, too high a bias can lead to resputtering of the deposited

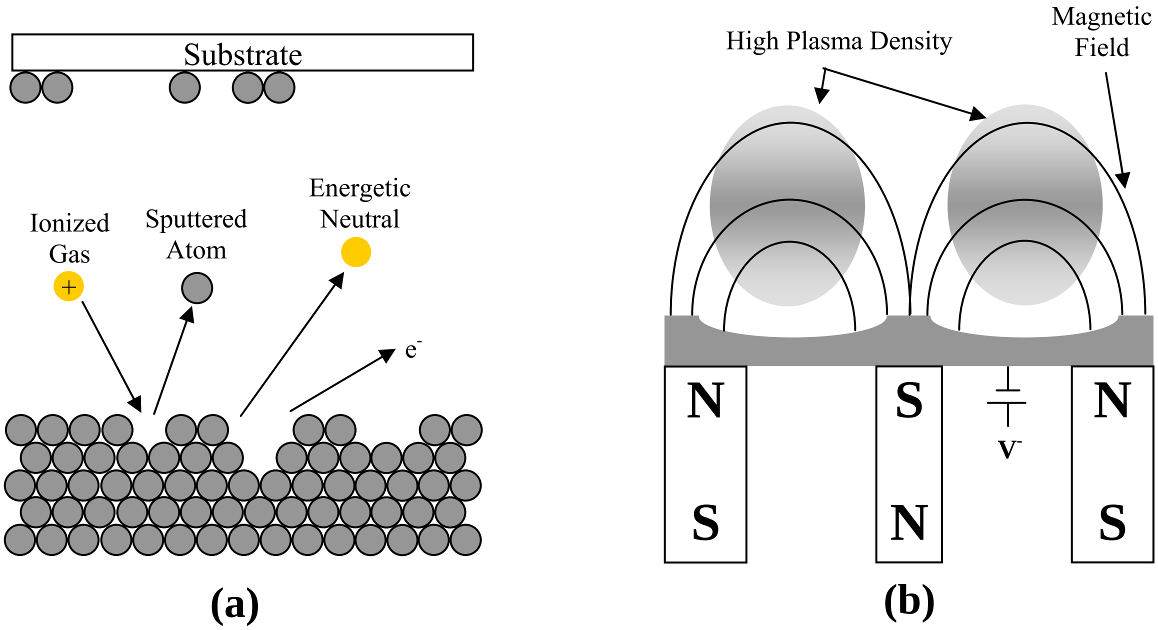

Figure 3.6 Schematic representations of a) the sputtering process at the target surface and depositing species on the substrate, and b) magnetron configuration.

material. If no bias is applied, the substrate is considered to be at ‘floating potential’.

Reactive sputtering includes the use of a secondary gas that contains an element to be deposited. Typical examples are nitrogen and acetylene for depositions of nitrides and carbides, respectively. Complex oxide films, such as $BaSrO_4$ and $YBaCuO_4$ are also produce by this method. A typical benefit of reactive sputtering is a decrease in required substrate temperature. However, the sensitivity of sputtering-to-reactive gas ratios is very high, making this technique more difficult than elemental target sputtering. Reactive sputtering of binary carbide and nitride coatings is common in mass production.

3.2.2. Experimental Details

Thin films were deposited in a custom-built ultra-high vacuum magnetron sputtering chamber (TM Vacuum, Riverside, NJ). Two different cathode configurations were utilized during this thesis, one for the deposition of 211 end-member films, the other for the combinatorial synthesis discussed in Section 3.3. It should be noted; from herein the term end-member refers to a single MAX phase compound not alloyed, such as Nb_2AlC. The original configuration used in synthesizing the end-members shown in Fig. 3.7a made use of three 50.8-mm cathodes positioned directly over a rotating substrate holder, one each for a M-group element (Nb or Ti), Al, and C. In this configuration, Nb_2AlC and Ti_2AlC were synthesized and will be discussed in Chapter 5. While the original configuration was well suited for individual MAX-phase systems, it was not suitable for the combinatorial synthesis of ternary compounds. The chamber was re-configured with four cathodes: two 50.8-mm cathodes and two 25.4-mm cathodes (Fig. 3.7b). The 50.8-mm cathodes contained carbon and the A-group element (Al or Ge) while the 1-in targets contained M-group targets (Cr, Nb, Ti, or V). In this configuration

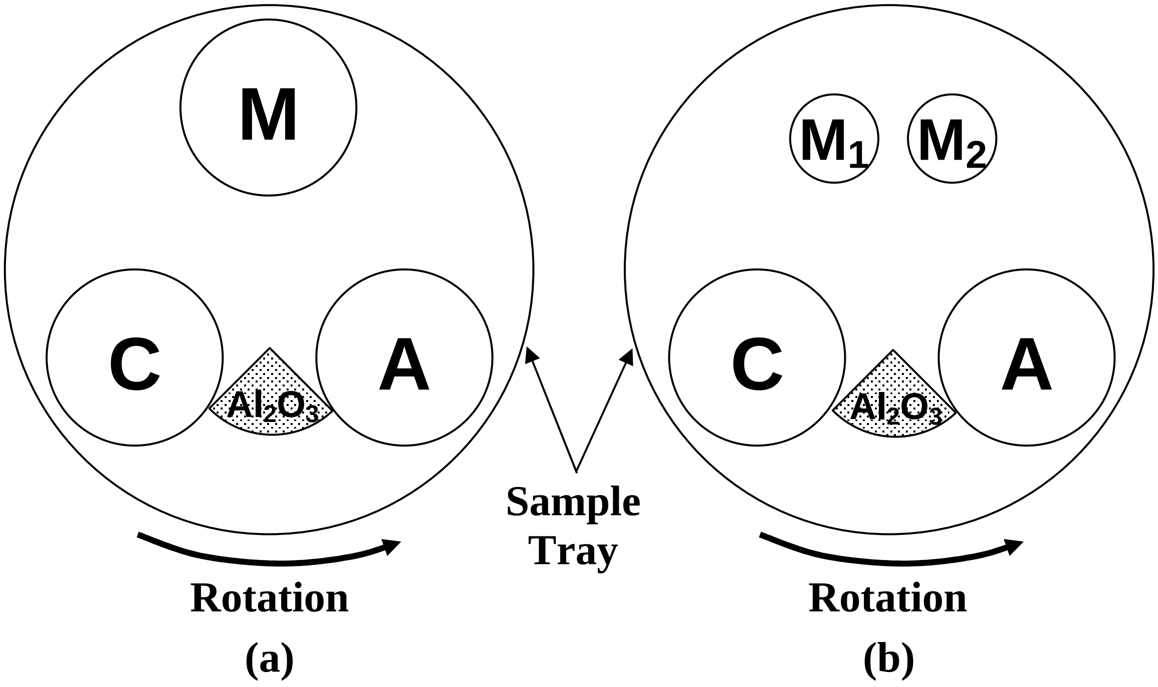

Figure 3.7 Overhead schematic representations of a) three 50.8-mm cathodes, and b) two 50.8-mm and two 25.4-mm cathodes. The sapphire substrate (Al_2O_3) is mounted on a 6-in sample tray and rotates directly under each cathode in a sputter down configuration. Letters in the schematics are: C-carbon, M-M group metal (Cr, Nb, Ti, or V), and A-A group element (Al or Ge).

V_2AlC, Cr_2AlC, V_2GeC, and Cr_2GeC were successfully synthesized. Three radio frequency (RF) and one direct current (DC) power supplies were used for the depositions.

The initial deposition system heater consisted of a molybdenum ribbon meandered between insulated posts inside an enclosed cylindrical furnace housing. Since the molybdenum ribbon was positioned vertically, this led to excessive side heating with significantly less heat directed towards the substrate positioned above the heater. This designed required the heating element temperature to be set extremely high to achieve a temperature of 750 °C, not high enough for synthesis of the materials desired in this thesis. The end result was overheating of the cathodes, ultimately leading to cathode failure. In order to achieve temperatures up to 1000 °C and cover a ø15.2-cm circle, a custom designed substrate heater was fabricated. Molybdenum foil was electro-discharged machined (EDM) into a circular meander, similar in shape to omega symbols. The new heater was mounted on a fused silica block such that the heater face was directed toward the substrate. A type K thermocouple was positioned below the heater equidistant to the sample holder to control temperature.

All depositions were performed using high purity elemental targets using Ar as the sputtering gas. The only exception was deposits from a compound Ti_3SiC_2 target, results of which are discussed in Appendix B. The substrate rotational rate was approximately 18 rpm with a substrate-cathode distance of 10 cm. Deposits of Ti_2AlC, Nb_2AlC, V_2AlC, Cr_2AlC, V_2GeC, Cr_2GeC were performed on ø50.8mm (0001) oriented epi-polished sapphire (Al_2O_3) wafers scribed and broken into ¼ pieces. For deposits containing Al, substrates of MgO and Si were also used for chemical composition analysis. The substrates were pre-cleaned with acetone and methanol and then dried with nitrogen. Substrates were placed on a sample holder over an opening which allowed for direct radiation from the heater. Synthesis temperature for all 211 systems was varied from room temperature to 950 °C, additionally 250 °C depositions were performed for high-temperature X-ray diffraction. A temperature ramp rate of 25 °C/min was applied along with a minimum 30 min hold time. Prior to deposition, a base pressure of 6.6×10^{-6} Pa was obtained. The substrate temperature was determined by optical pyrometer (Land Instruments Cyclops 153A) which was calibrated with a thermocouple. Chamber pressure was 0.8 and 1.3 mTorr for deposits in performed in configurations 3.7a and 3.7b, respectively. In some experiments the pressure was varied between 0.4-1.3 Pa. Ar gas flow during all depositions was 50 sccm. An average deposition rate of 200 nm/hour was typical for most deposits.

3.3. Combinatorial Method

The following section will discuss the combinatorial technique used to synthesize thin film solid solutions. Combinatorial experimentation was performed after successful synthesis of the respective end-members.

3.3.1. Introduction

Combinatorial methods are designed to accelerate the discovery, development, and optimization of innovative materials. The advent of combinatorial experimental methods has revolutionized industrial materials discovery by accelerating the research and development of a huge variety of materials systems and devices. The "combi" technique enables researchers to approach large, complex variable spaces in a more rapid, thorough, and coherent manner. Accordingly, this method holds great potential for synthesizing the vast number of possible solid solutions in the MAX phase family. As demonstrated in recent years, when combi tools are directed towards knowledge generation and complex materials science problems, academic researchers can reap the benefits that industrial practitioners of these techniques have seen in discovery and engineering. This thesis will demonstrate successful use of combinatorial method in the synthesis of three MAX phase solid solutions.

So far, only one combinatorial synthesis experiment has been reported, that being in the Cr-Al-C system.[45] In that study the authors determined the compositional dependence for the formation of Cr_2AlC. It was found that single phase Cr_2AlC was observed with deviation up to 6.3 at. % Al content, with possible explanations of X-ray insensitivity to secondary phases or substitution of Cr by Al. However, there has been no report on solid solutions of MAX phase films.

3.3.2. Experimental Details

During combinatorial depositions the two 25.4-mm cathodes were offset which created the compositional gradient (Fig. 3.8). Power settings were adjusted accordingly for all targets to achieve best uniformity and compositional gradient as determined by chemical composition analysis. The compositional gradient varied from 5-20 at. % across the substrate depending upon the power settings. All combinatorial deposits were performed on ø50.8mm (0001) oriented epi-polished sapphire (Al_2O_3) wafers. For deposits containing Al, Si wafers of approximately 10 mm × 50 mm were positioned

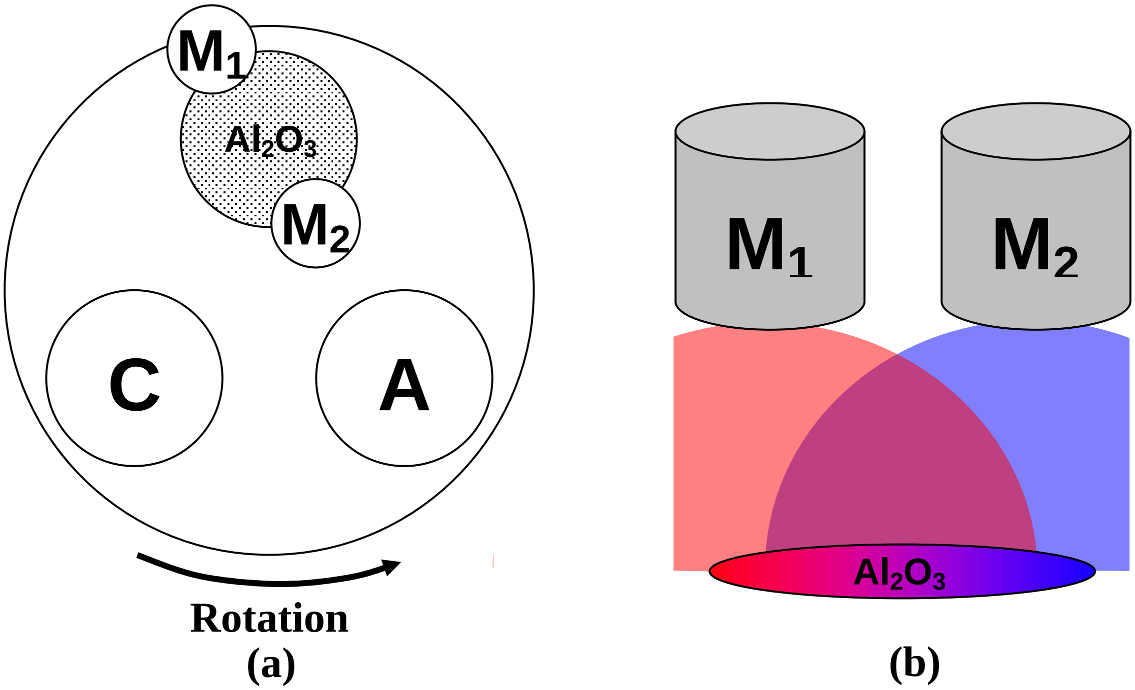

Figure 3.8 a) Overhead schematic representation of cathode configuration for combinatorial synthesis. An ø50.8 mm sapphire substrate (Al_2O_3) is mounted on a 15.2 cm sample tray and rotates directly under each of the two 50.8-mm cathodes and between the two 1-in cathodes in a sputter down configuration. b) Side view of the 25.4-mm cathodes demonstrating the gradient across the substrate produced by the cathode offset.

identical to the sapphire for use in compositional analysis. The substrates were pre-cleaned with acetone and methanol and then dried with nitrogen. In order to facilitate growth of $(Ti_{1-x}Nb_x)_2AlC$, 20-nm seedlayers of TiC (111) were deposited at a substrate temperature of 700 °C at 50 sccm and 1.3 Pa. No seedlayers were utilized in $(V_{1-x}Cr_x)_2AlC$ or $(V_{1-x}Cr_x)_2GeC$ depositions. Combinatorial synthesis substrate temperature was 850 °C with a ramp rate of 25 °C/min along with a minimum 30 min hold time. Prior to deposition, a base pressure of 6.6×10^{-6} Pa was obtained. The substrate temperature was determined by optical pyrometer (Land Instruments Cyclops 153A) which was calibrated with a thermocouple. A temperature gradient of 50 °C was observed across the substrate. All deposits were then performed at 1.3 Pa with an Ar flow of 50 sccm for 60 minutes with an average deposition rate of 100-200 nm/hour.

Chapter 4: Characterization Techniques

This chapter contains a brief description of the various characterization techniques that were used on the thin films produced. Although there are numerous other techniques focus will be on those used in this thesis.

4.1. Structure/Microstructure

After synthesis of a film, its crystal structure(s) needs to be identified. The following section will discuss the techniques used to identify the crystalline phases grown.

4.1.1. X-ray Diffraction

X-ray diffraction is a powerful technique used to determine crystal structure, grain size, orientation, and strain to name a few. The technique utilizes Bragg's Law[46]; $n\lambda=2d(\sin\theta)$, where n is an integer related to the diffracting plane, λ the wavelength of the X-rays, d the spacing between the planes in the atomic lattice, and θ the angle between the incident ray and the scattering planes. The incident X-rays elastically scatter off the

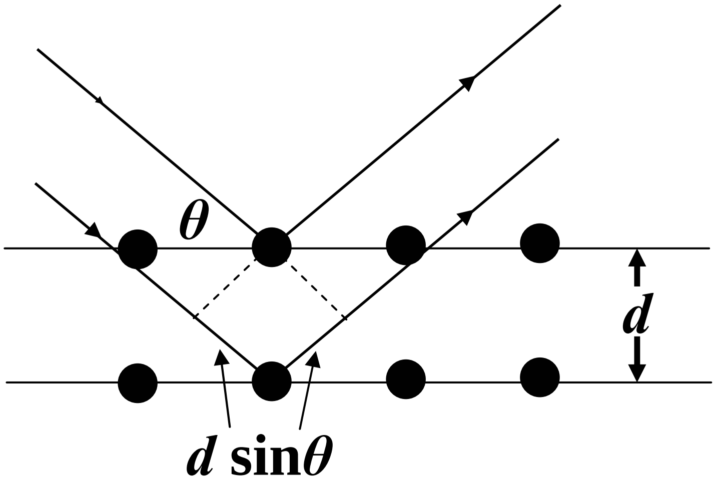

Figure 4.1 Schematic representation of Bragg's Law. Incident X-rays are elastically scattered by atoms in the lattice, constructive interference occurs at angles that satisfy Bragg's Law.

crystal lattice of the material being measured (Fig. 4.1). Typical XRD configuration of measurement is called θ-2θ, where θ is the angle of the incident beam and 2θ the angle between the incident beam and detector. This configuration is also referred to as powder diffraction as it is limited to out-of-plane which is not important for powder samples as they are polycrystalline.

If the film grows textured or epitaxially only the orientation growing out-of plane will be observed, therefore no in-plane information is available. In order to alleviate this one can use a different technique known as 4-circle diffraction or phi-scans (ϕ). Here the incident beam and detector are fixed at angles associated to the out-of-plane diffraction angles for both the film and substrate. The sample rotates through 360 degrees (ϕ) diffracting when Bragg's Law is satisfied. Calculations are then performed to determine the in-plane orientation with respect to the substrate.

X-ray diffraction (XRD) of thin films was performed on a Scintag X_2 diffractometer configured in standard θ-θ Bragg-Bretano geometry utilizing Cu-K_α radiation and Si(Li) Peltier-cooled solid-state detector. Spectra were fit to a Pearson7 lineshape by Scintag software DMSNT 1.36b. Lattice calculations were performed using a Nelson-Riley plot (d_θ vs. $\cos\theta^2/\sin\theta$), where d_θ is the lattice spacing found through Bragg's Law calculation and θ the incident angle.[47] The heterogeneous strain was determined from Williamson-Hall plots, $\beta(\cos\theta)$ vs. $(\sin\theta)$, of θ-2θ scans, where β is the full-width-at-half-maximum and θ as defined previously.[48] Average tilt was determined from modified Williamson-Hall plots, $\beta(\sin\theta)/\lambda$ vs. $\sin\theta)/\lambda$, of rocking curve measurements, where λ is the X-ray wavelength and β and θ defined previously.[48] ϕ scans were performed with a Bruker D8 4-circle diffractometer utilizing Cu-K_α radiation.

High-temperature X-ray diffraction (HTXRD) was completed with an Edmund Bühler HDK-2.3 diffraction furnace mounted on the Scintag X_2 diffractometer. Approximately 1 cm^2 samples scribed and broken from deposited films were placed directly on the Pt heating element, a Pt/Rh-30% thermocouple was bonded to the back of the heater for temperature control. Measurements were taken every 25 °C from 500-1100 °C. In order to prevent oxidation, measurements were performed under vacuum (~10^{-3} Pa).

4.1.2. Scanning Electron Microscopy (SEM)

The scanning electron microscope (SEM) is a type of electron microscope that images the sample surface by scanning it with a high-energy beam of electrons. The electrons interact with the atoms that make up the sample producing signals that contain information about the sample's surface topography, composition, and other properties. Several types of signals result from the electron beam interaction with the material including secondary electrons, back-scattered electrons, Auger electrons, characteristic X-rays and light. With secondary electron imaging (SEI), the SEM can produce very high-resolution images of a sample surface, revealing details about 1 to 5 nm in size. SEM micrographs have a very large depth of field yielding a characteristic three-dimensional appearance useful for understanding the surface structure of a sample. Characteristic X-rays are the second most common imaging mode for an SEM. X-rays are emitted when the electron beam removes an inner shell electron from the sample, causing a higher energy electron to fill the shell and emit energy. These characteristic X-rays are used to identify the elemental composition of the sample. Electron microscopy within this thesis was performed with a LEO 1530VP SEM.

4.1.3. Transmission Electron Microscopy (TEM)

The transmission electron microscope (TEM) is similar to that of a SEM. A high-energy beam of electrons is used to probe the material in question. Unlike the SEM, which images the sample surface, the TEM produces an image on a fluorescent screen as a result of electrons passing through a thin sample of the material. The electrons interact with the atoms that make up the sample producing signals that contain information about the sample's crystal structure, composition, and other properties. Electrons which are scattered over small angles are a result of composition leading to phase contrast imaging. Electrons that interact with the crystal structure produce diffraction patterns useful in phase identification and determining lattice constants. Similar to an SEM, characteristic X-rays are generated and can be used for determination of chemical composition. Unlike the SEM though, a TEM is capable of significantly higher accelerating voltages (200kV). A TEM is capable of imaging down to 1 Å at a magnification of over one million times. The biggest challenge in TEM is in sample preparation. Electron microscopy within this thesis was performed with a field-emission TEM (JEOL JEM-2100F).

4.1.4. Raman Spectroscopy

Raman spectroscopy utilizes inelastic scattering of monochromatic light upon molecules in a material. A typical experimental setup consists of a laser light source, confocal microscope, and spectrometer. This technique studies the vibrational, rotational, and other low-frequency modes associated with atomic interactions in materials. Results give insight into the crystal structure and bonding characteristics, such as stiffness, of the material. Raman is usually compared with results from *ab initio* calculations of first-principle calculations, group theory, and density functional theory (DFT) based upon space group and atomic position.[49]

Raman spectra were taken at room temperature with either a Renishaw 2000 or Jobin Yvon U100 spectrometer with either a HeNe laser (633 nm) or Ar-ion lasers (514.5 nm or 532 nm). Spectra were collected in static mode with a 60-s exposure time and up to thirty accumulations. Experimental peak positions were calculated through Lorentzian fitting with a system resolution of 2 cm^{-1}.

4.1.5. Atomic Force Microscopy (AFM)

Atomic force microscopy (AFM) is a very high-resolution type of scanning probe microscopy, with possible resolutions of fractions of a nanometer. The AFM is one of the primary tools for imaging, measuring, and manipulating matter at the nanoscale. Piezoelectric components facilitate tiny but accurate and precise movements by electronic command enable the precision scanning. The AFM consists of a cantilever with a sharp tip at its end that is used to scan the specimen surface (Fig. 4.2). The cantilever is

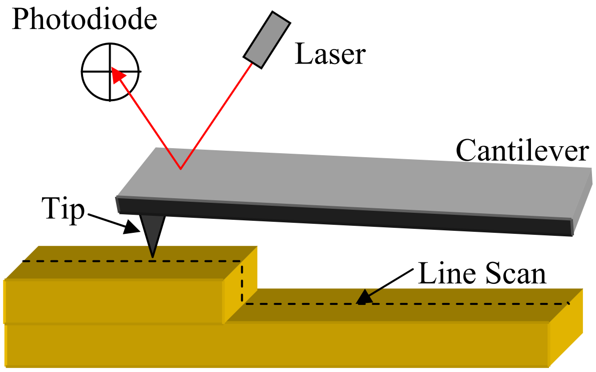

Figure 4.2 Schematic of an atomic force microscope. A sharp tip is in contact or within close proximity to the surface being imaged. A photodiode measures deflection of the incident laser beam that occurs due to displacement of the cantilever by surface topography while mapping over the x-y plane is performed.

typically silicon or silicon nitride with a tip radius of curvature on the order of nanometers. When the tip is brought into proximity of a sample surface, electrostatic forces between the tip and the sample lead to a deflection of the cantilever according to Hooke's law.[50] Typically, the deflection is measured using a laser spot reflected from the back surface of the cantilever into an array of photodiodes.

AFM was performed using a JEOL SPM-5200 in non-contact mode. Average roughness values (R_a) were obtained from 10 μm x 10 μm and 25 μm x 25 μm scans. For combinatorial synthesis, the very nature of the growth of compositional gradient samples often leads to a concomitant thickness gradient across the substrate. Thus for comparison purposes, it is more meaningful to calculate the relative roughness (R_a/t_f), where R_a is the average roughness and t_f the film thickness.

4.2. Composition

Determining the chemical composition of deposited films is the most important characterization step in studies of the synthesis of a material. Phase diagrams provide insight into the range of compositions phases existing within a given system. Compounds such as most binary carbides exhibit a large range of carbon composition which leads to variations in the lattice constants. In addition, multiple phases can exist depending on the composition. The MAX phases, being hexagonal in crystal structure, are thought to be a point phase in their respective ternary phase diagram. Currently, the compositional variation is not well known in the MAX phases which phase stability exists. Therefore film composition should be as close to stoichiometric as possible to limit possible secondary phases from forming and synthesize the highest quality films. Two composition techniques were utilized in this thesis as discussed below.

4.2.1. Energy Dispersive X-ray Spectroscopy (EDS)

Energy dispersive X-ray spectroscopy (EDS) measures the entire energy spectrum of X-rays emitted from the material being analyzed. This type of equipment is typically mounted on a scanning electron microscope (SEM). The most beneficial aspects of this technique are that it does not require standards for calibration and the ability to collect the entire spectrum at once. This though comes at the cost of resolution, where typical values are 130 eV. This issue is apparent when investigating low Cr concentrations in V and Cr solutions, where the energy separation is 11 eV between V $_{\beta1}$ and Cr Kα_1. In addition, and most importantly, EDS is unable to quantify elements lighter than sodium. This includes carbon, one of the key elements in MAX-phases. Therefore only the M:A and M_1:M_2:A ratios were measured for end-member and solid solution films, respectively. Another important consideration pertains to the penetration depth of the electron beam. The higher the beam voltage, the deeper the beam penetrates the film and quite possibly into the substrate. This is a two fold issue; first for deposits of Al-containing films on Al_2O_3, there is no way to distinguish between the Al signal from the substrate or film. To circumvent this issue, Si and/or MgO substrates were also included in deposits. Second, consideration must be given in the case of Si substrate where secondary excitation of Al and C is produced from Si X-rays. Subsequent analysis of films deposited on Si and MgO substrates typically showed a 2-5% increase in Al signal for Si substrates over MgO.

Chemical composition was analyzed using an EDAX EDS equipped on the LEO 1530VP SEM operating with an accelerating voltage of 11 kV. Due to limitations of carbon detection with EDS only Ti, Nb, V, Cr, Al, and Ge were quantifiable with a standard 3% error.

4.2.2. Wavelength Dispersive X-ray Fluorescence (WDXRF)

Wavelength dispersive X-ray fluorescence (WDXRF) is a compositional measurement technique which uses X-rays to excite electrons into higher energy states. Special crystals within the spectrometer diffract the characteristic X-rays generated by the electron transition where the detectors scan the diffracted angle specific to the element being analyzed. This gives the advantages of high resolution, down to 10 eV, and the ability to quantify light elements (down to B). WDXRF also has the advantage of measuring most materials unlike conditions required for a SEM, measurements can be performed under vacuum or atmosphere pressure and samples can be solids, liquids, and nonconductive. Disadvantages of this technique are the limited spot size (<500 μm) and additional analysis time required as each element is scanned individually and most important the system requires standards of similar chemistry and structure. Elemental quantification of all elements, including carbon, was performed with a Rigaku ZSX Primus II WDXRF utilizing Rh K_α radiation standardized to stoichiometric bulk samples.

4.3. Electrical and Thermal Transport

Electrical and thermal transport measurements were carried out on etched microbridges shown in Figures 4.3a and 4.3b, respectively. The bridges were defined by standard photolithographic techniques followed by a wet etch in H_2O + HF + HNO_3 for most systems and Transene Chromium Cermet Etchant TFE© heated to 50 °C for all chromium-containing films. Film thickness was measured on etched samples with an Ambios XP-2 stylus profilometer. The resistivity, Hall effect, and magnetoresistance

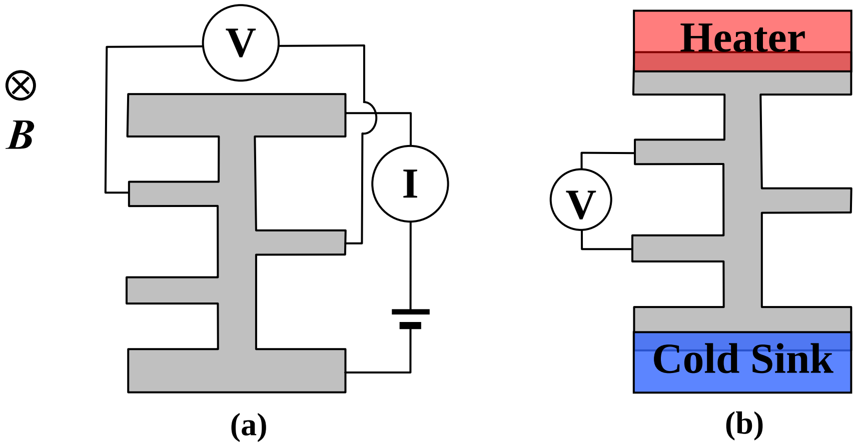

Figure 4.3 Schematics of a) four-probe technique for measuring resistivity, Hall effect, and magnetoresistance with the applied magnetic field perpendicular to the films surface and b) thermal transport for measuring Seebeck effect.

were measured as a function of temperature T for $0.4 \text{ K} \leq T \leq 300 \text{ K}$ range and in magnetic fields B up to 9 T with a Quantum Design Physical Properties Measurement System (PPMS) using a four-probe technique. The Seebeck voltage was measured as a function of temperature T for $2 \text{ K} \leq T \leq 300 \text{ K}$ range also wit the PPMS.

4.3.1. Resistivity

Resistivity measures a materials ability to conduct electrical charge and follows the equation[51]:

$$\sigma = \frac{1}{\rho} = e(n\mu_n + p\mu_p) \tag{4.1}$$

where n and p are the electron and holes carrier densities, respectively; μ_n and μ_p their respective mobilities; e the electronic charge; σ the electrical conductivity. All MAX-phase films measured herein exhibited metal-like behavior, therefore Matthiessen's rule applies.[52] Measurements as a function of temperature give insight into the types of scattering that occurs from defects and impurities, as well as the electron-phonon

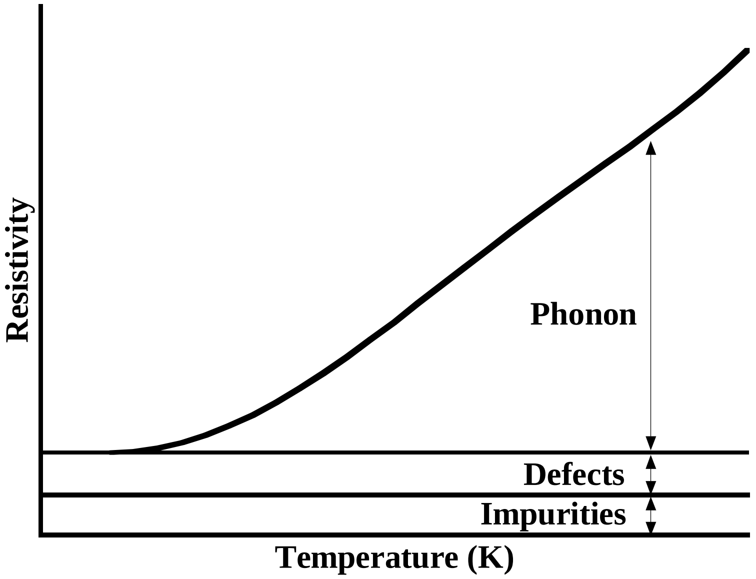

Figure 4.4 Total resistivity for metal-like conductors as defined by Matthiessen's Rule.

coupling (Figure 4.4). The residual resistivity ratio (RRR) defined as $\rho_{293\,\mathrm{K}}/\rho_{4\,\mathrm{K}}$ is a good indication of a materials quality. For example, copper can have values ranging from several tens to several thousands depending upon its purity.

4.3.2. Hall Effect

The Hall effect results from the deflection of the charge carrier (electron or hole) in a material due to the presence of a magnetic field. The Hall voltage (R_H) is measured transverse to the applied electric current when a perpendicular magnetic field is applied (Fig. 4.3a). A more detailed analysis is described in 4.3.4. For single-band materials where a single charge carrier is dominant, the following applies[51]:

$$R_H = \frac{1}{en} \tag{4.2}$$

In the low-field limit of the two-band model, the following applies[51]:

$$R_H = \frac{(\mu_p^2 p - \mu_n^2 n)}{e(\mu_p p + \mu_n n)^2} \tag{4.3}$$

4.3.3. Magnetoresistance

Magnetoresistance is a material property where an applied external magnetic field changes its electrical resistance. The measurement technique is the same as for Hall effect. Ordinary magnetoresistance only changes the resistance at most a few percent; however giant magnetoresistance, colossal magnetoresistance, and tunnel magnetoresistance materials can change their resistance orders of magnitude, though the mechanism is different for these types of magnetic materials. These materials provide next generation of magnetic data storage and sensors. Single band magnetoresistance can be defined as[51]:

$$\frac{\Delta\rho}{\rho(B=0)} = \alpha B^2 \tag{4.4}$$

where $\Delta\rho$ is the change in ρ with field, α the magnetoresistance coefficient, and B the magnetic flux density. For more complex systems a two-band model is required and follows[51]:

$$\alpha = \frac{\mu_n \mu_p np(\mu_n + \mu_p)^2}{(\mu_n n + \mu_p p)^2} \tag{4.5}$$

4.3.4. Carrier Concentration and Mobility

Figure 4.5a represents the raw data from a typical measurement of R_H and α at a fixed temperature. The positive non-saturating quadratic can be fit with a second-order polynomial equation where the square term and intercept are related to α and the linear term related to R_H. In the low-field limit of the two-band model Eqs. 4.1, 4.3, and 4.5

apply. With three equations but four unknowns, one can either solve for *p* as a function of *n*, or alternatively assume $n \approx p$. In order to stay consistent with previous results [5, 27, 30, 31] the latter will be followed and solve for *n(= p)*, μ_n, and μ_p. Figure 4.5b is a representative result for allowed values of *n* at various temperatures. As can be observed as temperature decrease so does the range for *n*, a direct result the higher mobility of the charge carriers.

4.3.5. Seebeck Effect

The Seebeck effect is the difference in voltage potential across a temperature gradient (Fig 4.3b). This effect, along with the opposite known as Peltier effect, is utilized in heating/cooling devices and power generation. Sample configuration is similar to that of resistivity measurements; however the current leads provide heat input and cooling sink with the voltage sensors also measuring temperature. Since sapphire has

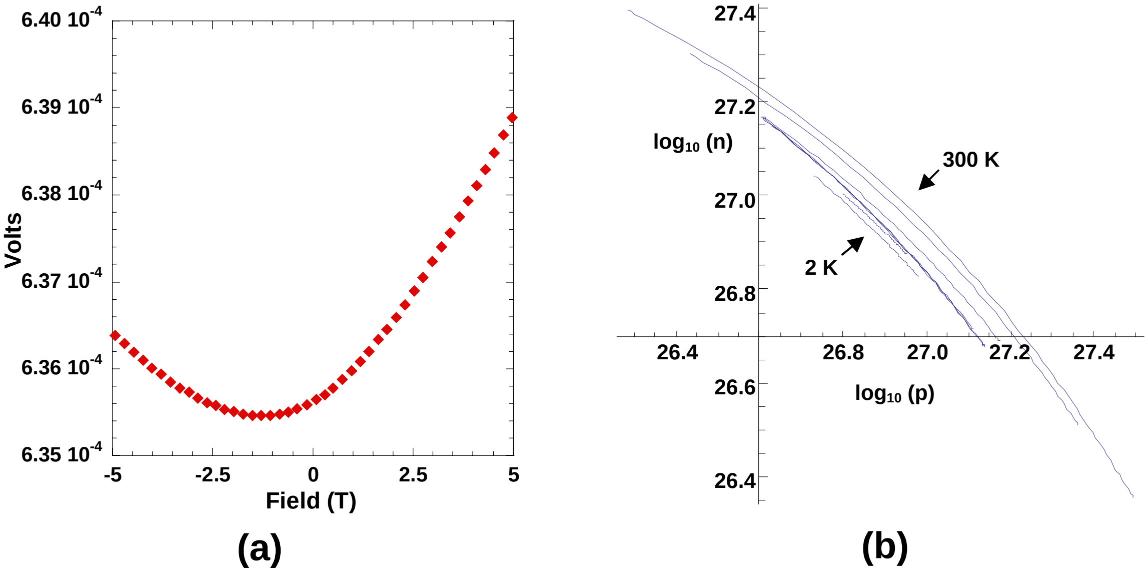

Figure 4.5 a) Representative data from magnetotransport measurements showing positive non-saturating quadratic behavior. b) Representative plot for allowed values for *n* assuming $n \approx p$ from two-band analysis.

such a high thermal conductivity the spacing of the voltage/temperature leads should be maximized to produce a measureable Δ*T*.

4.4. Mechanical and Tribological

Mechanical and tribological properties of films are very important for applications where the coating is to be used for protective purpose. The next two sections will discuss measuring the elastic and frictional properties of films.

4.4.1. Nanoindentation

In order to obtain mechanical properties such as hardness from a material, different types of testing can be used, including microhardness indentation, compression and tensile modulus, and ultrasonic time-of-flight to name a few. All these, however, are designed for bulk materials of certain dimensions. Mechanical properties of films are a challenge; however nanoindentation is a technique that can provide elastic properties

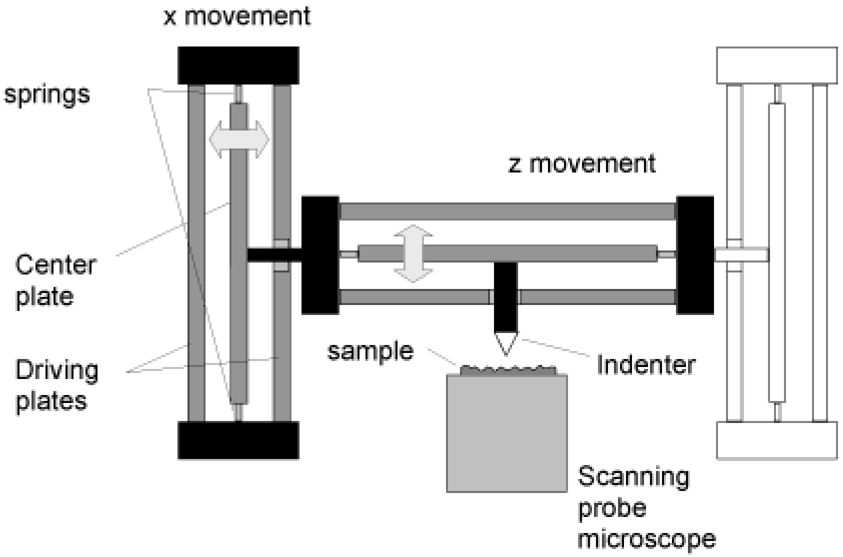

Figure 4.6 Schematic of a Hysitron TriboScope dual-axis capacitive measurement tribological testing unit. The two transducer system measures indentation (z-axis) or lateral force friction (x-axis). Displacement of the center plate with respect to the outer electrodes is measured continuously using a capacitance technique.

when properly performed. Nanoindentation is very similar to microhardness testing with the exception of indentation size and sensitivity of the electronics. Three types of indentation tips are generally available, Berkovich, cube corner, and spherical. The most important consideration for such measurements will be film thickness. For indentation testing, the indent should be no more than 10% of the film thickness; indents performed beyond this will be subject to substrate effects. In order to obtain enough elastic information only films of thickness > 500 nm will be considered for mechanical testing. Only a few measurements were obtained for samples of Nb_2AlC.

4.4.2. Lateral Force Friction

An important potential use of MAX phases, since the basal planes can have extremely low coefficient of friction.[53] The presence of predominantly *c*-axis orientation should minimize the friction while the domains of other orientations may prevent the film from delaminating. Friction was measured with a spherical tip (10-µm radius) on a Hysitron TriboScope used with the JEOL 5200 (Figure 4.6). Lateral force friction measurements are performed by contacting the tip with the film to the prescribed load. Ultra-sensitive capacitive sensors translate the lateral motion of the tip as the sample moves. The subsequent friction results are averaged after initial start scan data is removed. For each sample, measurements were performed in multiple locations under loads of up to 1000 µN with error representing the standard deviation of the measurements. In general, the tip diameter should be at least two orders of magnitude larger than the average surface features observed by AFM scans to minimize surface defect effects. Additionally, atmospheric conditions of temperature and humidity should be monitored as they can impact the results.

Chapter 5: MAX Phase Thin Films in the Ti-Nb-Al-C System

This chapter presents the results for films in the Ti-Nb-Al-C systems. Synthesis and characterization of the Ti_2AlC and Nb_2AlC phases were performed first. Optimal synthesis conditions from the two aforementioned films was determined and applied towards to the synthesis of $(Ti_{1-x}Nb_x)_2AlC$ films.

5.1. Ti_2AlC Thin Films

In the following sections synthesis and characterization of Ti_2AlC thin films will be discussed. Results from this set of experimentation are part of published results in "Investigation of $(Ti_{1-x}Nb_x)_2AlC$ by combinatorial method".[54] Ti_2AlC thin films were first synthesized by Wilhelmsson *et al.*[55] Their studies found epitaxial growth of Ti_2AlC on sapphire occurred at temperatures above 700 °C with highest crystalline quality at 900 °C. A room-temperature resistivity value of 44 μΩ-cm was measured for films deposited at 900 °C. Walter *et al.* investigated coating Ti_2AlC on steel from a stoichiometric compound target in the temperature range of 800-900 °C.[56] Their findings determined the films were Ti deficient requiring additional Ti from a secondary target to achieve proper composition.

5.1.1. Ti_2AlC Synthesis

Only a limited number of depositions of Ti_2AlC were performed in order to verify system capabilities and synthesis requirements. Initial attempts found the deposition system incapable of achieving the required high temperatures for synthesis. Upon completion of a new heater design, described in Section 3.2.2, successful deposits were performed. Figure 5.1 shows the XRD pattern of a 940 nm thick Ti_2AlC film deposited at 875 °C directly on sapphire. The film contained two impurity phases, a small

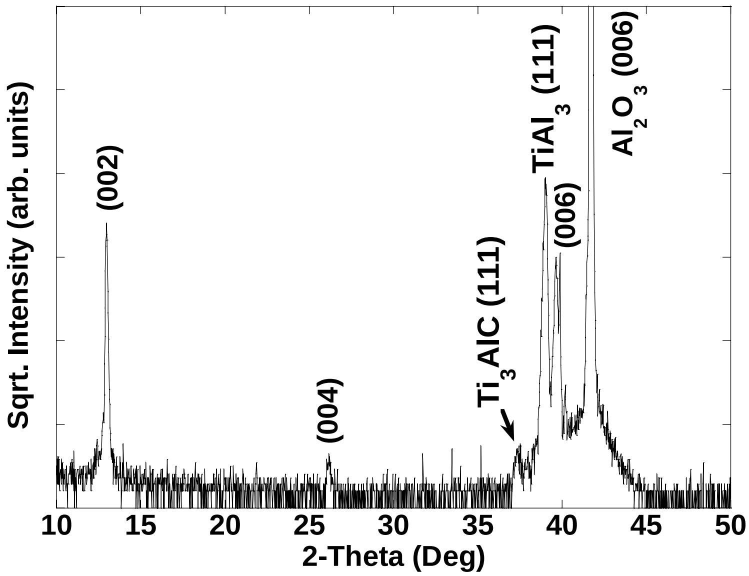

Figure 5.1 X-ray diffraction pattern of Ti_2AlC thin film deposited on sapphire at 875 °C. The film contained secondary phases of Ti_3AlC and $TiAl_3$ due to incorrect composition.

amount of Ti_3AlC and an appreciable amount of $TiAl_3$. EDS found the films Ti composition to be 54 at. % instead of the desired 66 at. %, viz. Al rich. Wilhelmsson also reported Ti_3AlC in deposits of stoichiometric Ti_2AlC at temperatures above 700 °C.[55] Comparison of X-ray diffraction intensities (Fig. 5.1) and composition results from EDS agree the $TiAl_3$ forms to consume the excess Al in the system.

While it has been shown that TiC forms as an interfacial layer between the sapphire and MAX phase films in Ti-Si-C systems,[57-59] this was not the case in the as-deposited film. It is quite possible that the secondary phases provide some lattice relaxation. Interestingly, low temperature deposits yielded the correct composition yet deposits at high temperature led to a Ti deficient film. While one would believe Al to be deficient due to its lower melting point it is not fully known why this was observed. Although phase-pure films were not synthesized, results showed that Ti_2AlC could be synthesized in our chamber at commensurate temperatures to those mentioned previously. Additionally, the calculated *c*-lattice constant for Ti_2AlC was found to be 13.6316 (109) Å, in good agreement with the bulk value of 13.6 Å.

5.1.2. Ti_2AlC Results and Discussion

Figure 5.2 shows resistivity as a function of temperature for the Ti_2AlC thin film. Interestingly, the room-temperature resistivity was only slightly higher with that reported by Wilhelmsson even though the film contained multiple phases. Not surprisingly the film showed an increase in room temperature resistivity over bulk,[30] as expect in thin films due to the higher scattering potential from defects. Hall coefficient as a function of temperature is plotted in Figure 5.3a. R_H was negative for all temperatures in agreement with TiC and bulk Ti_2AlC with a slightly lower value than the latter.[30, 60] Magnetoresistance as a function of temperature is shown in Figure 5.3b. Values were

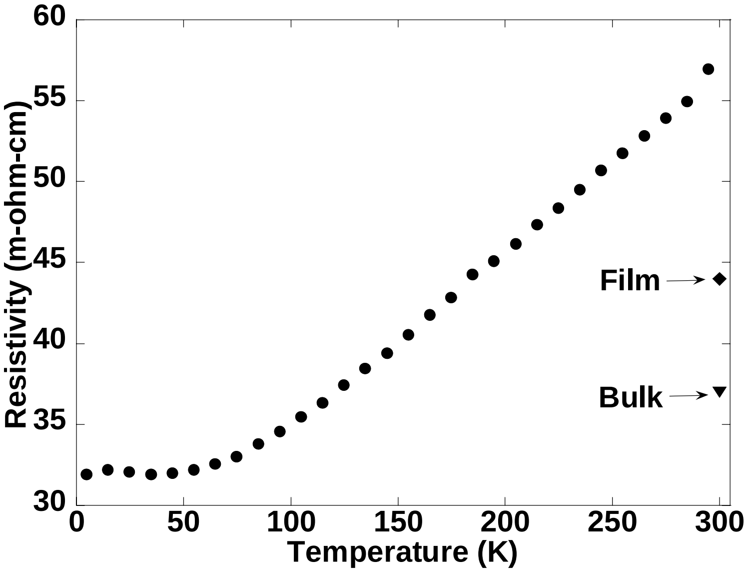

Figure 5.2 Resistivity as a function of temperature for Ti_2AlC thin film. Room temperature resistivity was higher than that reported in film [55] and bulk [29].

small with little temperature dependence and approximately an order of magnitude smaller than that found in bulk.[30] With small R_H values and positive quadratic, non-saturating magnetoresistances a two-band model is required to analyze experimental results as described in Section 4.3.4. Similar to what has been reported in previous studies of MAX Phases, [5, 27, 30, 31] $n \approx p \approx 1.3 \times 10^{27}$ m^{-3} even though the composition was off MAX phase stoichiometry. This suggests the electronic transport is rather robust with respect to chemical composition.

AFM measurements (Fig. 5.4) showed the films to be rough with an average roughness (R_a) of 76 nm. Uniformly spaced features protruded from the film surface, most likely related to the other phases observed in XRD. Since the film was almost 1 μm thick, the relative roughness was ~8%.

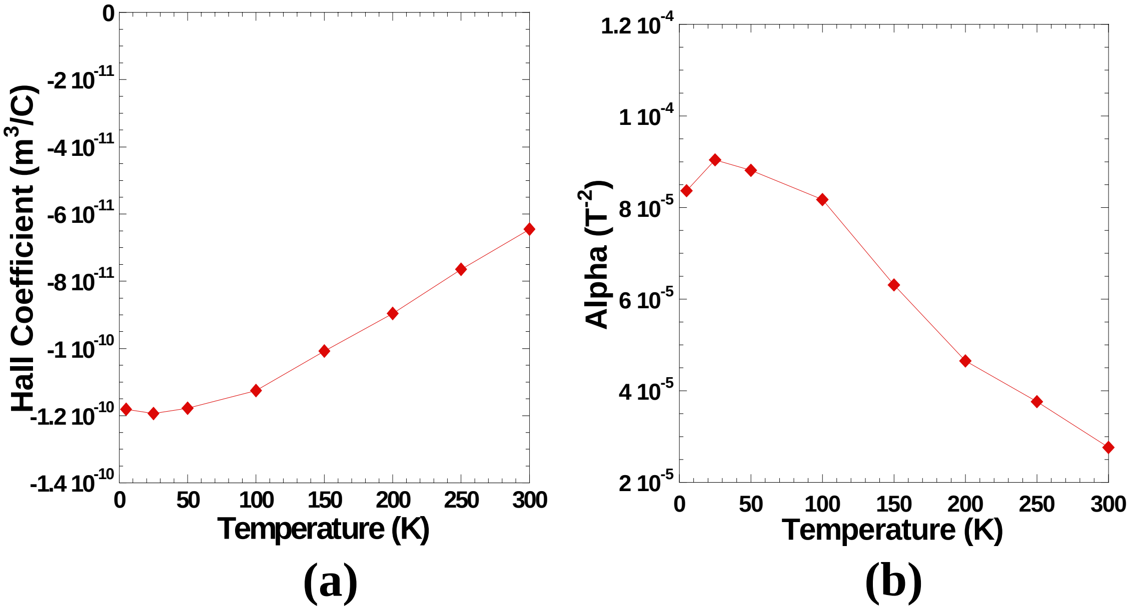

Figure 5.3 a) Temperature dependence of Hall coefficient for Ti_2AlC thin films. b) Magnetoresistance as a function of temperature.

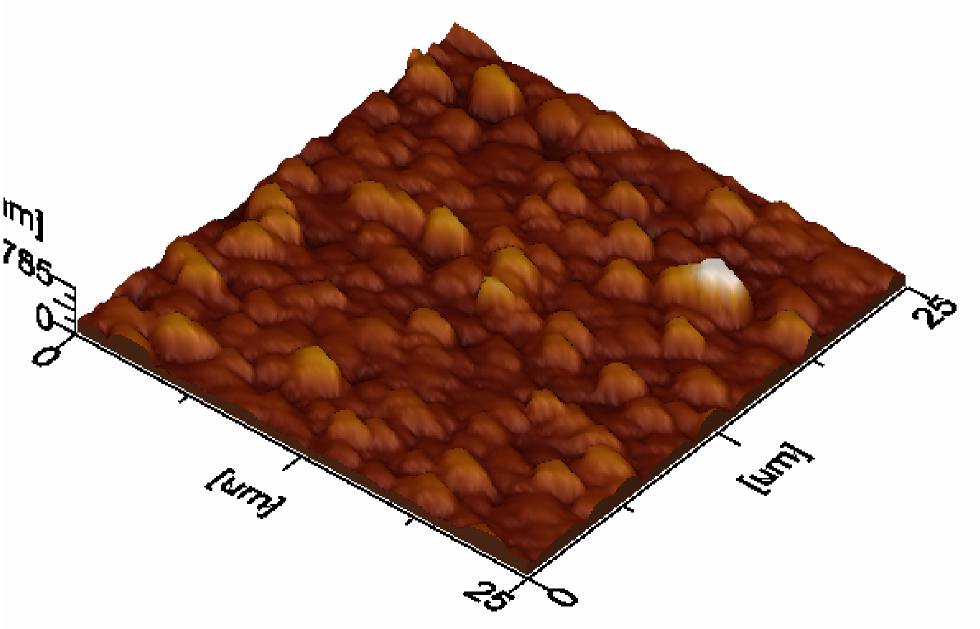

Figure 5.4 Atomic force microscopy image of Ti_2AlC thin film deposited on sapphire at 875 °C. Uniformly spaced features protrude from the film surface yielding an average roughness of ~8% the film thickness.

5.1.3. Ti_2AlC Conclusion

Thin films of Ti_2AlC were deposited on sapphire at 875 °C. Films were found to be Ti deficient, indicating either higher scattering or oxygen contamination in the system. Electronic transport showed metal-like behavior with room temperature resistivity higher than published results for bulk and thin films due to incorrect composition. Both the Hall coefficient and magnetoresistance were analyzed within a two-band model with a carrier concentration $n \approx 1.3 \times 10^{27}$ m^{-3}, in agreement with that of bulk suggesting electronic transport is robust with respect to compositional variations. AFM revealed a moderately rough surface with an average roughness of ~8% of the film thickness attributed to secondary phases.

5.2. Nb_2AlC Thin Films

In the following sections results of the synthesis and characterization of Nb_2AlC thin films will be discussed. There have been no reported publications on the synthesis of Nb_2AlC thin films prior to this work. Results have been published in *Thin Solid Films* as "Synthesis and characterization of Nb_2AlC thin films". [61]

5.2.1. Nb_2AlC Synthesis

Nb_2AlC was a phase which had not yet been synthesized in film. Figure 5.5 shows the ternary phase diagram for the Nb-Al-C systems at 1000 °C found in Ref. [62]. From this the Nb_2AlC denoted by the "H", originally called Hagg phases,[63] exists as

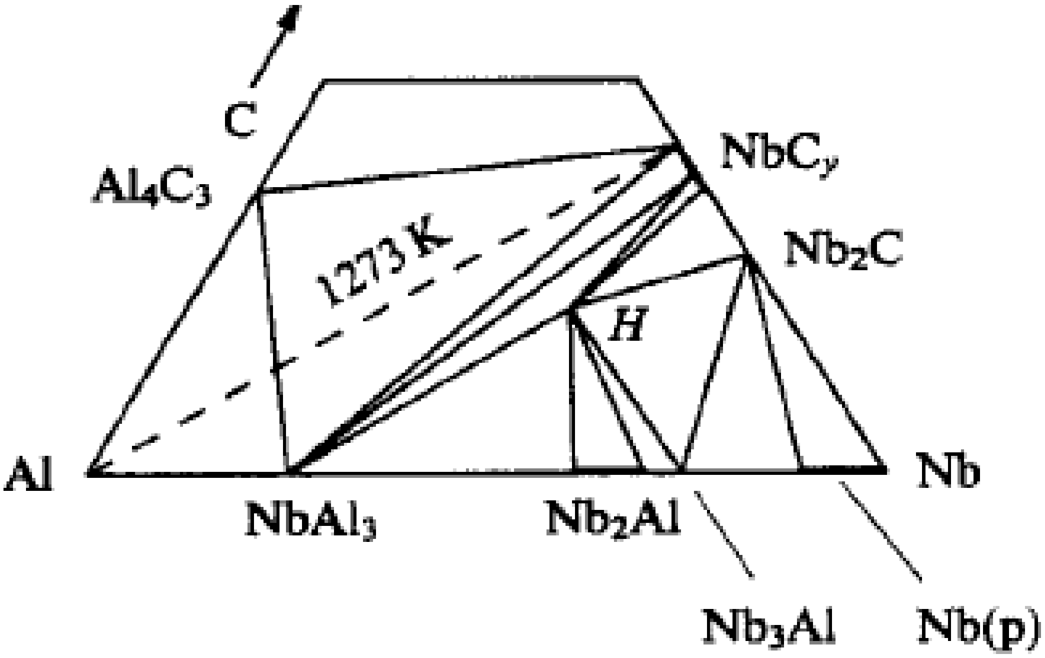

Figure 5.5 Ternary phase diagram for Nb-Al-C systems at 1000 °C from Ref. [62] Nb_2AlC is denoted by the "*H*".

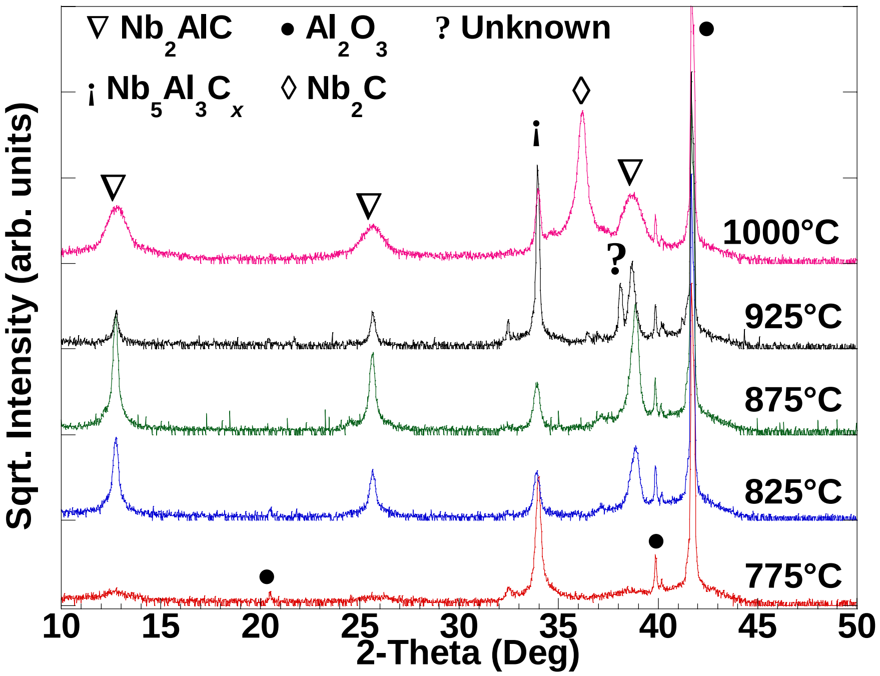

Figure 5.6 X-ray diffraction patterns of Nb_2AlC films deposited at various temperatures. Nb_2AlC texturing is observed at 825 ºC. All films contained secondary phase of $Nb_5Al_3C_x$.

a point phase with binary carbides of NbC_y and Nb_2C and alloys of Nb_2Al and Nb_3Al. Since carbon content can only be qualitatively determined by EDS, carbon content was initially estimated by optimizing films of (111) NbC and (001) Nb_2C grown on sapphire at 850 ºC. The power settings for Nb, Al, and C were 100, 90, and 200 W, respectively, for depositions between 775 and 1000 ºC. Epitaxial films of Nb_2AlC were synthesized directly on *c*-axis sapphire and seedlayers of NbC (111) with the best results directly on sapphire (Fig. 5.6). All films contained a secondary phase believed to be $Nb_5Al_3C_x$. This structure was observed in many other $M_5Al_3C_x$ (53x) ternary systems such Zr, Ta, and Hf as well as the Ti-Si-C and Ti-Ge-C systems. At 775 ºC only $Nb_5Al_3C_x$ was observed with the onset of the Nb_2AlC (002) peak.

Similar to what was found for Ti_2AlC and reported in ref [55] formation of *c*-axis textured Nb_2AlC was observed for deposition temperatures above 800 ºC up to 1000 ºC along with a secondary phase of $Nb_5Al_3C_x$ with the strongest MAX phase XRD peaks at 875-900 ºC. Significant broadening of the MAX phase peaks for the 1000 ºC deposit indicated some disorder in the lattice structure. Interestingly, Nb_2AlC films did not grow on seedlayers of Nb_2C (001) even though the lattice mismatch was almost zero, whereas on the sapphire and NbC (111) the mismatch was around 2%.

Figure 5.7 shows X-ray diffraction patterns of Nb_2AlC films deposited directly on sapphire at 900 °C for thicknesses ranging from 45-800 nm. Clearly, the secondary phase of $Nb_5Al_3C_x$ appeared stronger in the thicker films while the MAX phase reduced substantially. This seems to indicate that the $Nb_5Al_3C_x$ becomes the more stable phase; however, it was not clear as to the importance of carbon content as it was not measurable at the time of synthesis.

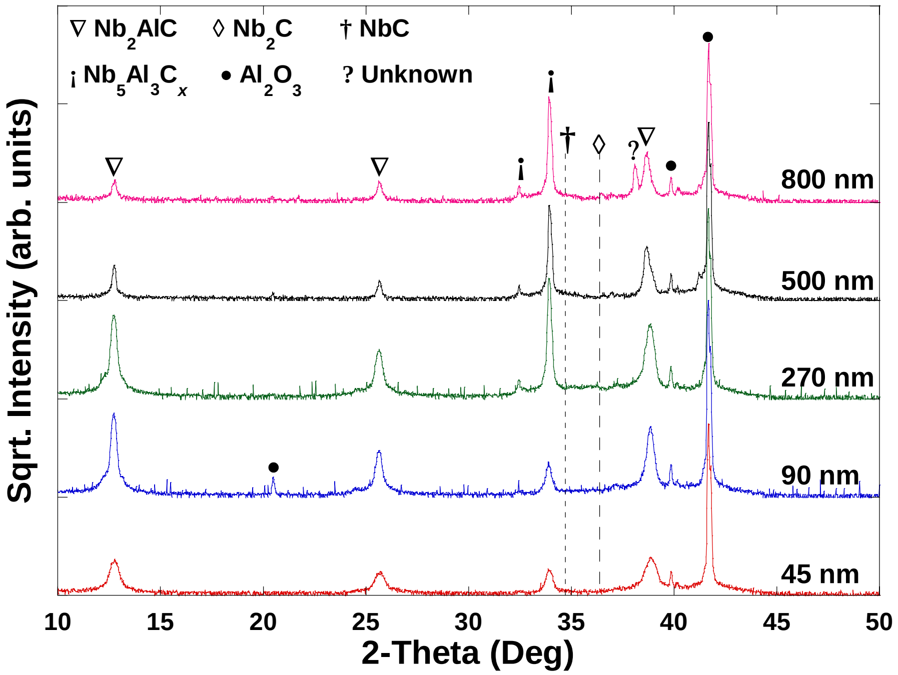

Figure 5.7 X-ray diffraction patterns of various thickness of Nb_2AlC thin films deposited on sapphire at 900 °C. The peak around 33.9° is newly identified phase $Nb_5Al_3C_x$, clearly more intense in thicker films.

Subsequently, a set of films were grown at 900 ºC with varying carbon content with the goal of making single phase Nb_2AlC. Figure 5.8 shows the XRD results for films deposited with various carbon power settings. As expected from the investigation of carbon stoichiometry of NbC and Nb_2C, the strongest diffraction peaks due to Nb_2AlC were observed at a power setting of 200 W; however, $Nb_5Al_3C_x$ was generally observed whenever Nb_2AlC was present. At the highest carbon concentration, the only instance where Nb_2AlC was found without $Nb_5Al_3C_x$, when the MAX phase was the minority phase and the film was predominately NbC. At low carbon concentrations only the $Nb_5Al_3C_x$, NbC, and Nb_2C phases were present. Varying the deposition pressure between 5-18 mTorr had no discernable effect on the resulting films.

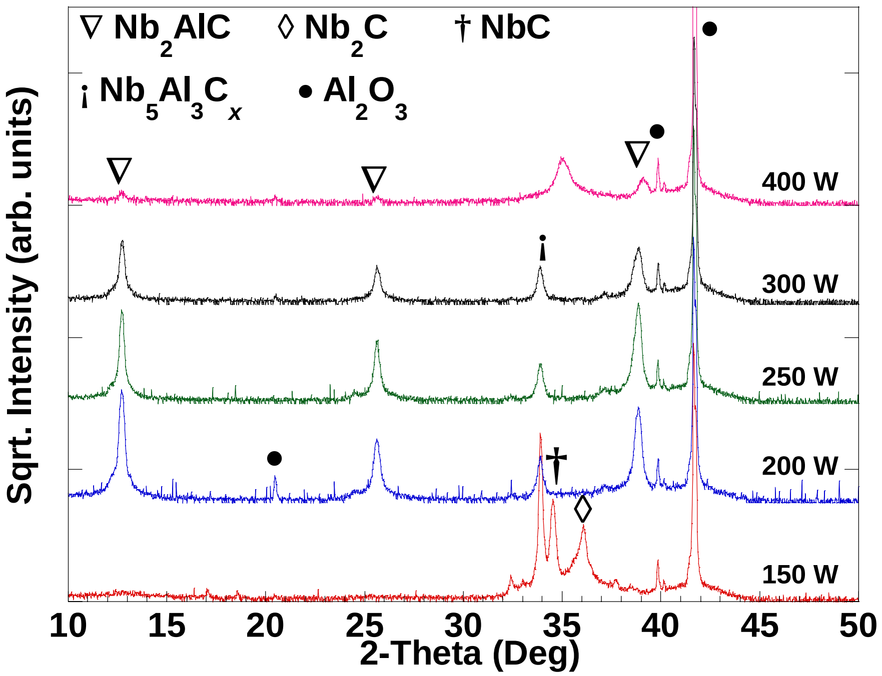

Figure 5.8 X-ray diffraction patterns of Nb_2AlC films deposited at various carbon power settings. Nb_2AlC is observed for carbon power settings with the strongest diffraction occurring between 200-250 W. Secondary phase of $Nb_5Al_3C_x$ is observed in all deposits except the highest carbon power where the predominate phase was Nb_2C.

Nb_2AlC films were also grown on (111) MgO substrates at 6 mTorr and 900 ºC without a seedlayer (Fig. 5.9a). The lattice mismatches between Nb_2AlC and (111) MgO was 4.1%, with the film experiencing a compressive strain. Along with the MAX phase, $Nb_5Al_3C_x$ and an unknown peak around 41.1° were also observed. Despite repeated attempts, albeit was not possible to grow Nb_2AlC films on substrates of Si, R-plane sapphire, or polycrystalline Al_2O_3 substrates. However, polycrystalline $Nb_5Al_3C_x$ was observed on polycrystalline Al_2O_3 substrates (Fig. 5.9b). Lattice refinement of the film found the *a*- and *c*-axis lattice constants to be 7.8096 (76) Å and 5.2753 (15) Å, respectively. Table 5.1 lists the calculated *c* lattice constants for various Nb_2AlC thin films.

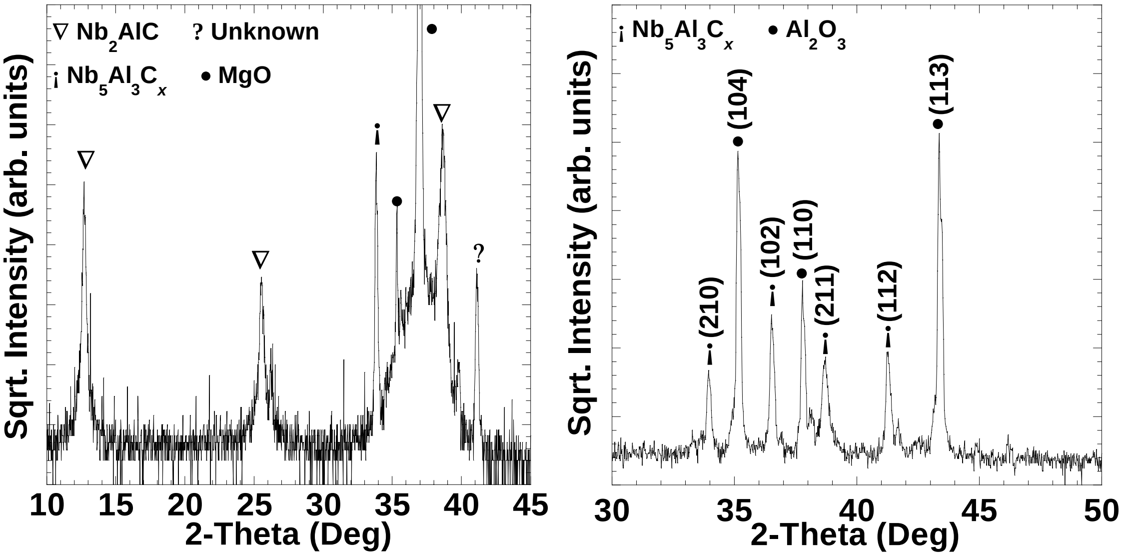

(a) (b)

Figure 5.9 XRD patterns of a) Nb_2AlC thin film grown on MgO (111). $Nb_5Al_3C_x$ and an unknown peak around 41.1° are also observed. b) Polycrystalline $Nb_5Al_3C_x$ growing on polycrystalline Al_2O_3.

Both sets of films grown on sapphire and MgO at 925 °C were epitaxial, as seen from the XRD ϕ scans (Fig. 5.10a) with in-plane relationships of $[1\bar{1}0]_{Al_2O_3} \parallel [100]_{Nb_2AlC}$ and $[101]_{MgO} \parallel [100]_{Nb_2AlC}$, respectively. In-plane relationships for $Nb_5Al_3C_x$ and Al_2O_3 are shown in Fig. 5.10b. Clearly, a two-fold symmetry (twinning) exists between the film and substrate. It is not surprising $Nb_5Al_3C_x$ showed twinning since the *a*-axis lattice parameter is significantly larger than that of sapphire and Nb_2AlC *a*-axis lattice parameters, this must be a means of lattice relaxation. More in depth results are discussed in the following section.

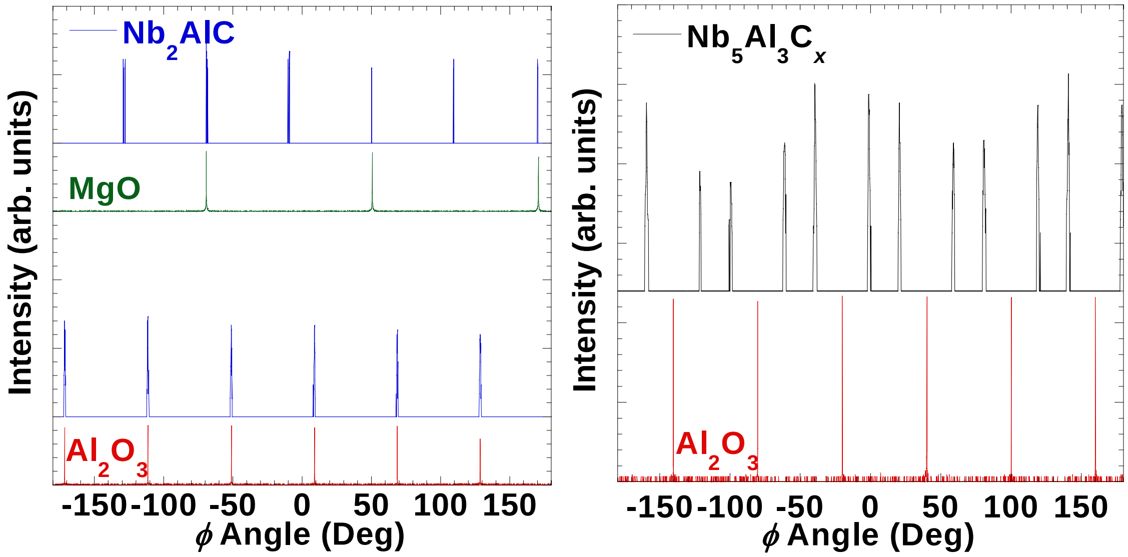

(a) (b)

Figure 5.10 a) Phi scans showing epitaxial relationship of Nb_2AlC on MgO (top) and Al_2O_3 (bottom). b) Phi scan of $Nb_5Al_3C_x$ on Al_2O_3 showing twinning. Films were deposited at 925 °C.

Table 5.1 Properties of Nb_2AlC thin films

Temperature (°C)	Seedlayer /Substrate	*c*-axis (Å)	Resistivity, ρ_{RT} (μΩ-cm)	RRR	Roughness *Ra* (nm)	Friction
925	NbC	13.9049 (67)	54	4.3	10.3 (7)	0.116 (46)
925	Al_2O_3	13.8495 (411)	93	2.3	-	-
900	Al_2O_3	13.8858 (60)	66	2.7	34 (6)	0.070 (32)
850	Al_2O_3	13.8928 (28)	90	1.9	9.1 (18)	0.071 (39)
800	Al_2O_3	13.8857 (539)	-	-	7.2 (4)	0.088 (38)
925	MgO	13.9601 (271)	-	-	8.8 (8)	0.116 (58)
Bulk	-	13.888[a]	39[b]	~2.5[b]	-	-

[a] Reference [17]
[b] Reference [30]

5.2.2. Nb_2AlC Results and Discussion

SEM micrographs of 90 and 270 nm thick Nb_2AlC films shown in Figure 5.11 revealed two different surface morphologies. For 90 nm thick films (Fig. 5.11a), films contained large surface crystals some of hexagonal shape and faceted texture. Thicker films (Fig. 5.11b) showed the surface crystals merged together, forming voids in-between. At this point it can be deduced that the secondary phase of $Nb_5Al_3C_x$ are the hexagonal surface crystals based upon physical shape and continued growth in thicker films, in agreement with the XRD results. This suggested the Nb_2AlC was the base film with the $Nb_5Al_3C_x$ crystals eventually overtaking, leading to predominately surface growth. It was not possible to quantify either phase by EDS as the substrate composition skewed the Al results.

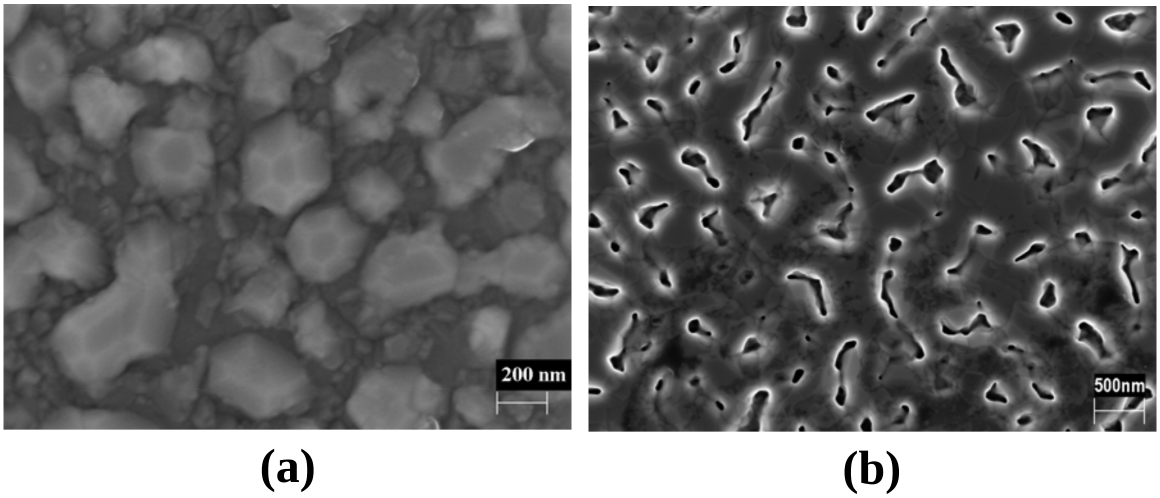

(a) (b)

Figure 5.11 Scanning electron microscope micrographs of a) 90 nm thick Nb_2AlC film clearly showing hexagonal shaped crystals, found to be $Nb_5Al_3C_x$, protrude from the film surface and b) 270 nm thick Nb_2AlC film revealing voids due to the merging of surface crystals. Both films were deposited on sapphire at 900 °C.

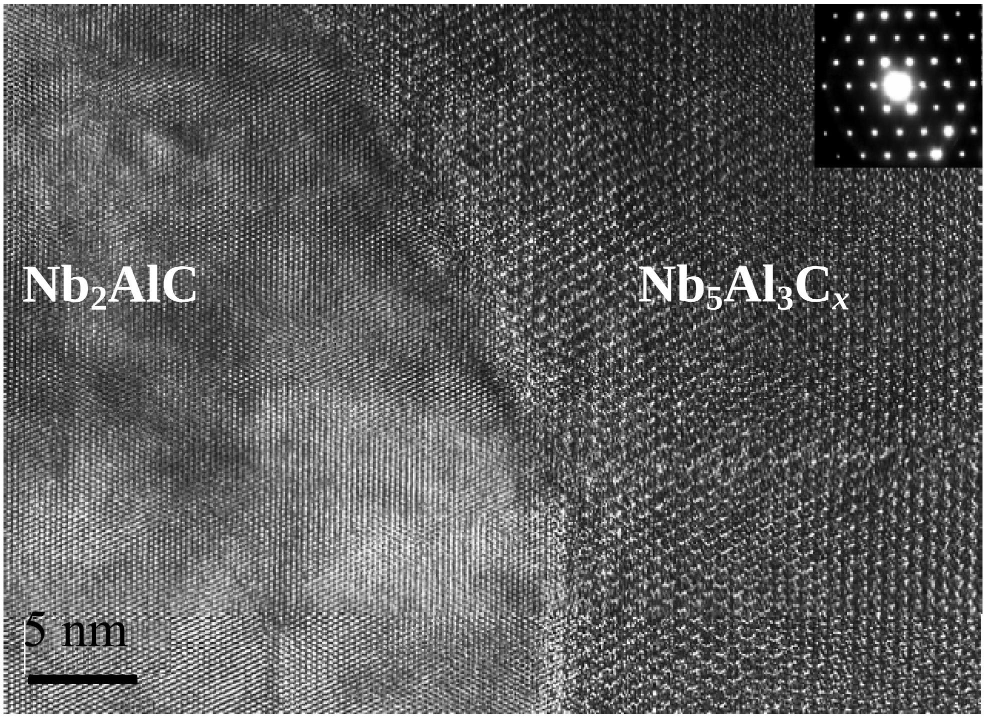

Figure 5.12 Plan-view high-resolution transmission electron micrscope image of Nb_2AlC thin film deposited sapphire at 900 ºC clearly shows two different hexagonal structures. The left side is Nb_2AlC, the right $Nb_5Al_3C_x$, which has a noticeably larger a-lattice constant. Electron diffraction (upper right) confirmed the hexagonal structure with *a*- and *c*-axis lattice constants of 7.746 Å and 5.246 Å, respectively.

Plan-view HRTEM image of an optimized film grown on *c*-axis sapphire (Fig. 5.12) shows two different hexagonal structures – the one on the left was Nb_2AlC and the other had a large *a*-axis lattice parameter. Selected area electron diffraction (SAED) shown in Fig. 5.13 confirmed that this phase (top layer) grows epitaxially *c*-axis oriented with *a*- and *c*-axis lattice constants of 7.746 Å and 5.246 Å, respectively, the latter of which gives rise to the (002) diffraction peak observed at 33.9º. While $Nb_5Al_3C_x$ does not exist in bulk,[64] these lattice constants were clearly consistent with those of other $M_5A_3C_x$ compounds [58, 65]. As can be seen from Fig. 5.13 the in-plane relationship is; $[110]_{Al_2O_3} \parallel [100]_{Nb_2AlC} \parallel [110]_{Nb_5Al_3C_x}$. It can be speculated that since $Nb_5Al_3C_x$ forms at

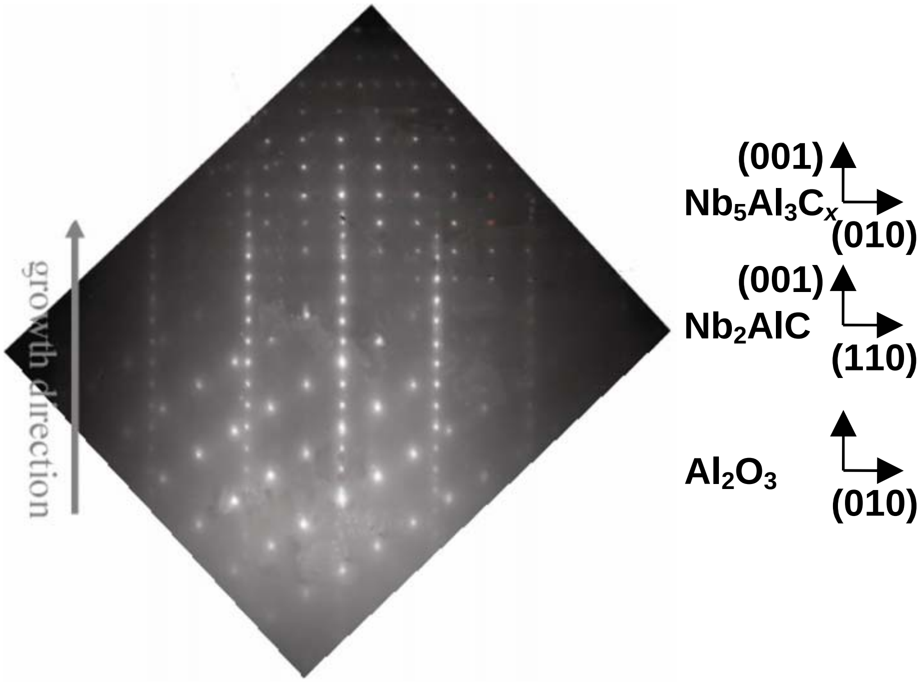

Figure 5.13 Selected area electron diffraction pattern (Left) of a cross section of a 270 nm thick Nb_2AlC film grown on sapphire at 900 ºC. The epitaxial relations between the Al_2O_3, Nb_2AlC, and $Nb_5Al_3C_x$ layers is shown Right.

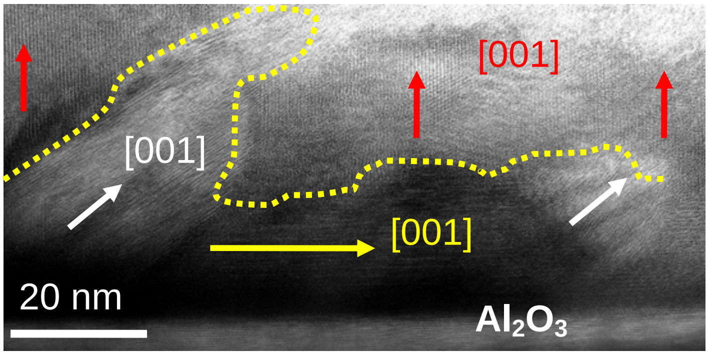

Figure 5.14 Transmission electron microscope cross-section of Nb_2AlC. As seen, initial growth appeared as *a*-axis followed by *c*-axis. Also observed was tilted plane growth.

lower temperature as compared to that of the MAX phases; it was a stabilized phase due to the presence of lattice strain. This behavior may be similar to what happens with epitaxial films of V_2GeC which always have intergrowths of V_8C_7 [66].

TEM cross-sectional analysis (Fig. 5.14) confirmed that the films were predominately single phase. Surprisingly, at the substrate-film interface was an *a*-axis oriented Nb_2AlC layer. Why growth begins this way is not fully understood at this time; however, it may be a means of lattice relaxation. As the thickness increased, tilted planes formed, followed by an orientation change to predominantly (001). It is even more remarkable that (001) Nb_2AlC grows rather well textured on (100) Nb_2AlC but not on any hexagonal (001) seedlayers or substrates with lower lattice mismatch strains.

Figure 5.15 shows the topography of a 90 nm thick film grown on *c*-axis sapphire. The average surface roughness values were generally ≈ 15 % of the total film thickness for all films. Individual grains with hexagonal facets were ~ 350 nm in size with smooth plateau-like tops.

As a result of the complex surface morphology and the $Nb_5Al_3C_x$ phase, nanoindentation and lateral force scratch testing were difficult. However; friction and indentation testing was performed. Table 5.1 lists the average friction coefficients for Nb_2AlC thin films performed at 1000 μN. The values were all small (< 0.12) with smaller values found for films grown directly on sapphire. Multiple nanoindentation results of an 800 nm thin film are shown in Figure 5.16. Initial stress-strain followed a linear behavior up to ~0.1-0.15, where a sudden decrease in stress was observed. It is believed that this decrease was associated with the collapsing of voids and pinholes present in the film, as observed in the SEM images. The elastic modulus, *E*, was 133 GPa for all measurements,

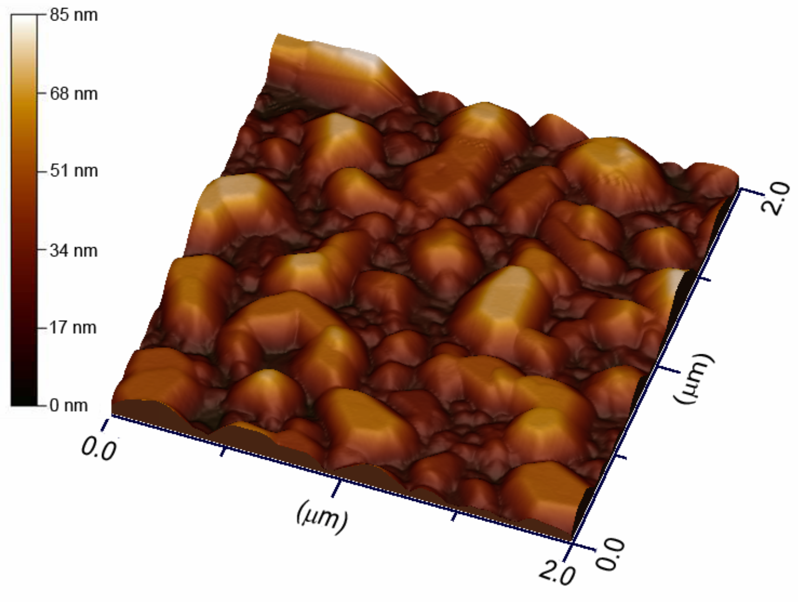

Figure 5.15. Atomic force microscope image of 90 nm thick Nb_2AlC thin film deposited on sapphire at 900 °C. Large features typically hexagonal in shape with smooth plateau-like tops protruded from the film surface. Average roughness was ~15% of the film thickness.

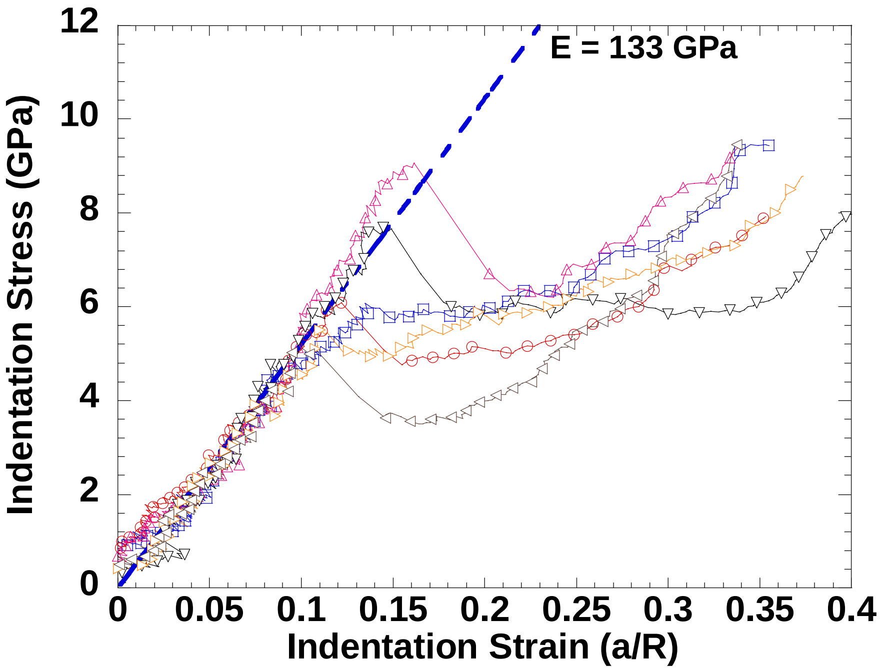

Figure 5.16 Nanoindentation of 800 nm thick Nb_2AlC film. The sudden decrease in stress was most likely due to the collapsing of pinholes and voids in the film. A Young's modulus of 133 GPa was observed for all indents prior to sudden decrease.

much less than that observed for the bulk material of 286 GPa.[30] The large difference is not fully understood at this time; however it can be surmised the measured value is that of the $Nb_5Al_3C_x$ phase growing on top of the Nb_2AlC.

There are four first-order Raman active phonon modes in the M_2AX family,[67] three were observed in films of Nb_2AlC (Fig. 5.17). The lower (ω_1) and middle (ω_2, ω_3) modes are attributed to longitudinal modes in the basal plane while the upper mode (ω_4) to a longitudinal mode along the *c*-axis. Table 5.2 lists the Raman positions for thin film, bulk and calculated modes. While the agreement between film and bulk was reasonable, agreement with calculated values was considerably better.[67, 68] The largest difference

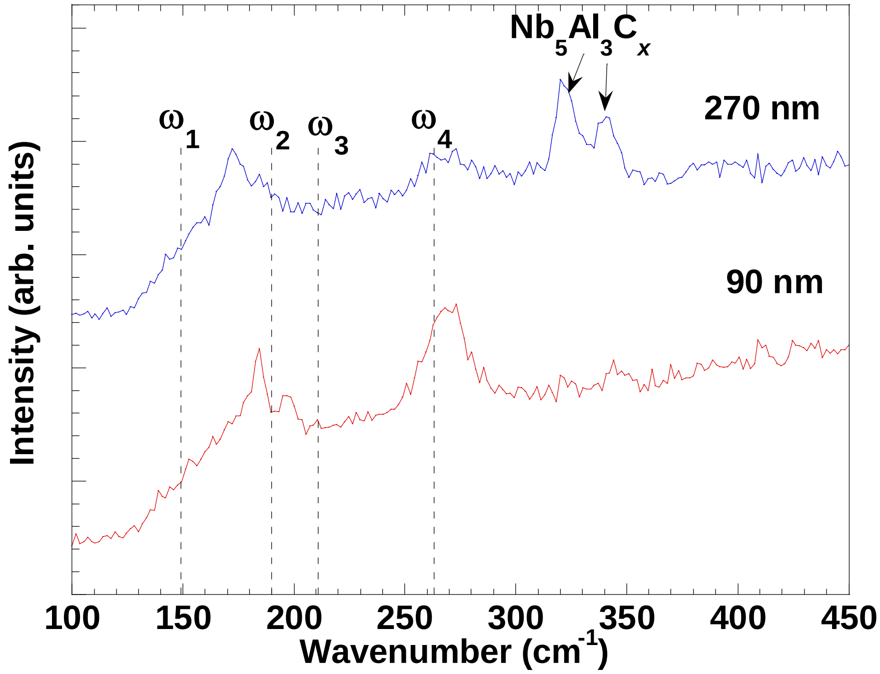

Figure 5.17 Raman spectra of 90 and 270 nm thick Nb_2AlC films deposited at 900 °C. Three of the four modes observed in bulk (dashed lines) are observed in thin film. The shift in the middle two modes was due to lattice strain as those modes are related to bonding in the ab-plane. Two additional modes around 320 and 345 cm^{-1} observed in the 270 nm thick film were associated with $Nb_5Al_3C_x$, in agreement with XRD and TEM results.

Table 5.2 Raman modes for Nb_2AlC.

	Raman Shift (cm^{-1})				
	ω_1	ω_2	ω_3	ω_4	Ref.
Film	-*	198	184	270	This Work
Bulk	149.4	~211	~190	262.8	[67]
Calculated	148	197.7	181.5	268.3	[67]
Calculated	144	211	193	251	[68]

* Below system measurement range.

between the bulk and film occurred for the ω_2 and ω_3 modes, which are longitudinal modes in the basal plane where the atoms are somewhat constrained due to lattice strain. There were also peaks near 320 and 345 cm^{-1} observed in the 270 nm thick film, which were attributed to $Nb_5Al_3C_x$. The fact these peaks are observed in the thicker film is in good agreement with XRD results (Fig. 5.7) showing stronger diffraction intensities for the $Nb_5Al_3C_x$ in thicker films indicating more phase presence. In addition, cross-section TEM analysis (Fig. 5.13) revealed the $Nb_5Al_3C_x$ grows predominately on top of the Nb_2AlC phase, making it more measurable by Raman.

The electrical resistivity, ρ, of all films was metal-like down to 2 K (Figs. 5.18, 5.19, 5.20). Resistivity as a function temperature for Nb-Al-C thin films deposited at various temperatures is shown in Figure 5.18. The highest temperature deposited film yielded the highest room temperature resistivity due to the strong presence of Nb_2C. The film deposited at 875 °C, which was the most phase pure Nb_2AlC, showed the lowest resistivity. The film deposited at 775 °C was predominately $Nb_5Al_3C_x$. Resistivity as a function temperature for different thickness Nb-Al-C thin films deposited at 900 °C is

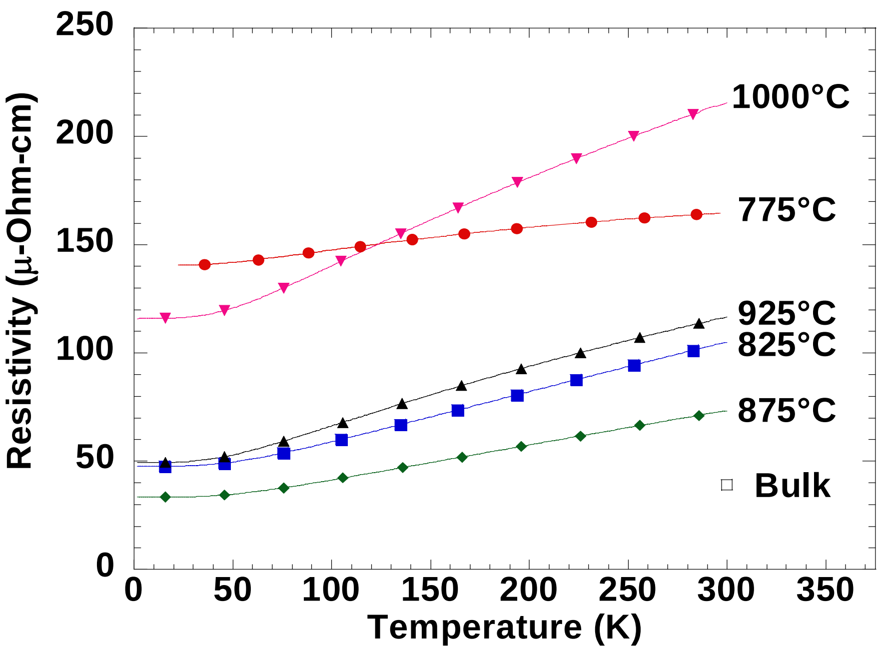

Figure 5.18 Resistivity as a function temperature for Nb-Al-C thin films deposited at various temperatures. The highest temperature deposited film yielded the highest room temperature resistivity due to the strong presence of Nb_2C. The film deposited at 875 °C, which was the most phase pure Nb_2AlC, showed the lowest resistivity. The film deposited at 775 °C was predominately $Nb_5Al_3C_x$.

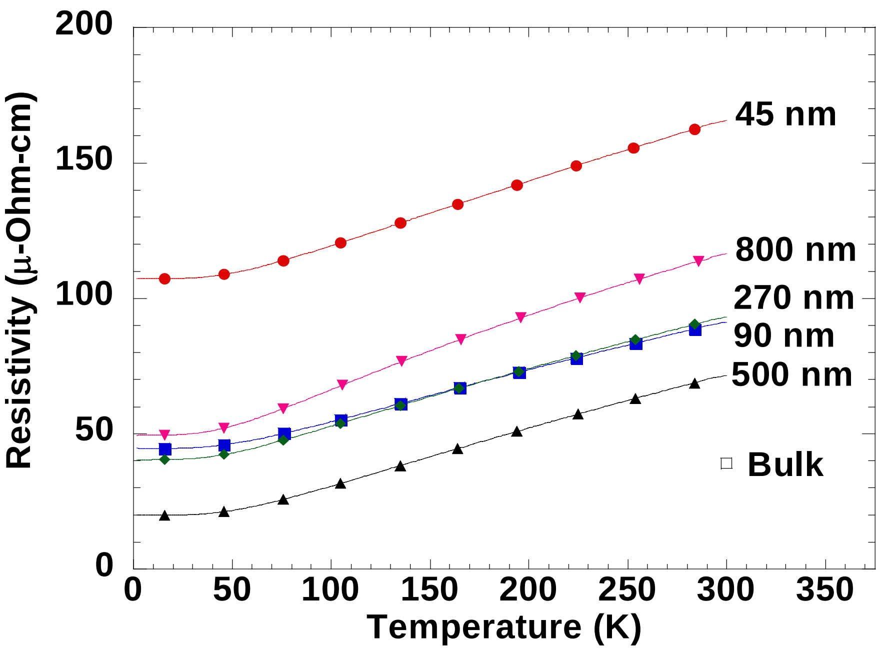

Figure 5.19 Resistivity as a function temperature for different thickness Nb-Al-C thin films deposited at 900 °C. The thinnest film yielded the highest resistivity due to higher scattering potential.

shown in Figure 5.19. The thinnest film yielded the highest resistivity due to higher scattering potential. Figure 5.20 shows resistivity as a function temperature for Nb-Al-C thin films deposited at various carbon cathode powers. The lowest power setting yielded the highest resistivity and likewise the highest power setting the lowest resistivity. The room-temperature value of ρ in the stoichiometric films was about twice that of the bulk even though the RRR were about the same at ~ 2.5.[30] This suggests that unlike the Ti_2GeC system,[5] there was measurable anisotropy in the conductivity. Table 5.1 lists the room-temperature resistivity values for various Nb_2AlC films. Low-temperature transport revealed a superconducting transition at 440 mK (Fig. 5.21). In a previous study,[30] low-temperature measurements were conducted to 5 K using a parallel-piped sample of approximate dimensions 1 mm x1 mm x12 mm. Re-measuring the same Nb_2AlC bulk sample to 1.8 K did not show any superconducting transition. It was believed the large sample size, which required a significantly higher current in order to obtain measurable voltages, was experiencing Ohmic heating at the contacts, which increased the sample temperature above the transition threshold. Sample size was reduced to 0.9 mm x 0.06 mm x 1.8 mm and subsequently re-measured (Fig. 5.21) at lower current, revealing the onset of superconduction with an estimated critical temperature of ≈ 390 mK. This suggests that the carbon stoichiometry of the film was probably rather close to that of the bulk, since it is well known that the T_c of niobium carbide depends rather sensitively on the carbon content [69].

Magnetotransport was performed on Nb_2AlC thin films of various thickness and carbon cathode power settings deposited on sapphire at 900 °C. The Hall coefficient, R_H, is plotted in Fig. 5.22a as a function of temperature. Values were mostly independent of

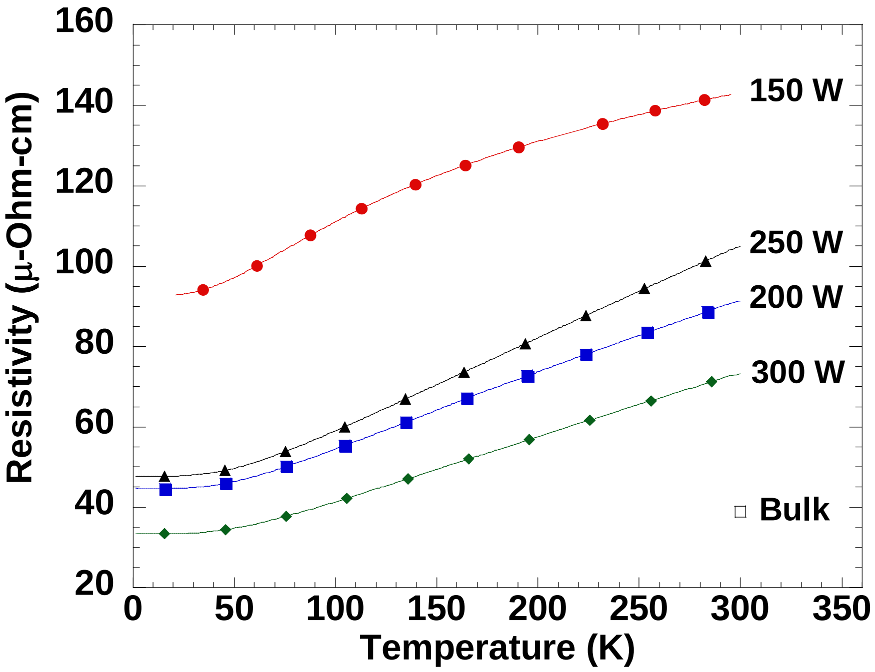

Figure 5.20 Resistivity as a function temperature for Nb-Al-C thin films deposited at various carbon cathode powers. All showed metal-like behavior with the lowest power setting yielding the highest resistivity and likewise the highest power setting the lowest resistivity.

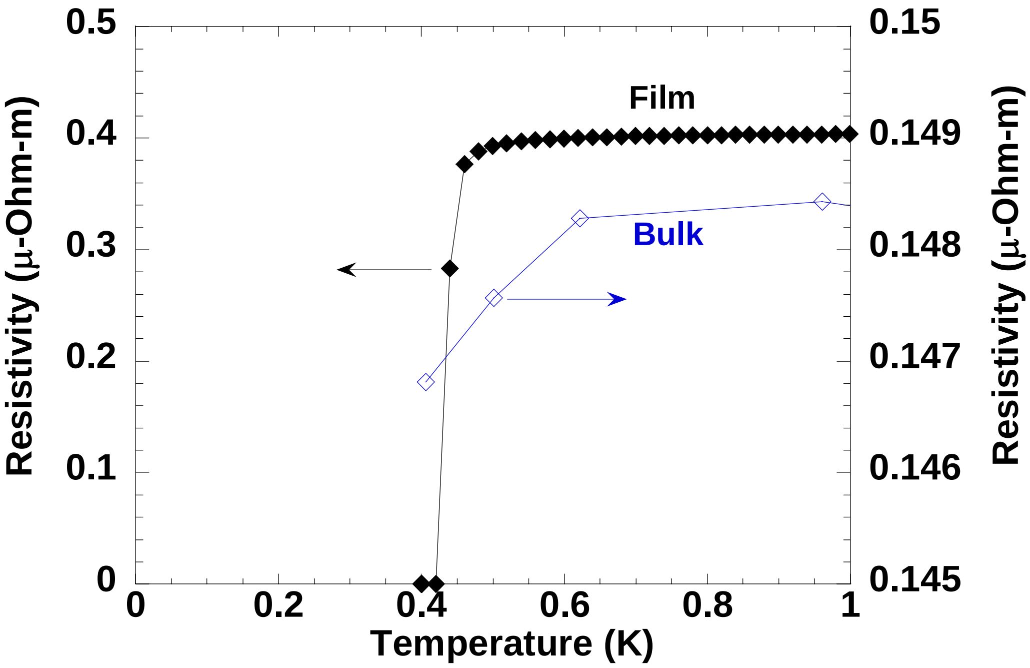

Figure 5.21 Low-temperature electronic transport of Nb_2AlC thin film (solid marker) deposited on sapphire at 900 °C and bulk (open marker). A superconducting transition around 440 mK was observed in thin film and the onset observed in bulk.

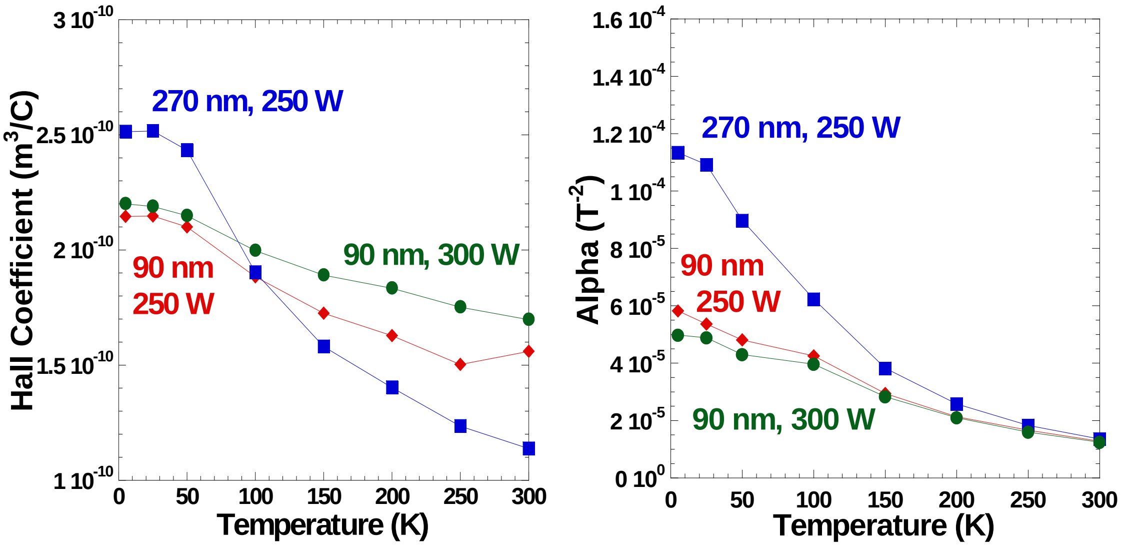

Figure 5.22 Magnetotransport results for Nb_2AlC thin films of various thickness and carbon cathode power settings deposited on sapphire at 900 °C. a) Temperature dependence of Hall coefficient. Values were mostly independent of carbon power setting, while small variation was observed for film thickness. b) Magnetoresistance as a function of temperature. Values were almost identical for both carbon power settings, while a small increase was observed for the thicker films at low temperature.

carbon power setting, while small variation was observed for film thickness. Values were similar to those found in bulk with exception to sign.[30] Figure 5.22b is a plot of magnetoresistance, α, as a function of temperature. Values were small and increase slightly at lower temperatures, in excellent agreement with previous results.[30] Values for both carbon power settings were almost identical, while a slightly larger increase was observed for the thicker film at low temperature consistent with the higher RRR value observed in the film. At this point it is apparent from films deposited at different carbon power settings that variations in carbon composition do not impact magnetotransport properties significantly. With small R_H values and positive quadratic, non-saturating magnetoresistances a two-band model is required to analyze experimental results as described in Section 4.3.4. Results are in agreement to what has been reported in previous electronic transport studies of MAX phases with the carrier concentration was found to be $n \approx 1.75 \times 10^{27}$ m^{-3}.[5, 27, 30, 31]

5.2.3. Nb_2AlC Conclusion

In conclusion, epitaxial thin films of Nb_2AlC were synthesized on (001) sapphire and (111) MgO with and without binary carbide seedlayers. The best results were obtained on *c*-axis sapphire at 900 °C without the use of seedlayers. All films contained intergrowths of a new epitaxial phase $Nb_5Al_3C_x$ with *a*- and *c*-axis lattice constants of 7.746 Å and 5.246 Å, respectively. Film roughness was approximately 15% the film thickness with large hexagonal surface crystals attributed to the new phase. The resistivity was metal-like and appears to have weak anisotropy. A superconducting transition was found at 440 mK. Both the Hall coefficient and magnetoresistance were small and positive with a carrier concentration found from a two-band analysis of $n \approx p \approx 1.75 \times 10^{27}$ m^{-3}. Lateral force friction yields a low friction value of 0.062. The elastic modulus as found by nanoindentation was 133 GPa, significantly lower than that of bulk, attributed to voids within the film and secondary phase $Nb_5Al_3C_x$.

5.3. $(Ti_{1-x}Nb_x)_2AlC$ Thin Films

Following the successful synthesis of Ti_2AlC and Nb_2AlC the chamber was modified for combinatorial depositions. Results have been published in *Applied Physics Letters* as “Investigation of $(Ti_{1-x}Nb_x)_2AlC$ by combinatorial method”.[54] For comparison purposes, only one bulk composition in the $(Ti_{1-x}Nb_x)_2AlC$ system has been previously synthesized and characterized, that being $(Ti_{0.5}Nb_{0.5})_2AlC$.[16, 17] Complete mixing was observed with the resistivity of the solution higher that both end-members.

Mechanical testing found no indication of solid solution hardening. Wang and Zhou published a theoretical study on elastic stiffness in the M_2AlC (M = Ti, V, Cr, Nb) systems.[70, 71] Their findings suggested the shear modulus c_{44}, which is directly related to hardness, saturated to a maximum as the valence electron count is in the range of 8.4-8.6. For the systems studied only $(M,M')_2$AlC (M and M' = V, Nb, and Cr) should show solid solution hardening, in agreement with results for bulk $(Ti_{0.5}Nb_{0.5})_2AlC$ which showed no hardening.[17]

5.3.1. $(Ti_{1-x}Nb_x)_2AlC$ Synthesis

Initial attempts of depositing directly on sapphire resulted in only binary $(Ti_{1-x}Nb_x)C$ and Ti_2AlC phases. It is well established that Ti-based MAX phase films usually require a seedlayer to facilitate growth,[57-59] although other materials in the MAX phase family such as Nb_2AlC[61] and V_2GeC[66] grow better directly on sapphire. Therefore, a ~15 nm seedlayer of TiC was deposited prior to the MAX phase synthesis. Here two things should be noted. One, the seedlayer was deposited *in-situ* and therefore there was a gradient across the substrate due to the Ti target position. Second, deposition temperature of the seedlayer was 700 ºC, a temperature low enough to prevent the solid state reaction of TiC and Al_2O_3 forming Ti_2AlC, as described in Appendix A. EDS measurements showed that $(Ti_{1-x}Nb_x)_2AlC$ was deposited for x ranging from 0.03-0.96 while the M-A ratio was maintained between 1.9-2.1. XRD results (Fig. 5.23) clearly showed (001) MAX phase peaks along with the initial TiC seed layer and a secondary phase of $(Ti_{1-x}Nb_x)C$ (111). However, it should be noted that Nb_2AlC [61] and V_2GeC [66] films always showed secondary phases regardless of film chemistry, similar to the pseudo-binary carbide $(Ti_{1-x}Nb_x)C$ found in the present films. ϕ scans, Figure 5.25,

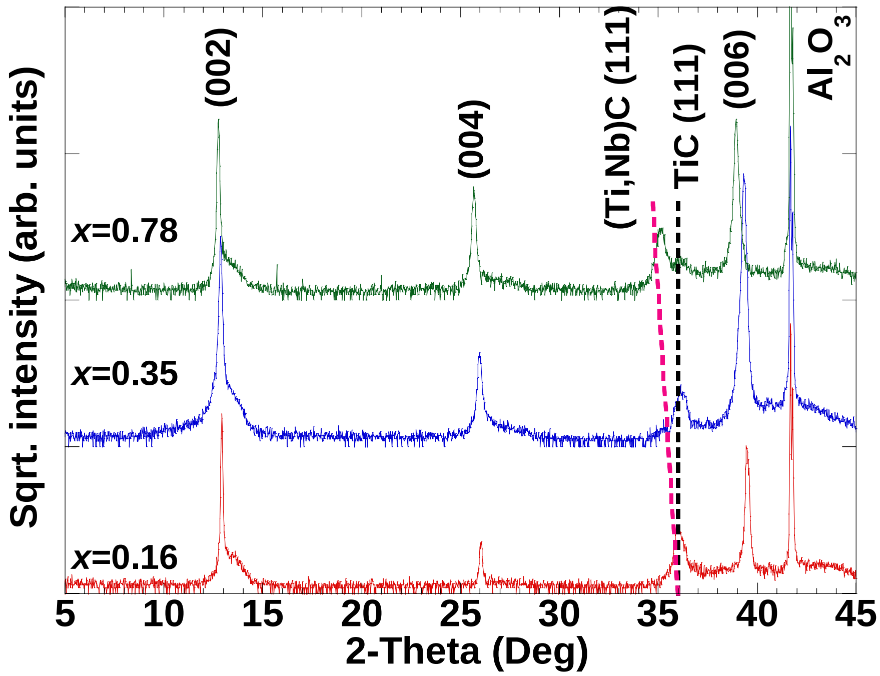

Figure 5.23 X-ray diffraction patterns for different compositions of $(Ti_{1-x}Nb_x)_2AlC$ thin films grown on TiC (111) seedlayers show textured growth in the (001) orientation. A shift in seedlayer peak position indicated possible incorporation of Nb forming (Ti,Nb)C.

confirmed that the films were epitaxial with the same in-plane relationship as the end members.

Interestingly, two new phases were observed during combinatorial synthesis. Figure 5.24a shows XRD of single phase $(Ti_{1-x}Nb_x)_3AlC_2$. Table 5.3 shows XRD results observed for the thin film compared to known values of Ti_3AlC_2 and theoretical values of Nb_3AlC_2.[72, 73] Vegard’s law indicates substitution of Ti by Nb up to approximately 9 at. %, in good agreement with EDS measurements. The second new phase observed was $(Ti_{1-x}Nb_x)_4AlC_3$, shown in Figure 5.24b. Clearly the phase was not strongly ordered as observed by noting the peak widths. Table 5.4 shows XRD results for the thin film compared to the theoretical values for Ti_4AlC_3 and Nb_4AlC_3.[73] Vegard’s law indicates the substitution of Nb to be less than the composition determined by EDS. This possibly indicated a slight miscibility issue, however, lattice calculations of the observed $(Ti_{1-x}Nb_x)C$ phases indicate a higher than measured Nb concentration suggesting that the 413 may be in complete solution while the remaining Nb was utilized in the binary phase. This was not the case for 312 films as calculations from $(Ti_{1-x}Nb_x)C$ did not follow a linear behavior, most likely due to carbon composition. In both cases, the 312 and 413 phases emerge as single phase followed by conversion to the 211 phase. Attempts to synthesize either phase individually (non-combinatorial) proved unsuccessful yielding the solid solution 211 phase only suggesting the phases were highly metastable.

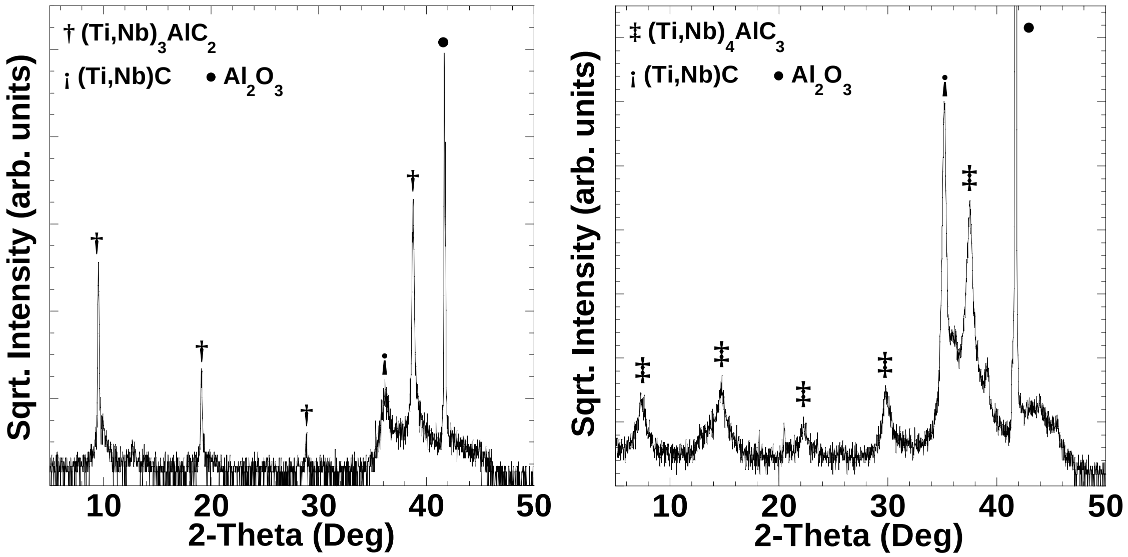

(a) (b)

Figure 5.24 a) Representative X-ray diffraction pattern of $(Ti_{1-x}Nb_x)_3AlC_2$ thin film grown on TiC (111) seedlayer. The 312 phase was observed for x~0.08-0.10 as measured by EDS. b) Representative XRD of $(Ti_{1-x}Nb_x)_4AlC_3$ thin film grown on TiC (111) seedlayer. The 312 phase was observed for x~0.55-0.60 as measured by EDS.

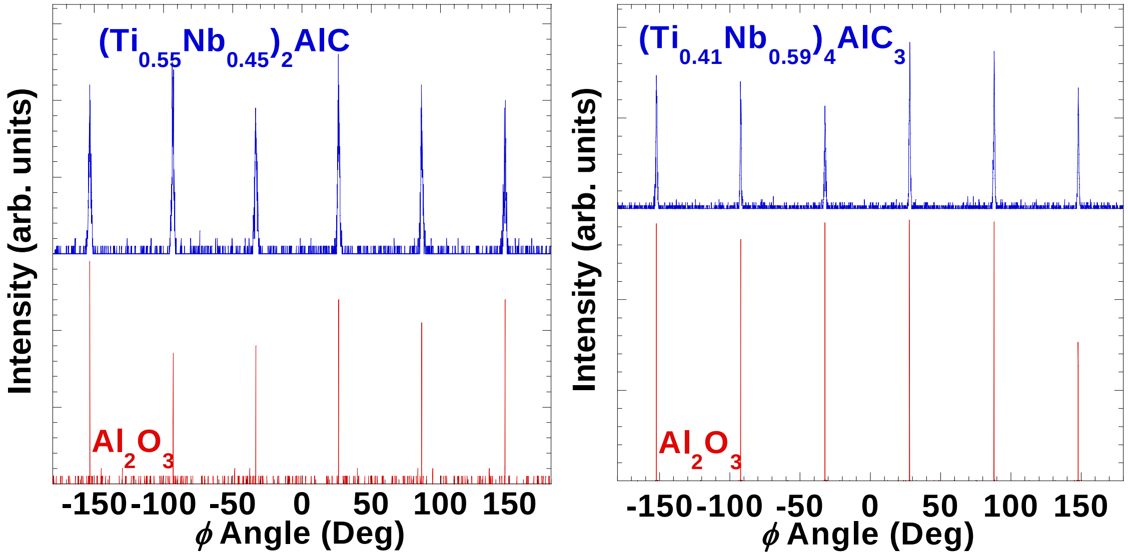

(a) (b)

Figure 5.25 Phi scans showing epitaxial relationship between Al_2O_3 and a) $(Ti_{0.55}Nb_{0.45})_2AlC$ b) $(Ti_{0.41}Nb_{0.59})_4AlC_3$.

Table 5.3 XRD analysis for Ti_3AlC_2 and theoretical Nb_3AlC_2 compared to those observed in $(Ti_{1-x}Nb_x)_3AlC_2$ films. Nelson-Riley analysis (Section 4.1.1) was used to calculate observed *c*-axis lattice constant. Calculated Nb (at. %) was extrapolated by assuming linear behavior (Vegard's law) between end member *c*-axis lattice constants.

	Ti_3AlC_2	Nb_3AlC_2	Sample A	Sample B	Sample C	Sample D
hkl	2θ (°)[a]	2θ (°)[a]	Observed 2θ (°)			
(002)	9.517	9.19	9.579	9.521	9.503	9.523
(004)	19.154	18.44	19.123	19.108	19.080	19.099
(006)	28.925	27.82	-	28.824	28.803	-
(008)	38.817	37.39	38.921	38.790	38.756	38.750
(0010)	49.196	47.24	-	-	-	-
(0012)	59.933	57.47	-	-	-	-
(0014)	71.289	68.24	-	70.953	70.913	70.968
(0016)	83.518	79.74	-	-	-	-
c lattice (Å)	18.501	19.241	18.5422 (644)	18.5715 (73)	18.5792 (64)	18.5805 (16)
Nb calculated (at. %)			4.5	7.7	8.6	8.7
Nb from EDS (at. %)			8.5	9.4	10.2	10.1
Resistivity (μΩ-cm)			97	83	70	63
RRR			1.4	1.5	1.5	1.5
Roughness, *Ra* (nm)			4.2 (11)	2.8 (5)	3.7 (8)	5.7 (8)

[a] Theoretical calculation Ref [73]

Table 5.4 XRD analysis for theoretically predicted phases Ti_4AlC_3 and Nb_4AlC_3 compared to those observed in $(Ti_{1-x}Nb_x)_4AlC_3$ films. Nelson-Riley analysis (Section 4.1.1) was used to calculate the *c*-axis lattice constant. Calculated Nb (at. %) was extrapolated by assuming linear behavior (Vegard's law) between end member *c*-axis lattice constants. Similarly, calculated Nb (at. %) from $(Ti_{1-x}Nb_x)C$ was extrapolated by assuming linear behavior between end member *a*-axis lattice constant.

hkl	Ti_4AlC_3 2θ (°)[a]	Nb_4AlC_3 2θ (°)[a]	Sample A	Sample B	Sample C	Sample D	Sample E
					Observed 2θ (°)		
(002)	7.50	7.26	7.346	7.392	7.388	7.392	7.395
(004)	15.03	14.54	14.687	14.672	14.743	14.650	-
(006)	22.62	21.89	22.306	22.275	22.221	22.406	22.424
(008)	30.32	29.33	29.892	29.818	29.895	29.858	29.808
(0010)	38.16	36.89	37.438	37.474	37.480	37.426	37.357
(0012)	46.19	44.63	-	-	-	-	-
(0014)	54.47	52.59	-	-	-	-	-
(0016)	63.07	60.83	-	-	-	-	-
(0018)	72.08	69.44	70.757	70.780	-	-	-
(0020)	81.65	78.52	-	80.022	79.968	79.985	79.998
c lattice (Å)	23.5841	24.364	23.9259 (524)	23.9751 (464)	23.9739 (329)	23.9418 (994)	23.9367 (749)
Nb calculated (at. %)			43.9	50.2	50.1	46.0	48.8
Nb from EDS (at. %)			60.0	58.6	57.6	55.6	55.0
Nb calculated from $(Ti_{1-x}Nb_x)C$ (at. %)			66.8	70.4	68.4	65.3	62.7
Resistivity (μΩ-cm)			217	283	213	236	193
RRR			1.05	1.03	1.04	1.07	1.1
Roughness, *Ra* (nm)			24.2 (8)	-	21.7 (10)	20.7 (12)	23.2 (36)

[a] Theoretical calculation Ref [73]

5.3.2. $(Ti_{1-x}Nb_x)_2AlC$ Results and Discussion

Figure 5.26a shows the *c*-axis lattice constant as a function of *x* and the observed linear relation agrees with Vegard's law and confirms the solubility across the entire range. A slight increase in lattice constant over the expected value results from the compressive stress of the substrate based on the surface reconstruction of sapphire.[73] Figure 5.26b shows the lattice parameter of the $(Ti_{1-x}Nb_x)C$ secondary phase, the results of which also agreed well with Vegard's law. The deviations in its lattice parameter are most likely due to non-stoichiometry commonly found in the binary carbide systems.[74]

AFM measurements found the films had roughness values ranging from 6-45 nm. As mentioned in Section 4.1.5, the very nature of the growth of compositional

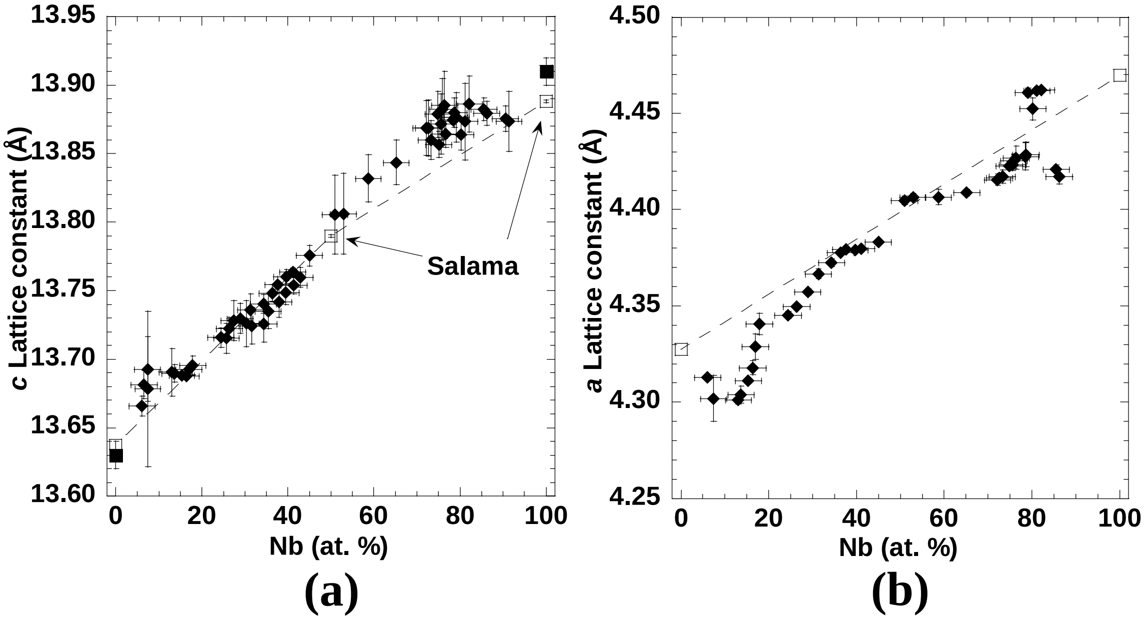

Figure 5.26 a) *c*-axis lattice constant of $(Ti_{1-x}Nb_x)_2AlC$ as a function of Nb concentration. No miscibility gap was observed across the full range of solutions. Values were in excellent agreement with those observed in bulk. b) *a*-lattice constant as a function of Nb concentration of minor secondary phase $(Ti_{1-x}Nb_x)C$ also shows linear behavior for the solid solutions. The dashed lines serve as a guide for the eye between bulk values.

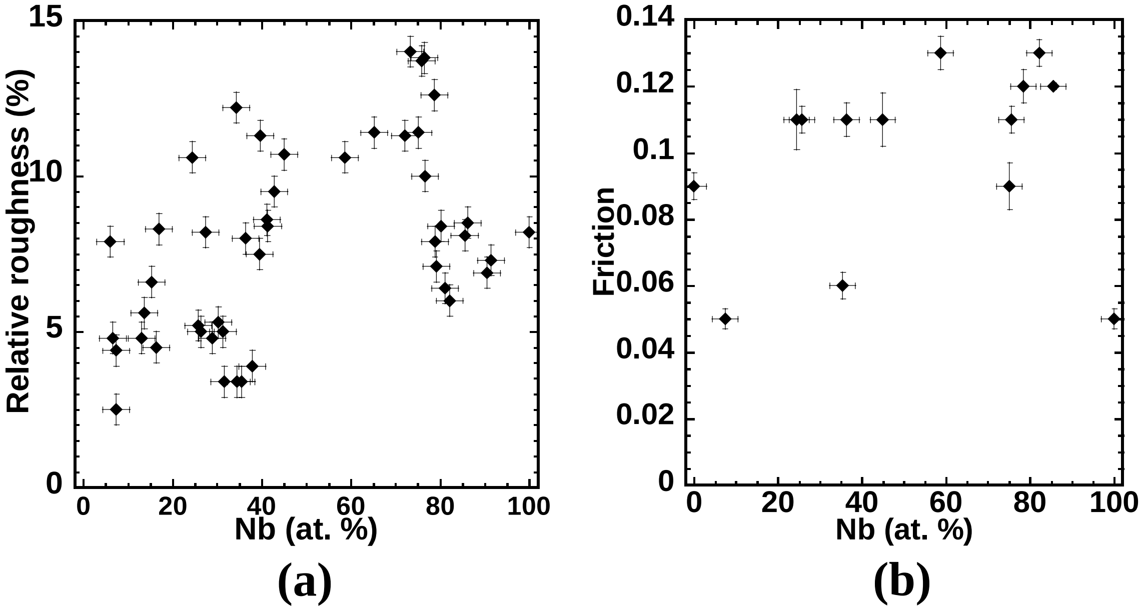

Figure 5.27 a) Relative surface roughness as a function of Nb concentration. b) Coefficient of friction as a function of Nb concentration. Overall the friction does not appear to be affected by substitution.

gradient samples often leads to a concomitant thickness gradient across the substrate. Thus for comparison purposes, it is most meaningful to plot the relative roughness, *i.e.*, the ratio of the average roughness to the film thickness (Fig. 5.27a). Although there was significant scatter in the data, the relative roughness was largest near $x \sim 0.5$.

Results of friction testing are shown in Fig. 5.27b. The friction coefficients are all reasonably small (< 0.14) with an average value of ~ 0.1. In all cases, the coefficient was independent of load. Not surprisingly, the friction was largest for the roughest samples. The present values are significantly larger than those reported for the basal plane of bulk Ti_3SiC_2 [75] but are commensurate with the value of 0.1 found by Emmerlich *et al.*[53] in films of Ti_3SiC_2, although there were some films with coefficients of ~0.05.

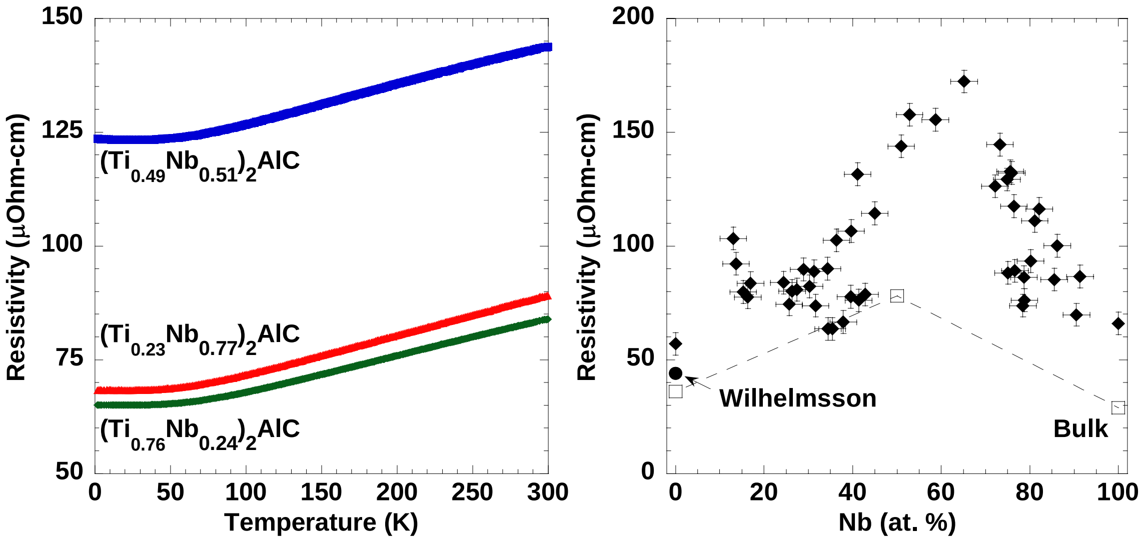

(a) **(b)**

Figure 5.28 a) Resistivity as a function of temperature for $(Ti_{0.76}Nb_{0.24})_2AlC$, $(Ti_{0.49}Nb_{0.51})_2AlC$, $(Ti_{0.23}Nb_{0.77})_2AlC$ thin films. All films showed metal-like behavior. b) Room-temperature resistivity as a function of Nb concentration for $(Ti_{1-x}Nb_x)_2AlC$ films. The observed peak around 60 at. % Nb along with all film values higher than those observed in bulk is in good agreement with solid solution scattering. The dashed line represents a guide for the eye between bulk values.

Electronic transport measurements showed that the films had metal-like conduction (Fig. 5.28a), but none showed superconductivity down to 1.8 K. While it was earlier shown that Nb_2AlC becomes superconducting at 0.4 K,[76] given the average electron count in the solid solution, it is not surprising there was no indication of superconductivity down to 1.8 K.[61] The room-temperature resistivity as a function of Nb concentration is shown in Fig. 5.28b. As expected, with small RRR values and increased resistivities over end members, solid solution scattering strongly affects the electronic transport.

Hall coefficient as a function of temperature for various Nb concentrations is shown in Figure 5.29a. Interestingly, all films showed a negative coefficient similar to

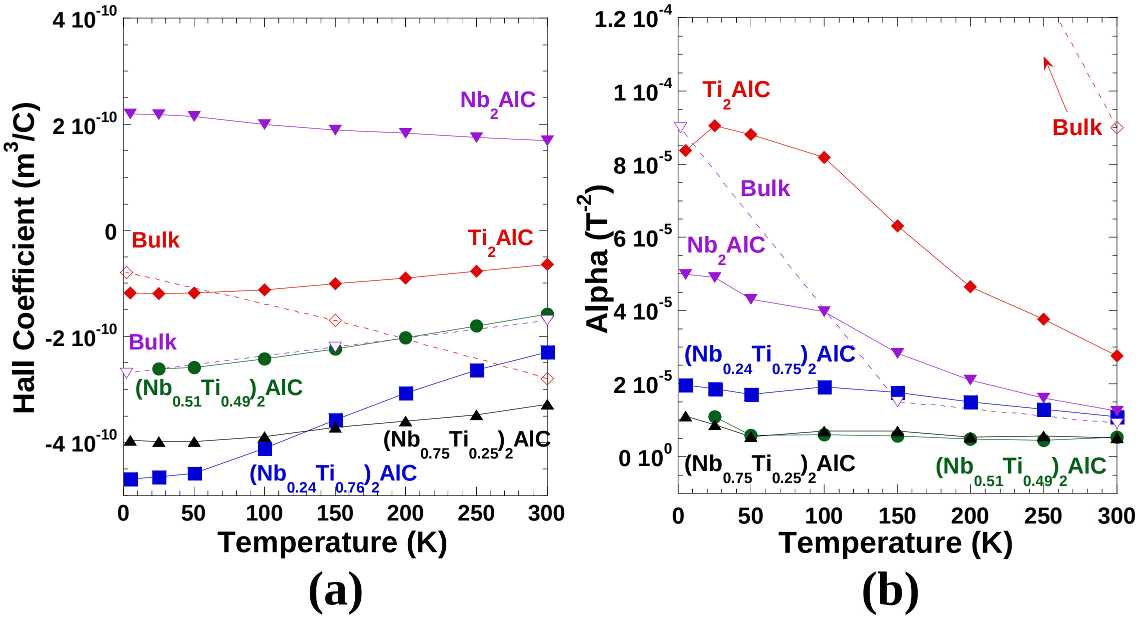

Figure 5.29 Magnetotransport results for $(Ti_{1-x}Nb_x)_2AlC$ films (solid markers) deposited on sapphire at 850 °C along with bulk (open markers) Ti_2AlC and Nb_2AlC. a) Temperature dependence of Hall coefficient (R_H). All solid solution films values were small and negative similar to values observed in bulk. b) Magnetoresistance (α) as a function of temperature. Values were all similar and small with little temperature dependence for solid solution films indicating solid solution scattering dominates transport.

Ti_2AlC, unlike the results shown for Nb_2AlC, which showed a positive R_H. Magnetoresistance (Fig. 5.29b) revealed values lower than end-members with little temperature dependence, not surprising as a result of the small RRR values. With small R_H values and positive quadratic, non-saturating magnetoresistances a two-band model is required to analyze experimental results as described in Section 4.3.4. Carrier concentration for $n \approx p$ as a function of temperature for $(Ti_{1-x}Nb_x)_2AlC$ thin films and bulk is shown in Figure 5.30. Unlike what was observed in Ti_2AlC and Nb_2AlC thin films and has been reported in previous studies of bulk MAX phases,[77] the carrier concentration for solid solutions regardless of Nb concentration was found to be $n \approx p \approx$

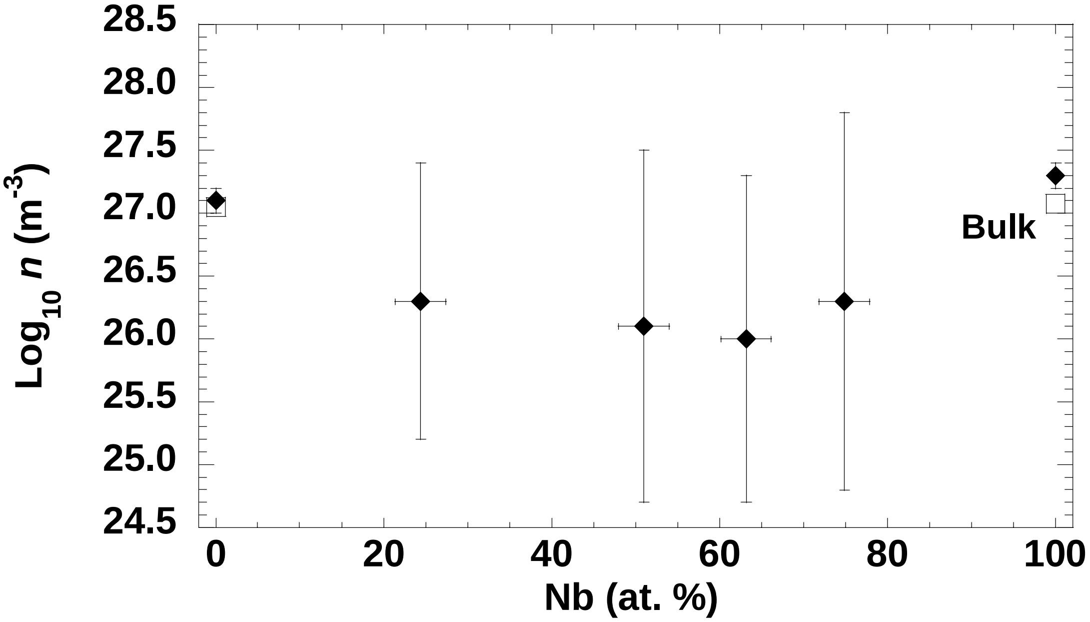

Figure 5.30 Carrier concentration as a function of temperature for $(Ti_{1-x}Nb_x)_2AlC$ thin films (closed markers) and bulk (open markers). End-member films were in good agreement with bulk values, while up to an order of magnitude decrease was observed for solid solutions. Error bars represent the allowed values of *n* based upon calculations for $n \approx p$ from the two-band model described in Section 4.3.4.

1-3 × 10^{26} m^{-3}. Although the change in *n* was approximately an order of magnitude lower than either end-member, this suggested that mixing on the M-sites may affect the electronic structure of the material. Additionally, the mobility of the charge carriers can be found through two-band analysis. Figure 5.31 plots the temperature dependence of electron and hole mobilities. As was observed in resistivity measurements, the mobilities are subject to temperature dependent scattering. The bulk values extracted from Ref. [5, 27, 30, 31] were higher than their respective film counterparts. The solid solutions revealed the lowest mobilities with little temperature dependence, demonstrating the significant amount of scattering within the material.

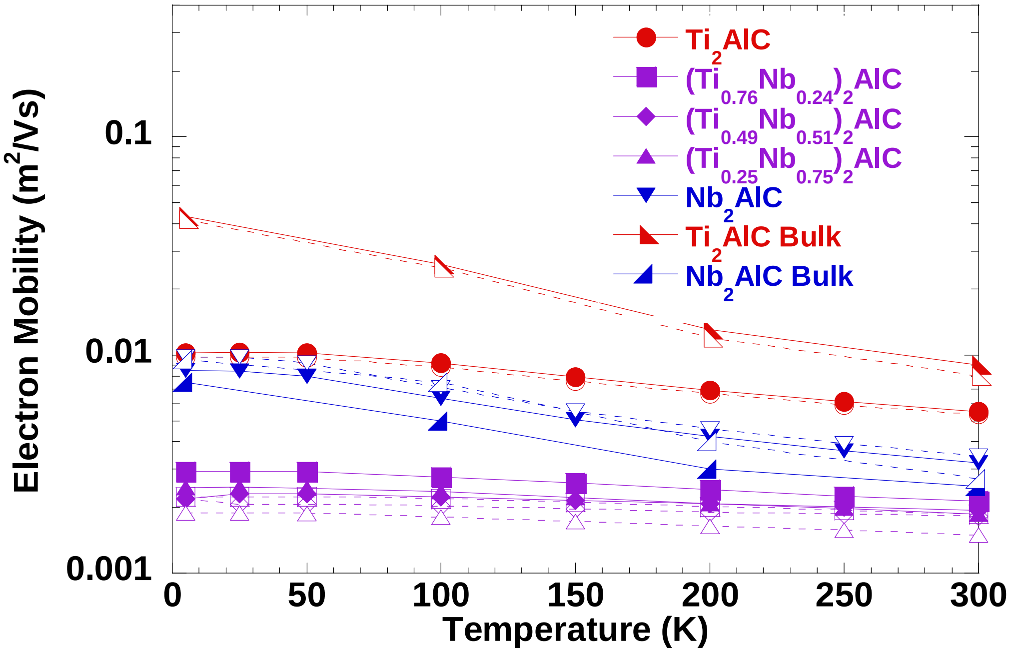

Figure 5.31 Semilogarithmic plot of the temperature dependence of electron (solid markers) and holes (open markers) for Ti_2AlC, Nb_2AlC, and $(Ti_{1-x}Nb_x)_2AlC$ thin films. Bulk values were extracted from values reported by Hettinger. In general, bulk values were higher than film values. The solid solutions revealed the lowest mobilities with little temperature dependence, demonstrating the significant amount of scattering within the material.

Electrical transport and surface roughness for $(Ti_{1-x}Nb_x)_3AlC_2$ and $(Ti_{1-x}Nb_x)_4AlC_3$ films are listed in Tables 5.3 and 5.4, respectively. Interestingly, for 312 solutions, the resistivity decreased as Nb concentration increased possibly due to higher quality of the film as observed by XRD. 413 solutions showed much higher resistivities (~200-300 μΩ-cm) compared to 211 solutions, most likely due to the increased disorder in the phase, as observed by XRD. In addition, the 413 films were significantly rougher than the 211 and 312 films, which can also explain the observed increase in resistivity through scattering.

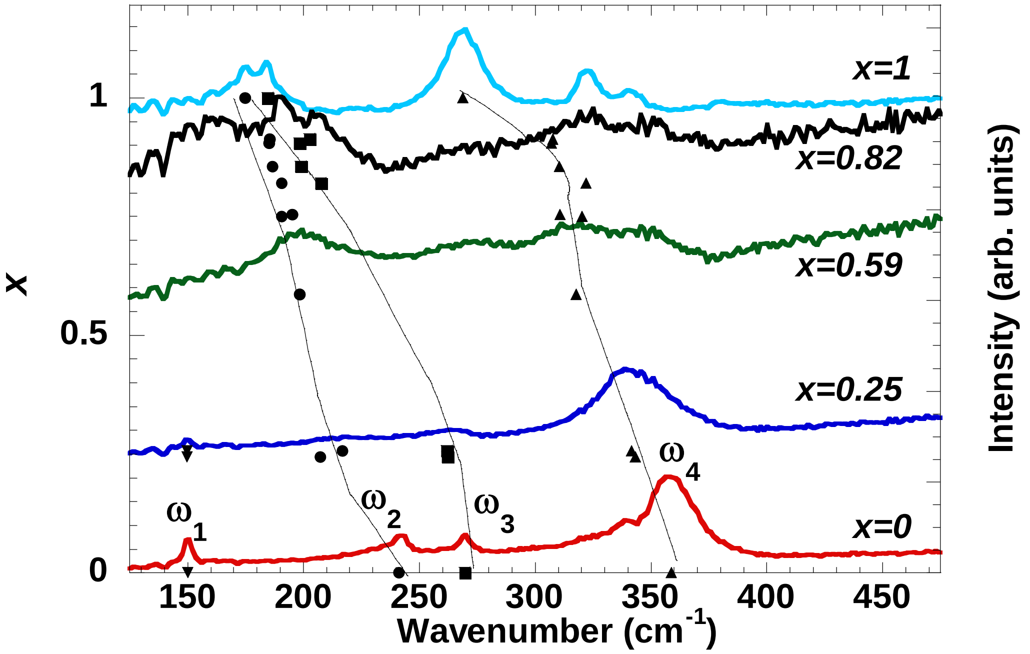

Figure 5.32 Raman spectra for various thin films of $(Ti_{1-x}Nb_x)_2AlC$. Markers indicate the positions of vibrational modes as a function of Nb concentration. The lines serve as a guide for the eye. The results suggest enhanced stiffness in the Nb-rich region.

Selected Raman spectra are shown in Fig. 5.32. Of the four first-order modes in the M_2AX family,[30] two were consistently observed. The lower (ω_1) and middle (ω_2, ω_3) modes are attributed to longitudinal modes in the basal plane and the upper mode (ω_4) to a longitudinal mode along the *c*-axis. The disappearance of the modes is likely directly attributable to increased Raman linewidth, indicative of mixing at the M site. Surprisingly, one observed mode did not show monotonic changes with x, but actually ω_4 had a maximum near $x \sim 0.75$.

At a very simple level the elastic modulus $E \sim M\omega^2/V^{1/3}$ where M is the reduced mass of the mode, ω a characteristic phonon frequency, and V the unit cell volume. In each of the four Raman modes, the C atoms do not participate so $M = 1/2(M_A+2M_M)$ where M_A is the mass of the A-group atom and M_M that of the transition metal. The change in cell volume is only a few percent between the two end members,[67] and this approximation yields the modulus of Nb_2AlC ~ that of Ti_2AlC, as expected. For the solid solution, this approximation leads to hardening in all samples, with E nearly twice that of the end members for $x = 0.75$. The present results are in contrast to substitution on the A-group which led to some softening[78] and X which had some hardening.[18, 20, 77]

5.3.3. $(Ti_{1-x}Nb_x)_2AlC$ Conclusions

Solid solutions of $(Ti_{1-x}Nb_x)_2AlC$ thin films were synthesized by a combinatorial method by magnetron sputtering at 850 ºC. X-ray diffraction showed all films grew *c*-axis oriented and epitaxial to the substrate. Most films contained a minor secondary phase of $(Ti_{1-x}Nb_x)C$. Complete solid solution mixing was observed for all compositions and phases following Vegard's law. Electrical transport measurements showed typical metal-like conduction, with room temperature resistivities ranging between 65-160 μΩ-cm with the highest value observed at $x \approx 0.6$ due to solid solution scattering. All films had small Hall coefficients and magnetoresistances indicating the electrical conductivity of these materials is compensated. The carrier concentration from two-band analysis was found to be $n \approx p \approx 1\text{-}3 \times 10^{26}\ \mathrm{m}^{-3}$ regardless of Nb concentration and an order of magnitude lower than either end-member, suggesting that mixing on the M-sites may affect the electronic structure of the material. Friction studies found an average coefficient of friction of ~ 0.1 with the highest values roughly occurring where the surface roughness was highest. Raman spectroscopy indicated the possibility of significant solid solution hardening through enhanced bonding along the *c*-axis. Two new MAX phases $(Ti_{1-x}Nb_x)_3AlC_2$ and $(Ti_{1-x}Nb_x)_4AlC_3$ were only observed during combinatorial experimentation suggesting they were highly metastable phases.

Chapter 6: MAX Phase Thin Films in the V-Cr-Al-C System

This chapter presents the results for films in the V-Cr-Al-C systems. Synthesis and characterization of the Cr_2AlC and V_2AlC phases was performed first. Optimal synthesis conditions from the two aforementioned films was determined and applied towards to the synthesis of $(V_{1-x}Cr_x)_2AlC$ films.

6.1. Cr_2AlC Thin Films

There is limited data reported on Cr_2AlC thin films in the literature.[24, 79] Walter *et al.* investigated coating Cr_2AlC on steel from a stoichiometric compound target in the temperature range of 450-900 °C.[45, 80-82] Their findings determined films to be amorphous at 450 °C and crystallized above 500 °C. Unlike a similar study on deposition of Ti_2AlC from a compound target that led to Ti deficiency,[80] composition of the films was within 5% of the Cr_2AlC target at all deposition temperatures. Schneider has reported *ab initio* calculations and synthesis and elastic properties of Cr_2AlC films.[56] Theoretical calculations of magnetism were unable to determine a stable magnetic structure, while the Cr-C bonding showed ionic and covalent contributions similar to cubic CrC. The elastic modulus found from nanoindentation of thin films was ~17 ±6% lower than *ab initio* calculations. Mertens *et al.* performed the only combinatorial synthesis on a MAX phase prior to the work presented in this thesis.[81, 82] The most important finding presented in their work was a compositional range for single phase Cr_2AlC. Single phase Cr_2AlC was found to exist between Cr/C ratio of 1.72-1.93, Cr/Al ratio of 1.42-2.03, and up to 6.3 at. % deviation from stoichiometric composition for Al. The lattice parameters of Cr_2AlC were found to be independent of composition, however.

In the following sections the results of synthesis and characterization of thin films in the Cr-Al-C system will be presented. Results found within this thesis have been submitted for publication as "Synthesis and characterization of epitaxial Cr-Al-C thin films on sapphire".

6.1.1. Cr_2AlC Synthesis

X-ray diffraction patterns for films grown between 550 – 875 ºC without buffer layers are shown in Figure 6.1. Only (00l) peaks of Cr_2AlC were observed for films grown at temperatures above 550 ºC, indicating *c*-axis growth. Strongest diffraction was observed in films deposited at 800 ºC, suggesting it is the optimal temperature for high

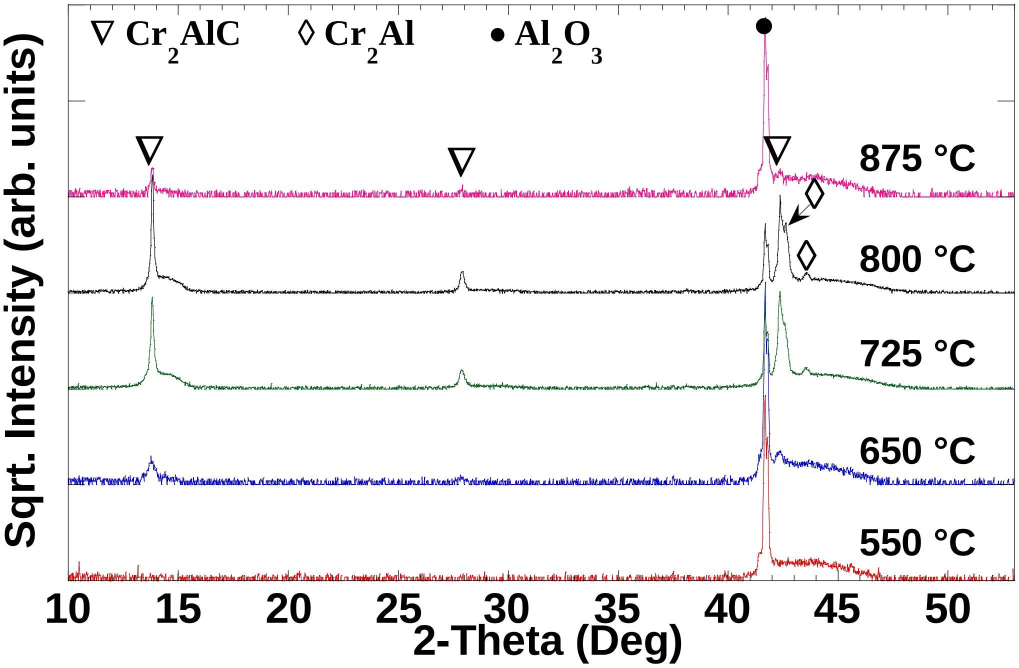

Figure 6.1 X-ray diffraction patterns of Cr_2AlC thin films deposited on Al_2O_3 at various temperatures showing diffraction from the (00l) orientation. Crystalline Cr_2AlC was observed at temperatures above 550 ºC, with strongest diffraction occurring in films deposited at 800 ºC. A secondary phase of Cr_2Al was observed in some films.

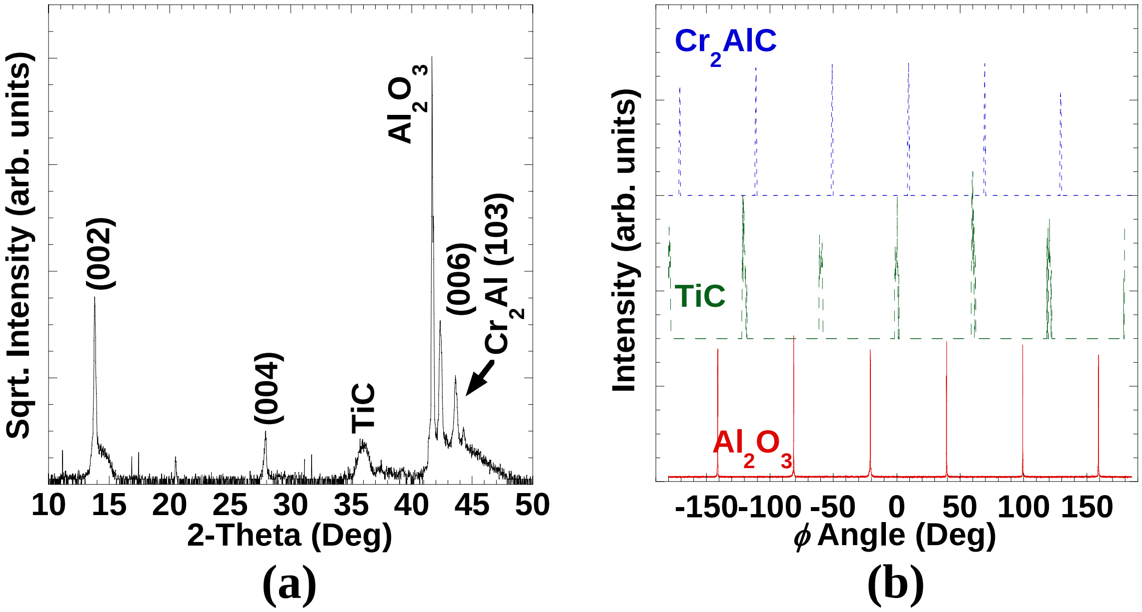

Figure 6.2 a) X-ray diffraction pattern of Cr_2AlC thin film deposited on TiC at 850°C showing diffraction from the (00l) orientation. The peak seen at 43.53º is associated with Cr_2Al (103). b) 4-circle X-ray diffraction revealed twinning in the TiC buffer layer along with 6-fold symmetry for Cr_2AlC indicating epitaxial growth.

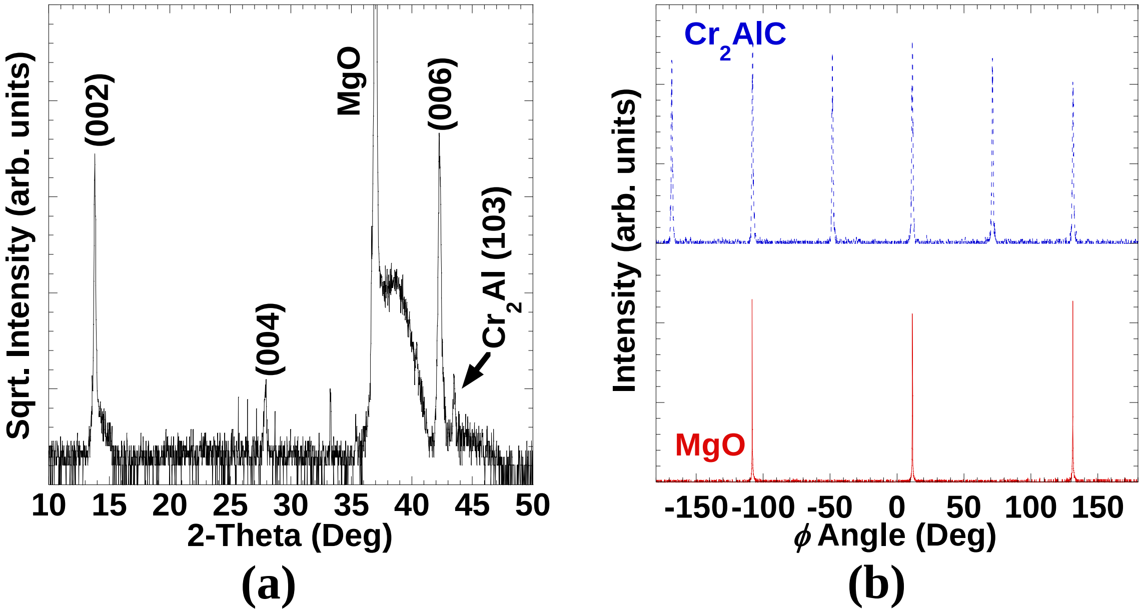

Figure 6.3 a) X-ray diffraction pattern of Cr_2AlC thin film deposited on MgO (111) at 850°C showing diffraction from the (00l) orientation. The peak seen at 43.53º is associated with Cr_2Al (103). b) 4-circle X-ray diffraction revealed 6-fold symmetry for Cr_2AlC indicating epitaxial growth.

crystallinity, while no MAX phase was observed at temperatures above 875 ºC. A secondary phase of Cr_2Al was observed in some films. Cr_2AlC films were also grown on (111) MC (M = Ti or V) buffer layers and MgO (111). X-ray diffraction results (Figs. 6.2a and 6.3a) were similar to that of deposits on sapphire at commensurate temperatures; however XRD intensities were lower indicating lower crystalline quality.

ϕ scans showed that the films were in fact epitaxial. For films grown on (111) MC (M = Ti or V) buffer layers (Fig. 6.2b), the in-plane relations are given by $[1\bar{1}0]_{Al_2O_3} \parallel [101]_{MC} \parallel [100]_{Cr_2AlC}$. Interestingly, the MC grew twinned even thought the mismatch between the binary and sapphire was ~3.1% tensile, while Cr_2AlC was epitaxial with a mismatch to TiC of ~6.9% tensile. Films grown on MgO were also epitaxial, as seen from the XRD ϕ scans (Fig. 6.3b) with in-plane relationships of $[101]_{MgO} \parallel [100]_{Cr_2AlC}$. The

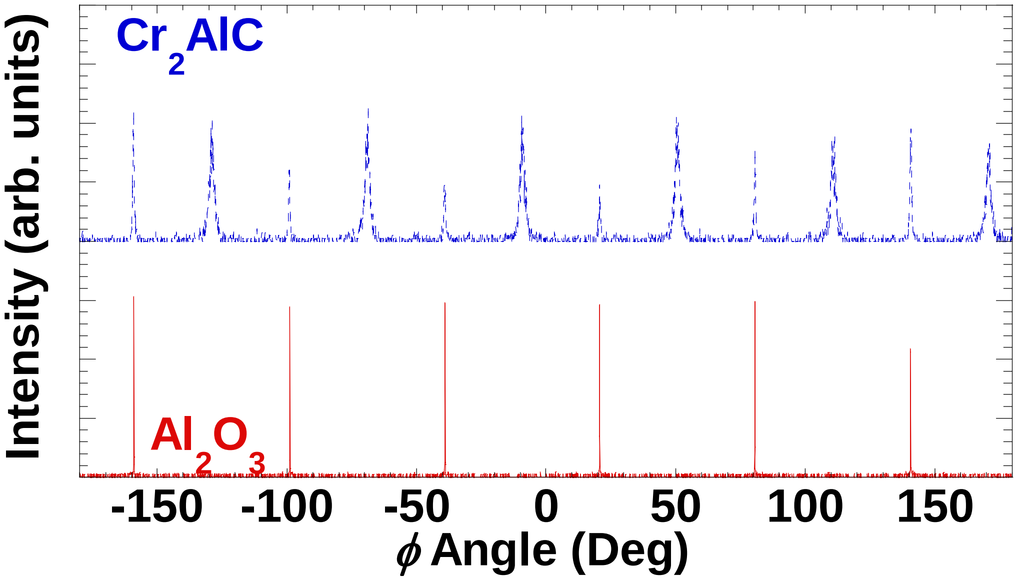

Figure 6.4 4-circle X-ray diffraction revealed epitaxial growth of Cr_2AlC along with twinning most likely due to the large lattice strain.

Table 6.1 Properties of Cr_2AlC thin films deposited at various temperatures on sapphire or TiC or VC seedlayers.

Temperature (°C)	Seedlayer	Average tilt (°)	Heterostrain (ppm)	*c*-axis lattice constant (Å)
875	-	-	-	12.770 (1)
775*	-	0.16 (2)	350 (140)	12.773 (3)
700	-	0.34 (12)	1200 (300)	12.777 (3)
625	-	-	-	12.779 (7)
875	VC	0.39 (4)	1700 (200)	12.788 (2)
850	TiC	0.11 (1)	750 (100)	12.773 (2)

* Deposited at room temperature, annealed at 775 °C

lattice mismatch between MgO and Cr_2AlC is ~4% tensile. Films grown directly on sapphire were twinned with $[1\bar{1}0]_{Al_2O_3} \parallel [100]_{Cr_2AlC}$ or $[100]_{Al_2O_3} \parallel [100]_{Cr_2AlC}$ (Fig. 6.4). The former was similar to that found in other MAX phases grown without buffer layers [45]; however, those other phases did not exhibit any twinning. The lattice mismatch between the *a*-axis lattice constant of Cr_2AlC and that from the surface reconstruction of *c*-plane α-Al_2O_3 [24, 83] was quite large at ~10%, and epitaxial growth should not be anticipated. The twinning must result as a means to compensate for the large strains.

To investigate this, X-ray rocking curve measurements were completed for all films whose XRD pattern showed at least three (00l) peaks. Table 6.1 lists the heterogeneous strain determined from Williamson-Hall plots of θ-2θ measurements and average tilt determined from modified Williamson-Hall plots of rocking curve measurements.[74] In addition, the *c*-axis lattice parameters found from Nelson-Riley plots are also given in Table 6.1.[48] It is to be noted that the film thicknesses determined from modified Williamson-Hall plots were, within the error of measurement, in agreement with those determined from profilometry.

6.1.2. Cr_2AlC Results and Discussion

All values of the *c*-axis lattice constant were less than those of the bulk value of 12.821 Å,[84] but by no more than 0.3%. If the films were fully clamped to the substrate/seedlayer, from the calculated elastic constants of Cr_2AlC and the relaxed lattice parameters of VC and TiC, one would have anticipated out-of-plane strains ε_c of -5.5, -4.0 and -1.7% for no, TiC, and VC seedlayers, respectively, using $\varepsilon_c = -2\ \varepsilon_{ab} c_{13}/c_{11}$ where ε_{ab} is the in-plane strain and c_{11} and c_{13} the appropriate calculated elastic constants[78]. Since the films were nearly relaxed, the critical thickness must be considerably smaller than 100 nm, which is reasonable given the large interfacial strains [78].

Of the four first-order Raman active phonon modes in the M_2AX family,[85] three were consistently observed in films of Cr_2AlC (Fig 6.5). The lower (ω_1) and middle

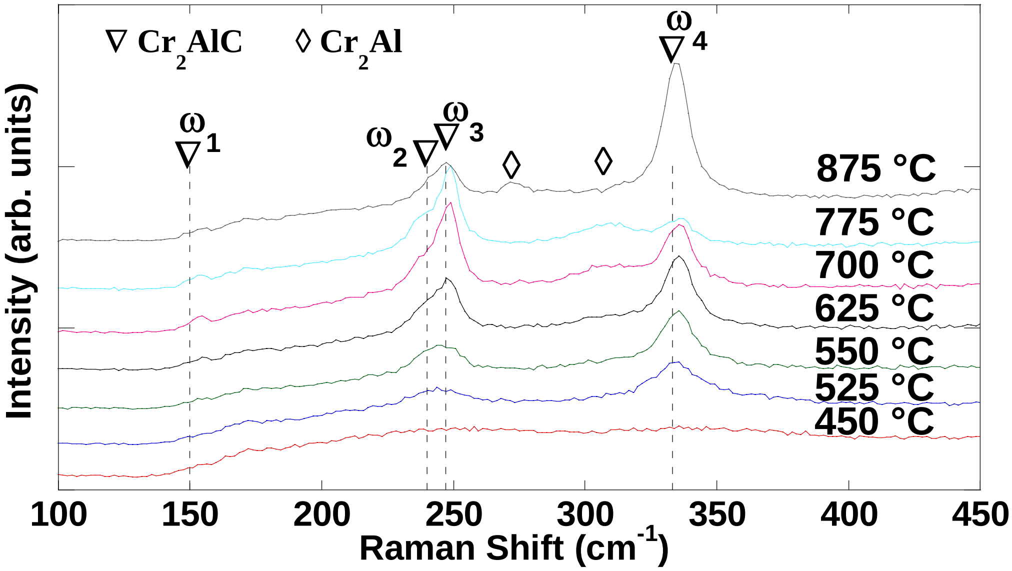

Figure 6.5 Raman spectra of Cr_2AlC films deposited at various temperatures. Three of the four modes observed in bulk (dashed lines) were consistently observed in thin film. The additional modes observed around 270 and 310 cm^{-1} in the 700 and 775 °C films were associated with Cr_2Al, in agreement with XRD results.

(ω_2, ω_3) modes were attributed to longitudinal modes in the basal plane and the upper mode (ω_4) to a longitudinal mode along the *c*-axis. Table 6.2 lists the experimental and calculated Raman shifts for bulk Cr_2AlC [67]. Raman modes associated with Cr_2AlC (~153, 248, and 335 cm^{-1}) were observed for deposition temperatures down to 525 °C. In addition, it was sometimes possible to resolve a mode at 237 cm^{-1}, which was not resolved in the bulk material.[67, 68] Since no Cr_2AlC XRD peaks were observed for deposition temperatures below 625 °C, films grown between 525 and 625 °C must have been nanocrystalline or amorphous. Additional Raman peaks were sometimes found at ~270 and 310 cm^{-1} labeled ω_A and ω_B, respectively. It is noted that the Raman mode at ~ 310 cm^{-1} was associated with Cr_2Al (discussed below), which has the same Cr-Al ratio as the MAX phase.

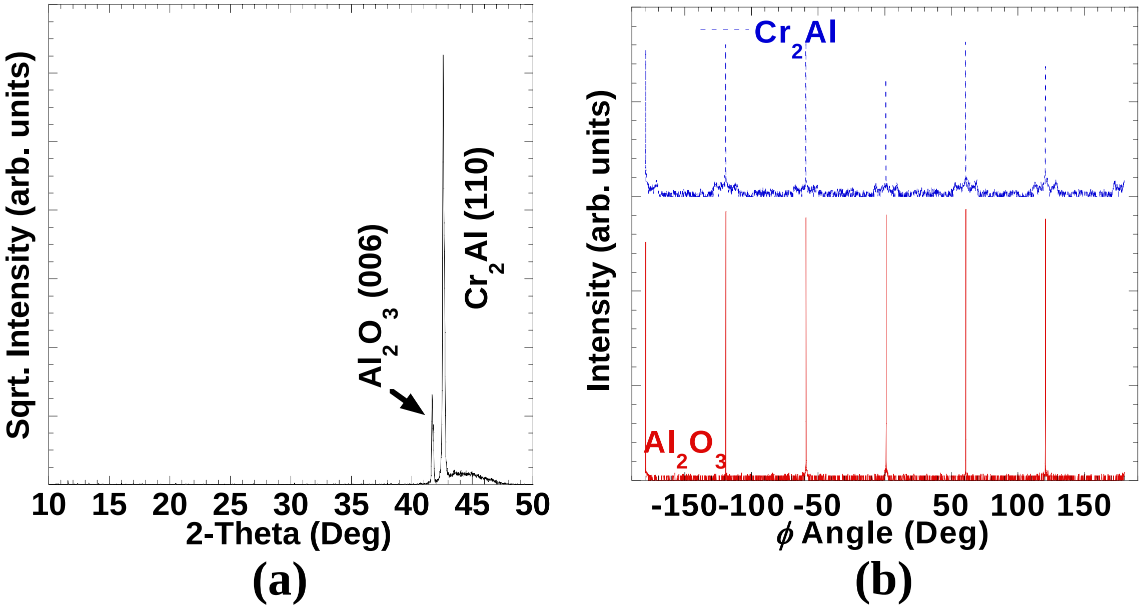

Figure 6.6 a) X-ray diffraction pattern of Cr_2Al thin film deposited on Al_2O_3 at 800 °C showing diffraction from the (110) orientation. b) 4-circle diffraction revealed epitaxial growth along with twinning.

To confirm the presence of Cr_2Al, $Cr_{0.67}Al_{0.33}$ was deposited at 800 °C on *c*-axis oriented sapphire. The only stable bulk Cr-Al intermetallics are Cr_5Al_8 and Cr_2Al, and the two XRD peaks (Fig. 6.6a) could only be indexed to (110) and (220) of the latter tetragonal phase. ϕ scan (Fig. 6.6b) indicated that the film was twinned with three possible variants. Cr_2Al is an ordered body-centered Cr-Al alloy with ordering along the *c*-axis so that the (103) and (110) surfaces are quite similar in structure, differing in the arrangement of the Al and Cr atoms. Figure 6.7a shows possible growth modes of (103) Cr_2Al on (001) Cr_2AlC and Figure 6.7b (110) Cr_2Al on (001) sapphire. The (103) orientation seems preferred due to the arrangement of the Cr atoms of the MAX phase while the (110) grows because of the positions of the Al atoms in sapphire. Cr_2Al belongs to space group *I*4/*mmm* with Cr in site 4e and Al in 2a [67] and should have only two first-order Raman modes. The Raman spectrum (Fig. 6.9) of the Cr_2Al (110) film on

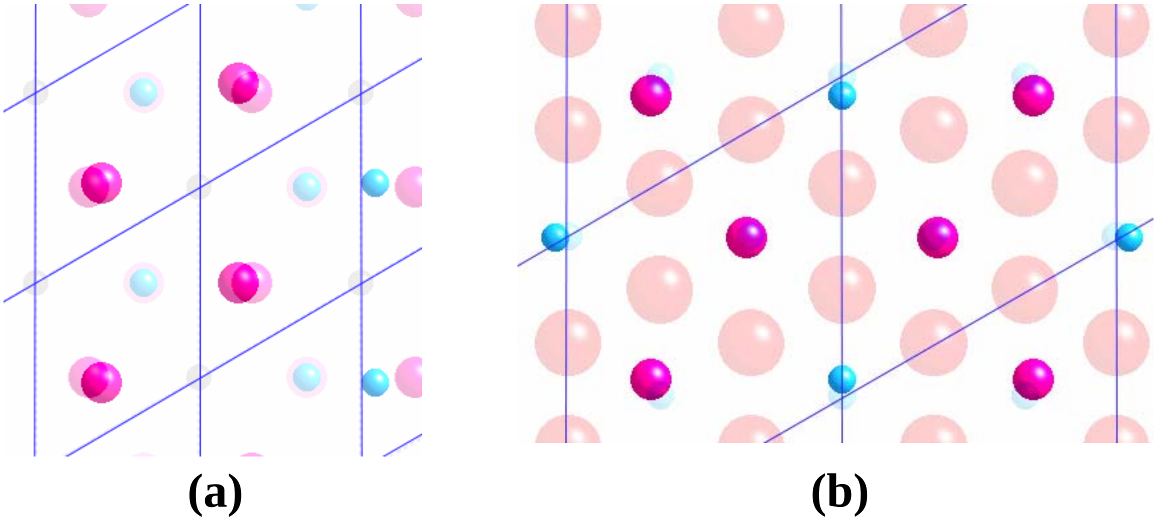

Figure 6.7 Possible growth modes of Cr_2Al surfaces, a) (103) surface on (001) Cr_2AlC and, b) (110) surface on (001) sapphire. The lighter colors are the substrate atoms and the lines define the *ab*-plane of the substrate unit cell.

sapphire had only two peaks – 240 and 310 cm^{-1} – the same as those found in the MAX films with Cr_2Al (103) orientation (Figs. 6.1-6.3).

Subsequently, Cr-C films were deposited at 800 °C on *c*-axis oriented sapphire to investigate the extra Raman peak at 270 cm^{-1} found in some MAX phase films. There are three primary binary chromium carbides, Cr_3C_2, Cr_7C_3 and $Cr_{23}C_6$. The XRD peaks of the deposited films were indexed to (lll) reflections of $Cr_{23}C_6$ (Fig. 6.8a). ϕ scan (Fig. 6.8b) indicated epitaxial growth with an in-plane relationship of $[1\bar{1}0]_{Al_2O_3} \parallel [211]_{Cr_{23}C_6}$. Previous work on thin films of $Cr_{23}C_6$ has reported polycrystalline growth only.[86]

Several Raman modes were observed in $Cr_{23}C_6$ films (Fig. 6.9) are listed in Table 6.2. $Cr_{23}C_6$ has the cubic space group *Fm*3*m* with C in site 24e and Cr in sites 48h, 32f, 8c, and 4a.[87, 88] Group theory suggests there should be thirteen Raman active

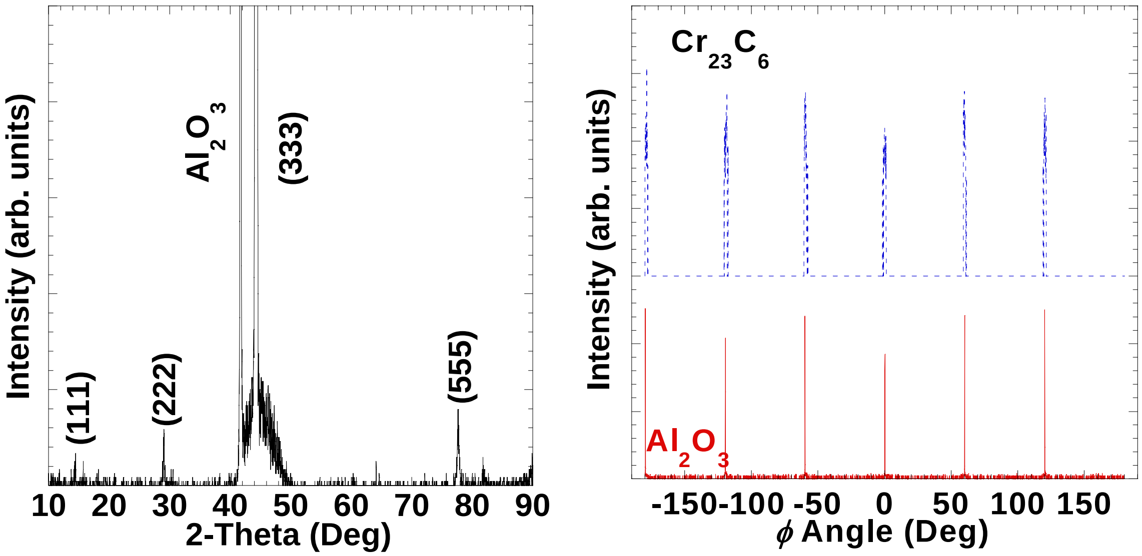

(a) (b)

Figure 6.8 a) XRD pattern of $Cr_{23}C_6$ thin film deposited on Al_2O_3 at 800°C showing diffraction from the (111) orientation. b) 4-circle diffraction reveals epitaxial growth along with twinning.

modes, and several were found although none matched the 270 cm^{-1} mode found in some of the Cr_2AlC films.

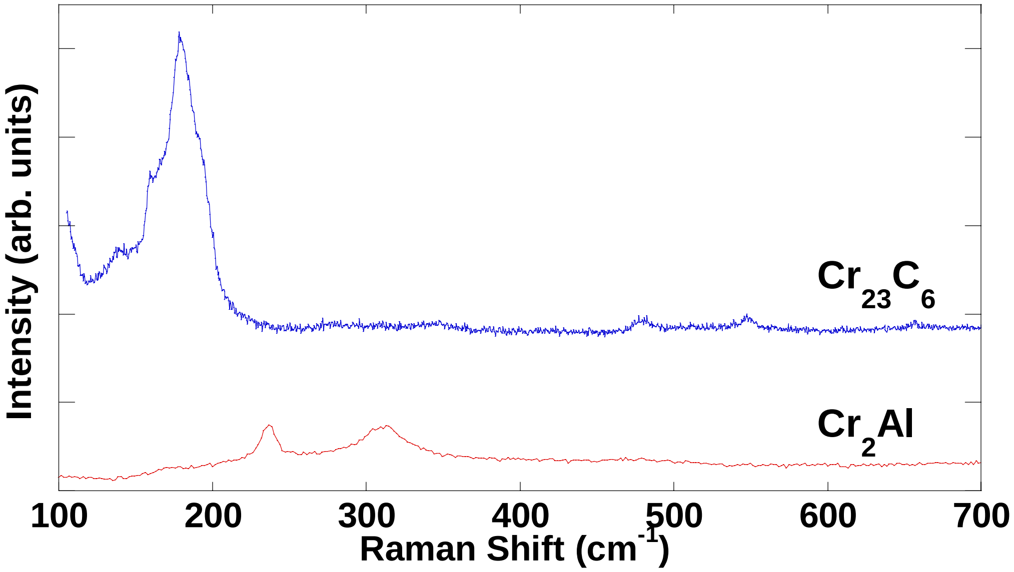

Figure 6.9 Raman spectra of Cr_2Al and $Cr_{23}C_6$ thin films deposited on sapphire at 800 °C. Two modes were observed in Cr_2Al, in agreement with expected visible Raman modes for the tetragonal structure. $Cr_{23}C_6$ contained numerous modes; the most intense occurred between 100-200 cm^{-1}.

Table 6.2 Properties of Cr_2AlC thin films

Phase	Deposition	Raman Shift (cm^{-1})						Electrical		Physical	
Cr_2AlC Film	Temperature (°C)	ω_1	ω_2	ω_3	ω_4	ω_A	ω_B	ρ_{RT} ($\mu\Omega$-cm)	RRR	Roughness R_a (nm)	Friction Coefficient
No seed	875	153	246	-	335	273	-	91	2.9	26	0.074 (2)
No seed	775	154	249	239	335	-	310	51	3.0	20	0.057 (1)
No seed	775*	152	243	-	333	-	-	51	2.9	1.5	0.050 (8)
No seed	700	154	249	241	335	-	310	53	3.2	10	0.045 (3)
No seed	625	154	248	240	336	-	310	97	1.7	10	0.072 (6)
No seed	550	153	245	-	335	-	-	79	2.7	4	0.050 (4)
No seed	525	-	244	-	335	-	-	139	1.3	3	0.050 (4)
TiC seed	850	152	247	238	334	271	-	88	1.9	48	0.074 (4)
VC seed	725	151	247	236	334	-	-	51	3.4	20	0.037 (4)
Bulk	-	150.9[a]	246.3[a]	-	339.2[a]	-	-	75[b]	5.0[b]	-	-
Calculated[a]	-	156	247	237	345	-	-	-	-	-	-
Calculated[c]	-	160	271	261	358	-	-	-	-	-	-
Cr_2Al	800	236	312	-	-	-	-	111	1.6	13	0.049 (8)
$Cr_{23}C_6$	800	247	287	310	343	503	573	128	2.8	23	0.090 (10)

[a] Reference [89]

[b] Reference [67]

[c] Reference [30]

* Deposited at room temperature, annealed at 775 °C

Subsequently, *ex situ* annealing of amorphous films was investigated. Figure 6.10 shows the temperature dependence of XRD patterns of Cr-Al-C deposited directly on *c*-axis oriented sapphire at room temperature. There were no peaks seen in scans at temperatures below 650 °C. At 650 °C the (002) Cr_2AlC peak emerged, and the (103) Cr_2Al peak appeared at 775 °C which likely grew on top of Cr_2AlC. By 900 °C neither phase was detectable and (111) $Cr_{23}C_6$ peaks appeared. Clearly, the binary carbide was the most stable phase at high temperature in thin films grown on sapphire, which is rather different from the bulk phase diagram.[68]

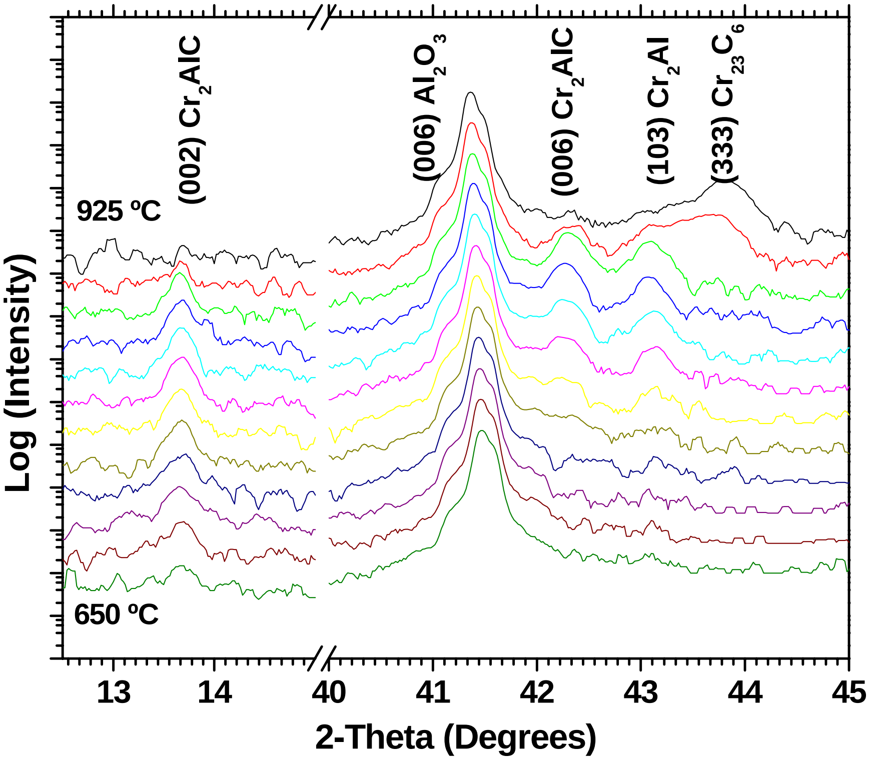

Figure 6.10 High temperature X-ray diffraction of Cr_2AlC deposited directly on Al_2O_3 at room temperature. At approximately 650°C the (002) peak begins to emerge indicating the formation of textured Cr_2AlC. Cr_2AlC (006) and Cr_2Al (103) appear around 750°C; both phases disappear above 900°C with the emergence of $Cr_{23}C_6$.

Typical AFM results for Cr_2AlC epitaxial films are shown in Fig. 6.11a. Clearly the surface was rough with large features protruding from the film surface possibly due to the Cr_2Al secondary phase observed in most films. Figure 6.11b shows an SEM image of the same film, revealing large round or oval (~1 µm) crystals, some with hexagonal facets, similar to those observed in Nb_2AlC.[90] Overall, the Cr_2AlC films showed a large variation in surface roughness with lower deposition temperatures resulting in smoother films. It is notable that amorphous films deposited at low temperature (~200 °C), which was then annealed *in situ* at 775 °C yielding Cr_2AlC, was significantly smoother than those deposited at higher temperatures, indicating surface diffusion and island growth was dominate during high temperature deposits.

Results of friction testing are listed in Table 6.2. The friction coefficients were all reasonably low (< 0.1). In all cases, the coefficient was independent of load. The

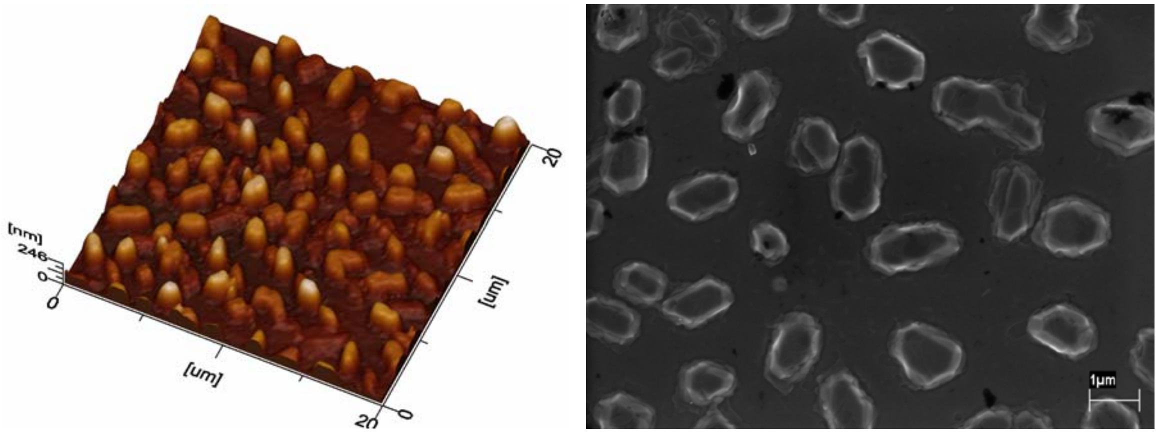

(a) **(b)**

Figure 6.11 a) AFM scan of Cr_2AlC thin film deposited at 775°C on Al_2O_3 substrate. b) SEM image of the same film. Crystal features, possibly Cr_2Al, clearly protruded from a fairly flat film surface.

$Cr_{23}C_6$ film showed the highest friction coefficient while the Cr_2AlC films had the lowest.

All films showed metal-like electrical behavior (Fig. 6.12). There was no obvious correlation between the resistivity of the Cr_2AlC films and deposition conditions except that films grown between 700 and 775 °C had the lowest resistivity and the highest RRR values, suggesting the least local disorder. These resistivity values were somewhat lower than the reported bulk value,[30] possibly indicating some anisotropy.[91] There have been minimal studies on the electrical transport of the other phases. Reports on bulk polycrystalline $Cr_{23}C_6$ [92] and annealed polycrystalline thin films of Cr_2Al [93] indicated room-temperature resistivity values of 128 μΩ-cm and over 200 μΩ-cm, respectively. While the former value matches the present results, the latter

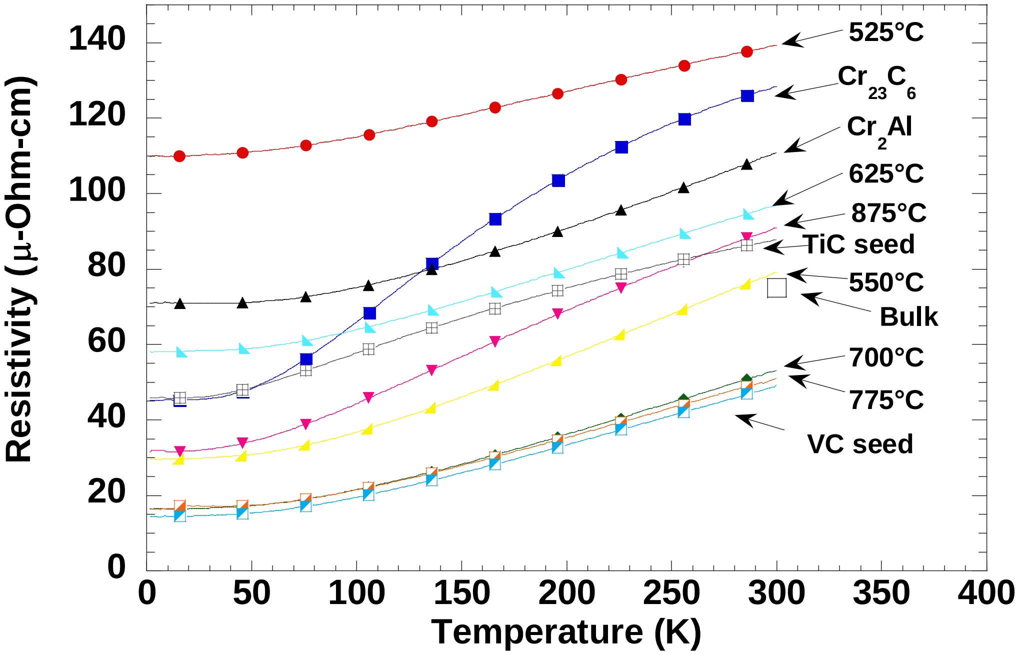

Figure 6.12 Resistivity as a function temperature for various Cr-Al-C thin films. All showed metal-like electrical conductivity behavior down to 2 K. Cr_2AlC deposited at 700-775 °C showed resistivity values lower than bulk possibly indicating some anisotropy in electrical transport. Bulk value from Hettinger.[30]

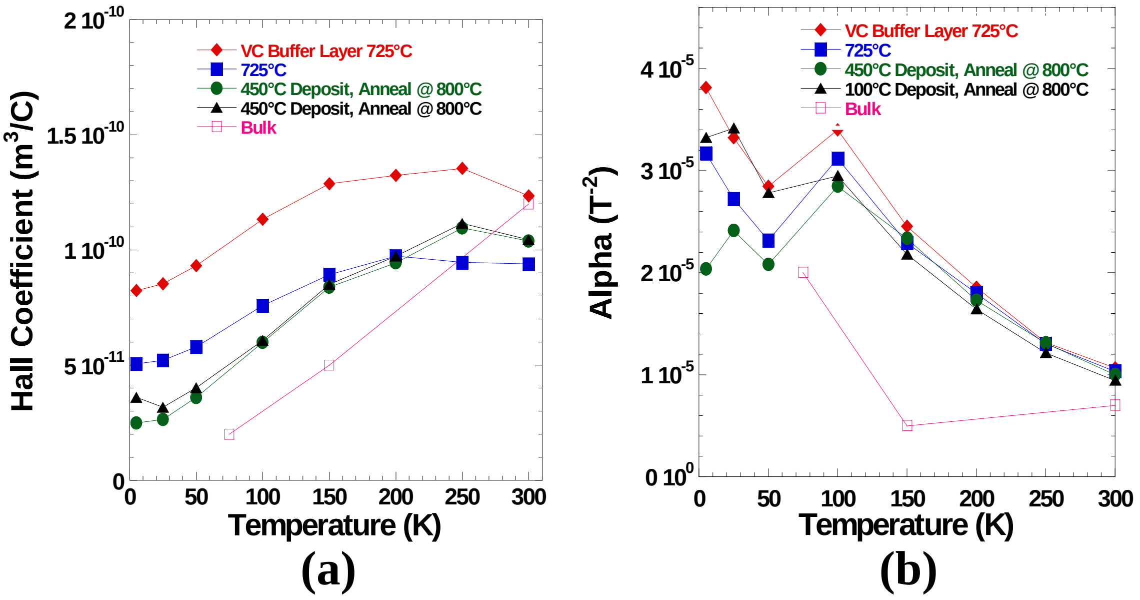

Figure 6.13 Magnetotransport results for Cr_2AlC thin films deposited under different conditions. a) Temperature dependence of Hall coefficient. Values were mostly independent of condition with only a slight increase for films deposited on VC buffer layers. b) Magnetoresistance as a function of temperature. Values were almost identical for all films regardless of deposition conditions. Bulk values from Hettinger.[30]

value is somewhat higher than that found in the current Cr_2Al film.

The Hall coefficient as a function of temperature for Cr_2AlC thin films deposited under different conditions, shown in Figure 6.13a. All films showed positive coefficients in good agreement with previous results for bulk material.[30] Magnetoresistance (Fig. 6.13b) revealed small values with little temperature dependence and nearly any difference with respect to deposition condition. At this point it is apparent deposition conditions do not impact magnetotransport properties significantly. With small R_H values and positive quadratic, non-saturating magnetoresistances a two-band model is required to analyze experimental results, as described in Section 4.3.4. Similar to what has been reported in previous studies of MAX phases,[30] the carrier concentration was found to be $n \approx p \approx$

2.4-3.5 × 10^{27} m^{-3}, in good agreement with 1.2 × 10^{27} m^{-3} found in bulk material.[5, 27, 30, 31]

6.1.3. Cr_2AlC Conclusion

Thin films of Cr-Al-C were synthesized on *c*-axis sapphire and seedlayers of TiC and VC. Epitaxial films of Cr_2AlC grew between 625 and 875 °C with, and without buffer layers, while nanocrystalline films of the compound could be grown at temperatures as low as 525 °C as indicated by Raman spectroscopy. Epitaxial films of both Cr_2Al and $Cr_{23}C_6$ were also grown to confirm their presence and orientation in Cr_2AlC films. Annealing of amorphous films deposited at room temperature produced epitaxial Cr_2AlC at 650 °C, epitaxial Cr_2Al at 775 °C, and epitaxial $Cr_{23}C_6$ at 900 °C. All films showed metal-like conduction down to 2 K. Films deposited between 700-775 °C had resistivity values less than bulk possibly indicating some anisotropy. Hall coefficient and magnetoresistance values were similar to bulk with carrier concentrations determined from two-band analysis of $n \approx p \approx$ 2.4-3.5 × 10^{27} m^{-3}.

The surface roughness of the Cr_2AlC films decreased with deposition temperature, while films grown at low temperature (~200 °C) and annealed *in situ* at 775 °C were the smoothest, indicating that surface diffusion with island growth occurred at high temperatures. The friction coefficients were all reasonably small (< 0.075) with the lowest values observed in the most phase-pure Cr_2AlC films, suggesting secondary phases induce increased friction.

6.2. V_2AlC Thin Films

The first reported synthesis of V_2AlC films was by Schneider *et al.*[30] Their work concentrated on *ab initio* calculations of structure, spin polarization, and bonding compared to that of results found in thin films. They concluded modern electronic structure theory provided an accurate description of V_2AlC. More recently, Sigmonrong *et al.* synthesized thin film V_2AlC on sapphire at various temperatures. The authors found phase pure polycrystalline V_2AlC films grow on a ~12 nm thick transition layer at temperatures above 750 °C. [94] Additionally, at substrate temperatures higher than 850 °C, the formation of V_2C, in addition to the V_2AlC phase was observed due to Al deficiency in the films.

In the following sections synthesis and characterization of thin films in the V-Al-C system are discussed. Results from this thesis are in preparation for publication as "Synthesis and characterization of V-Cr-Al-C thin films by combinatorial method".

6.2.1. V_2AlC Synthesis

V_2AlC thin films were successfully grown on VC seedlayers at temperatures up to 950 °C (Fig. 6.14). The calculated lattice mismatch between V_2AlC on VC (111) is ~1%. Most deposits contained a secondary phase of V_2C the formation of which is discussed in more detail below. Epitaxial V_2AlC was observed down to 650 °C, similar to that found in the Cr_2AlC system [95] and lower than that of Ti_2AlC.[45, 56, 80] The strongest diffraction of V_2AlC occurred for temperatures between 650-900 °C indicating the most ordered regime. Temperatures above 900 °C resulted in predominately V_2C with only weak V_2AlC and VC peaks observed due to Al deficiency in the films. Lattice parameter calculations for V_2AlC deposited at various temperatures are listed in Table 6.3. For temperatures between 725-850 °C the average c lattice was approximately 13.138 (4) Å, in excellent agreement with the bulk value of 13.14 Å and 13.11Å and 13.21 Å found in thin films.[55] At temperatures below 725 °C the c lattice constant

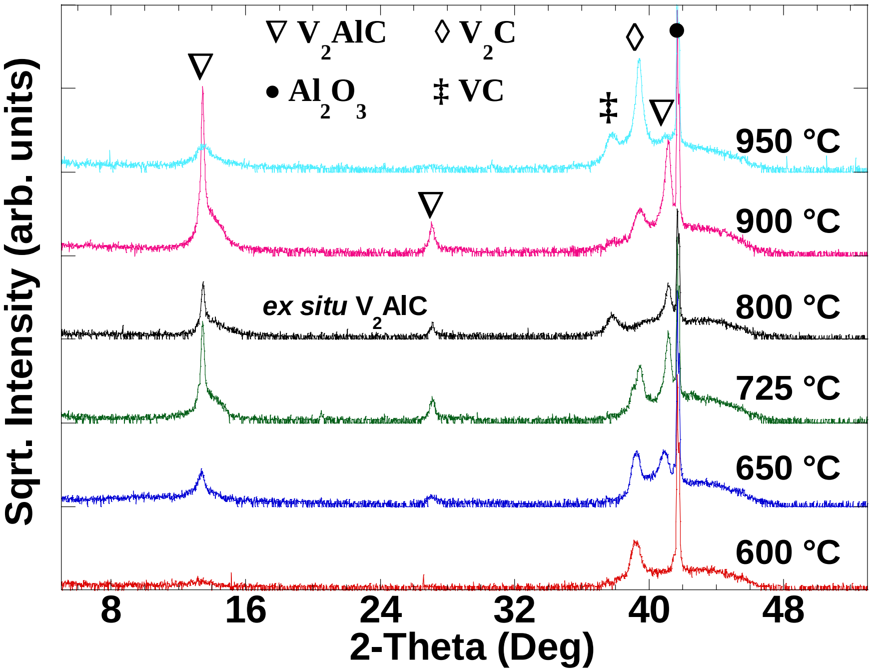

Figure 6.14 X-ray diffraction patterns for V_2AlC thin films grown on VC seedlayers at various temperatures. All films were grown *in situ* on VC except for the 800 °C, which was grown *ex situ*. Textured growth in the (001) orientation was observed down to 650 °C. Notable is the disappearance of the VC peak in all films grown *in situ* due to the instability of the phase at high temperatures in the presence of V resulting in a phase transformation into V_2C.

increased significantly indicating unit cell expansion due to vacancies or weaker bonding in the structure.

Also notable was the disappearance of the VC (111) seedlayer peak in all *in situ* deposits (Fig. 6.14). It is believed that the less stable MX binary incorporated V and converted to the more stable V_2C phase. This seems sensible considering that the lattice mismatch (~0.3%) favors the hexagonal binary carbide. In addition, the fact the VC and V_2C do not appear in the same XRD diffractograms and the intensity of the V_2C is the same indicates the phase is contained at the interface of the substrate and film. This, however, was not the case for the e*x situ* XRD seedlayer film. Figure 6.15 is a XRD overlay of the VC seedlayer and V_2AlC film deposited at 800 °C. Clearly, the seedlayer intensity remains identical following MAX phase synthesis. It is not fully understood why the VC did not disappear here; however, it can be assumed that the exposure to the atmosphere allowed for possible oxide formation that in turn prevented decomposition of VC. This shows the instability of the binary carbide at high temperature when in the presence of additional elements. Lastly, the C composition was slightly higher for the *ex situ* film than the other films at ~26 at. % (compared to 24 at. %), this additional carbon possibly allowed the VC to remain stable in the presence of V during the MAX phase deposit.

In an attempt to understand this effect and examine the crystallization of V_2AlC, HTXRD was performed on V-Al-C films deposited on VC and TiC seedlayers at room temperature. Unlike the observed crystallization of Cr_2AlC (Section 6.1.2) and Cr_2GeC (Section 7.1.2) at temperatures around 650 °C, no phase formation of any kind was observed up to 1100 °C. The aforementioned experimentation was performed under vacuum. Experiments performed in a He atmosphere resulted in numerous vanadium oxide phases demonstrating the sensitivity of V in the presence of oxygen.

V_2AlC thin films were also successfully grown directly on sapphire and TiC seedlayers (Fig. 6.16) at temperatures of 900 °C. The calculated lattice mismatch between V_2AlC on TiC (111) is ~ 5%. A total of three depositions on TiC seedlayers were performed, herein labeled as A, B, and C. Interestingly, depositions on TiC resulted in V_2AlC along with new phases of V_3AlC_2 and V_4AlC_3 (Fig. 6.16). These phases were not observed for deposits on VC or those directly on sapphire. V_4AlC_3 was observed in samples A, B, and C, while V_3AlC_2 was observed in only A and B. Deposition

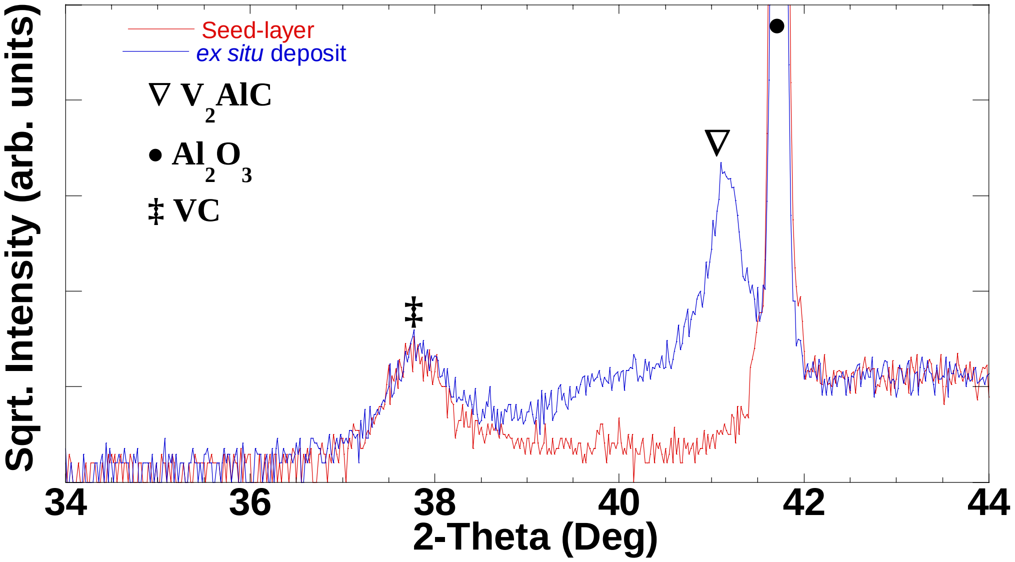

Figure 6.15 X-ray diffraction pattern overlay of VC (111) seedlayer and V_2AlC (001) grown *ex situ* on the seedlayer at 900 °C. Unlike *in situ* deposits of V-Al-C on VC (Fig. 6.14) phase transformation of VC into V_2C was not observed. Possibly an oxidation layer or the slightly higher C content allowed the VC phase to remain stable at high temperature in the presence of V.

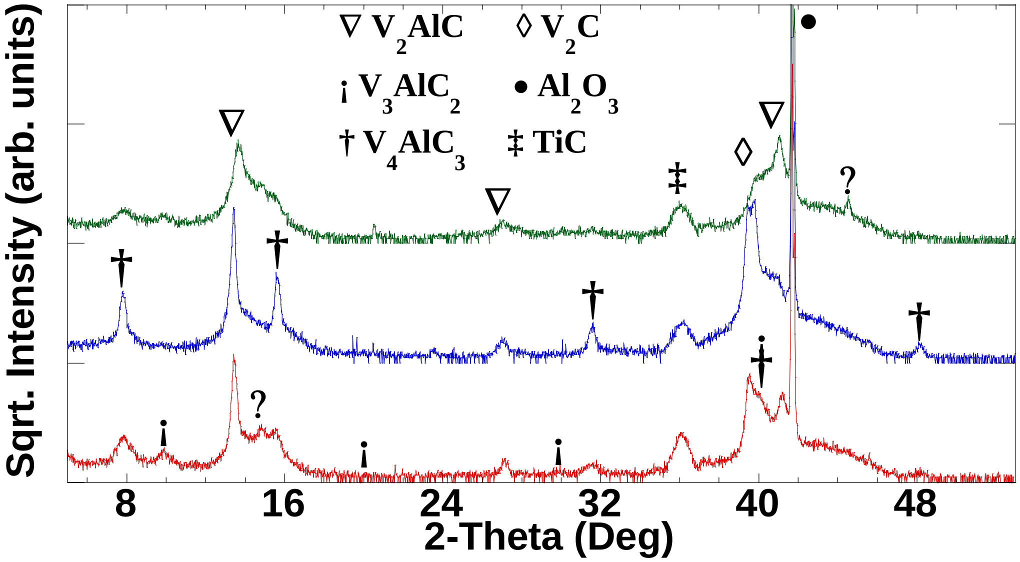

Figure 6.16 X-ray diffraction patterns for V-Al-C thin films grown on TiC (111) at 900 °C showing textured growth in the (001) orientation. Phases of V_3AlC_2 and V_4AlC_3 were only observed when grown on TiC seed-layers. Most films contained secondary phase of V_2C.

parameters for the three deposits were identical with the exception of cathode power. Compositional analysis showed sample A to have a higher than desired Al content, equating to a M/A ratio of ~1.2, far from the ratio for any MAX phase. Samples B and C had similar M/A ratios of ~ 1.6, while all three samples had carbon compositions approximately 24 at. %. At this point it can be speculated that a solid-state reaction most likely is occurring between the TiC and the V-Al-C deposited material resulting in the new phases similar to depositions of TiC on Al_2O_3 above 750 °C resulting in Ti_2AlC (Appendix A). Why these 312 and 413 phases appeared only in the presence of TiC and with M/A ratios far from either phase is not clear. TEM - which was not performed on these samples - could shed some light on the growth of these phases, especially at the TiC seedlayer interface. Tables 6.4 and 6.5 list the XRD data and lattice calculations of V_3AlC_2 and V_4AlC_3, respectively.

V_2AlC thin films were also successfully grown directly on sapphire (Fig. 6.17) at various carbon cathode powers at 900 °C. The calculated lattice mismatch between V_2AlC on sapphire is ~8%, not conducive for epitaxial growth. Films deposited at 200 W and 230 W resulted in strong diffraction of (001) V_2AlC with small amounts of V_2C and an unknown phase around 43°. At 250 W the quality of the V_2AlC peaks decreased along with the disappearance of the two minor phases observed at lower carbon powers. Also observed in the 250 W films were diffraction peaks around 6° and 8°, which were attributed to $V_5Al_2C_3$ and V_4AlC_3, respectively. The former phase is a combination of the 211 and 312 phases forming a supercell-like structure and thus producing the observed diffraction. This so-called 523 phase was also observed in the Ti-Si-C system.[7, 94, 95] Although the V_4AlC_3 phase was barely observable, the fact it was observed in deposits on

TiC indicates the phase can exist without the Ti present. It should be remembered the films compositions were targeted for 211 chemistry, therefore observations of these other MAX phases in films far from their stoichiometry demonstrates how metastable the phases are.

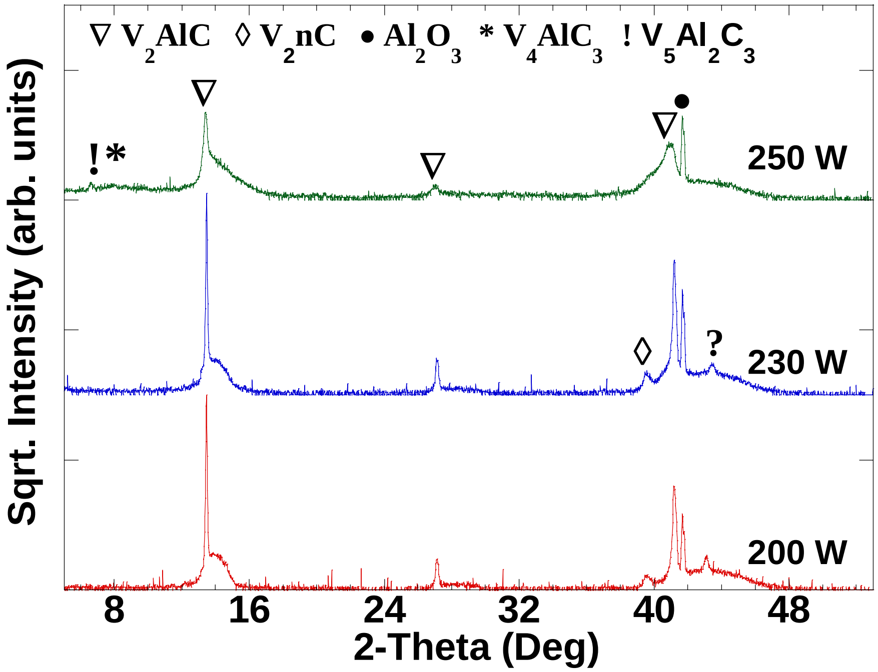

Figure 6.17 X-ray diffraction patterns for V_2AlC thin films grown on sapphire at various carbon cathode powers at 900 °C. Films deposited at 200 W and 230 W resulted in strong diffraction of (001) V_2AlC with small amounts of V_2C and an unknown phase around 43°. At 250 W the quality of the V_2AlC peaks decreased along with the disappearance of the two minor phases observed at lower carbon powers. Also observed in the 250 W film was diffraction around 6° and 8°, which were attributed to $V_5Al_2C_3$ and V_4AlC_3, respectively.

Table 6.3 Properties of V_2AlC thin films deposited on sapphire or TiC or VC seedlayers.

Temperature (°C)	Substrate/ Seedlayer	*c* lattice (Å)	Resistivity ρ_{RT} (μΩ-cm)	RRR	Roughness *Ra* (nm)	Friction Coefficient
900	Al_2O_3	13.1331 (12)	78	1.6	9.6	0.079 (46)
900	VC	13.1389 (69)	65	1.4	9.6	0.106 (39)
800[A]	VC	13.1423 (102)	50	1.6	1.9	0.106 (16)
725	VC	13.1391 (42)	47	1.6	6.4	0.067 (18)
650	VC	13.2039 (605)	117	1.2	5.8	0.066 (19)
600	VC	13.4000 (2000)	139	1.1	1.8	0.084 (22)
900[B]	TiC	13.1120 (45)	62	1.5	4.0	0.075 (28)
900[C]	TiC	13.1160 (66)	54	1.3	1.8	0.092 (17)
900[D]	TiC	13.3091 (484)	54	1.9	8.4	0.070 (34)
-	Bulk	13.14[a]	25[b]	5[b]	-	-

[A] *ex situ* deposit

[B] Contained minor phases of V_3AlC_2 and V_4AlC_3

[C] Contained minor phases of V_3AlC_2 and V_4AlC_3

[D] Contained minor phase of V_4AlC_3

[a] Ref [58]

[b] Ref [7]

Table 6.4 XRD peaks from bulk Ti_3AlC_2, theoretically predicted V_3AlC_2, and those observed in thin film. Nelson-Riley analysis (Section 4.1.1) was used to calculate the observed *c*-axis lattice constant.

	Ti_3AlC_2	V_3AlC_2	Sample A	Sample B
hkl	2θ (°)[a]	2θ (°)[b]	Observed 2θ (°)	
(002)	9.517	9.860	9.878	9.850
(004)	19.154	19.800	-	-
(006)	28.934	29.890	29.931	-
(008)	38.817	40.230	-	-
(0010)	49.212	50.920	-	-
(0012)	59.953	62.110	-	-
(0014)	71.314	74.000	74.140	-
(0016)	83.518	86.910	86.920	-
c lattice (Å)	18.5010	17.9336	17.9037 (97)	17.9445 (700)

[a] JCPDS #52-0875

[b] Theoretical calculation Ref [30]

Table 6.5 XRD peaks for theoretically predicted Ti_4AlC_3 and V_4AlC_3 and those observed in thin film. Nelson-Riley analysis (Section 4.1.1) was used to calculate the observed *c*-axis lattice constant.

hkl	Ti_4AlC_3 2θ (°)[a]	V_4AlC_3 2θ (°)[a]	Sample A	Sample B Observed 2θ (°)	Sample C
(002)	7.500	7.760	7.7944	7.837	7.857
(004)	15.030	15.550	15.623	15.580	-
(006)	22.620	23.410	23.539	-	-
(008)	30.320	31.390	31.620	31.535	31.537
(0010)	38.160	39.530	39.680	39.529	-
(0012)	46.190	47.890	48.121	-	-
(0014)	54.470	56.520	56.870	-	-
(0016)	63.070	65.520	-	-	-
(0018)	72.080	75.000	75.559	-	-
(0020)	81.650	85.120	85.720	85.18	-
c lattice (Å)	23.5841	22.7950	22.6506 (114)	22.7874 (354)	22.7343 (500)

[a] Theoretical calculation Ref [73]

6.2.2. V_2AlC Results and Discussion

ϕ scans (Fig. 6.18a and 6.18b) showed that the films grown on VC and sapphire were epitaxial. As discussed in the previous section, films grown on VC (111) did not produce 2-θ diffraction patterns of the MX binary, but instead the M_2X binary. ϕ scans confirmed this to also be the case since no in-plane relations were observed for VC, however, the in-plane relation for V_2C was found to be $[1\bar{1}0]_{Al_2O_3} \parallel [100]_{V_2C} \parallel [100]_{V_2AlC}$. Films grown without buffer layers had an in-plane relation of $[1\bar{1}0]_{Al_2O_3} \parallel [100]_{V_2AlC}$. This was similar to that found in other MAX phases grown without buffer layers [73]. For unknown reasons in-plane diffraction of the TiC seedlayer was not observed, therefore no relation could be ascertained for the substrate/seedlayer or seedlayer/MAX film. This may have been due to the wrong ϕ angles chosen for 4-circle analysis.

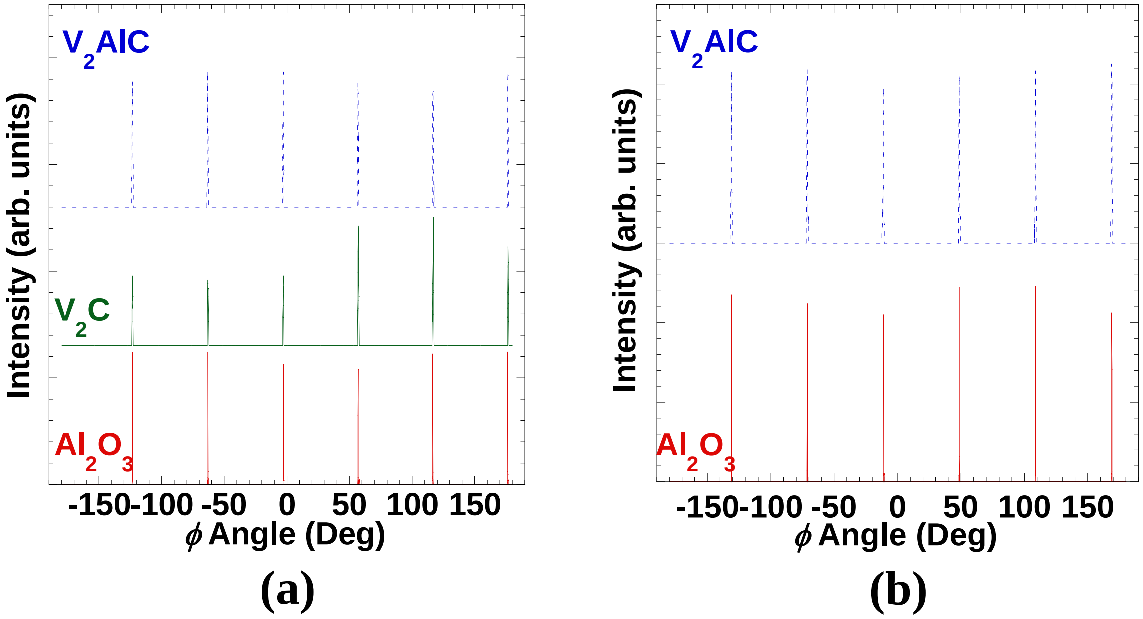

Figure 6.18 a) 4-circle XRD pattern of V_2AlC thin film deposited on VC at 900 °C. Epitaxial relationship is clear between substrate, V_2C, and V_2AlC. b) 4-circle diffraction revealing epitaxial growth for V_2AlC film grown directly on Al_2O_3.

AFM results (Fig. 6.19) for V_2AlC films deposited at various carbon cathode powers found the film to be slightly smoother than the Cr_2AlC films and without the large faceted surface features observed in the latter (Fig. 6.11). Clearly, there are fewer surface features as the C content was increased suggesting less segregated secondary phase growth. The average roughness for 10 x 10 μm images of the 200W, 230 W, and 250 W films was 23.4 nm, 13.6 nm, and 11.3 nm, respectively. Closer examination of the 250 W deposited film, shown in Figure 6.19d revealed sub-nanometer roughness (~0.8 nm) for the background film, indicating uniform surface diffusion and film growth. Additional results of roughness testing are listed in Table 6.3. As anticipated, lower deposition temperature yielded smoother films, which was expected since the amount of surface diffusion relates directly to the energy available to the system thus limiting island growth.

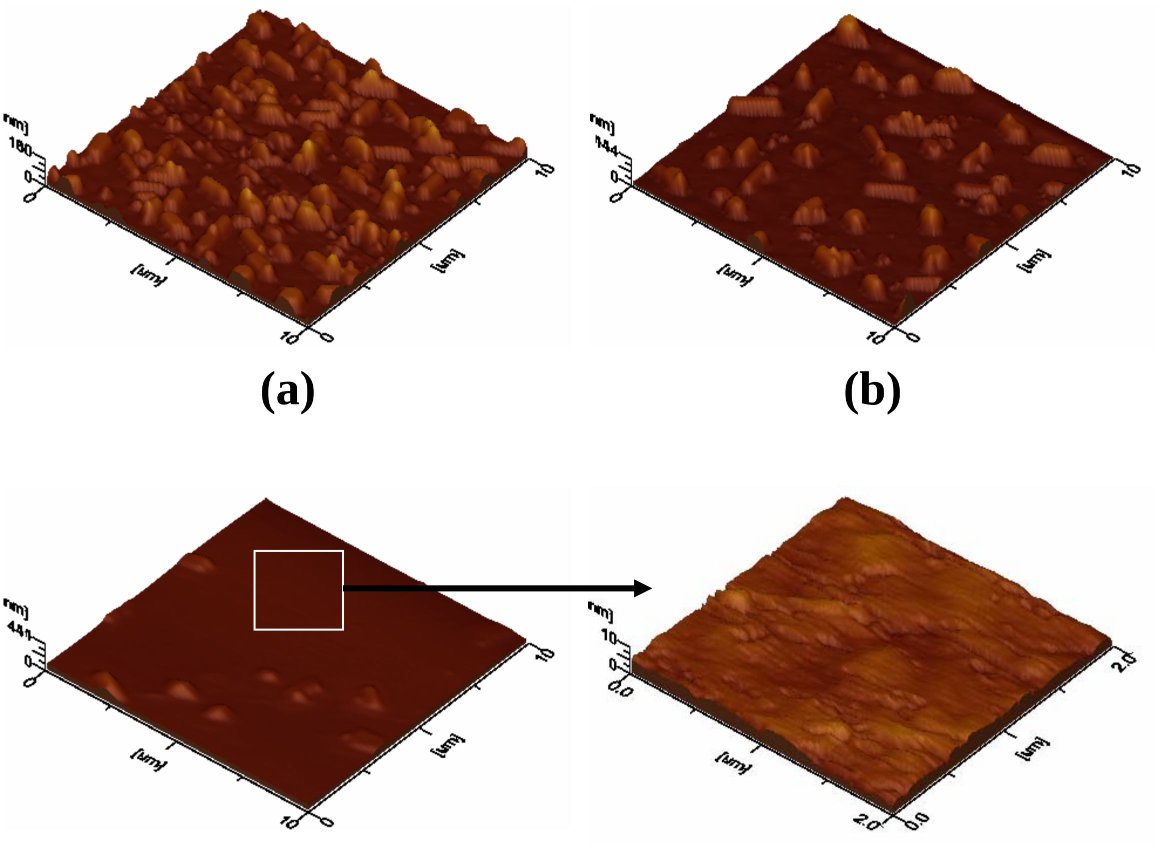

(a) **(b)**

(c) **(d)**

Figure 6.19 Atomic force microscope images of V_2AlC thin films deposited on sapphire at 900 °C with carbon cathode powers of a) 200 W, b) 230 W, c) 250 W, and d) 250 W. 10 x 10 µm images (a-c) clearly there are fewer surface features as carbon is increased suggesting less segregated secondary phase growth. The average roughness of (a), (b), and (c) was 23.4 nm, 13.6 nm, and 11.3 nm, respectively. Closer examination of the 250 W deposited film (Figure (d)) revealed sub-nanometer roughness (~0.8 nm) for the background film, indicating uniform surface diffusion and film growth.

The average roughness of films deposited on VC ranged from ~2-10 nm, while deposits on sapphire were about twice as rough ~10-20 nm, not surprising since the lattice strain between sapphire and V_2AlC is quite large. Interesting to note though, the 800 °C *ex situ* deposit showed a much lower roughness than films deposited at higher and lower temperatures. Results of friction testing are listed in Table 6.3. The friction coefficients are all small ranging from 0.063 to 0.106 with no observable trend. In all cases, the coefficient was independent of load.

All V_2AlC films showed metal-like electrical behavior (Fig. 6.20). Films deposited at 725 °C and 825 °C showed the lowest resistivities and were in good agreement with the value found in bulk.[24, 83] An increase in resistivity was observed for all other deposition temperatures and substrates. All films had small RRR values (< 2), compared to that found in bulk of ~5,[30] indicated significant disorder, most likely induced by the presence of minor phases like VC and V_2C. Based on these results, there may be reasonable anisotropy within the system, however, phase pure films are required

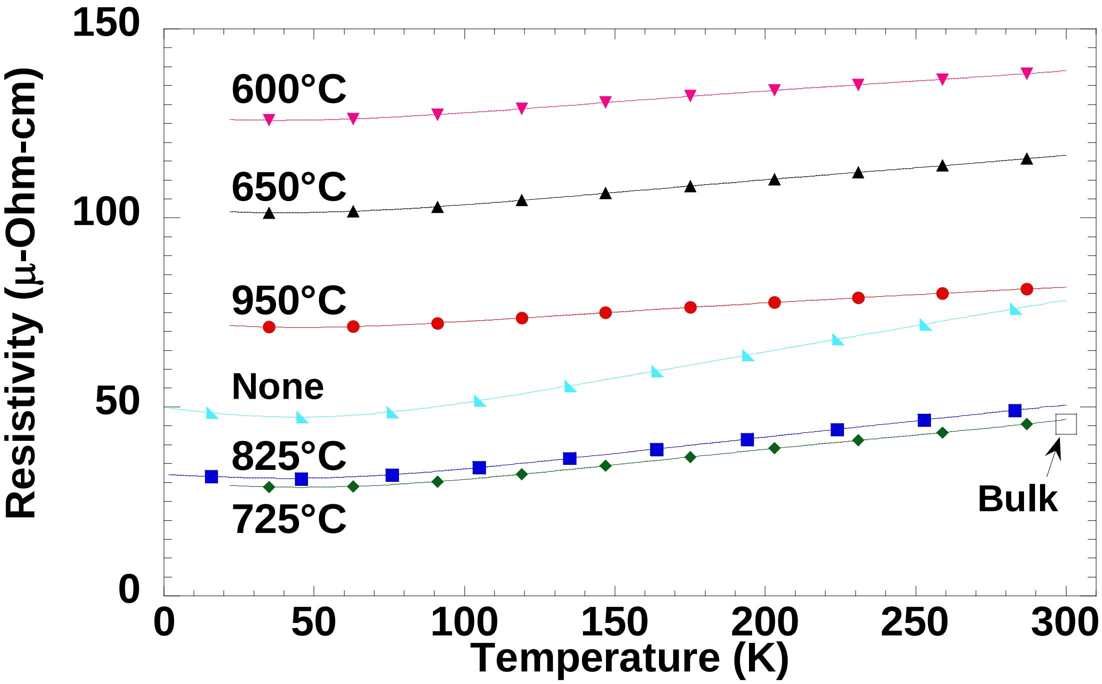

Figure 6.20 Resistivity as a function temperature for various V_2AlC thin films deposited on VC seed-layers at various temperatures. The curve labeled 'None' represents a V_2AlC film directly grown on Al_2O_3 at 900 °C.

in order to justify this statement. Interestingly, V_2AlC films grown on TiC, which contained V_3AlC_2 and V_4AlC_3 phases, had values commensurate with single phase V_2AlC indicating that the V_3AlC_2 and V_4AlC_3 phases were good conductors as well (Table 6.3).

Hall coefficient as a function of temperature for V_2AlC thin films deposited on sapphire at 900 °C with various carbon cathode powers, shown in Figure 6.21a. All films showed a negative coefficient nearly identical in value regardless of carbon cathode power, in good agreement with previous results for the bulk material [30]; however, films exhibited a slight decrease in Hall coefficient with temperature in contrast to the bulk, which exhibited little temperature dependence.

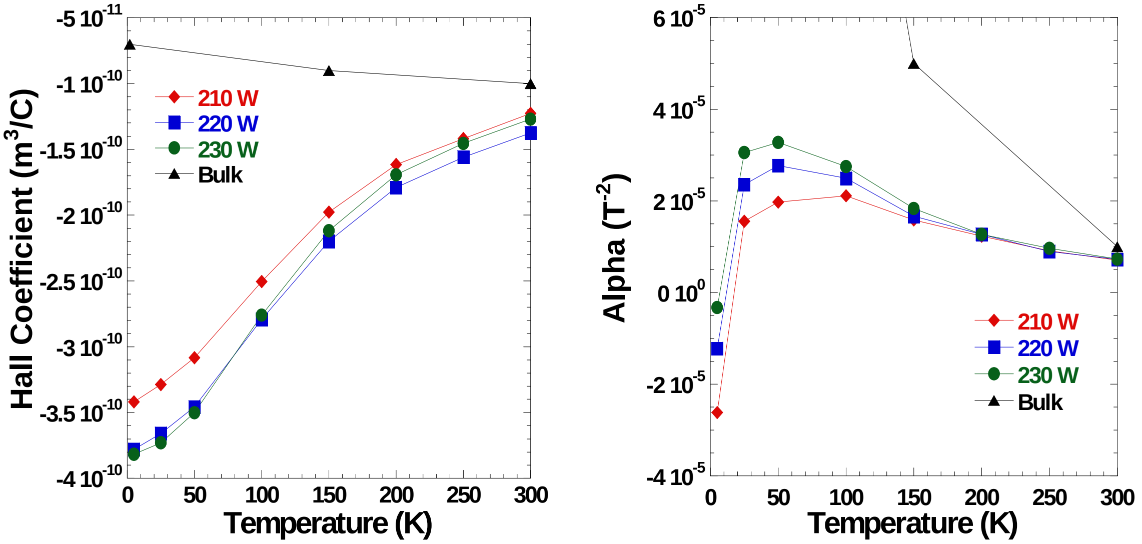

(a) (b)

Figure 6.21 Magnetotransport results for V_2AlC thin films deposited on sapphire at 900 °C with various carbon cathode powers. a) Temperature dependence of Hall coefficient. Values were nearly identical regardless of carbon cathode power. b) Magnetoresistance (MR) as a function of temperature. Values were almost identical for all films regardless of deposition parameters with only a slight increase in value at lower temperatures as carbon power was increased. Interestingly, the MR becomes negative for all films at 2 K indicating some magnetic phase is present in the film. Bulk values from Hettinger.[30]

Magnetoresistance (Fig. 6.21b) revealed small values of α, with little temperature dependence for $T \geq 5$ K. Values were almost identical for all films regardless of deposition parameters, with only a slight increase in value at lower temperatures as carbon power was increased. Interestingly, at $T = 2$ K the magnetoresistance becomes negative indicating some magnetic phase is present. Negative magnetoresistance occurs in magnetic material and is controlled by spin-orbit scattering. By aligning magnetic spins, scattering is reduced effectively increasing the conductivity. Considering all known theoretical calculations and experimental results of V_2AlC, [29, 30, 77, 94] it does not seem reasonable to associate magnetic behavior with the MAX phase. Currently, it is believed the magnetic behavior observed can be associated with an

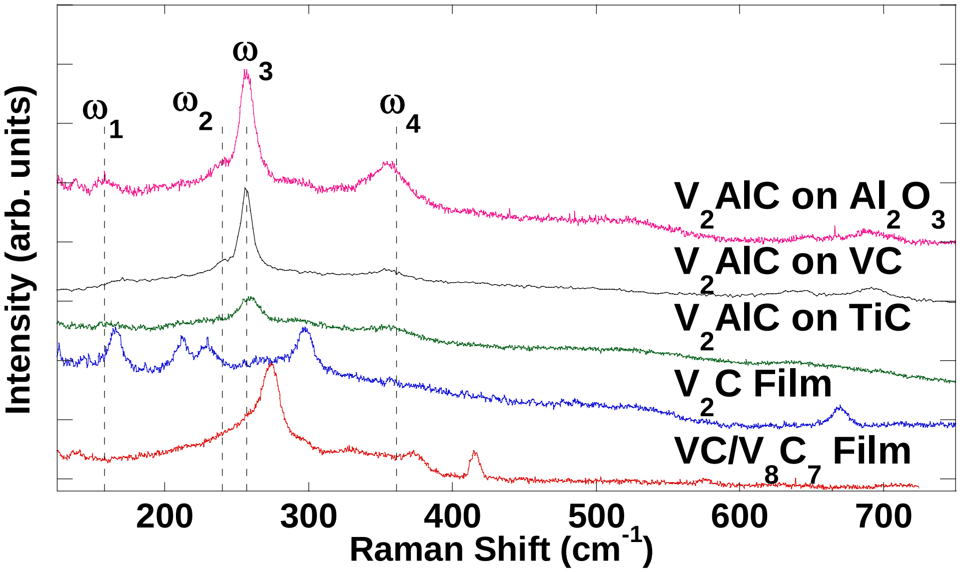

Figure 6.22 Raman spectra of VC, V_2C, and V_2AlC films deposited at 900 °C. Two of the four modes observed in bulk V_2AlC (dashed lines) were consistently observed in thin film. Neither of the binary carbides were observed in the V_2AlC films indicating the phases were below the penetration depth of laser. No modes from the V_4AlC_3 phase were observed in the TiC seedlayer film suggesting the phase was also near the substrate interface.

impurity, most likely a vanadium oxide, which have exhibited similar properties.[96] With small R_H values and for positive quadratic, non-saturating magnetoresistances a two-band model is required to analyze experimental results as described in Section 4.3.4. Similar to what has been reported in previous studies of MAX phases, the carrier concentration was found to be $n \approx 1.3\text{-}2.2 \times 10^{27}$ m^{-3}, slightly lower, but in good agreement with 2.7×10^{27} m^{-3} found in the bulk material.[5, 27, 30, 31]

Raman spectra for V_2AlC films grown on sapphire, TiC, and VC along with binary carbide films of VC-V_8C_7 and V_2C are shown in Figure 6.22. Two of the four peaks associated with V_2AlC were consistently observed in the thin films. Neither of the binary carbides were observed in the V_2AlC films indicating the phases were below the penetration depth of laser. No modes from the V_4AlC_3 phase were observed in the TiC seedlayer film suggesting the phase was also near the substrate interface.

6.2.3. V_2AlC Conclusion

Epitaxial thin films of V_2AlC were successfully grown on *c*-axis sapphire, VC, and TiC buffer layers between 575 and 900 °C. New phases of V_3AlC_2 and V_4AlC_3 were observed in films grown on TiC seedlayers presumably due to solid state reaction between V-Al-C deposition and the seedlayer. The average surface roughness of the V_2AlC films was lower for films grown on VC buffer layers than directly on sapphire substrates attributed to the small lattice mismatch between the MAX phase and buffer layer. The friction coefficients were all small with the lowest values observed on films grown on VC seedlayers. All films exhibited metal-like electrical conduction with small RRR values indicating significant scattering from impurity phases. The lowest room-temperatures resistivities were measured for films synthesized between 725-825 ºC. Hall coefficient and magnetoresistance values similar to bulk with the carrier concentration found to be $n \approx p \approx 1.3\text{-}2.2 \times 10^{27}$ m^{-3}. A negative magnetoresistance was observed at 2 K indicating the possible presence of a magnetic phase.

6.3. $(V_{1-x}Cr_x)_2AlC$ Thin Films

The first solid solutions of $(V_{1-x}Cr_x)_2AlC$ (x = 0.25, 0.5, 0.75) were reported by Schuster *et al.* in 1980.[30] Complete mixing on the M-site was observed for samples annealed at 1000 ºC for 2-5 weeks. Zhou *et al.* synthesized $(V_{0.5}Cr_{0.5})_2AlC$ and the new phases of $(V_{0.5}Cr_{0.5})_3AlC_2$, $(V_{0.5}Cr_{0.5})_4AlC_3$, and $(V_{0.5}Cr_{0.5})_5Al_2C_3$ by reactive hot pressing.[7] More recently, Tian *et al.* synthesized bulk solid solutions of $(Cr_{1-x}V_x)_2AlC$ (x = 0, 0.1, 0.25, and 0.5) by pulsed discharge sintering.[28] Complete mixing was observed along with a linear increase in Vickers hardness with V content.

Sun *et al*. performed the first theoretical solubility study in the $(M_xM'_{2-x})AlC$ (M and M' = Ti, V, Cr) systems.[61] The findings based on total density of states analysis and the energy of formation suggest complete solid solution mixing should occur for all systems except $(Ti_{1-x}Cr_x)_2AlC$. Wang and Zhou published two theoretical studies of elastic stiffness in the M_2AlC (M = Ti, V, Cr, Nb) systems.[97] The findings suggested that the shear modulus c_{44}, which is directly related to hardness, saturates to a maximum as the valence electron count is in the range of 8.4-8.6. For the systems studied only $(M,M')_2AlC$ (M and M' = V, Nb, and Cr) should show solid solution hardening, in agreement for results of bulk $(Ti_{0.5}Nb_{0.5})2AlC$, which showed no hardening.[70, 71]

This section pertains to solid solutions of $(V_{1-x}Cr_x)_2AlC$. The results from this study, along with those for V_2AlC are to be combined and submitted for publication as “Synthesis and characterization of V_2AlC and $(V_{1-x}Cr_x)_2AlC$ thin films”.

6.3.1. $(V_{1-x}Cr_x)_2AlC$ Synthesis

Thin films of $(V_{1-x}Cr_x)_2AlC$ were successfully deposited at 850 ºC for x ranging from 0.15-0.90 with V-Cr compositional gradients ranging from 5-20 at. % across any given substrate while the M-A ratio was maintained between 1.6-2.5. Carbon content across the samples ranged from 18-26 at. % (Fig. 6.23). As can be seen only films between $x=0.4\text{-}0.6$ were close to correct stoichiometry. Outside this region, the films were carbon deficient. Unfortunately these samples were synthesized prior to carbon analysis capability and were chosen based upon phase identification from XRD. XRD results (Fig. 6.24a) revealed (00l) MAX phase peaks along with a secondary phase of $(V_{1-x}Cr_x)_2C$ (00l), which was detected in most films. Figure 6.24b clearly shows the shift in

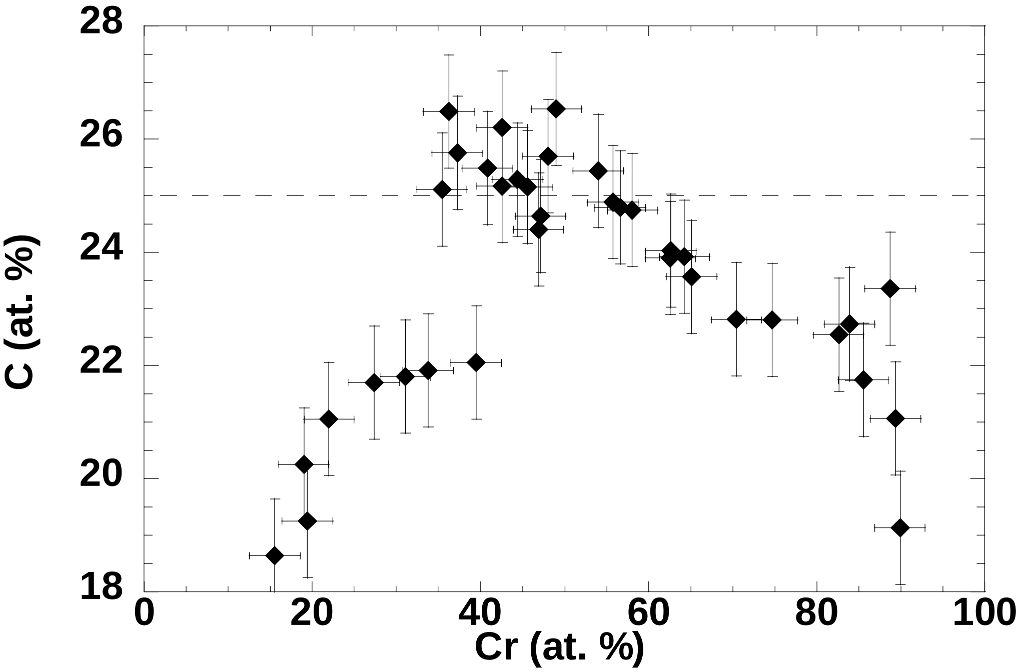

Figure 6.23 Carbon concentration across the range of $(V_{1-x}Cr_x)_2AlC$ film samples. Only films between $x = 0.35\text{-}0.6$ were near stoichiometric values for the 211 phase (dashed line), outside this range the films were carbon deficient.

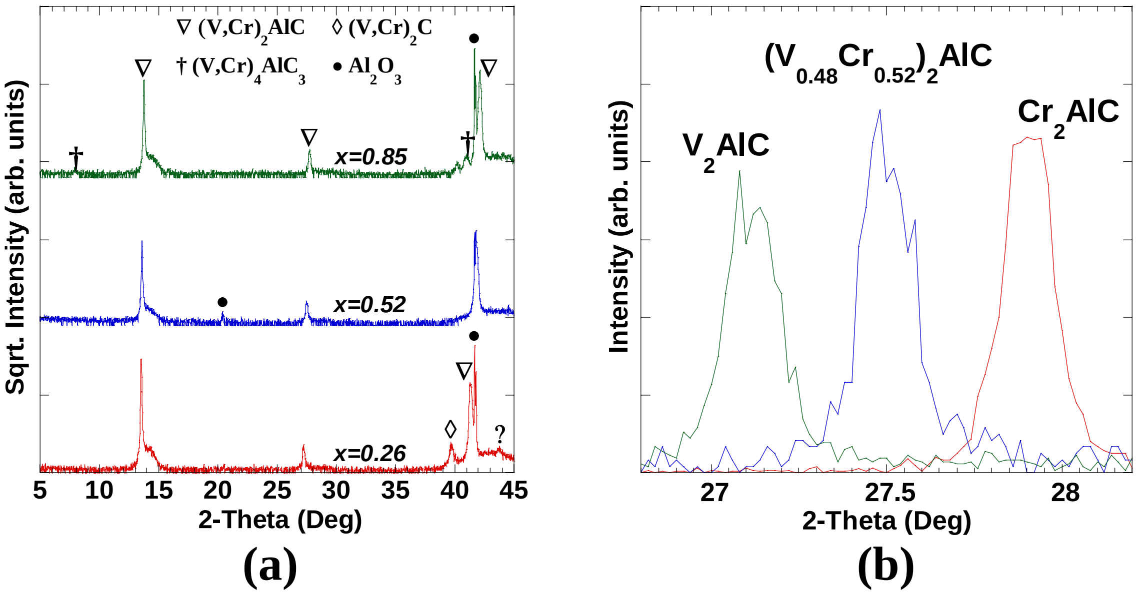

Figure 6.24 a) X-ray diffraction patterns of $(V_{1-x}Cr_x)_2AlC$ thin films. Secondary phases of $(V,Cr)_2C$ and $(V,Cr)_4AlC_3$ were observed in some films. b) Overlay of the (004) peak from X-ray diffraction patterns of V_2AlC, $(V_{0.48}Cr_{0.52})_2AlC$, and Cr_2AlC showing solid solution mixing.

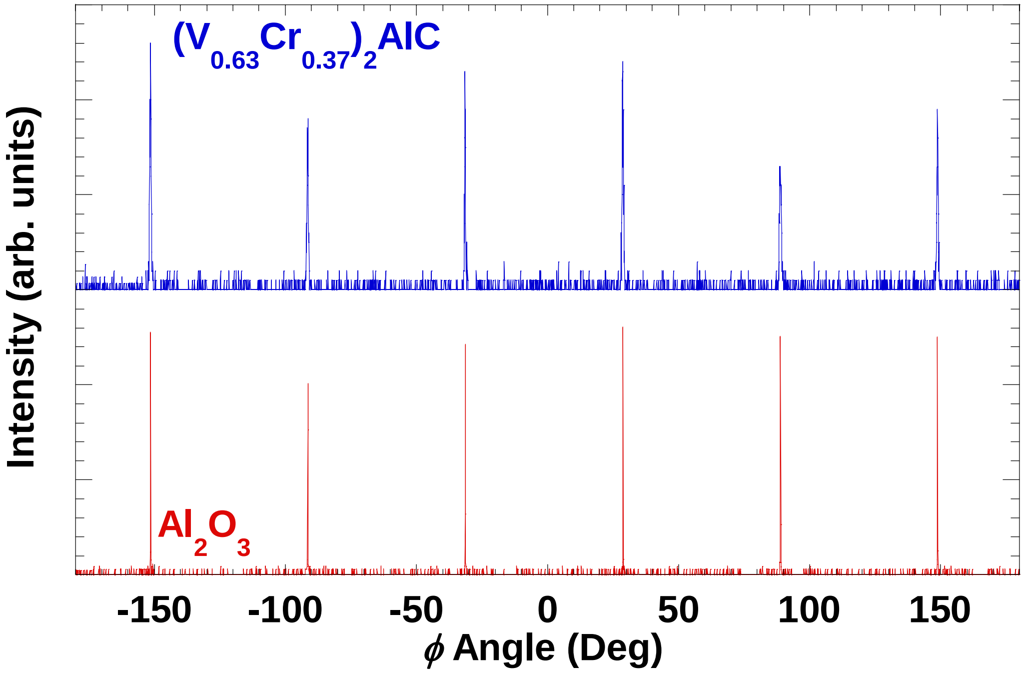

Figure 6.25 Phi scans showing epitaxial relationship between Al_2O_3 and $(V_{0.63}Cr_{0.37})_2AlC$.

the (004) peak for the solid solution showing complete mixing occurred. ϕ scans, shown in Figure 6.25, confirmed that the films were epitaxial. As is the case for Cr_2AlC and V_2AlC, the in-plane relationship is $[1\bar{1}0]_{Al_2O_3} \parallel [100]_{(V,Cr)_2AlC}$.

Also observed during combinatorial synthesis was the formation of $(V_{1-x}Cr_x)_4AlC_3$ (Fig. 6.24a). Predominately single phase $(V_{1-x}Cr_x)_4AlC_3$ occurred when $x = 0.35\text{-}0.45$, while mixed phase with $(V_{1-x}Cr_x)_2AlC$ occurred when $x = 0.7\text{-}0.85$. Figure 6.26 shows XRD patterns of $(V_{0.61}, Cr_{0.39})_4AlC_3$. While it was shown in Section 6.2.1 that the formation of V_4AlC_3 occurred on TiC seedlayers, the emergence of this phase without a seedlayer, but alloyed with Cr makes this unique. This is interesting as the chemistry

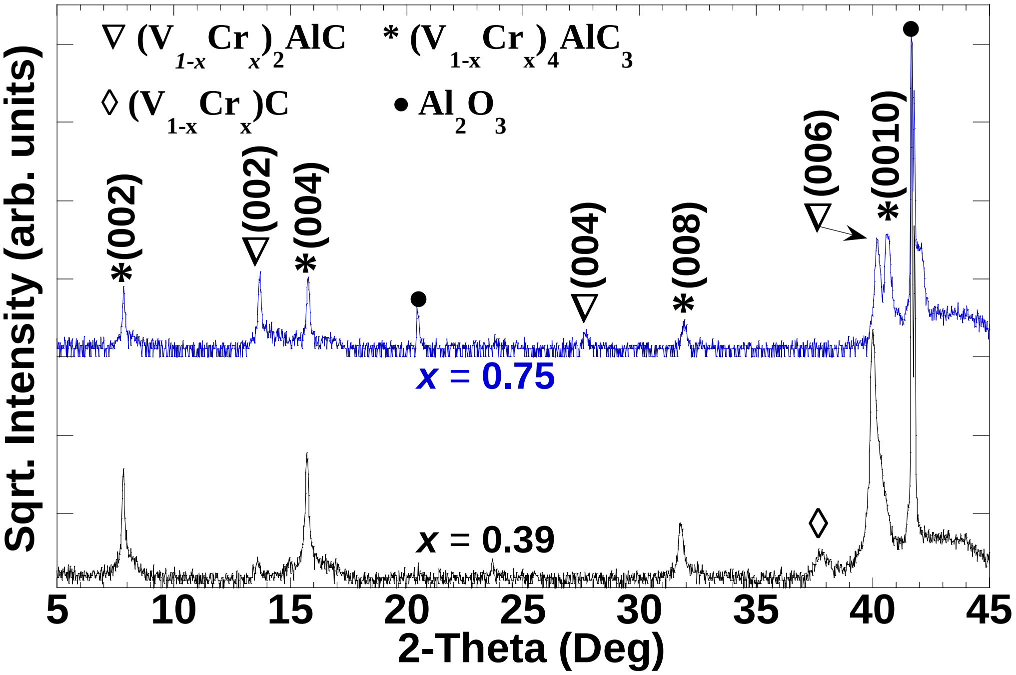

Figure 6.26 X-ray diffraction patterns of $(V_{0.25}, Cr_{0.75})_4AlC_3$ (top) and $(V_{0.61}, Cr_{0.39})_4AlC_3$ (bottom) thin films showing (001) growth. Predominately single phase occurred when $x = 0.35\text{-}0.45$, while mixed phase with $(V_{1-x}Cr_x)_2AlC$ occurred when $x = 0.7\text{-}0.85$. A secondary phase of $(V_{1-x}Cr_x)$ C was also observed.

was tuned for M_2AlC. According to literature, this is the first report for the possible existence of Cr_4AlC_3. Additional work needs to be performed to understand this phenomenon.

6.3.2. $(V_{1-x}Cr_x)_2$AlC Results and Discussion

Figure 6.27 shows the measured *c*-axis lattice constant as a function of *x*. The observed linear relation agreed with Vegard's law for solid solutions. The solid and dashed lines represent guides to the eye for the linear relation between thin film results and bulk values, respectively.[17] Agreement was very good between the film and bulk, even though compressive stresses existed from the substrate on the film based on the hexagonal surface reconstruction of sapphire.[98, 99] An increase in lattice constant over

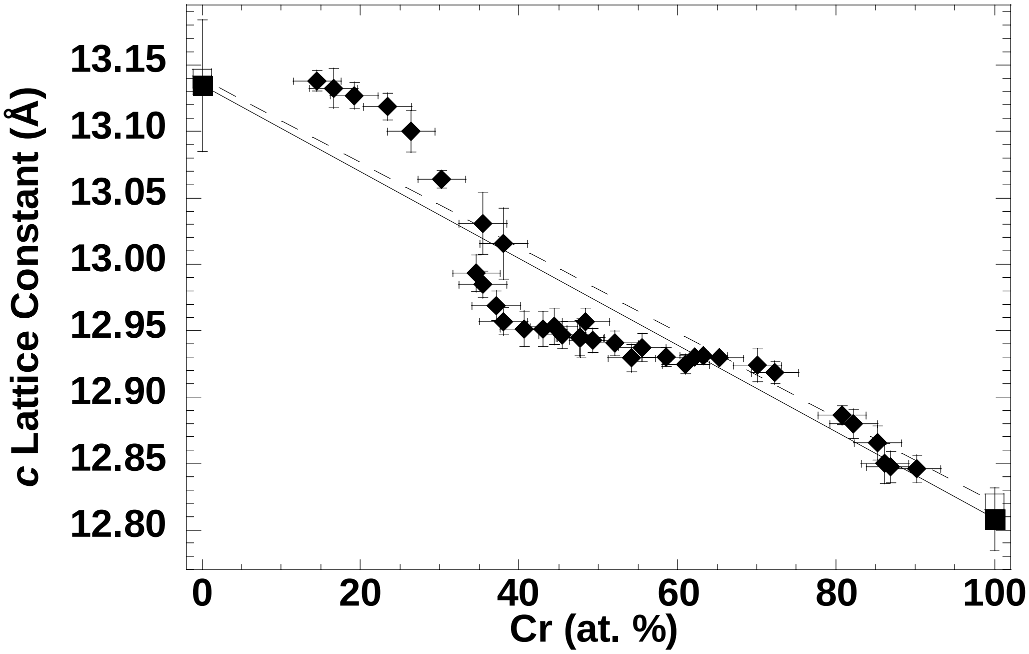

Figure 6.27 Calculated *c*-lattice constant as a function of Cr concentration shows linear behavior for the solid solutions of $(V_{1-x}Cr_x)_2$AlC. The decrease between $x = 0.35\text{-}0.6$ can be attributed to correct carbon stoichiometry for the 211 phase. Solid and dashed lines represent guides for the eye for thin film and bulk values.

the expected value for $x = 0.15\text{-}0.3$ is most likely due to the carbon deficiency noted earlier, also observed in the Cr-V-Ge-C system.[100] Interestingly, a decrease in lattice constant was observed between $x = 0.35\text{-}0.5$, where the C content was at or slightly above stoichiometry.

Figure 6.28a shows the lattice parameters of $(V_{1-x}Cr_x)_4AlC_3$, the line represents a linear fit of the data. The extrapolated value for V_4AlC_3 was significantly less than that found in bulk material by Etzkorn *et al.*[101] It is quite possible this phase was not entirely a solid solution with the measured chemistry, merely residing in a stable range of Cr substitution.

Figure 6.28b shows the lattice parameters of the $(V_{1-x}Cr_x)_2C$ secondary phase,

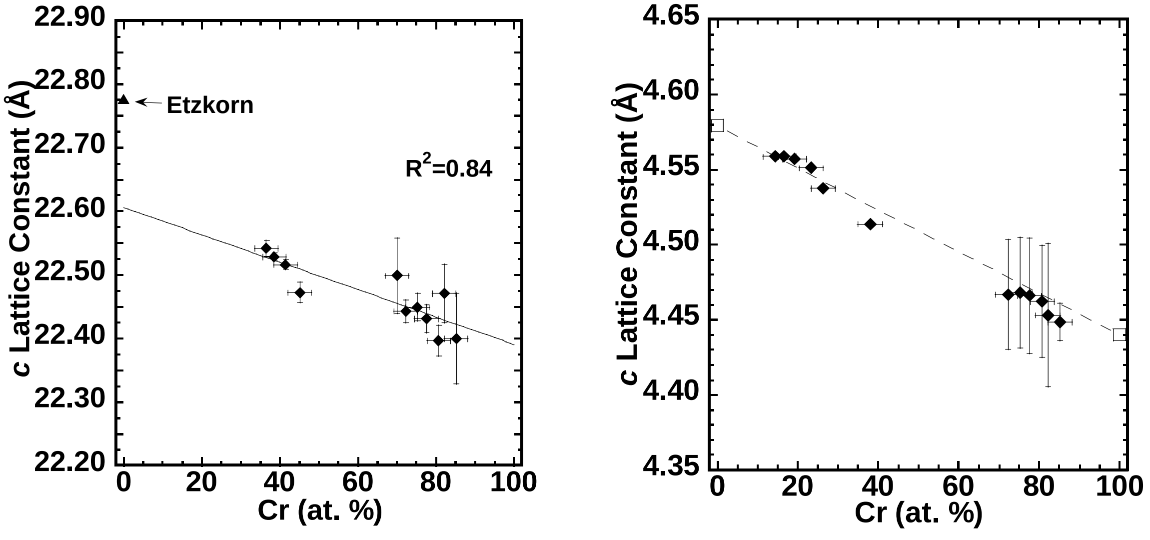

(a) (b)

Figure 6.28 a) Calculated *c*-lattice constant as a function of Cr concentration for the solid solutions of $(V_{1-x}Cr_x)_4AlC_3$. Solid line represents the linear fit of the data. Extrapolating the data indicates a lower than observed value for bulk V_4AlC_3 from Etzkorn. b) Calculated *c*-lattice constant as a function of Cr concentration shows linear behavior for the solid solutions of $(V_{1-x}Cr_x)_2C$. Open markers and dashed line represents a guide for the eye for bulk values.

the results of which also agreed well with Vegard's law. The large error for $x = 0.7\text{-}0.9$ most probably resulted from overlap of the M_2C and substrate peaks. It is quite interesting to observe the M_2C structure at such high Cr concentrations since Cr_2C is a less stable phase and the lattice mismatch with sapphire very large at ~12%. The open markers and dashed line represent a guide for the eye for values from bulk.[102, 103]

AFM measurements indicated that the films had roughness values ranging from 2-56 nm. A plot of the relative roughness, i.e., the ratio of the average roughness to the film thickness is shown in Figure 6.29a. Most samples exhibited relative roughness values of < 15%, with the exception for $x > 0.75$. Why this large increase is observed is not fully understood, however, it most likely was due to the fact that $(V_{1-x}Cr_x)_2C$, $(V_{1-x}Cr_x)_4AlC_3$, and $(V_{1-x}Cr_x)_2C$ were observed in this chemistry range.

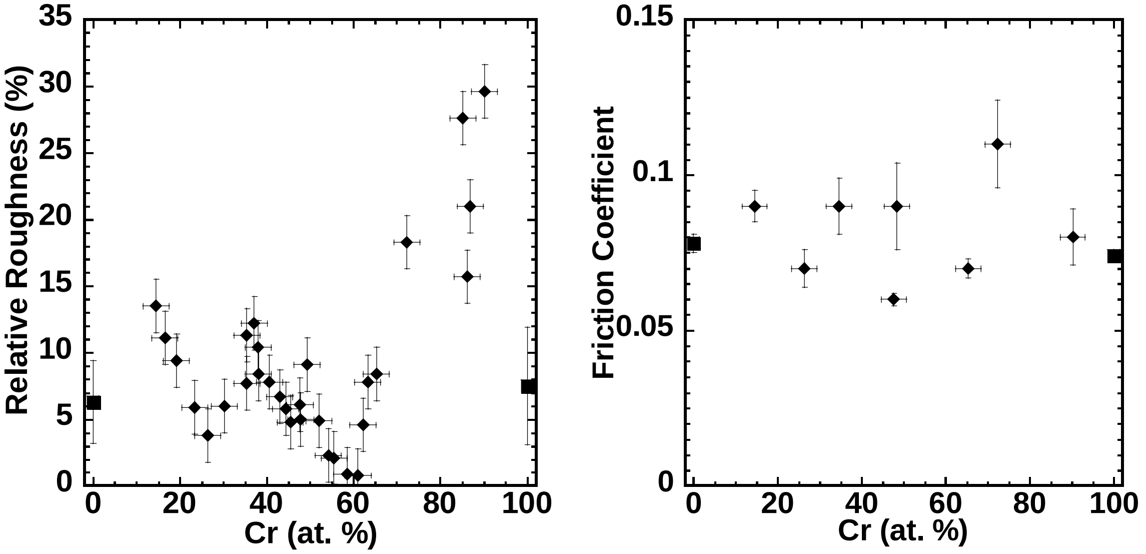

(a) (b)

Figure 6.29 a) Relative surface roughness (R_a/thickness) as a function of Cr concentration for $(V_{1-x}Cr_x)_2AlC$ thin films. b) Surface friction of $(V_{1-x}Cr_x)_2AlC$ thin films as a function of Cr concentration as found by lateral force testing. Overall friction does not appear to be affected by solid solutioning.

Results of friction testing are shown in Figure 6.29b. The friction coefficients were all reasonably low (< 0.11), with an average value of ~ 0.08. In all cases, the coefficient was independent of load. Interestingly, the coefficient of friction was independent of sample roughness unlike previous observations in the $(Ti_{1-x}Nb_x)_2AlC$ and $(V_{1-x}Cr_x)_2GeC$ systems.[54, 100] The present values were significantly higher than those reported for the basal plane of bulk Ti_3SiC_2,[53] but were commensurate with the value of 0.1 found by Emmerlich in films of Ti_3SiC_2,[76] although some films with coefficients of ~0.05 were reported.

Electronic transport measurements showed that the films had metal-like conduction (Fig. 6.30a). The room-temperature resistivity as a function of Cr concentration is shown in Figure 6.30b, where a maximum was observed around $x=0.4$.

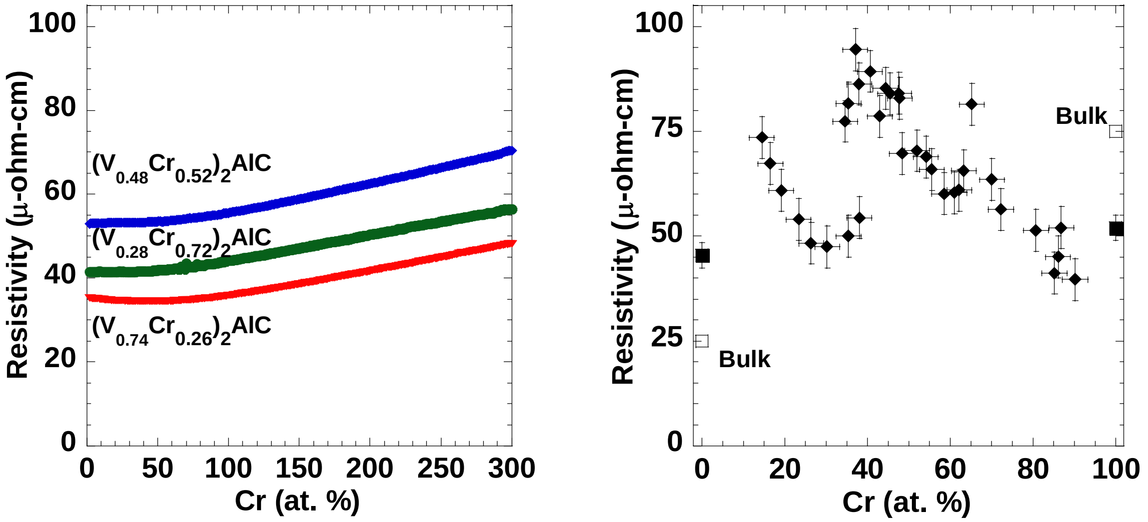

(a) (b)

Figure 6.30 a) Resistivity as a function of temperature for $(V_{0.72}Cr_{0.28})_2AlC$, $(V_{0.48}Cr_{0.52})_2AlC$, $(V_{0.28}Cr_{0.72})_2AlC$ thin films. All films showed metal-like behavior. b) Room-temperature resistivity as a function of Cr concentration for $(V_{1-x}Cr_x)_2AlC$ thin films. The observed peak around $x=0.4$ is typical with solid solution scattering.

As expected, solid solution scattering plays an important role in the electronic transport. Hall coefficient as a function of temperature for various Cr concentrations is shown in Figure 6.31a. Interestingly, all films showed a positive coefficient similar to, and slightly higher than Cr_2AlC, unlike the results observed for V_2AlC, which showed a negative R_H. Magnetoresistance (Fig. 6.31b) revealed values smaller than the end-members with little temperature dependence. Unlike the negative magnetoresistance observed in V_2AlC at 2 K, all values in solid solutions were positive. A minimum of near zero was observed around 50 K followed by a slight increase. Additional measurements of samples with high V concentration (>85 at. %) should provide some insight to the critical amount of Cr, which prohibits the negative magnetoresistance observed in V_2AlC.

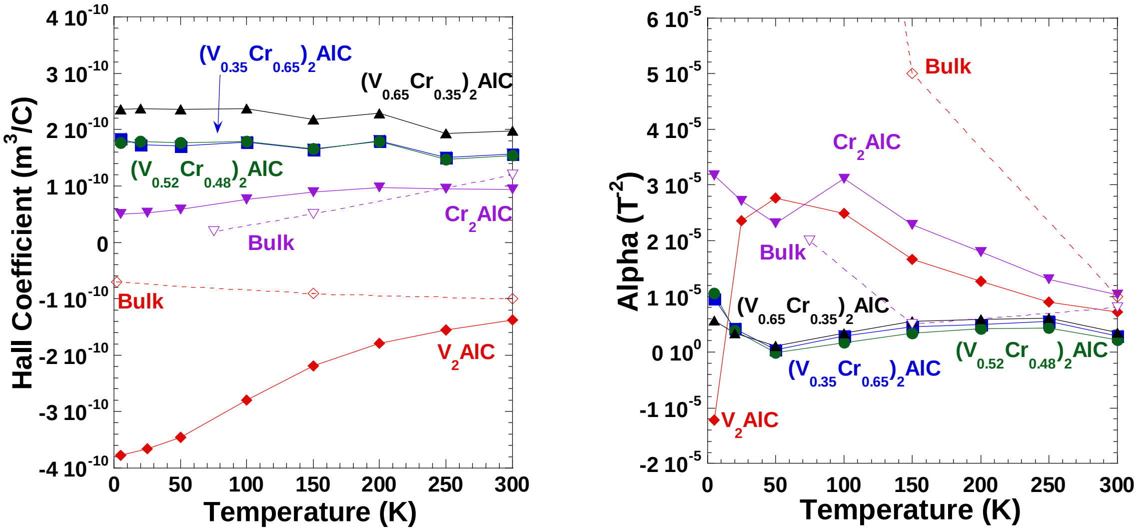

(a) **(b)**

Figure 6.31 Magnetotransport results for $(V_{1-x}Cr_x)_2AlC$ films (solid markers) deposited on sapphire at 850 °C along with bulk (open markers) V_2AlC and Cr_2AlC. a) Temperature dependence of Hall coefficient (R_H). All solid solution films values were small and positive similar to values observed in bulk Cr_2AlC. b) Magnetoresistance (α) as a function of temperature. Solid solution values were all similar and small with little temperature dependence indicating solid solution scattering dominates transport. A minimum of near zero was observed in solid solution films around 50 K.

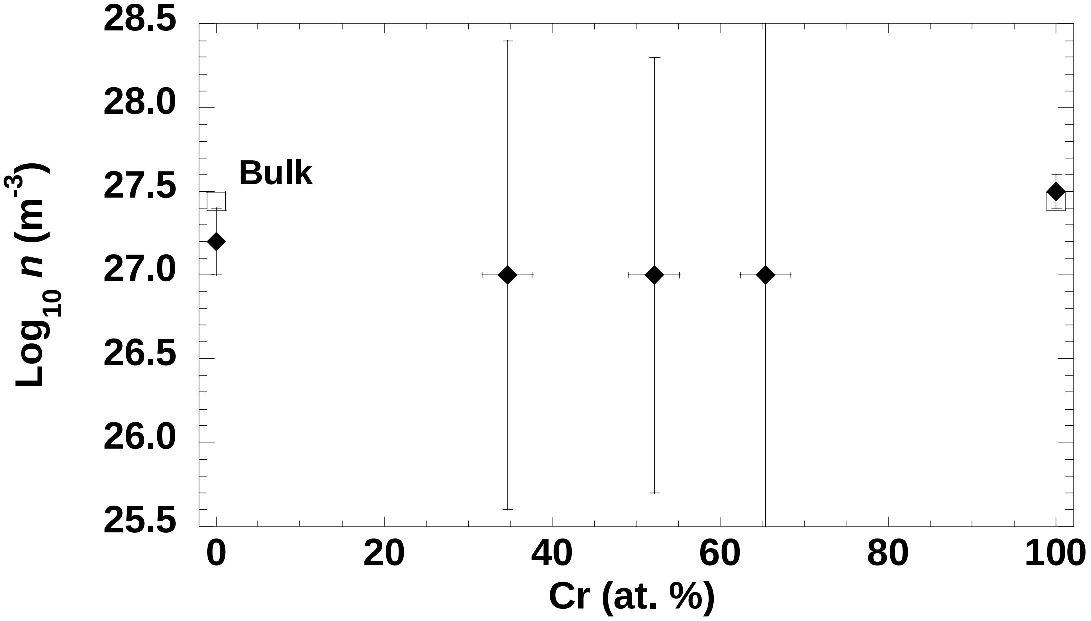

Figure 6.32 Carrier concentration as a function of temperature for $(V_{1-x}Cr_x)_2AlC$ thin films (closed markers) and bulk (open markers). End-member films were in good agreement with bulk values, while up to an order of magnitude decrease was observed for solid solutions. Error bars represent the allowed values of n based upon calculations for $n \approx p$ from the two-band model described in Section 4.3.4.

Hall coefficients and positive magnetoresistances were analyzed within a two-band model resulting in carrier concentrations range of $n \approx p \approx 8.9\text{-}10 \times 10^{26}$ m^{-3}, shown in Figure 6.32. Unlike the decrease in carrier concentration observed in $(Ti_{1-x}Nb_x)_2AlC$ thin films, $(V_{1-x}Cr_x)_2AlC$ values are only slightly lower than end-members. This finding was interesting, indicating M-group substitution does not appear to affect carrier concentration in this solid solution system. Additionally, the mobility of the charge carriers can be found through two-band analysis. Figure 6.33 plots the temperature dependence of electron and hole mobilities. As was observed in resistivity measurements, the mobilities are subject to temperature dependent scattering. The bulk values extracted from Ref. [30] were higher than their respective film counterparts. Interestingly, the solid

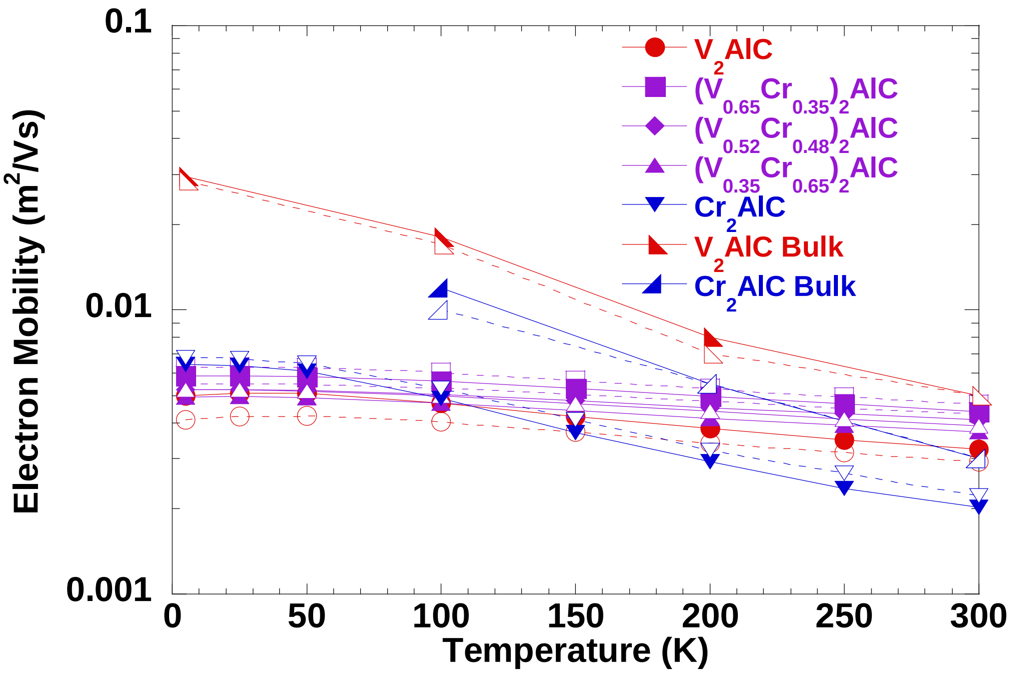

Figure 6.33 Semilogarithmic plot of the temperature dependence of electron (solid markers) and holes (open markers) for V_2AlC, Cr_2AlC, and $(V_{1-x}Cr_x)_2AlC$ thin films. Bulk values were extracted from values reported by Hettinger. In general, bulk values were higher than film values. Interestingly, the solid solutions revealed slightly higher mobilities above 200 K than end-member films with little temperature dependence, suggesting the secondary phases present in the end-members caused the scattering within the material.

solutions revealed slightly higher mobilities above 200 K than end-member films with little temperature dependence, suggesting the secondary phases present in the end-members caused the scattering within the material.

Selected Raman spectra are shown in Fig. 6.34. There are four first order modes in the M_2AX family, most were consistently observed. The lower three modes are attributed to longitudinal modes in the basal plane and the upper mode to a longitudinal mode along the *c*-axis.[67, 68] The disappearance of some modes is likely directly attributable to increased Raman linewidth, indicative of mixing on the M sites. Unlike

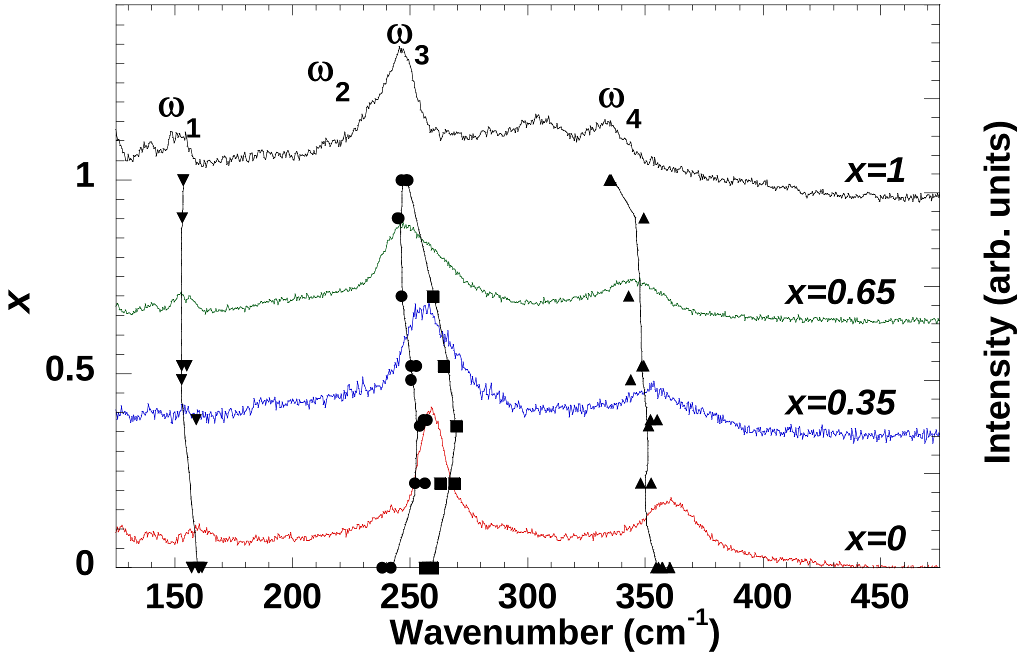

Figure 6.34 Raman spectra for various thin films of $(V_{1-x}Cr_x)_2AlC$. Markers indicate the positions of vibrational modes as a function of Cr concentration. The lines serve as a guide for the eye. No solid solution hardening was observed.

previous findings in the $(Nb_{1-x}Ti_x)_2AlC$ system[54], only minimal changes were observed, indicating no change in modulus.

6.3.3. $(V_{1-x}Cr_x)_2AlC$ Conclusion

Solid solutions of $(V_{1-x}Cr_x)_2AlC$ thin films were synthesized by a combinatorial method by magnetron sputtering on sapphire at 850 °C. X-ray diffraction showed the films to be *c*-axis oriented and epitaxial to the substrate. Most films contained a minor secondary phase of $(V_{1-x}Cr_x)_2C$. Complete solid solution mixing is observed for all compositions and phases following Vegard's law. Electrical transport measurements show typical metal-like conduction with room temperature resistivities ranging between 40-95 μΩ-cm with the highest value observed at $x \approx 0.4$ due to solid solution scattering. All films had small Hall coefficients and magnetoresistances indicating the electrical conductivity of these materials is compensated. Magnetotransport results were analyzed within a two-band model resulting in carrier concentrations for $n \approx p \approx 8.9\text{-}10 \times 10^{26}$ m^{-3} indicating M-group substitution does not appear to affect carrier concentration. Friction studies found an average coefficient of friction of ~ 0.08. Raman spectroscopy shows no sign of solid solution hardening. A new phase of $(V_{1-x}Cr_x)_4AlC_3$ was also observed in two compositional regions suggesting possible phase stability depending upon film stoichiometry. Extrapolation of the c lattice values of $(V_{1-x}Cr_x)_4AlC_3$ indicated incomplete solubility for the phase.

Chapter 7: MAX Phase Thin Films in the V-Cr-Ge-C System

This chapter contains the results for films in the V-Cr-Ge-C systems. Synthesis and characterization of the Cr_2GeC and V_2GeC phases was performed first. Optimal synthesis conditions from the two aforementioned films was determined and applied towards to the synthesis of $(V_{1-x}Cr_x)_2GeC$ films.

7.1. Cr_2GeC Thin Films

This section pertains to thin films of Cr_2GeC. There have been no reports to date of Cr_2GeC being synthesized in thin film. The results from this study, along with Cr_2GeC and $(V_{1-x}Cr_x)_2GeC$, are to be combined and submitted for publication as "Thin films in the Cr-V-Ge-C systems synthesized by combinatorial method".

7.1.1. Cr_2GeC Synthesis

Epitaxial Cr_2GeC (001) thin films were successfully grown directly on sapphire substrates at temperatures up to 925 °C (Fig. 7.1a and b). This result wais interesting since the calculated lattice mismatch between Cr_2GeC on sapphire is ~7% tensile strain, generally not conducive for textured or epitaxial growth. Textured growth was observed down to 650 °C for Cr_2GeC. Most deposits contained secondary phases of polycrystalline Cr_3GeC and/or hexagonal $Cr_5Ge_3C_x$ (002). Lattice refinement of the orthorhombic Cr_3GeC, indicated the lattice constants to be a=2.8912 (50) Å, b=10.2509 (63) Å, c=7.7223 (51) Å, in good agreement with the reported values of 2.89 (9) Å x 10.33 (9) Å x 7.72 (4) Å.[104] Lattice calculations for c-axis oriented $Cr_5Ge_3C_x$ yield a value of 4.8592 (28) Å.

The existence of these other phases could be expected due to their similar chemistries and with the large lattice mismatch of Cr_2GeC these impurity phases may

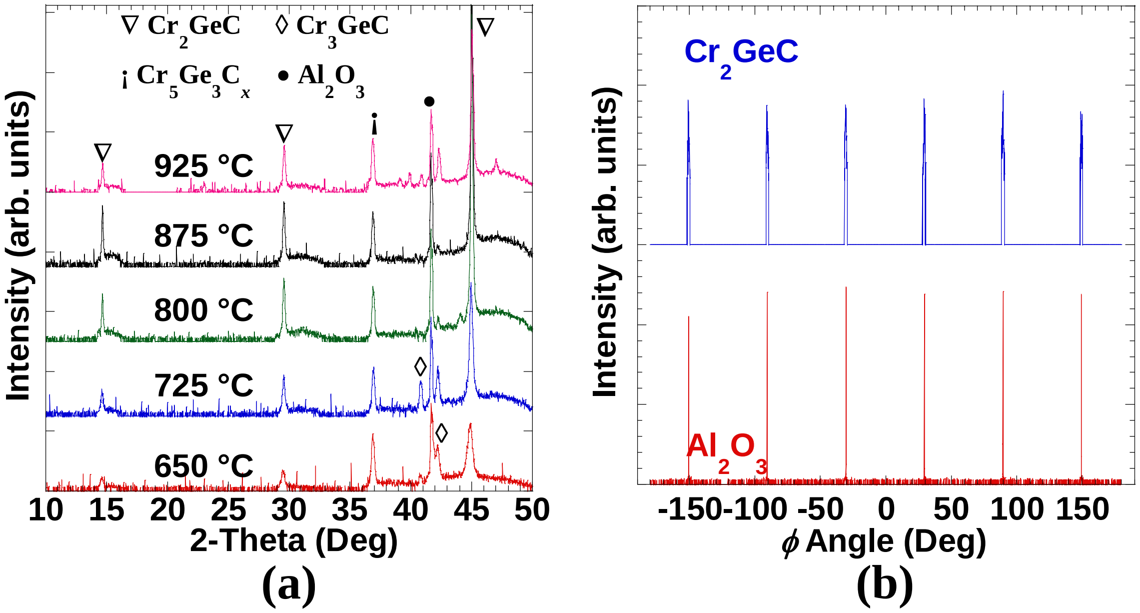

Figure 7.1 a) X-ray diffraction patterns for different synthesis temperatures of Cr_2GeC thin films grown on sapphire show textured growth in the (001) orientation. Phase crystallization occurs around 600°C. Secondary phases of $Cr_5Ge_3C_x$ and Cr_3GeC were observed in most films. b) 4-circle diffraction reveals 6-fold symmetry indicating epitaxial growth.

form as a means to relieve the strain. To test this hypothesis, deposits on VC (111) seedlayers yielded similar results with respect to the secondary phases present even though the lattice mismatch is ~0.2% for Cr_2GeC. Table 7.1 lists the measured c-axis lattice parameter for Cr_2GeC at various temperatures. Another explanation may be that the impurity phases formed due to slight chemistry variations, especially for carbon.

7.1.2. Cr_2GeC Results and Discussion

Only the binary phase diagram has been established for Cr-Ge. Cr-Ge contains five known compounds; Cr_3Ge, Cr_5Ge_3, $Cr_{11}Ge_8$, CrGe, and $Cr_{11}Ge_{19}$.[105] Cr_3Ge andCr_5Ge_3 have M-A ratios closest to those found in the MAX phase family. Cubic Cr_3Ge has lattice strains of ~3% when growing (111) on sapphire. Tetragonal Cr_5Ge_3 was not anticipated to grow in a textured orientation with respect to sapphire due to structure

Table 7.1 Properties of Cr_2GeC bulk and thin films grown directly on sapphire.

Temperature (°C)	*c*-axis (Å)	Resistivity, ρ_{RT} (μΩ-cm)	RRR	Roughness, R_a (nm)	Friction Coefficient
925	12.0763 (8)	49	14.7	46	0.044 (3)
875	12.0770 (11)	40	18.2	48	0.101 (6)
800	12.0785 (14)	47	21.5	69	0.111 (70)
725	12.0785 (89)	59	15.3	42	0.083 (50)
650	12.1105 (44)	67	9.5	32	0.076 (51)
875	12.0892 (16)	42	4.4	45.1	0.065 (2)
Bulk	12.1080 (40)[a]	54[b]	6.8[b]	-	-

[a] Reference [110]

[b] Reference [111]

mismatch. Since Cr_5Ge_3 only forms a tetragonal crystal structure, a rough estimate of the lattice constants for hexagonal Cr_5Ge_3 may be found using the ratios of lattice constants for both tetragonal structures in Cr_5Ge_3 and V_5Ge_3, viz. *a*-Cr_5Ge_3/*a*-V_5Ge_3 and *c*-Cr_5Ge_3/*c*-V_5Ge_3, and applying these to the lattice constants of hexagonal V_5Ge_3.[106] This approximation yielded *a*- and *c*-lattice constants for hexagonal Cr_5Ge_3 of 7.6Å and 4.9Å, respectively, the latter in good agreement with the calculated value of 4.8592(28) Å mentioned earlier. It may be possible for carbon to sit interstitially within this cell, as Parthé found tetragonal Cr_5Ge_3 maintains the *T*1 structure with the addition of 5 at. % carbon.[107-109]

In an effort to identify any unknown XRD peaks in Cr-Ge-C and to verify others, various depositions of Cr-Ge and Ge-C were performed on sapphire at 900 °C. The film with Cr:Ge 3:1 composition resulted in cubic (100) textured Cr_3Ge with a calculated *a*-lattice constant of 4.6254 (17) Å (Fig 7.2a), in good agreement with bulk value of 4.614 Å. This was somewhat surprising as the small lattice mismatch should have allowed for

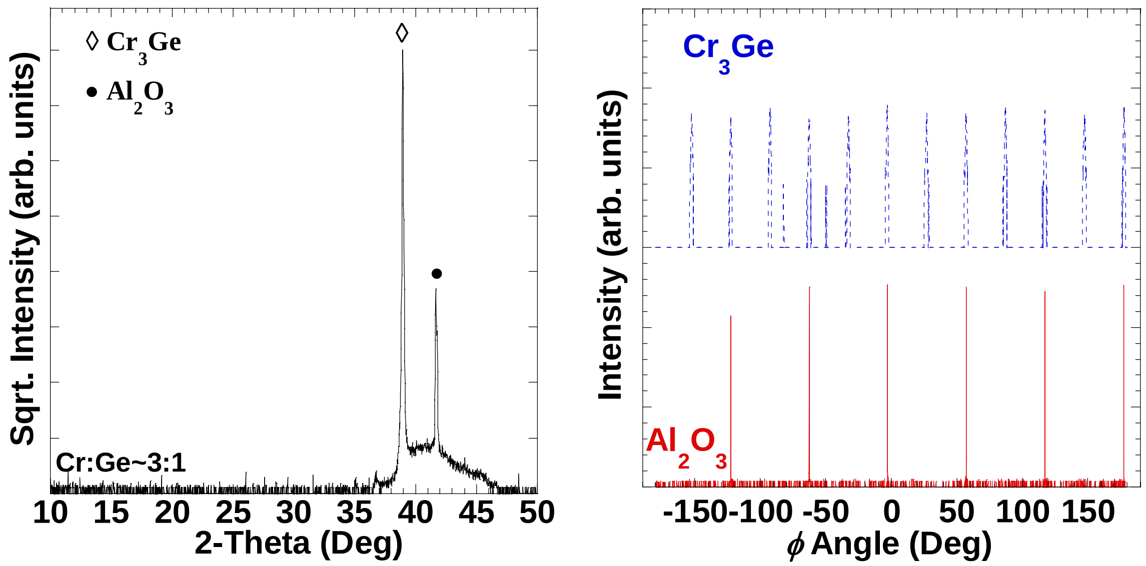

(a) (b)

Figure 7.2 a) X-ray diffraction pattern for a thin film deposited on sapphire at 900 °C with a Cr:Ge composition ratio of ~3:1 revealed Cr_3Ge (100). b) 4-circle XRD of Cr_3Ge showing epitaxial relation with twinning.

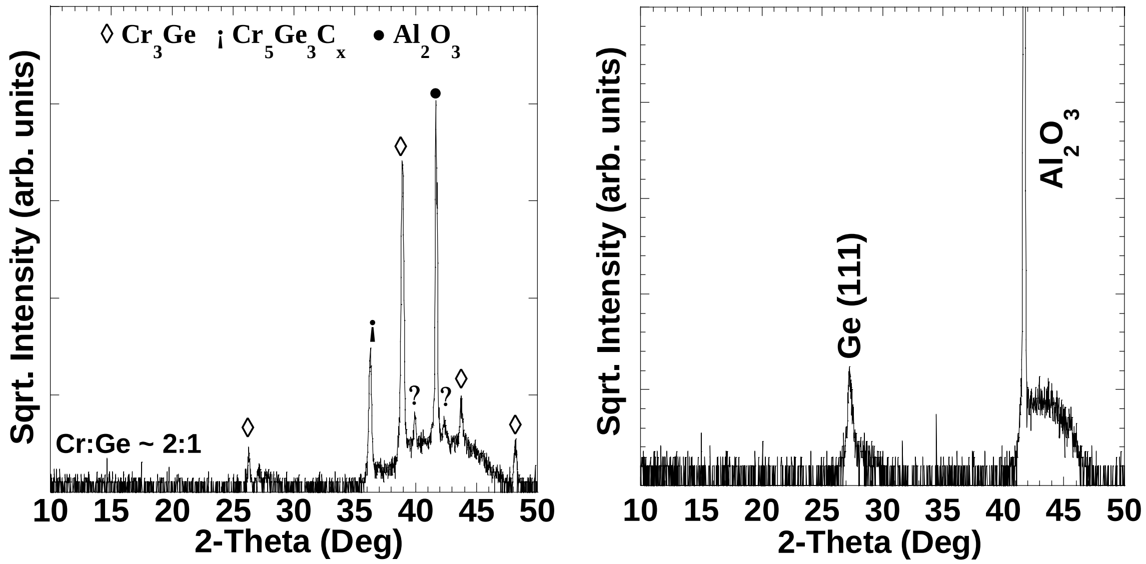

(a) (b)

Figure 7.3 X-ray diffraction patterns for thin films deposited on sapphire at 900 °C with a) Cr:Ge composition ratio of ~2:1 revealing polycrystalline Cr_3Ge, hexagonal Cr_5G_3 (002), and a few unidentified peaks and b) Ge-C deposit showing only weak Ge (111).

(111) growth. 4-circle XRD (Fig. 7.2b) confirmed that the Cr_3Ge film was epitaxial with three variants of twinning present.

The film with Cr:Ge near 2:1 shown in Figure 7.3a resulted in mixed phases of hexagonal Cr_5Ge_3 (00l) and quasi-polycrystalline Cr_3Ge where the (100) was the preferred orientation. Lattice calculation of the former yielded a *c*-axis lattice constant of 4.9485 (23) Å and lattice refinement of the latter had a cubic lattice constant of 4.6228 (15) Å. This was unique, since hexagonal Cr_5Ge_3 is not known to exist, although many other transition metal germanides such as V_5Ge_3 and Ta_5Ge_3 exhibit both the hexagonal and tetragonal structures. This confirmed that the phase observed during Cr-Ge-C deposits was that of hexagonal $Cr_5Ge_3C_x$. Deposition of Ge-C (Fig. 7.3b) resulted in Ge (111), which was not surprising since no known compounds of the two exist.

Images collected using an SEM showed large crystals, some hexagonal in shape, protruding from the film surface. Figure 7.4 shows an SEM image of a Cr_2GeC film deposited at 900 °C. Chemical analysis by EDS revealed that the h and XRD showing a peak consistent with the (002) orientation these features were attributed with the $Cr_5Ge_3C_x$ phase. Likewise, the splinter-like shapes and large grains (Fig. 7.4) had a ≈ 72:28 Cr:Ge molar ratio, in this case very close to the 75:25 ratio of the tetragonal Cr_3GeC system. XRD of the film confirmed the presence of polycrystalline Cr_3GeC, therefore these features were attributed to the Cr_3GeC phase. The majority of the film, i.e. material between the features, had a Cr:Ge ratio of ≈ 67:33 in accord with the MAX phase ratio. The splinter-shaped and hexagonal crystals exhibited preferred orientations with the substrate as denoted by the alignment of the crystals

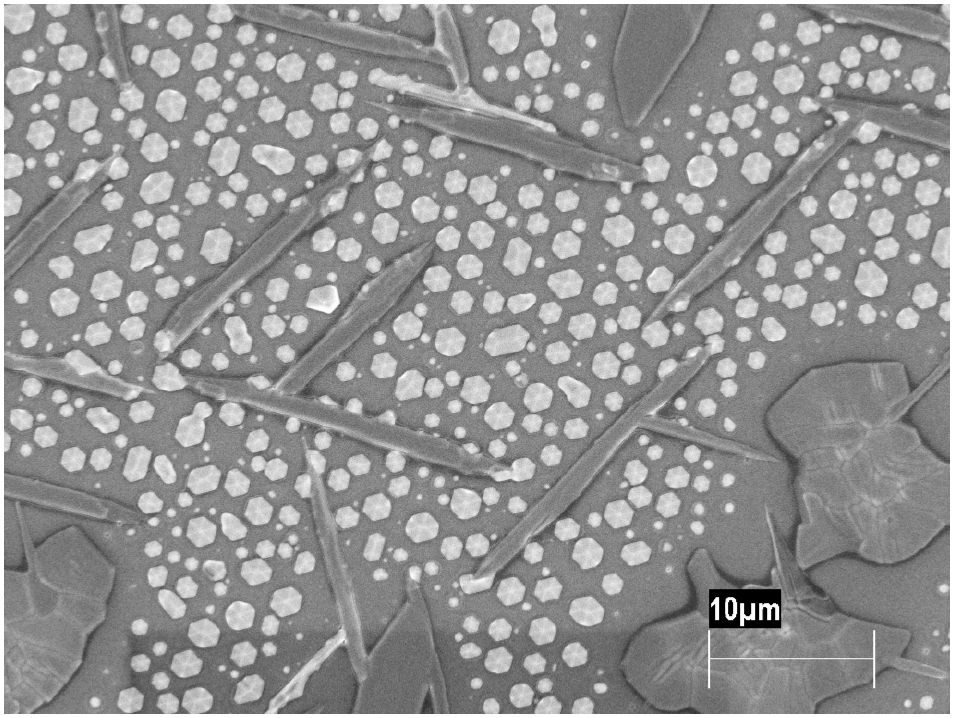

Figure 7.4 SEM image of a Cr_2GeC thin film deposited at 900 °C. Chemical analysis of the various shapes observed revealed the splinters and large grains to be Cr_3GeC, the bright hexagonal crystals to be $Cr_5Ge_3C_x$, and the background film to be Cr_2GeC.

Atomic force microscopy found the high-temperature deposited films to be very rough. Table 7.1 lists roughness values for samples synthesized at various deposition temperatures. Similar results were also reported in the Nb_2AlC system.[112] Low-temperature deposits (<500 °C) yielded smooth films in both systems, as expected, however, no crystalline phases were observed. On the other hand, post-annealed samples maintained a smooth surface with a surface roughness < 2 nm. This indicated that island growth and phase separation were the dominant growth mechanisms at higher temperatures, while random atom dispersion and amorphous film growth occurred at low temperatures.

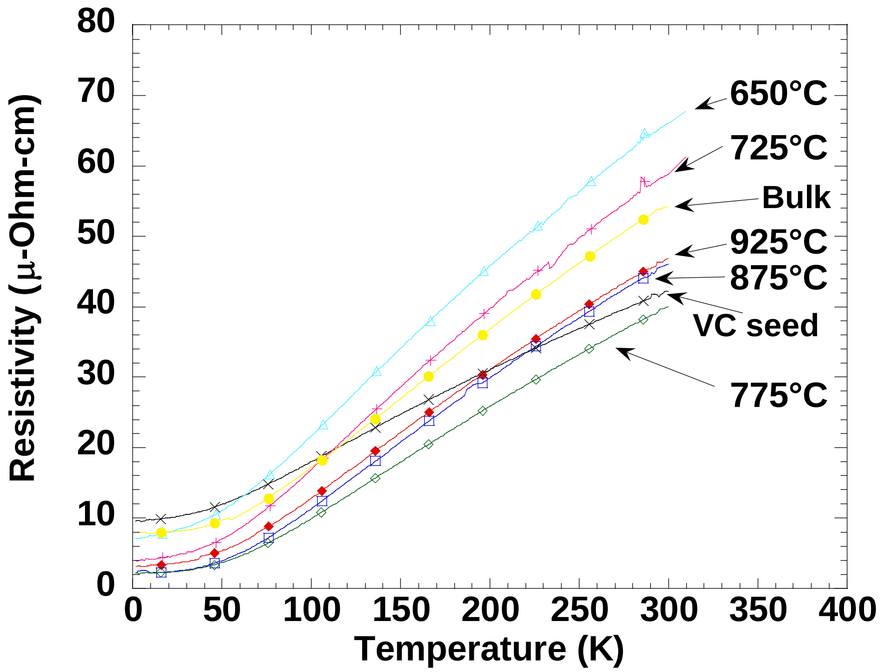

Figure 7.5 Resistivity as a function of temperature for Cr_2GeC thin films deposited at various temperatures. All showed metal-like behavior down to 2 K. Room temperature resistivity values of most films were lower than that of bulk indicating some anisotropy may be present.

All films showed metal-like electrical conductivity (Fig. 7.5). There was no obvious correlation between the resistivity of Cr_2GeC films and deposition conditions except that films grown between 775 and 925 °C had the lowest resistivity and the highest RRR values, suggesting the least local disorder. Cr_2GeC films exhibited the highest RRR values of all MAX phase films reported in this thesis, with the highest being ~24. Even the lowest of 4.4 for Cr_2GeC grown on a VC seedlayer was higher than that of any other MAX phase thin film studied in this thesis, indicating a large electron-phonon coupling. The resistivity values of films deposited above 725 °C are somewhat smaller than the measured bulk value, possibly indicating some anisotropy.

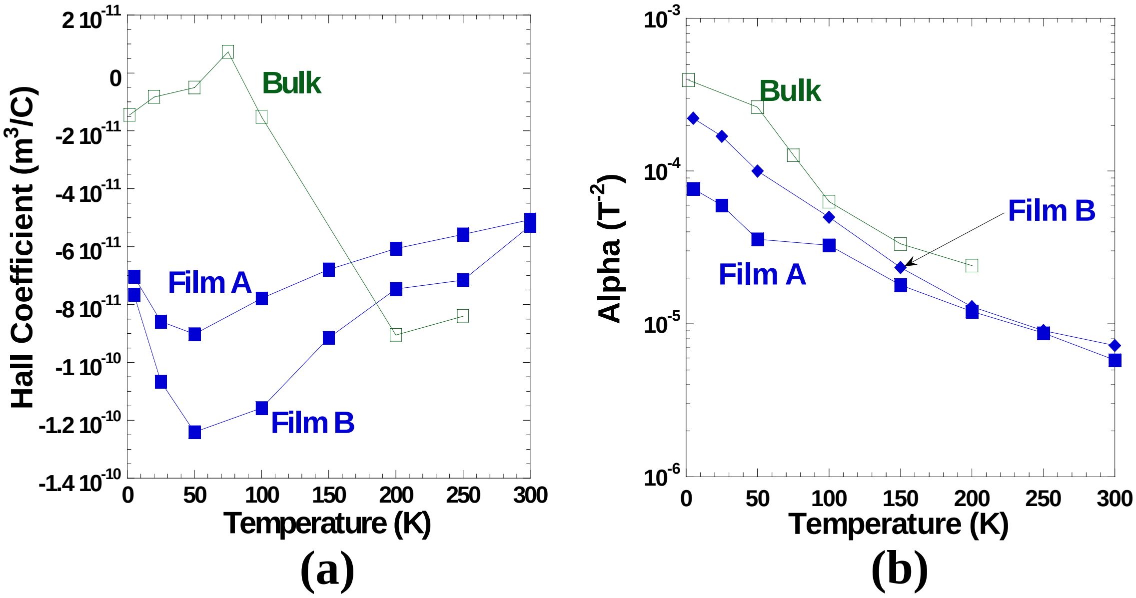

Figure 7.6 Magnetotransport results for Cr_2GeC bulk and thin films deposited on sapphire at 900 °C. Film B was slightly higher quality than Film A. a) Temperature dependence of Hall coefficient showed similar values for films and bulk above 150 K. Below 150 K the bulk value decrease approximately an order of magnitude. b) Semi-log plot of magnetoresistance (MR) as a function of temperature. MR values increased as temperature decreased typical in most MAX phases. Not surprising, MR values mimicked the RRR values of the materials where bulk had the highest RRR and Film A the lowest RRR.

Hall coefficient as a function of temperature of thin films and bulk is shown in Figure 7.6a. Both films and bulk showed negative coefficients, in agreement with their respective binary carbide.[61] The R_H value of the films was almost an order of magnitude larger than the bulk material for T < 150 K. Magnetoresistance (Fig. 7.6b) of thin films and bulk revealed modestly small values with little temperature dependence for T > 150 K. Below 150 K α increased more for bulk and Film B, in agreement with the higher RRR values observed in the resistivity measurements. With small R_H values and positive quadratic, non-saturating magnetoresistances a two-band model was required to analyze experimental results as described in Section 4.3.4. Similar to what has been

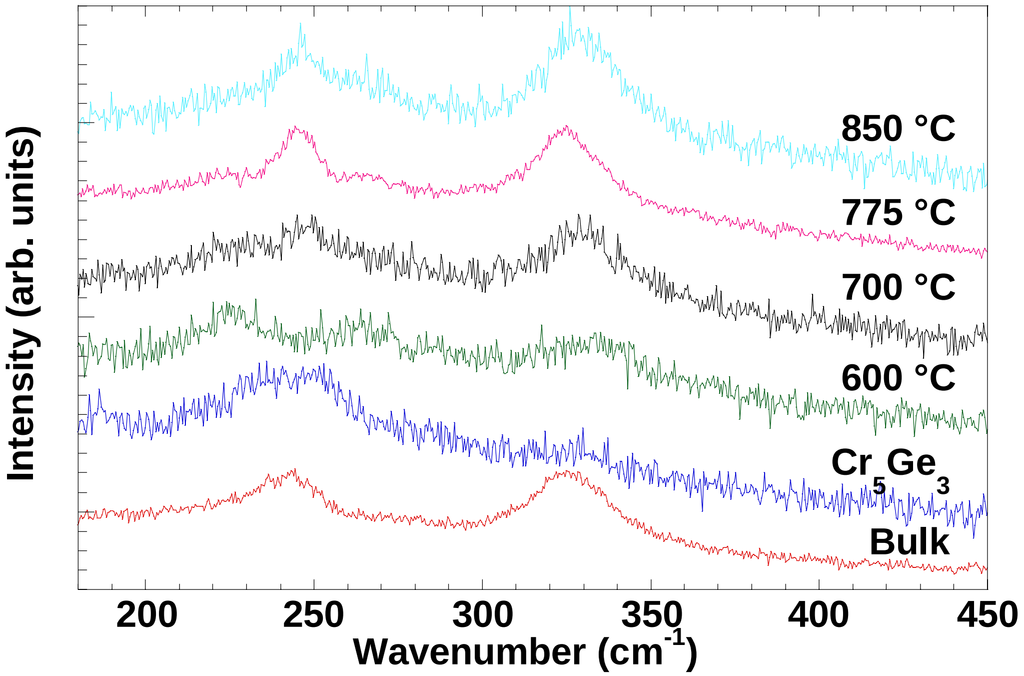

Figure 7.7 Raman spectra of Cr_2GeC deposited at various temperatures, bulk, and Cr_5Ge_3 thin film. Two modes associated with Cr_2GeC were observed; longitudinal in-plane around 245cm^{-1} and out-of-plane around 325cm^{-1}.

reported in previous studies of MAX phases [5, 27, 30, 31] $n_{film} \approx 1.7 \times 10^{27}$ m^{-3}, however; $n_{bulk} \approx 2.7 \times 10^{24}$ m^{-3}. Interestingly, there appeared to be a large difference between the bulk and thin films possibly indicating a large anisotropy. If one assumes a 2:1 ratio between *ab*-plane (what was measured in the films) and *c-axis* electronic transport, then the out-of-plane transport would yield a carrier concentration in the 10^{21} m^{-3} range to be equivalent to the bulk value. Additional work is needed to verify this; growing Cr_2GeC *a-axis* oriented, where transport would measure the out-of-plane direction.

Raman spectra for various deposition temperatures of Cr_2GeC along with that of the $Cr_5Ge_3C_x$ film and bulk Cr_2GeC are shown in Figure 7.7. Only two of the four vibrational modes were observed. The peak around 245 cm^{-1} is related to the in-plane shear mode between the M and A. The peak seen in all depositions that varied between 325-332 cm^{-1} was believed to be the out-of-plane mode originally reported to be at 301 cm^{-1}. There appeared to be a discrepancy here, while the reported position was at 301 cm^{-1} the *ab-initio* calculated position was 352 cm^{-1}.[68] The peak observed by Leaffer *et al.* can be associated with Ge since a strong line is found at 300 cm^{-1} and it is fairly common for Ge to segregate from these materials.[68] In addition, there was a peak in their work that was left unidentified near 320 cm^{-1}. Therefore, the out-of-plane mode for Cr_2GeC should be observed between 320-330 cm^{-1}.

The Seebeck coefficients for bulk and thin film Cr_2GeC are shown in Figure 7.8. Only data for T ~ 150-300 K was obtained for the thin film, a result of the difficulty in

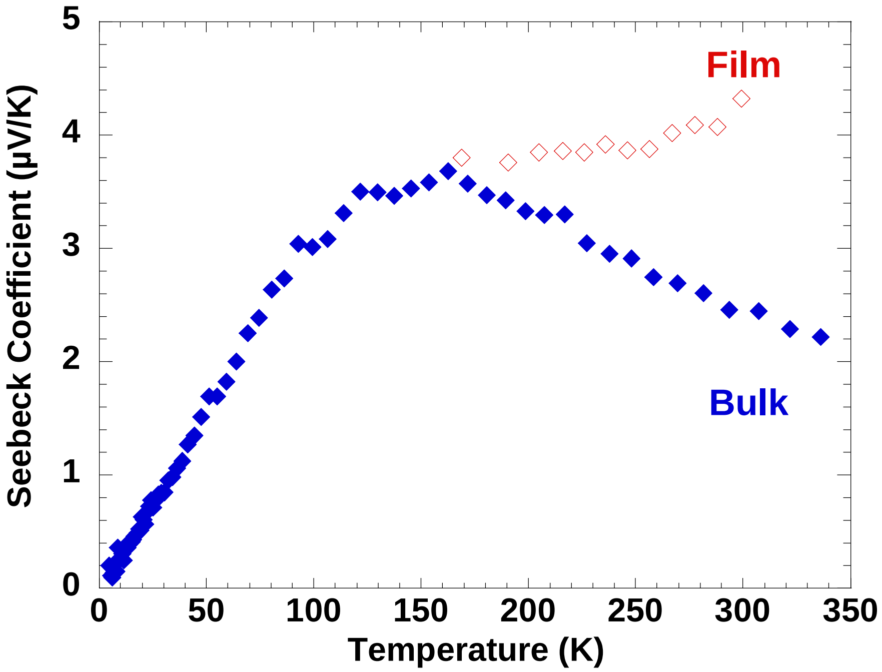

Figure 7.8 Seebeck coefficient of Cr_2GeC thin film and bulk material. Only for $T > 150$ K were values for thin films measurable due to the high thermal conductivity of sapphire.

measuring the temperature difference due to the high thermal conductivity of sapphire. Interestingly, the Seebeck coefficient in the film remains around 4 μV/K for T > 150 K, while the bulk sample showed a decrease. Further experiments are needed to understand this difference and to complete the full range of temperature analysis. Also notable were the signs of Seebeck coefficient and R_H which did not agree, indicating that a multiband model is required to describe the electronic transport.

In order to investigate the crystallization of Cr-Ge-C films, high-temperature XRD was performed. Experiments were conducted on 1x1 cm^2 samples of Cr-Ge-C films deposited directly on sapphire or on seedlayers of TiC (111) and VC (111) at both RT

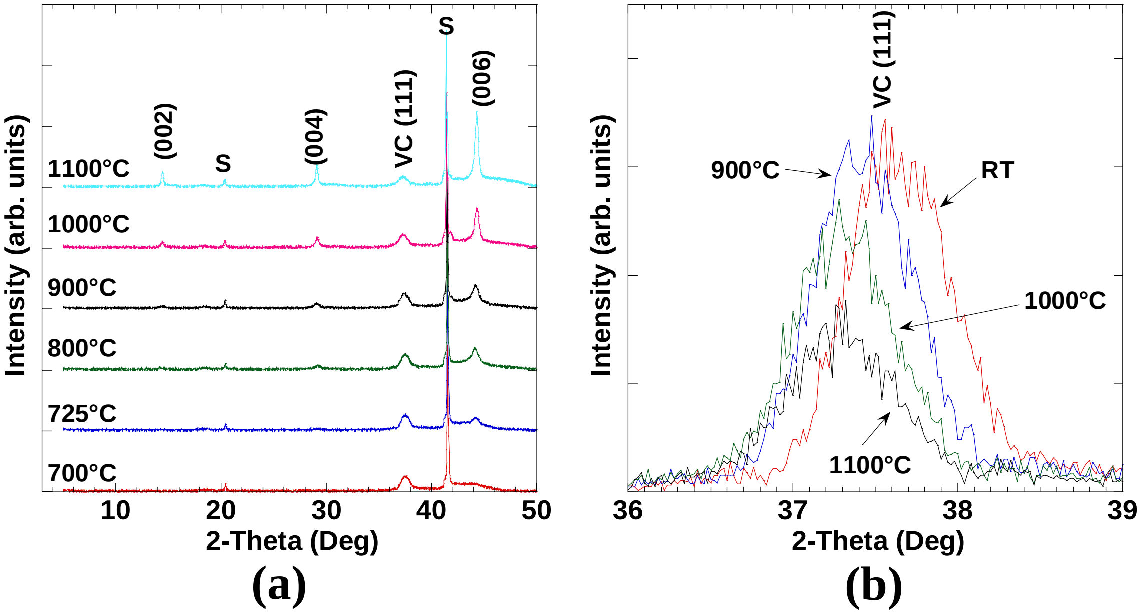

Figure 7.9 a) High-temperature X-ray diffraction patterns of a Cr-Ge-C thin film deposited on VC (111) at 250°C. Textured growth of Cr_2GeC in the (001) orientation is observed around 725°C and continues to the maximum temperature of 1100°C. Measurements were performed under vacuum (~10^{-4} Torr) to prevent oxidation. The substrate peak is denoted with an S. b) Overlay of high-temperature XRD patterns of the VC (111) seed-layer. The decrease in intensity indicates possible incorporation of VC into the Cr_2GeC film. The shift to the left is associated with thermal expansion.

and 250 °C. The sample was placed directly on the Pt heater element in the high-temperature furnace and pumped down to ~10^{-5} Torr. No crystalline phases were observed up to 700 °C for both the room temperature and 250 °C depositions (Fig. 7.9a). Emergence of the Cr_2GeC (006) peak was observed at 725 °C and continued to intensify as temperature was increased to a maximum of 1100°C. Two statements should be made here. First, the mechanism for crystallization here must be a type of bulk diffusion even though the path length is relatively short. Unlike *in situ* deposition where the sputtering process adds energy to the atoms and surface diffusion is the primary mechanism, this increase in synthesis temperature over *in situ* would be consistent with the observation that phase formation occurred in depositions carried out at 600 °C. Second, it can be assumed that the temperature of the sample, while placed directly on the Pt heater, was less than that measured by the thermocouple bonded to the heater, especially under vacuum. The difference in actual sample temperature and thermocouple reading is a function of temperature with deviation of up to 100 °C. [5, 65]

Closer examination of the VC (111) peak (Fig. 7.9b) showed a decrease in intensity above 1000 °C, possibly indicating a solid state reaction between the seedlayer and MAX phase film. The shift in the peak to the left was a result of thermal expansion of the unit cell. Results for deposits directly on sapphire and TiC were identical, and therefore not shown, for phase formation temperature indicating that the crystallization temperature was approximately 725 °C. Unlike with the VC seedlayer, no reduction in the intensity of the TiC seedlayer peak was observed up to 1100 °C. Interestingly, none of the secondary phases observed for *in situ* deposits appeared in the post-annealed films, this which seemed to indicate that Cr_2GeC was the more stable phase.

7.1.3. Cr_2GeC Conclusion

Cr_2GeC (001) thin films were successfully grown directly on sapphire at temperatures up to 925 °C. Secondary phases of Cr_3GeC and the new phase of hexagonal $Cr_5Ge_3C_x$ were observed. SEM and AFM images showed splinter-shaped and hexagonal surface crystals associated with the Cr_3GeC and $Cr_5Ge_3C_x$ secondary phases, respectively. Electronic transport showed metal-like behavior with RRR values the highest observed in MAX phase films at ~24 indicating a strong electron-phonon coupling. Resistivity values of most films were lower than that of bulk indicating possible anisotropy in the conductivity. Hall coefficient and magnetoresistance were analyzed using a two-band model yielding $n \approx 1.7 \times 10^{27}$ m^{-3}. A large difference in carrier concentration between the bulk and thin film was observed, indicating possible anisotropy in electronic transport. High temperature XRD revealed textured formation of Cr_2GeC around 700 °C with no secondary phases observed up to 1100 °C.

7.2. V_2GeC Thin Films

Willhelmsson *et al.* have published information on the synthesis and characterization of V_2GeC thin films.[66] Their work determined the minimum synthesis temperature for V_2GeC to be 450 °C. Room-temperature resistivity ranged from 21-40 μΩ-cm depending upon synthesis temperature. Mechanical testing by nanoindentation found hardness and Young's modulus values of 6.7 ±2.7 and 189 ±13.4, respectively. Additionally observed were VC and ordered V_8C_7 inclusions within the MAX films.

This following section pertains to thin films of V_2GeC. The results from this study along with Cr_2GeC and $(V_{1-x}Cr_x)_2GeC$ are to be combined and submitted for publications as "Thin films in the Cr-V-Ge-C systems synthesized by combinatorial method".

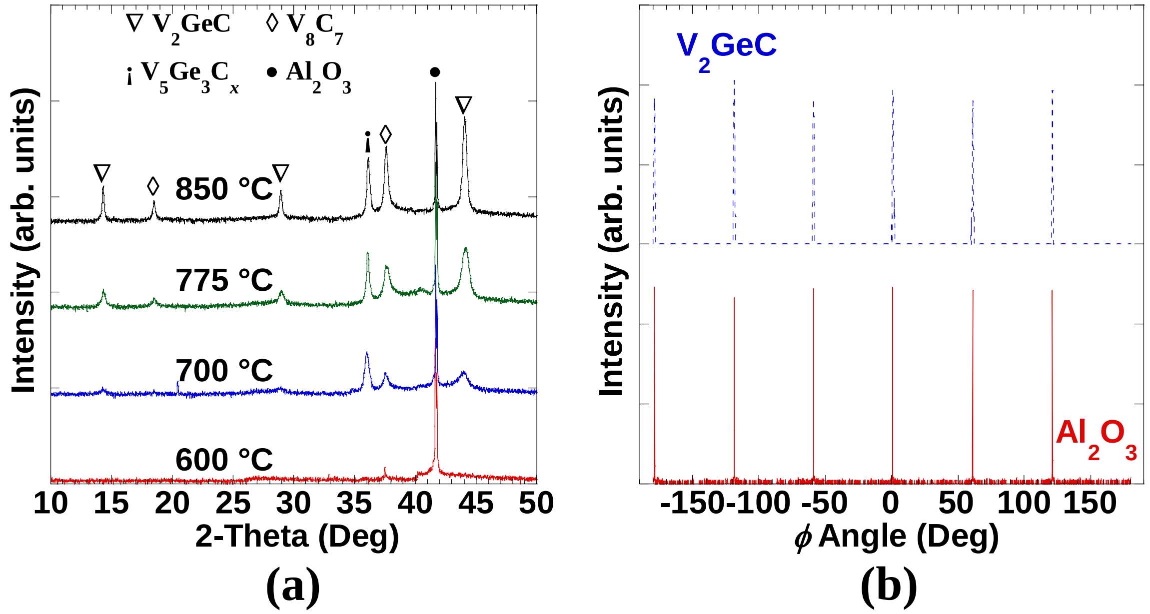

Figure 7.10 a) X-ray diffraction patterns for different synthesis temperatures of V_2GeC thin films grown on sapphire show textured growth in the (001) orientation. Phase crystallization occurs around 700°C. Secondary phases of $V_5Ge_3C_x$ and binary carbide V_8C_7 were observed in most films. b) 4-circle diffraction revealed 6-fold symmetry indicating epitaxial growth.

7.2.1. V_2GeC Synthesis

Epitaxial V_2GeC (001) thin films were successfully grown directly on sapphire at temperatures up to 900 °C (Figs. 7.10a and b). This result was interesting since the calculated lattice mismatch between V_2GeC on sapphire was ~5% tensile strain, generally not conducive for textured or epitaxial growth. Textured growth was observed down to 700 °C for V_2GeC. Table 7.2 lists the calculated c-lattice parameter for V_2GeC at various temperatures. Most deposits contained secondary phases of hexagonal $V_5Ge_3C_x$ (002), V_8C_7, and VC the latter two being cubic binaries also observed by Wilhelmsson in deposits of V_2GeC.[66] Lattice calculations for the c-axis oriented $V_5Ge_3C_x$ yield a value of 4.9676 (76) Å, similar to that of V_5Ge_3 (4.962 Å).[109] As mentioned previously, the existence of these other phases could be anticipated due to their similar chemistries and

Table 7.2 Properties of V_2GeC thin films grown directly on sapphire at various temperatures.

Temperature (°C)	*c*-axis (Å)	Resistivity, ρ_{RT} (μΩ-cm)	RRR	Roughness, R_a (nm)	Friction Coefficient
850	12.3071 (145)	41.6	2.4	49.1	0.057 (1)
775	12.3180 (114)	55.2	1.91	8.9	-
700	12.3784 (112)	55.4	1.93	22.2	-
650	-	67.5	-	20.6	-
Bulk[a]	12.25[a]	36[b]	22.5[b]	-	-

[a] Reference [6]

[b] Reference [113]

since the large lattice mismatch may require the formation of these impurity phases to relieve the strain. To test this hypothesis, deposits on VC (111) seedlayer were performed, yielding similar results with respect to the secondary phases present even though the lattice mismatch was ~1.9% for V_2GeC. Another explanation may be that the impurity phases formed due to slight chemistry variations, especially for carbon.

7.2.2. V_2GeC Results and Discussion

Only the binary phase diagrams have been established for V-Ge-C system. V-Ge system has four known compounds; V_3Ge, V_5Ge_3, $V_{11}Ge_8$, and $V_{17}Ge_{31}$.[114] Similar to the Cr system, V_3Ge and V_5Ge_3 will have M-A ratios close to those found in the MAX phase family. Cubic V_3Ge has a compressive lattice strain of 6.6% when growing (111) on sapphire. Tetragonal V_5Ge_3 is not anticipated to grow in a textured orientation with respect to sapphire due to structure mismatch, while the hexagonal V_5Ge_3C material may demonstrate c-axis growth.

In an effort to identify any unknown peaks and verify others, additional depositions of V-Ge and V-C were performed. Thin films with V:Ge 3:1 resulted in cubic (100) textured V_3Ge with a cubic lattice constant of 4.7751(5) Å. The films of V:Ge near

2:1 resulted in mixed phases of both hexagonal and tetragonal V_5Ge_3 (00l) and quasi-polycrystalline V_3Ge where the (100) was the preferred orientation. Lattice calculations of the hexagonal and tetragonal phases yield c-axis values of 4.9635(8) Å and 4.8625(17) Å, respectively. Deposits of V-C yielded cubic VC and V_8C_7 with cubic constants of 4.1509(10) Å and 8.3179(278) Å and hexagonal V_2C with a *c*-axis lattice constant of 4.5611(19) Å. All values were in good agreement with reported values. [103, 105, 108-110, 115-118]

Images collected using an SEM showed large plateau like features, some hexagonal in shape, protruding from the film surface. Figure 7.11 shows an SEM image of a V_2GeC film deposited at 875 °C. Chemical analysis using EDS revealed the

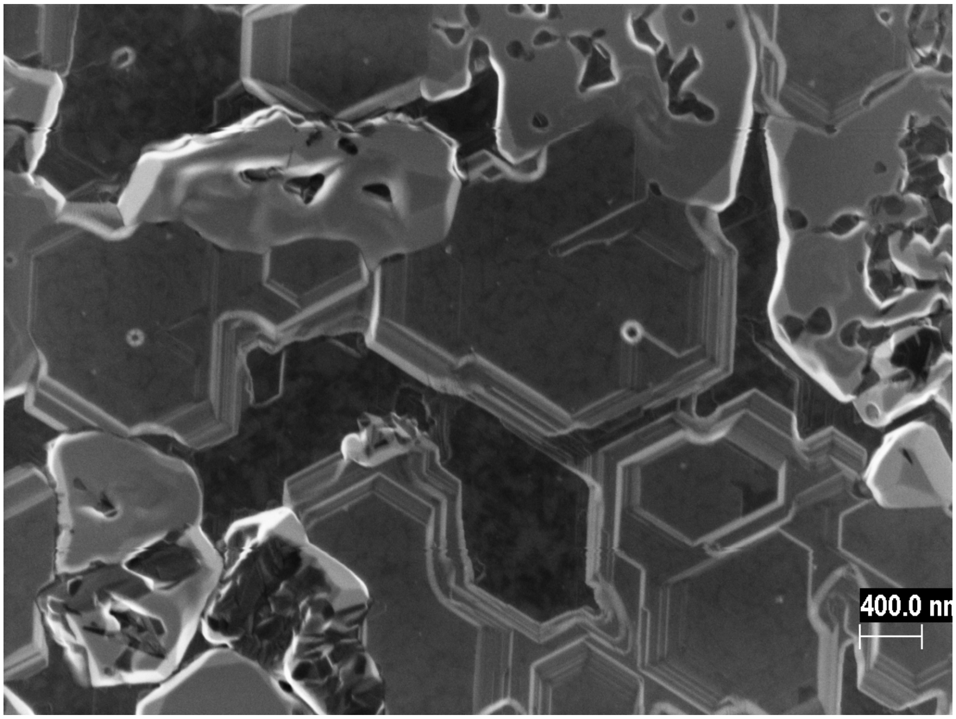

Figure 7.11 SEM image of a V_2GeC thin film deposited at 875 °C. Chemical analysis of the plateau shapes observed revealed a V:Ge composition of 68:32 at. % consistent for V_2GeC and the background film had a V composition range of 0.85-0.9.

hexagonal shapes to have a V:Ge at. % composition of 68:32, very close to the stoichiometry of V_2Ge. Combined with the hexagonal shape and XRD showing peaks consistent with the (001) orientation, these features were attributed with the V_2GeC phase. The background film, i.e. the material between the features, had a V:Ge ratio of 90:10, far from the MAX phase ratio. It is not clear what phase this may represent.

Atomic force microscopy found the films to be very rough. Table 7.2 lists roughness values for various deposition temperatures. Similar results were also reported in the Nb_2AlC system.[61] Low temperature deposits (<500 °C) yielded smooth films in both systems as expected, however, no crystalline phases were observed.

All films exhibited metal-like electrical conduction (Fig. 7.12). There was no

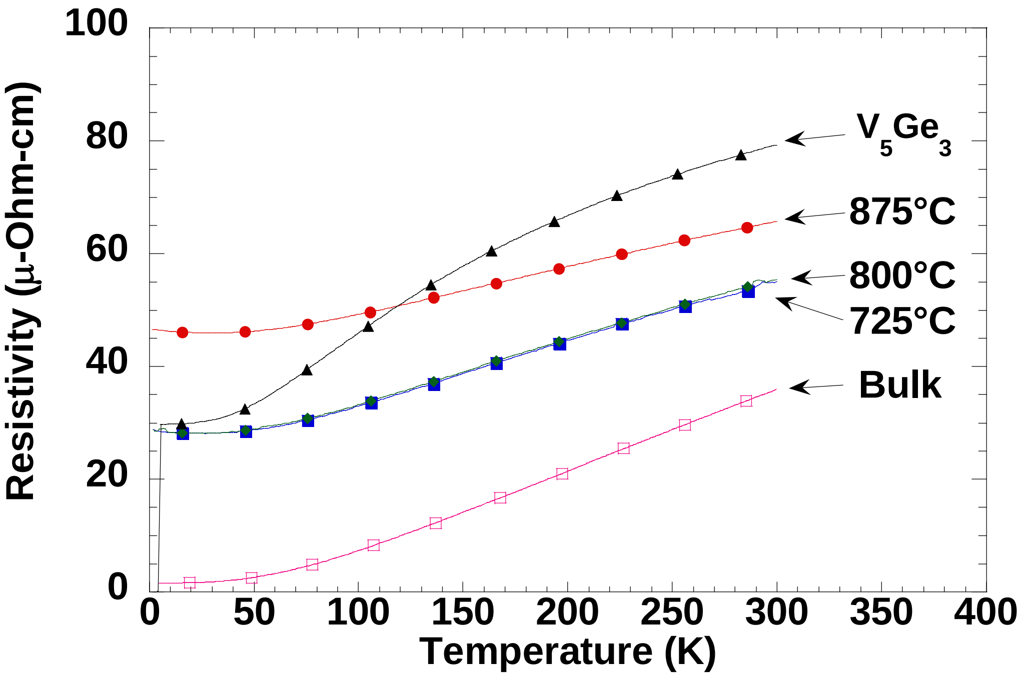

Figure 7.12 Resistivity as a function temperature for bulk V_2GeC and thin films deposited at various temperatures. All V_2GeC samples showed metal-like behavior down to 2 K. V_5Ge_3 revealed a superconducting transition of ~5 K.

obvious correlation between the resistivity of V_2GeC thin films and deposition temperatures except that films showed an increase in resistivity over that of bulk material. Clearly the films were not of high purity as compared to that of transport in the bulk material, where the RRR value of bulk was ~22.5.[119] V_5Ge_3 films exhibited a superconducting transition around 5 K.

Hall coefficients (R_H) as a function of temperature of thin films deposited on sapphire at 850 °C and 900 °C are shown in Figure 7.13a. Both films showed positive coefficients opposite to that of their respective binary carbide.[60] R_H values were similar for both films with only a very slight increase for films deposited at 850 °C.

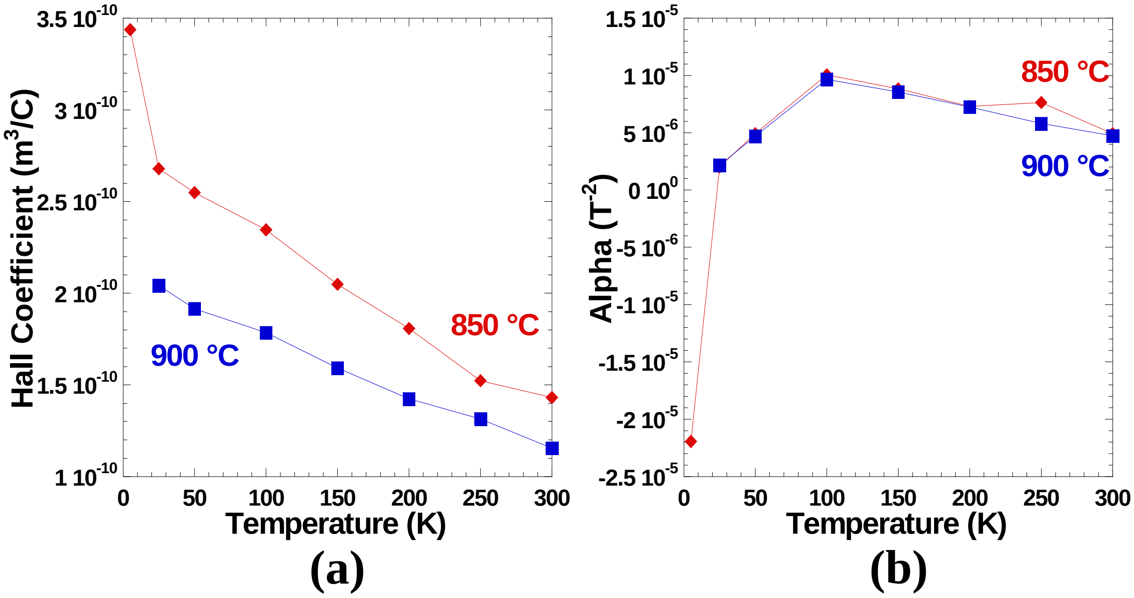

Figure 7.13 Magnetotransport results for V_2GeC thin films deposited on sapphire at 850 °C and 900 °C. a) Temperature dependence of Hall coefficient (R_H). R_H values were similar for both films with only a very slight increase for films deposited at 850 °C. b) Magnetoresistance (MR) as a function of temperature. MR values were identical for both films regardless of deposition temperature. Similar to what was observed in V_2AlC thin films, the MR was negative at 2 K indicating the presence of a magnetic impurity phase.

Magnetoresistance (α) of thin films (Fig. 7.13b) revealed modestly small positive values with little temperature dependence for T > 20 K, below which α decreases significantly. Similar to observations in V_2AlC thin films, at $T = 2$ K the magnetoresistance becomes negative indicating some magnetic phase is present. As discussed previously, negative magnetoresistance occurs in magnetic material and is controlled by spin-orbit scattering. By aligning magnetic spins, scattering is reduced effectively increasing the conductivity. As was concluded for V_2AlC thin films, it does not seem reasonable to associate magnetic behavior with the MAX phase. Currently, it is believed the magnetic behavior observed can be associated with an impurity, most likely a vanadium oxide, which have exhibited similar properties.[120] For temperatures above 20 K the two-band model can be used to analyze experimental results as described in Section 4.3.4. Unlike what has been reported in previous studies of MAX phases where $n \approx 1\text{-}3 \times 10^{27}$ m^{-3},[5, 27, 30, 31] the carrier concentration of V_2GeC thin films was $n \approx p \approx 2.7 \times 10^{26}$ m^{-3}.

Raman spectra for various deposition temperatures of V_2GeC thin films along with VC-V_8C_7, V_5Ge_3, and bulk V_2GeC are shown in Figure 7.14. Dashed and solid lines represent Raman modes theoretically calculated and observed in bulk by Leaffer *et al.*[68] Three of the four V_2GeC vibrational modes were observed, all related to the longitudinal in-plane modes between the M and A elements. The first peak appeared at approximately 140 cm^{-1}, the second at 226 cm^{-1}, and the third at 257 cm^{-1}. The position shifts from those observed in bulk material and low intensities were a result of in-plane lattice strain. Similar to what was observed in Cr_2AlC thin films, Raman modes were observed in the 600 °C V_2GeC deposition even though XRD showed no peaks indicating the film was nanocrystalline. Interestingly, the most intense peak observed in V_2GeC thin

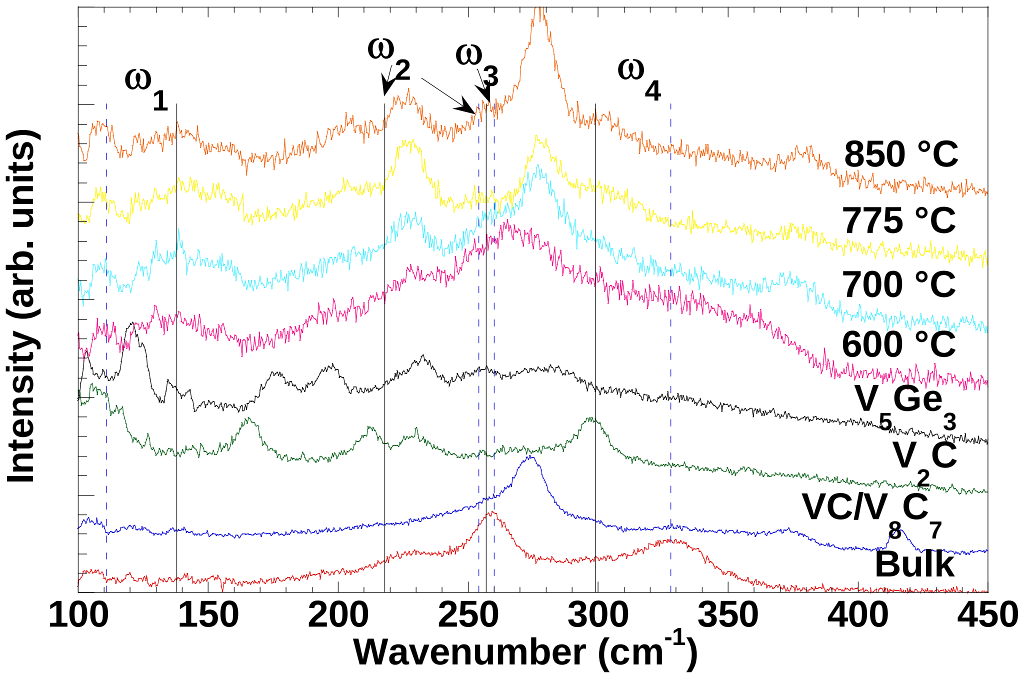

Figure 7.14 Raman spectra for thin films of V_2GeC deposited at various temperatures, VC/V_8C_7, V_5Ge_3, and bulk V_2GeC measured in this study. Dashed and solid lines represent Raman modes theoretically calculated and observed in bulk by Leaffer *et al*. Three V_2GeC modes were observed in films; all were longitudinal in-plane modes around 140 cm^{-1}, 225cm^{-1}, and 257cm^{-1}. VC/V_8C_7 modes also appear in the V_2GeC films.

films was not from the MAX phase, but instead from VC/V_8C_7. This suggests the phase grows on top of V_2GeC or was the primary phases in the films. The latter is less realistic since XRD results show strong diffraction from V_2GeC and only small diffraction from the binary phase indicating the film is predominately MAX phase.

At this point it is important to comment on the results found by Leaffer. First is the large difference between the theoretically predicted mode positions and those observed in the bulk for modes ω_1, ω_2, and ω_4. Why there are discrepancies is not the focus of the present work, however, it is important to note *ab-initio* calculations have proved useful in predicting mode positions,[67, 68] therefore consideration must be made when compared to experimental results. A good example is similar to what was reported in bulk Cr_2GeC, the V_2GeC ω_4 mode was also incorrectly identified at 299 cm^{-1}. The peak can be associated with Ge since a strong line is found at 300 cm^{-1} and it is fairly common for Ge to segregate from these materials.[65, 91] Clearly the bulk sample measured in this work revealed a peak around 330 cm^{-1}, in excellent agreement with *ab-initio* calculations. In addition, a peak around 108 cm^{-1} was observed in thin films, in good agreement with calculated value of 110 cm^{-1}. Whether this peak is related to the MAX phase remains to be proven since reported bulk and the measured thin films show a peak around 140 cm^{-1}. It should be noted such low Raman shifts are typically difficult to measure due to filtering out of the laser light, which can produce artificial peaks from interference fringes.

7.2.3. V_2GeC Conclusion

V_2GeC (001) thin films were successfully grown directly on sapphire at temperatures up to 925 °C. Secondary phases of V_8C_7 and hexagonal $V_5Ge_3C_x$ were observed. SEM and AFM images showed large plateau-like surface crystals associated with V_2GeC. Electronic transport showed metal-like behavior with values higher than bulk indicating significant scattering due to secondary phases. Hall coefficient and positive magnetoresistance were analyzed within a two-band model yielding $n \approx 2.7 \times 10^{26}$ m^{-3}. Magnetoresistance becomes negative at temperature at 2 K indicating the presence of a magnetic impurity phase. Raman spectroscopy indicated the presence of nanocrystalline V_2GeC for deposits at 600 °C.

7.3. $(V_{1-x}Cr_x)_2GeC$ Thin Films

The following section pertains to solid solutions of $(V_{1-x}Cr_x)_2GeC$. The results of from this study, along with V_2GeC and Cr_2GeC, are to be combined and submitted for publications as "Thin films in the Cr-V-Ge-C systems synthesized by combinatorial method".

7.3.1. $(V_{1-x}Cr_x)_2GeC$ Synthesis

After synthesizing Cr_2GeC and V_2GeC the Cr and V targets were offset in order to create a compositional gradient. EDS and WDXRF measurements showed that $(V_{1-x}Cr_x)_2GeC$ was successfully deposited at 850 ºC for x ranging from 0.05-0.94 with V-Cr compositional gradients ranging from 5-20 at. % across the substrate during any given deposition while the M-A ratio was maintained between 1.9-2.4. XRD results (Fig. 7.15a)

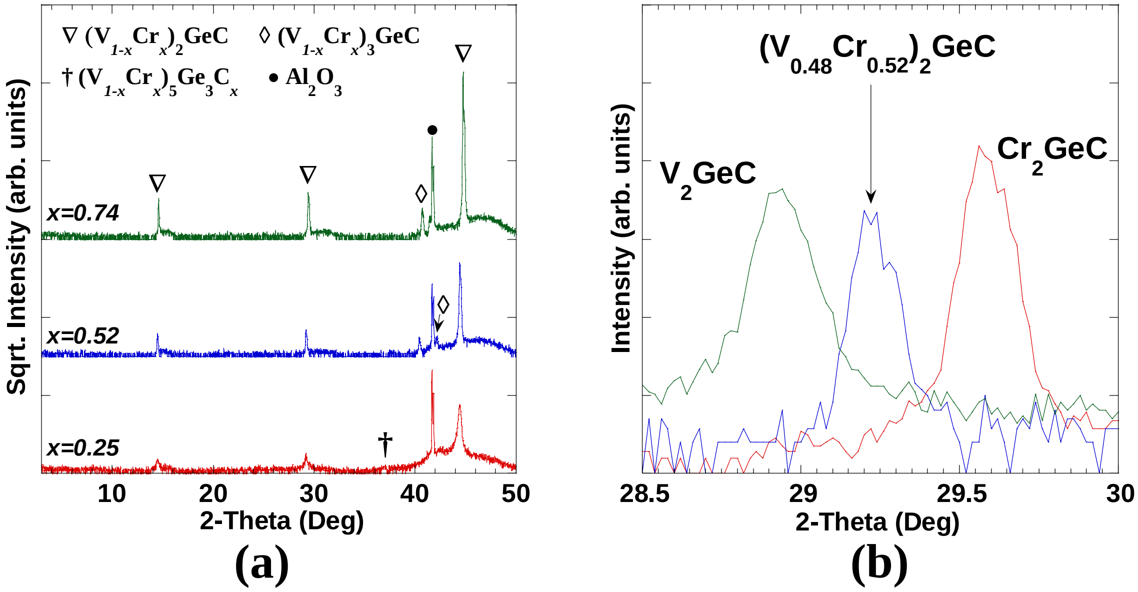

Figure 7.15 X-ray diffraction patterns of a) $(V_{1-x}Cr_x)_2GeC$ thin films deposited on sapphire at 850 °C. Minor phases of $(V_{1-x}Cr_x)_5Ge_3C_x$ and $(V_{1-x}Cr_x)_3GeC_x$ were observed in most films. b) Overlay of the (004) peak from X-ray diffraction patterns of V_2GeC, $(V_{0.48}Cr_{0.52})_2GeC$, and Cr_2GeC showing complete solid solution mixing.

showed predominately (00l) MAX phase peaks along with occasional minor secondary phases of hexagonal $(V_{1-x}Cr_x)_5Ge_3C_x$ (002) and cubic $(V_{1-x}Cr_x)_3GeC$ growing quasipolycrystalline. Figure 7.15b shows the (004) peak shift for $(V_{0.48}Cr_{0.52})_2GeC$ compared to both end members clearly demonstrating that alloying had occurred. 4-circle XRD of $(V_{0.53}Cr_{0.47})_2GeC$ is shown in Figure 7.16 revealed six-fold symmetry and confirmed that the films were epitaxial to the sapphire substrate. As was the case for Cr_2GeC and V_2GeC, the in-plane relationship was found to be $[110]_{Al_2O_3} \parallel [100]_{(V,Cr)_2GeC}$. Carbon content across the samples ranged from 18-25 at. % (Fig. 7.17), with films and were generally deficient in carbon, Samples for characterization were chosen based upon phase identification by XRD.

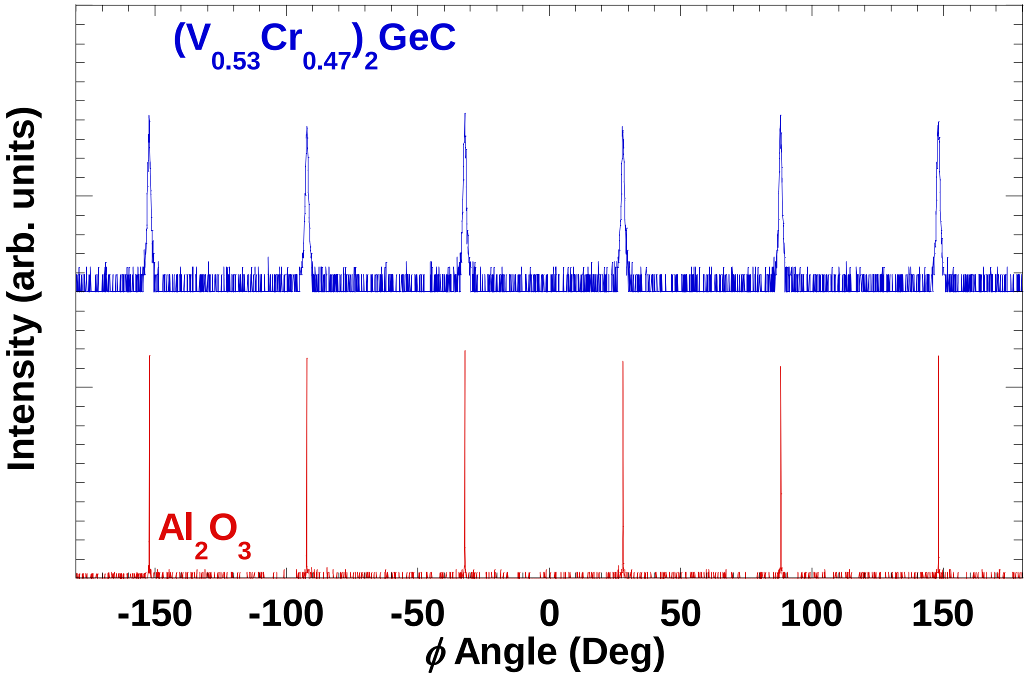

Figure 7.16 Phi scans showing epitaxial relationship between Al_2O_3 and $(V_{0.53}Cr_{0.47})_2AlC$.

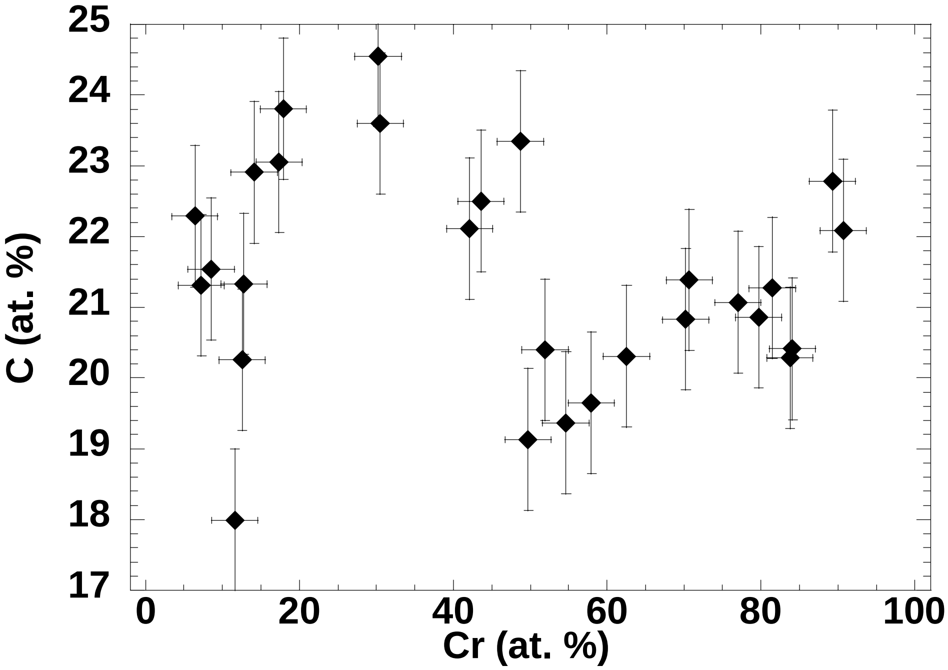

Figure 7.17 Carbon concentration across the range of film samples. The films were generally found to be C-deficient.

7.3.2. $(V_{1-x}Cr_x)_2GeC$ Results and Discussion

Figure 7.18 shows the measured *c*-axis lattice constant as a function of *x*. The solid and dashed lines represent a linear relationship between the thin film results and bulk values, respectively. The observed linear relation generally agrees with Vegard's law for solid solutions. One would expect a slight decrease in lattice constant relative to the bulk value as a result of the tensile stress of the substrate based on the surface reconstruction of sapphire.[74] This, however, was not observed as most films exhibited a lattice constant larger than the bulk value,[121, 122] yet still within the error of end-member film values. Not surprisingly, films with carbon concentrations near

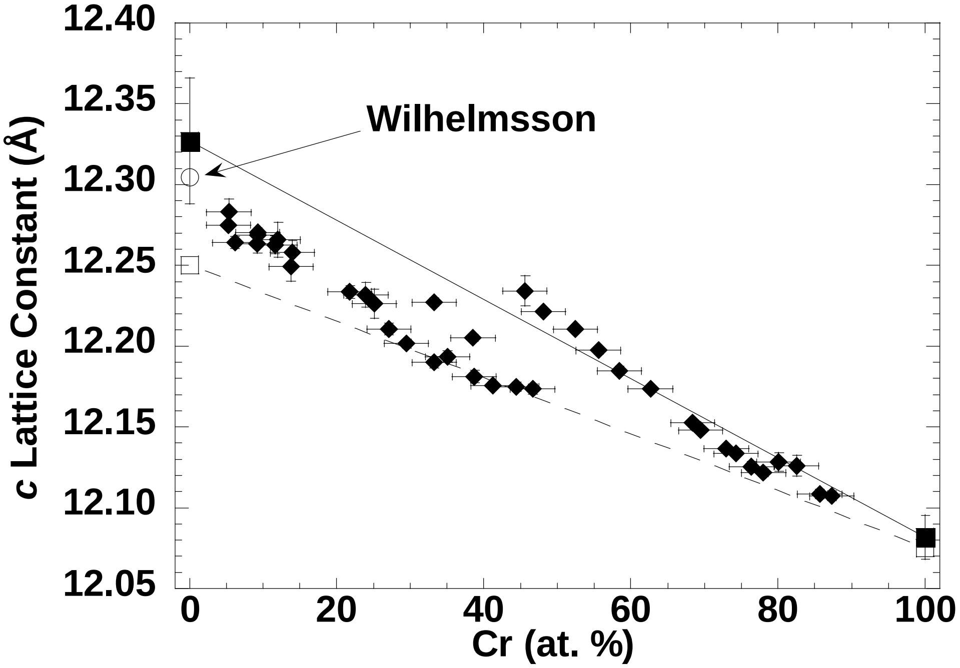

Figure 7.18 Calculated *c*-lattice constant as a function of Cr concentration shows linear behavior for the solid solutions of $(V1\text{-}xCrx)_2GeC$. The shift in lattice constant around *x=0.5* was believed to be associated with the large deficiency in carbon as shown in Fig. 7.17. The solid and dashed lines represent a linear relationship between thin film results and bulk values, respectively. Bulk Ref. [121, 122] and film from Wilhelmsson [66].

stoichiometry exhibited a lattice constant closer to that of bulk, especially for *x=0.15-0.40*. The jump in lattice constant at around 50 at. % Cr was most likely due to the carbon deficiency in the films, also observed in the Cr-Al-C systems.[91] These results indicated that there was a range of stoichiometry in carbon.

AFM measurements found that the films had surface roughness values ranging from 6-45 nm. The relative roughness (Fig. 7.19a) appeared to exhibit a decrease for almost all solutions, considerably for *x=0.2* where it was ~1%. This can be related to the near stoichiometry of those samples (Fig. 7.17). Above *x=0.4* the relative roughness increased for higher Cr containing samples, in agreement with results of Cr_2GeC films.

Results of friction measurements are shown in Fig. 7.19b. The friction coefficients for solid solutions were all low (< 0.06) with an average value of ~ 0.045. In

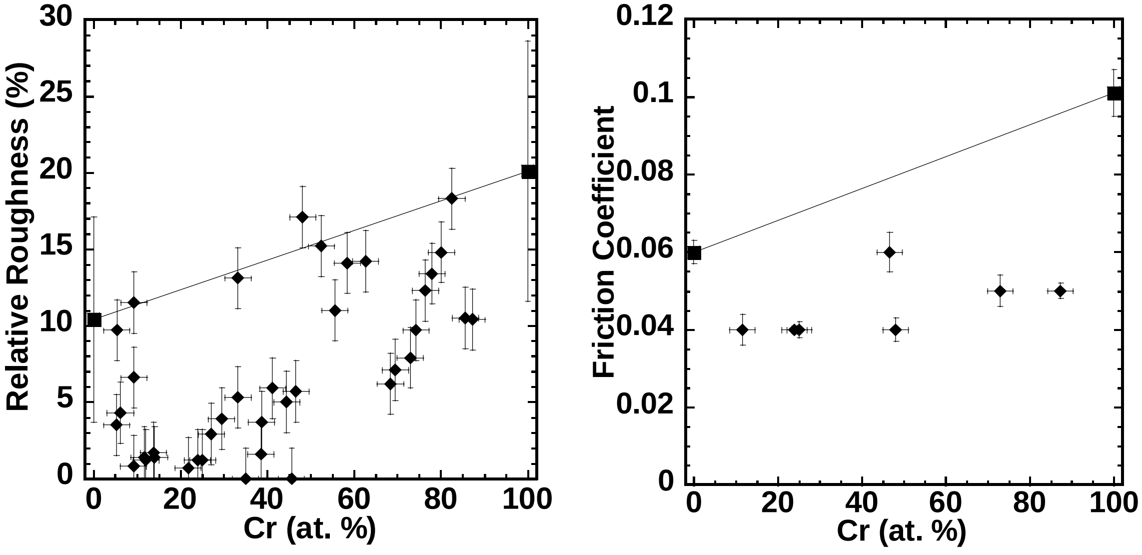

Figure 7.19 a) Relative surface roughness (R_a/thickness) as a function of Cr concentration. Films with carbon near stoichiometry show the lowest roughness around *x~0.2.* b) Surface friction as a function of Cr concentration as found by lateral force testing. Overall friction does not appear to be affected by solid solutioning or carbon composition with the exception the solutions being less than the end-members.

all cases, the coefficient was independent of load. The coefficient of friction was slightly higher for the rougher samples, which contained higher amounts of Cr. Interestingly, the coefficient of friction values for all solid solutions were less than both end-members. These values were also the lowest for all three solid solution systems studied. Similar to the previously described solid solution systems values were larger than those reported for the basal plane of bulk Ti_3SiC_2 [53] but were lower than the value of 0.1 found by Emmelich in films of Ti_3SiC_2.[76]

Electronic transport measurements showed that the films had metal-like conduction (Fig. 7.20a). Not surprising, the higher Cr-containing film showed a slightly larger RRR than the commensurate V-containing film. The room-temperature resistivity as a function of Cr concentration is shown in Fig. 7.20b. As expected, solid solution

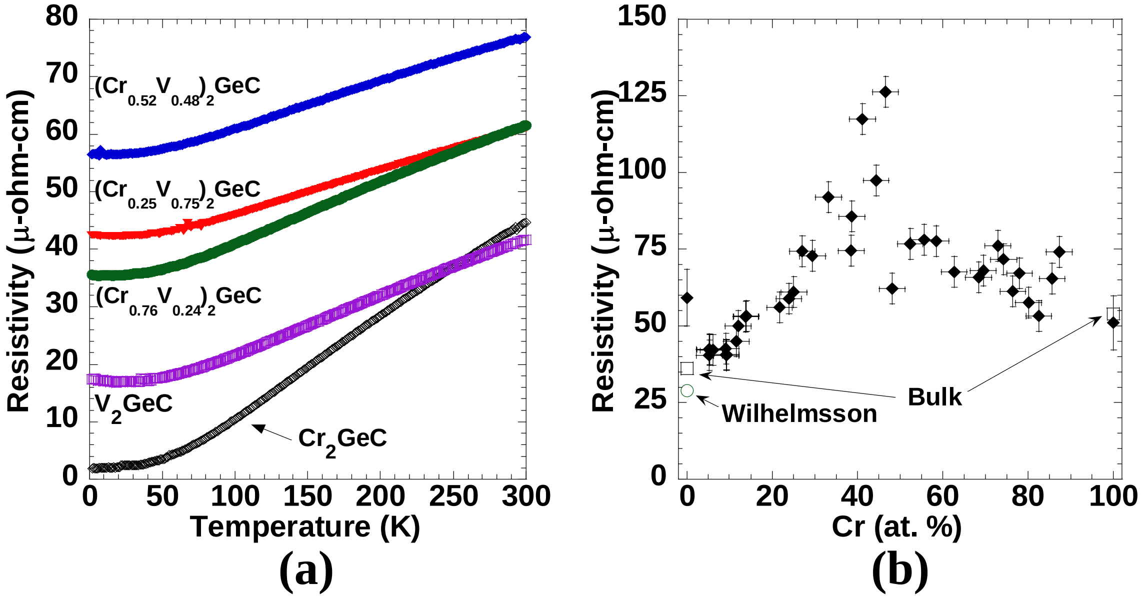

Figure 7.20 (a) Resistivity as a function of temperature for $(V_{0.75}Cr_{0.25})_2GeC$, $(V_{0.48}Cr_{0.52})_2GeC$, and $(V_{0.24}Cr_{0.76})_2GeC$ thin films. All films showed metal-like behavior. (b) Room-temperature resistivity as a function of Cr concentration. The observed peak around *x=0.5* is typical of solid solution scattering.

scattering played an important role in the electronic transport. Interestingly, the room-temperature resistivity value for V_2GeC films was higher than that for films with low concentrations of Cr (< 30 at. %). Wilhelmsson *et al.* found the resistivity of V_2GeC thin films to be sensitive to impurity concentration where phase-pure films deposited at 700 °C resulted in a room temperature resistivity of 21 μΩ-cm, films deposited at 850 °C where VC_x inclusions were observed resulted in resistivity of 29 μΩ-cm.[66] This again was believed to be associated to the number of impurities in the V-Ge-C system that becomes suppressed upon the addition of Cr.

Hall coefficient as a function of temperature for various Cr concentrations is shown in Figure 7.21a. All films showed a mostly positive coefficient with little

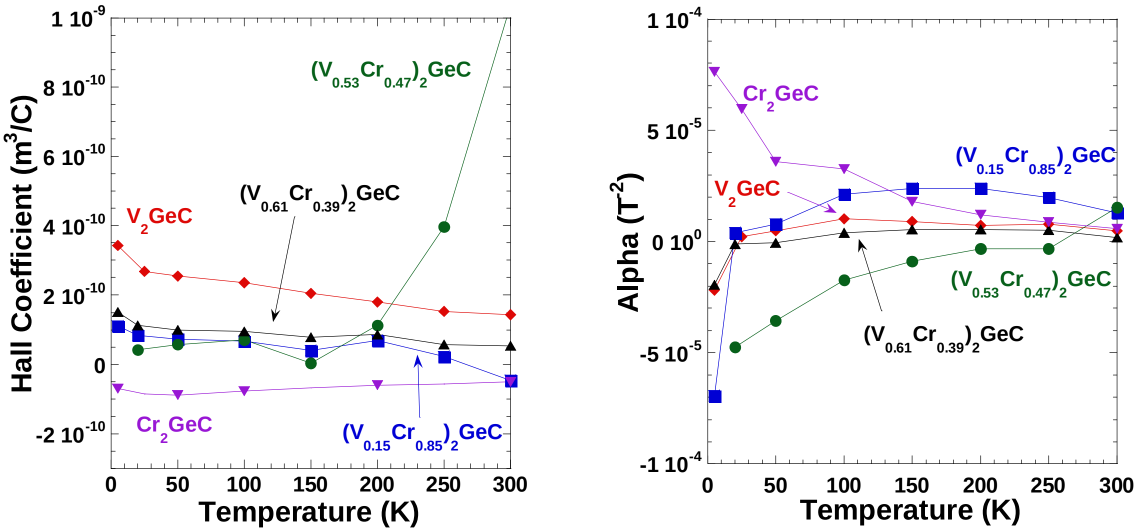

(a) **(b)**

Figure 7.21 Magnetotransport results for $(V_{1-x}Cr_x)_2GeC$ films deposited on sapphire at 850 °C. a) Temperature dependence of Hall coefficient (R_H). All solid solution films values were small and positive similar to values observed in bulk V_2GeC. b) Magnetoresistance (α) as a function of temperature. Solid solution values were all similar and small with little temperature dependence indicating solid solution scattering dominates transport. Similar to what was observed in V_2GeC films, the magnetoresistance of the solid solution was negative at 2 K indicating the presence of a magnetic impurity phase.

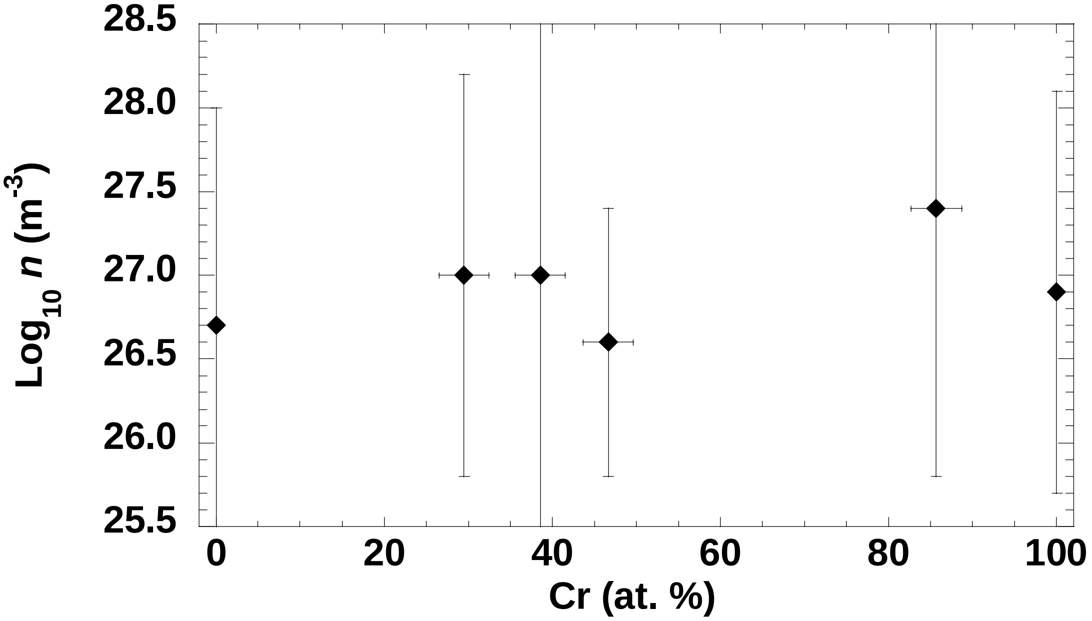

Figure 7.22 Carrier concentration as a function of temperature for $(V_{1-x}Cr_x)_2GeC$ thin films (closed markers) and bulk (open markers). End-member films were in good agreement with bulk values, while up to an order of magnitude decrease was observed for solid solutions. Error bars represent the allowed values of n based upon calculations for $n \approx p$ from the two-band model described in Section 4.3.4.

temperature dependence except for $(V_{0.53}Cr_{0.47})_2GeC$ which exhibited a larger value for T > 200 K. Magnetoresistance (Fig. 7.21b) revealed values which all turned negative as temperature decreased; the most sensitive was $(V_{0.53}Cr_{0.47})_2GeC$ which was negative at 250 K, this however, was believed to be an erroneous data set. The two-band model was applied to results with positive magnetoresistances resulting in carrier concentrations for $n \approx p \approx 4\text{-}25 \times 10^{26}$ m^{-3}, shown in Figure 7.22. This finding was interesting, indicating that M-group substitution did appear to affect carrier concentration somewhat. Additional work with more thorough analysis is required to understand the negative magnetoresistance behavior. Additionally, the mobility of the charge carriers can be found through two-band analysis. Figure 7.23 plots the temperature dependence of

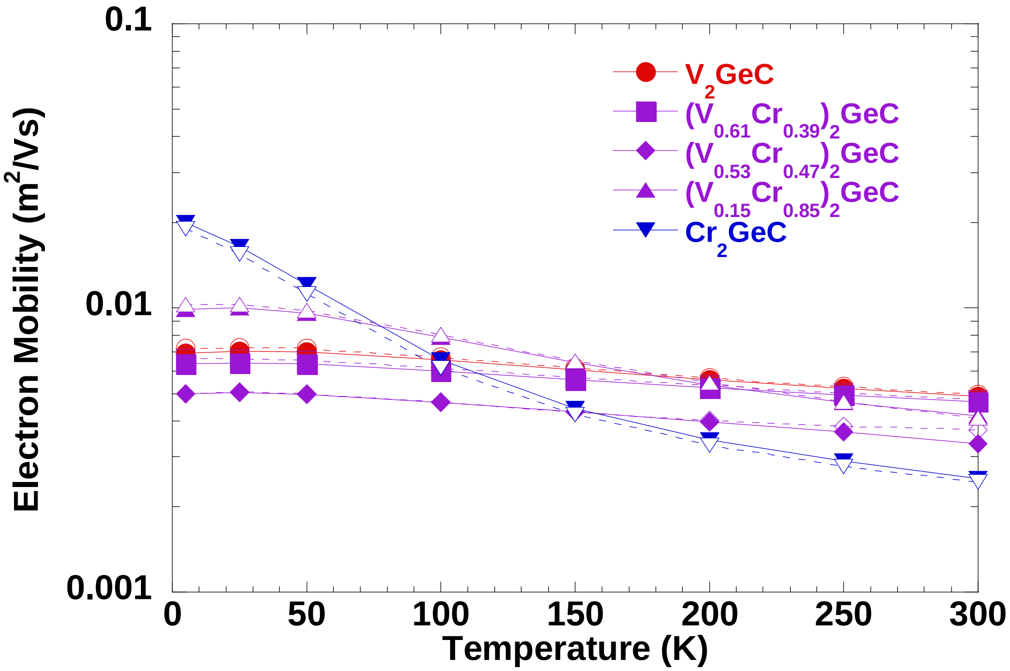

Figure 7.23 Semilogarithmic plot of the temperature dependence of electron (solid markers) and holes (open markers) for V_2GeC, Cr_2GeC, and $(V_{1-x}Cr_x)_2GeC$ thin films. Interestingly, the solid solutions revealed slightly higher mobilities above 150 K than Cr_2GeC films with little temperature dependence, suggesting phonon scattering is dominant in the material.

electron and hole mobilities. As was observed in resistivity measurements, the mobilities are subject to temperature dependent scattering. Interestingly, the solid solutions revealed slightly higher mobilities above 150 K than Cr_2GeC films with little temperature dependence, suggesting phonon scattering is dominant in the material.

Selected Raman spectra are shown in Fig. 7.24. Of the first-order modes in the M_2AX family, three were consistently observed. The lower three modes were attributed to a longitudinal modes in the basal plane and the upper mode to a longitudinal mode along the *c*-axis. The decrease in intensity of the modes was likely directly attributable to increased Raman linewidth, indicative of mixing at the M site. Unlike previous findings in the $(Nb_{1-x}Ti_x)_2AlC$ system[54] and similar to the $(V_{1-x}Cr_x)_2AlC$ system, only minimal

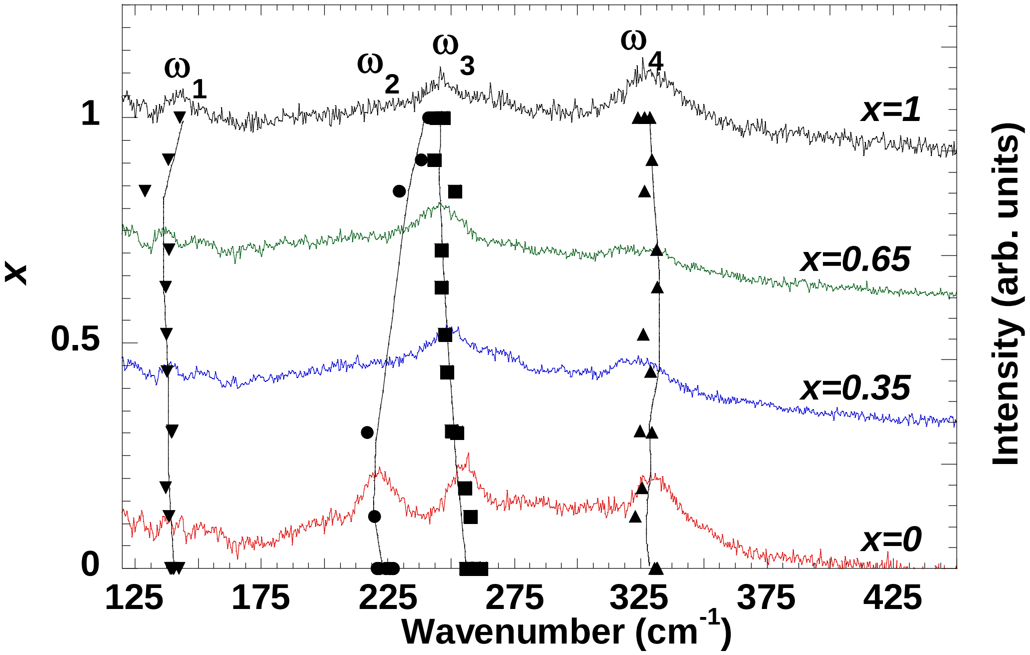

Figure 7.24 Raman spectra for various thin films of $(V_{1-x}Cr_x)_2GeC$. Three of the four modes were consistently observed. Markers indicate the positions of vibrational modes as a function of Cr concentration with the lines serving as a guide for the eye. No solid solution hardening was observed.

changes were observed, indicating no change in modulus. This was not in agreement with high pressure diamond anvil cell measurements of $(Cr_{0.5}V_{0.5})_2GeC$ where the calculated the bulk modulus was found to be 219 ± 5 GPa with $K' = 4.1 \pm 0.3$, which is higher than the end members V_2GeC and Cr_2GeC.[123] This lack of agreement may be due to the induced lattice strain in the films eliminating enhanced bonding and hence increased bulk modulus.

7.3.3. $(V_{1-x}Cr_x)_2GeC$ Conclusion

Thin films of $(V_{1-x}Cr_x)_2GeC$ were successfully synthesized on *c*-axis sapphire (Al_2O_3) substrates at 850 ºC by magnetron sputtering. Complete mixing was achieved for all solid solutions with no miscibility gap observed. X-ray diffraction showed the films to be *c*-axis oriented and epitaxial over the full range of compositions. High-temperature X-ray diffraction of amorphous films revealed crystallization around 675 ºC. Most alloyed films contained minor secondary phases of $(V_{1-x}Cr_x)_5Ge_3C_x$ and $(V_{1-x}Cr_x)_3GeC$, depending on the V/Cr ratio and carbon concentration. Electrical transport measurements showed typical metal-like conduction with a maximum around $x=0.5$ due to solid-solution scattering. Hall coefficients and positive magnetoresistances were analyzed within a two-band model resulting in carrier concentrations for $n \approx p \approx 4\text{-}25 \times 10^{26}$ m^{-3} All films showed a negative magnetoresistance at lower temperatures, more so for higher V-containing samples, indicating the presence of a magnetic phase. Atomic force microscopy showed most of the films to be rough attributed to the secondary phases present in the films. Lateral force coefficient of friction measurements revealed an average coefficient of friction for the solid solutions to be ~0.045, lower than both end-members. Raman results were in agreement with previous measurements for bulk materials with no indication of solid solution hardening or softening.

Chapter 8: Summary, Concluding Remarks, and Proposed Future Research Work

8.1. Summary

In this work, six individual MAX phases and three solid solution mixtures were synthesized as thin films by magnetron sputtering and combinatorial method. All films grew *c*-axis oriented and epitaxial regardless of lattice mismatch, with Cr_2AlC the only phase showing twinning. Of the individual phases two, Nb_2AlC and Cr_2GeC, were synthesized for the first time. The lowest synthesis temperature found for textured growth was ~550-575 °C for Cr_2AlC and V_2AlC, while the minimum for Nb_2AlC was 775 °C. Electrical transport measurements showed that all films behaved metal-like down to 2 K with superconductivity observed in Nb_2AlC around 440 mK. Films of Cr_2GeC showed the highest RRR values, up to 24, indicating high film quality and good electron-phonon coupling. Cr_2AlC and Cr_2GeC thin films had lower resistivities than their bulk counterparts suggesting some anisotropy in electrical conductivity. Hall coefficient and positive magnetoresistance were analyzed within a two-band model resulting in a carrier concentration of $n \approx p \approx 1.3\text{-}3.5 \times 10^{27}$ m^{-3} for all samples except V_2GeC, which was 2.7×10^{26} m^{-3}. A large difference in carrier concentration (~10^3) was observed between thin film and bulk Cr_2GeC. Negative magnetoresistances were observed in V_2AlC and V_2GeC at $T < 20$ K indicating the presence of a magnetic impurity phase. Most films were rough ($R_a > 5$ nm) with features protruding from the films surface, some hexagonal and faceted in shape, associated with the various secondary phases observed in the films. New phases of $Nb_5Al_3C_x$, V_3AlC_2, and V_4AlC_3, the latter two on TiC seedlayers only, were also observed.

Combinatorial synthesis resulted in complete solubility of the M-group elements in $(Ti_{1-x}Nb_x)_2AlC$, $(V_{1-x}Cr_x)_2AlC$, and $(V_{1-x}Cr_x)_2GeC$ on *c*-axis sapphire (Al_2O_3) substrates at 850 ºC. X-ray diffraction showed the films were *c*-axis oriented and epitaxial over the full range of compositions. Electrical transport showed all films behaved metal-like down to 2 K with maximums in resistivity around $x = 0.5$, typical for solid solution scattering. Hall coefficient and positive magnetoresistance were analyzed within a two-band model resulting in a carrier concentration of $n \approx p \approx 1\text{-}25 \times 10^{26}$ m^{-3} for all samples. Negative magnetoresistance was observed in $(V_{1-x}Cr_x)_2GeC$ solid solutions at low temperatures indicating the presence of a magnetic impurity phase. Atomic force microscopy showed most of the films to be relatively rough as result of the secondary phases present. Lateral force friction on $(V_{1-x}Cr_x)_2GeC$ films indicated an average coefficient of friction for the solid solutions to be ~0.045, lower than both end-members. Raman spectroscopy indicated the possibility of significant solid solution hardening along the *c*-axis around $(Ti_{0.25}Nb_{0.75})_2AlC$. New phases of $(V_{1-x}Cr_x)_5Ge_3C_x$, $(V_{1-x}Cr_x)_3GeC$, $(V_{1-x}Cr_x)_4AlC_3$, $(Ti_{1-x}Nb_x)_3AlC_2$, and $(Ti_{1-x}Nb_x)_4AlC_3$ were also observed suggesting the possibility of new end-member MAX phases.

8.2. Concluding Remarks

The MAX phases exhibit interesting and unique properties making them candidates in many applications. [9, 24, 29-33, 124, 125] At the time, limited work had been done in thin films on the vast number of MAX phases presently known in bulk; most thin film work being on Ti-A-C (A = Al, Ge, Si) systems.[55, 57-59, 65, 126, 127] Barsoum *et al.* wrote a proposal to NSF with the purpose of synthesizing MAX phase thin films using combinatorial method. The proposal was awarded (DMR-0503711) in which this work was made possible.

From the beginning it was a challenge to duplicate the synthesis conditions required for MAX phase film growth with the initial chamber configuration. [55, 57-59, 65, 126, 127] Only after a significant amount of redesigning, mostly in regards to substrate heating, as well as effort was this work even possible. With the heater design resolved, sample synthesis became very productive. This, though, led to the next and possibly biggest problem during the entire research, that being carbon quantification.

During the first three and a half years there was no means (in-house) to accurately determine carbon composition. In an effort to work around this and still perform productive research a rough approximation technique was employed. Since some of the MC (M = V, Nb, Ta) compounds have both MC and M_2C structures this can be used this to approximate the C content. By varying the carbon power, a series of experiments were performed in which XRD results would be used to determine the correct power setting for the desired phase. This technique was quite successful for an approximation. Numerous MAX phases and binary carbides were synthesized. However, as with any approximation and the fact the MC binaries have large compositional ranges, it was not ideal and in the end resulted in most films being carbon deficient. It was not until the last six months of this work, well after all samples were synthesized, that access to a WDXRF instrument made accurate carbon composition analysis a reality. The WDXRF will certainly reduce the amount of future work required to synthesize high quality films.

The last to discuss pertains to measurement considerations. Thin films can represent a challenge to characterize. Take for example Al-containing materials grown on Al_2O_3, obviously there exists a concern that when measuring the Al composition, is only the film being measured? Or is there signal from the substrate skewing the results. To resolve this problem, without the use of a surface analysis technique (which is not readily available), was to include additional substrates that did not contain Al, i.e. MgO and/or Si. The latter however, can induce some secondary excitation of Al since Si K_α is a higher energy than Al K_α, therefore MgO is preferred. Second, are overlaps in chemical analysis; the most prevalent was V-Cr. In this case the $V_{\alpha\text{-}2}$ overlapped with the $Cr_{\alpha\text{-}1}$ such that for high concentrations of V (> 90 at. %) the Cr signal was effectively lost in the V signal. There was no unique solution to this until the WDXRF was available, which, with its higher resolution, could resolve the two peaks. Thus, the limited results shown for high V-concentrations.

The other measurement consideration is that of mechanical properties. Film thickness is crucial for mechanical testing via nanoindentation. A common rule of thumb is to indent up to 10% of the film thickness, which leads to a minimum of 500 nm for reasonable results. Since most depositions were performed at a rate of ~200 nm/hr, the minimum deposition time would be 2-3 hours to produce measurable samples. Not that this is a long time by deposition standards, but when combined with the lack of C composition, forced this work to focus on phase formation, therefore shorter deposition times led to more samples. This was especially true for combinatorial samples, which had deposition rates as low as 100 nm/hr. Additionally, most samples were found to be very rough, making indentation difficult. While very little along the lines of mechanical testing was performed in this work, it is important that future efforts be made to characterize the samples. Following the suggestions in the proposed work below will certainly allow for this type of characterization to be performed.

Even with these issues, research was performed and was successful. New and previously known MAX phases along with other new phases were synthesized and characterized. It should also be stressed this was "foundational work" on MAX phase thin films for both Drexel and Rowan Universities. A lot was learned with regards to the synthesis requirements and the issues of measurements of thin films. Taken all together this resulted in a huge steps towards new and continued work in MAX phase thin films.

8.3. Proposed Future Research Work

While much was accomplished in this work, a lot more remains to be done. The shear number of solid solution possibilities requires the use of combinatorial method to investigate the full breadth of materials and properties in the MAX phase family. This work showed combinatorial method to be successful with only a short time of implementation. The following sections are some proposed ideas to improve and expand upon the work in combinatorial thin film synthesis.

8.3.1. Improving Current Combinatorial Synthesis Method

The combinatorial synthesis method applied in this work proved to be mostly successful. The reason the method was considered "mostly successful" was because not every experiment resulted in a complete use of the samples generated. The main issue was the gradient produced across the sample when attempting high-concentration ratios of one of the M-group elements, viz. $M_{1-x}M_x$ ($x > 0.75$). This gradient resulted in M-A and M-X ratios that were too far from stoichiometric values, the end result being samples that were unusable for characterization. A proposed solution to this would be to change the 2-inch targets which hold the A-group element and C to two 1-inch cathodes per target, i.e. two 1-inch C and two 1-inch A-group. These cathodes would be offset the same as the M-group elements, therefore the effective inside-outside ratios could be tuned to achieve the desired ratios for all solutions. This improvement should yield an almost 100% usable sample output per experiment, reducing what was required in this work of approximately 15 experiments down to 5-7 experiments.

8.3.2. Combinatorial Synthesis Method: Temperature Dependence Study

This work focused on combinatorial synthesis at a fixed temperature. While it was found that there was a natural temperature gradient with the current heater of ~50 °C one can expand upon this concept and purposely create a uniform temperature gradient across the sample. Redesigning the heater in order to create a gradient of ~200 °C should be easy. In this case, instead of a compositional gradient, now the cathodes would be positioned overhead to create compositional uniformity. This simply states it should be possible to generate samples from room temperature to 1000 °C in a mere five or so experiments using the ø50.8 mm sapphire substrates. Using larger substrates and cathodes could also reduce the number of depositions required to cover the desired temperature range.

The results from this type of combinatorial synthesis method, along with the composition method mentioned previously, would essentially generate the phase diagram for the MAX phases being examined. Additionally, the temperature gradient method could be used for any system in question, not just solid solutions. This could be utilized for a wide spectrum of materials going beyond the MAX phases, ultimately producing a large amount of results to assist in the understanding of materials.

8.3.3. Combinatorial Synthesis Method: Phase Diagram Determination

The last combinatorial method would essentially generate the phase diagram of the elements being studied. This type of combinatorial synthesis method has been used in the Cr-Al-C system.[45] In this design, three 2-inch cathodes would be positioned for straight down deposition. Looking from an overhead view, the center line separation between the triangulated cathodes is ~ 3.5 inches; therefore a 3-inch substrate could be position inside the triangle. A new heater of approximately 4-inch diameter designed for uniformity would be required.

For ternary systems elemental targets are used. The substrate position between the cathodes is fixed in place (no rotation) and at set temperature. Depositions will create a thin film phase diagram at a given temperature. At this point generating the samples is “easy”, the real challenge comes in characterization. Ideally, the sample integrity should remain unchanged, i.e. not broken into smaller samples, while initial compositional and structural characterizations are performed. Equipment used should have mapping capabilities, however, the 3-inch sample size most likely would be too big for most systems; therefore the sample will need to be broken into sizes capable of being measured.

This type of combinatorial method will provide a better understanding into the compositional variations for MAX phase systems. It will also generate the phase diagram for all other phases possible in the ternary system. Lastly, it can create new phases very quickly in a limited number of experiments.

List of References

[1] Anders A. A Brief History of Cathodic Arc Coating. New York: Springer, 2008.

[2] Jang CS, Jeon J-H, Song PK, Kang MC, Kim KH. Synthesis and mechanical properties of TiAlCxN1-x coatings deposited by arc ion plating. Surface and Coatings Technology 2005;200:1501.

[3] Diserens M, Patscheider J, Levy F. Improving the properties of titanium nitride by incorporation of silicon. Surface & coatings technology 1998;108:241.

[4] Veprek S. The search for novel, superhard materials. Journal of Vacuum Science & Technology A 1999; 17: 2401.

[5] Scabarozi TH, Eklund P, Emmerlich J, Högberg H, Meehan T, Finkel P, Barsoum MW, Hettinger JD, Hultman L, Lofland SE. Weak electronic anisotropy in the layered nanolaminate Ti 2 GeC. Solid State Communications 2008;146:498.

[6] Nowotony H. Strukturchemie Einiger Verbindungen der Ubergangsmetalle mit den elementen C, Si, Ge, Sn. Prog. Solid St. Chem. 1970;2:27.

[7] Schuster JC, Nowotny H, Vaccaro C. The Ternary Systems: Cr-Al-C, V-Al-C, and Ti-Al-C and the Behavior of the H-phases (M2AlC). J. Solid St. Chem 1980;32:213.

[8] Jeitschko W, Nowotony H. Die Kristallstruktur von Ti3SiC2 - ein neuer Komplexcarbid-Typ Monatshefte fur Chemie 1967;98:329.

[9] Barsoum MW, Yoo HI, Polushina IK, Rud' VY, Rud' YV, El-Raghy T. Electrical conductivity, thermopower, and Hall effect of Ti3AlC2, Ti4AlN3, and Ti3SiC2. Physical Review B 2000;62:10194.

[10] Barsoum M, El-Raghy T, Ali M. Processing and characterization of Ti2AlC, Ti2AlN, and Ti2AlC0.5N0.5. Metallurgical and Materials Transactions A 2000;31:1857.

[11] Barsoum MW, Brodkin D, El-Raghy T. Layered machinable ceramics for high temperature applications. Scripta Materialia 1997;36:535.

[12] Barsoum MW, El-Raghy T. Synthesis and Characterization of a Remarkable Ceramic: Ti3SiC2. J. Amer. Cer. Soc. 1996;79:1953.

[13] Barsoum MW, El-Raghy T, Rawn CJ, Porter WD, Wang H, Payzant EA, Hubbard CR. Thermal properties of Ti3SiC2. Journal of Physics and Chemistry of Solids 1999;60:429.

[14] Barsoum MW, Yoo HI, Polushina IK, Rud' VY, Rud' YV, El-Raghy T. Electrical conductivity, thermopower, and Hall effect of Ti3AlC2, Ti4AlN3, and Ti3SiC2. Phys. Rev. B 2000;62:10194.

[15] Barsoum MW, Golczewski J, Seifert HJ, Aldinger F. Fabrication and Electrical and Thermal Properties of Ti2InC, Hf2InC, and (Ti,Hf)2InC. J. Alloys Compounds 2002;340:173.

[16] Barsoum MW, Salama I, El-Raghy T, Golczewski J, Porter WD, Wang H, Seifert HJ, Aldinger F. Thermal and Electrical Properties of Nb2AlC, (Ti, Nb)2AlC and Ti2AlC. Metall. Mater. Trans. A 2002;33A:2775.

[17] Salama I, El-Raghy T, Barsoum MW. Synthesis and Mechanical Properties of Nb2AlC and (Ti,Nb)2AlC. J. Alloys Comp. 2002;347:271.

[18] Ganguly A, Zhen T, Barsoum MW. Synthesis and mechanical properties of Ti3GeC2 and Ti3(SixGe1-x)C2 (x = 0.5, 0.75) solid solutions. J. Alloys Comp. 2004;376:287.

[19] Gupta S, Barsoum MW. Synthesis and Oxidation of V2AlC and (Ti0.5,V0.5)2AlC in Air. J. Electrochem. Soc. 2004;151:24.

[20] Manoun B, Liermann HP, Gulve RP, Saxena SK, Ganguly A, Barsoum MW, Zha CS. Compression of Ti3Si0.5Ge0.5C2 to 53GPa. Appl. Phys. Lett. 2004;84:2799.

[21] Gupta S, Hoffman EN, Barsoum MW. Synthesis and oxidation of Ti2InC, Zr2InC, (Ti0.5,Zr0.5)2InC and (Ti0.5,Hf0.5)2InC in air J. Alloys Comp. 2006;426:168.

[22] Radovic M, Ganguly A, Barsoum MW, Zhen T, Finkel P, Kalidindi SR, Lara-Curzio E. On the elastic properties and mechanical damping of Ti3SiC2, Ti3GeC2, Ti3Si0.5Al0.5C2 and Ti2AlC in the 300–1573 K temperature range. Acta Mater. 2006;54:2757.

[23] Manoun B, Saxena SK, Hug G, Ganguly A, Hoffman EN, Barsoum MW. Synthesis and Compressibility of $Ti_3(Al_{1.0}Sn_{0.2})C_2$ and $Ti_3Al(C_{0.5},N_{0.5})_2$. J. Appl. Phys. 2007;101:113523.

[24] Scabarozi T, Ganguly A, Hettinger JD, Lofland SE, Amini S, Finkel P, El-Raghy T, Barsoum MW. Electronic and thermal properties of Ti3Al(C 0.5N0.5)2, Ti2Al(C0.5N0.5) and Ti2AlN. J. Appl. Phys. 2008;104:073713.

[25] Phataka NA, Saxenaa SK, Feib Y, Hu J. Synthesis of a new MAX compound (Cr0.5V0.5)2GeC and its compressive behavior up to 49 GPa. J. Alloys Comp. 2009;475:629.

[26] Tian W, Sun Z, Hashimoto H, Du Y. Synthesis, microstructure, and properties of (Cr1-xVx)2AlC solid solutions. J. Alloys Comp. 2009;484:130.

[27] Finkel P, Seaman B, Harrell K, Palma J, Hettinger JD, Lofland SE, Ganguly A, Barsoum MW, Sun Z, Li S, Ahuja R. Electronic, thermal, and elastic properties of Ti3 Si1-x Gex C2 solid solutions. Phys. Rev. B 2004;70:085104.

[28] Zhou Y, Meng F, Zhang J. New MAX-Phase Compounds in the V-Cr-Al-C System. J. Am. Ceram. Soc. 2008;91:1357.

[29] Lofland SE, Hettinger JD, Meehan T, Bryan A, Finkel P, Gupta S, Barsoum MW, Hug G. Electron-phonon coupling in M[n+1]AX[n]-phase carbides. Physical Review B (Condensed Matter and Materials Physics) 2006;74:174501.

[30] Hettinger JD, Lofland SE, Finkel P, Meehan T, Palma J, Harrell K, Gupta S, Ganguly A, El-Raghy T, Barsoum MW. Electrical transport, thermal transport and mechanical properties of M_2AlC (M = Ti, Cr, Nb and V). Phys. Rev. B 2005;72:115120.

[31] Finkel P, Hettinger JD, Lofland SE, Barsoum MW, El-Raghy T. Magnetotransport Properties of the Ternary Carbide Ti_3SiC_2: Hall Effect, Magnetoresistance and Magnetic Susceptibility. Phys. Rev. B 2001;65:035113.

[32] Finkel P, Barsoum MW, Hettinger JD, Lofland SE, Yoo HI. Low-temperature transport properties of nanolaminates Ti3AlC2 and Ti4AlN3. Phys. Rev. B 2003;67:235108.

[33] Scabarozi TH, Amini S, Finkel P, Leaffer OD, Spanier JE, Barsoum MW, Drulis M, Drulis H, Tambussi WM, Hettinger JD, Lofland SE. Electrical, thermal and elastic properties of the MAX-phase Ti2SC. J. Appl. Phys. 2008;104:033502.

[34] Lofland SE, Hettinger JD, Harrell K, Finkel P, Gupta S, Barsoum MW, Hug G. App. Phys. Lett. 2004;84:508.

[35] Farber L, Levin I, Barsoum M. HRTEM Study of a Low-Angle Boundary in Plastically Deformed Ti3SiC2. Phil. Mag. Letters 1999;79:163.

[36] Barsoum M, El-Raghy T. Room-temperature ductile carbides. Metallurgical and Materials Transactions A 1999;30:363.

[37] Barsoum MW. Dislocations, Kink Bands, and Room Temperature Plasticity of Ti3SiC2. Met. Mat. Trans. 1999;30A:1727.

[38] Kuroda Y, Low IM, Barsoum MW, El-Raghy T. Indentation Responses and Damage Characteristics of Hot Pressed Ti3SiC2. J. Aust. Ceram. Soc. 2001;37:95.

[39] Barsoum MW, Zhen T, Kalidindi SR, Radovic M, Murugaiah A. Fully reversible, dislocation-based compressive deformation of Ti3SiC2 to 1 GPa. Nat Mater 2003;2:107.

[40] El-Raghy T, Barsoum MW, Zavaliangos A, Kalidindi SR. Processing and Mechanical Properties of Ti3SiC2: II, Effect of Grain Size and Deformation Temperature. J. Amer. Cer. Soc. 1999;82:2855.

[41] Procopio AT, Barsoum MW, El-Raghy T. Characterization of Ti4AlN3. Metall. Mater. Trans. A 2000;31A:333.

[42] Tzenov NV, Barsoum MW. J. Am. Ceram. Soc. 2000;83:825.

[43] Smith DL. Thin-film Deposition Principle & Practice. New York: McGraw-Hill, 1995.

[44] Ohring M. Materials Science of Thin Films Deposition and Structure. San Diego: Academic Press, 2002.

[45] Mertens R, Sun Z, Music D, Schneider JM. Effect of the Composition on the Structure of Cr-Al-C Investigated by Combinatorial Thin Film Synthesis and ab Initio Calculations. Advanced Engineering Materials 2004;6:903.

[46] Cullity BD. Elements of X-Ray Diffraction. Lebanon, IN: Addison Wesley, 1978.

[47] Nelson JB, Riley DP. An experimental investigation of extrapolation methods in the derivation of accurate unit-cell dimensions of crystals. Proc. of the Phys. Soc. 1945;57:160.

[48] Williamson GK, Hall WH. X-ray line broadening from filed aluminium and wolfram. Acta Metallurgica 1953;1:22.

[49] MedeA. MedeA. Angel Fire, NM: Materials Design.

[50] Callister WD. Fundamentals of Materials Science and Engineering: An Interactive e . Text. New York: Wiley, 2000.

[51] McClure JW. Analysis of Multicarrier Galvanomagnetic Data for Graphite. Phys. Rev. 1958;112.

[52] Kittel C. Introduction To Solid State Physics. New York: Wiley, 1996.

[53] Myhra S, Summers JWB, Kisi EH. Ti3SiC2--A layered ceramic exhibiting ultra-low friction. Mater. Lett. 1999;39:6.

[54] Scabarozi TH, Gennaoui C, Roche J, Flemming T, Wittenberger K, Hann P, Adamsom B, Rosenfeld A, Barsoum MW, Hettinger JD, Lofland SE. Investigation of (Ti1-xNbx)2AlC by combinatorial method. App. Phys. Lett. 2009;95:101907.

[55] Wilhelmsson O, Palmquist J-P, Nyberg T, Jansson U. Sputtering of Ti2AlC and Ti3AlC2 thin films. Appl. Phys. Lett. 2004;85:1066.

[56] Walter C, Martinez C, El-Raghy T, Schneider JM. Towards large area MAX phase coatings on steel. Steel Research International 2005;76:225.

[57] Palmquist JP, Jansson U, Seppanen T, Persson POA, Birch J, Hultman L, Isberg P. Magnetron sputtered epitaxial single-phase Ti[sub 3]SiC[sub 2] thin films. Appl. Phys. Lett. 2002;81:835.

[58] Palmquist JP, Li S, Persson POA, Emmerlich J, Wilhemsson O, Högberg H, Katsnelson MI, Johansson B, Ahujia R, Eriksson O, Hultman L, Jansson U. Mn+1AXn Phases in the Ti–Si–C System Studied by Thin Film Synthesis and Ab Initio Calculations. Phys. Rev. B 2004;70:165401.

[59] Högberg H, Hultman L, Emmerlich J, Joelsson T, Eklund P, Molina-Aldareguia JM, Palmquist JP, Wilhelmsson O, Jansson U. Growth and characterization of MAX-phase thin films. Surf. Coat. Technol. 2005;193:6.

[60] Oyama ST. Chemistry of Transition Metal Carbides and Nitrides. London: Blackie Academic & Professional, 1996

[61] Scabarozi TH, Roche J, Rosenfeld A, Lim SH, Salamanca-Riba L, Yong G, Takeuchi I, Barsoum MW, Hettinger JD, Lofland SE. Synthesis and characterization of Nb2AlC thin films. Thin Solid Films 2009;517:2920.

[62] Gusev AI. Phase equilibria in M-X-X' and M-Al-X ternary systems (M=transition metal; X, X'=B, C, N, Si) and the crystal chemistry of ternary compounds. Russ. Chem. Rev. 1996;95:379.

[63] Jeitschko W, Nowotny H, Benesovsky F. Ternary Compounds Containing Carbon (V-Ge-C, Nb-Ga-C, Ta-Ga-C, Ta-Ge-C, Cr- Ga-C, AND Cr-Ge-C). Monatshefte fuer Chemie (Austria) 1963;94:844.

[64] Gusev AI. Phase equilibria in M-X-X' and M-Al-X ternary systems (M=transition metal; X, X'=B, C, N, Si) and the crystal chemistry of ternary compounds. Russian Chemical Reviews 1996;65:379.

[65] Högberg H, Eklund P, Emmerlich J, Birch J, Hultman L. Epitaxial Ti2GeC, Ti3GeC2, and Ti4GeC3 MAX Phase Thin Films Grown by Magnetron Sputtering. J. Mater. Res. 2005;20:779.

[66] Wilhelmsson O, Eklund P, Högberg H, Hultman L, Jansson U. Structural, electrical and mechanical characterization of magnetron-sputtered V–Ge–C thin films. Acta Mater. 2008;56:2563.

[67] Spanier JE, Gupta S, Amer M, Barsoum MW. Vibrational behavior of the M[n + 1]AX[n] phases from first-order Raman scattering (M = Ti,V,Cr, A = Si, X = C,N). Phys. Rev. B 2005;71:012103.

[68] Leaffer OD, Gupta S, Barsoum MW, Spanier JE. On the Raman Scattering From Selected M2AC Compounds. J. Mater. Res. 2007;22:2651.

[69] Giorgi AL, Szklarz EG, Storms EK, Bowman AL, Matthias BT. Effect of Composition on the Superconducting Transition Temperature of Tantalum Carbide and Niobium Carbide. Phys. Rev. 1962;125:837.

[70] Wang JY, Zhou YC. Ab initio elastic stiffness of nano-laminate (MxM'2-x)AlC (M and M' = Ti, V, and Cr) solid solutions. J. Phys. Condens. Matter 2004;16:2819.

[71] Wang JY, Zhou YC. Dependence of elastic stiffness on the electronic band structure of nanolaminate M2AlC (M = Ti, V, Nb, and Cr) ceramics. Phys. Rev. B 2004;69:21411.

[72] Barsoum MW. The MN+1AXN phases: A new class of solids : Thermodynamically stable nanolaminates. Progress in Solid State Chemistry 2000;28:201.

[73] Leaffer OD. Personal communication: Theoretical lattice calculations of Ti4AlC3, Nb4AlC3, Nb3AlC2, V3AlC2, V4AlC3.

[74] Renaud G. Oxide surfaces and metal/oxide interfaces studied by grazing incidence X-ray scattering. Surf. Sci. Rep. 1998;32:1.

[75] Storms EK, Krikorian NH. The Variation of Lattice Parameter with Carbon Content of Niobium Carbide. The Journal of Physical Chemistry 2002;63:1747.

[76] Emmerlich J, Gassner G, Eklund P, Hogberg H, Hultman L. Micro and Macroscale Tribological Behaviour of Epitaxial Ti3SiC2 Thin Films. Wear 2008;264:914.

[77] Lofland SE, Hettinger JD, Harrell K, Finkel P, Gupta S, Barsoum MW, Hug G. Elastic and Electronic Properties of Select M_2AX Phases. Appl. Phys. Letts. 2004;84:508.

[78] Scabarozi TH, Amini S, Leaffer OD, Ganguly A, Gupta S, Tambussi W, Clipper S, Spanier JE, Barsoum MW, Hettinger JD, Lofland SE. Thermal Expansion of Select MAX Phases Measured by High Temperature X-ray Diffraction and Dilatometry. J. Appl. Phys. 2009;105:013543.

[79] Radovic M, Ganguly A, Barsoum MW. Elastic Properties and Phonon Conductivities of Ti3AlCN and Ti2AlCN Solid Solutions. J. Mater. Res. 2008;23:1517.

[80] Walter C, Sigumonrong DP, El-Raghy T, Schneider JM. Towards large area deposition of Cr2AlC on steel. Thin Solid Films 2006;515:389.

[81] Schneider JM, Sun Z, Mertens R, Uestel F, Ahuja R. Ab initio calculations and experimental determination of the structure of Cr2AlC. Solid State Communications 2004;130:445.

[82] Schneider JM, Sigumonrong DP, Music D, Walter C, Emmerlich J, Iskandar R, Mayer J. Elastic properties of Cr2AlC thin films probed by nanoindentation and ab initio molecular dynamics. Scripta Materialia 2007;57:1137.

[83] Wilhelmsson O, Eklund P, Högberg H, Hultman L, Jansson U. Structural, electrical and mechanical characterization of magnetron-sputtered V–Ge–C thin films. Acta Materialia 2008;56:2563.

[84] Nelson JB, Riley DP. An experimental investigation of extrapolation methods in the derivation of accurate unit-cell dimensions of crystals. 1945:160.

[85] Fischer A, KŸhne H, Richter H. New Approach in Equilibrium Theory for Strained Layer Relaxation. Phys. Rev. Lett. 1994;73:2712.

[86] Rohrer GS. Structure and Bonding in Crystalline Materials: Cambridge University Press, 2001.

[87] Detroye M, Reniers F, Buess-Herman C, Vereecken J. Synthesis and characterisation of chromium carbides. Applied Surface Science 1997;120:85.

[88] Lin C-C, Hsieh W-J, Lin J-H, Chen U-S, Guo X-J, Shih HC. Formation and characterization of chromium carbide films deposited using a 90° bend magnetic filtered cathodic vacuum arc system. Surf. and Coat. Technol. 2006;200:5052.

[89] Bowman AL, Arnold GP, Storms EK, Nereson NG. Crystal Structure of $Cr_{23}C_6$. Acta Cryst. 1972:3102.

[90] Gusev AI. Phase Equilibria in the M-X-X'. Russ. Chem. Rev. 1996;95:379.

[91] Scabarozi TH, Eklund P, Emmerlich J, Högberg H, Meehan T, Finkel P, Barsoum MW, Hettinger JD, Hultman L, Lofland SE. Weak electronic anisotropy in the layered nanolaminate Ti 2 GeC. Solid State Commun. 2008;146:498.

[92] Suprunov VA, Freid MK. Physical properties of the iron-chromium carbides (Cr, Fe)23C6. Powder Metall. Met. Ceram. 1970;9:64.

[93] Ozawa P, Yoshizaki S, Takeyama S, Enjo T, keuchi K. Electrical Properties of Cr - Al Alloy Thin Films. IEEE T. Compon. Hybr. 1986;9:391

[94] Schneider JM, Mertens R, Music D. Structure of V2AlC studied by theory and experiment. J. Appl. Phys. 2006;99:013501.

[95] Sigumonrong DP, Zhang J, Zhou Y, Music D, Schneider JM. Synthesis and elastic properties of V2AlC thin films by magnetron sputtering from elemental targets. Journal of Physics D: Applied Physics 2009;42:185408.

[96] Meikap AK, Jana AR, De SK, Chatterjee S. Low temperature transport properties of thin disordered vanadium oxide films. J of Low Temp Phys 1991;85:295.

[97] Sun Z, Ahuja R, Schneider JM. Theoretical investigation of the solubility in (MxM'2-x)AlC (M and M' = Ti,V,Cr). Phys. Rev. B 2003;68:224112.

[98] ICDD. V2AlC PDF#29-0101.

[99] ICDD. Cr2AlC PDF#89-2275.

[100] Scabarozi TH, Steinmetz C, Applegate J, Gennaoui C, Benjamin S, Roche J, Barsoum MW, Lofland SE, Hettinger JD. Thin films in the Cr-V-Ge-C systems synthesized by combinatorial method. In Progress.

[101] Etzkorn J, Ade M, Hillebrecht H. V2AlC, V4AlC3-x (x =0.31), and V12Al3C8: Synthesis, Crystal Growth, Structure, and Superstructure. Inorg. Chem. 2007;46:7646.

[102] ICDD. Cr2C PDF#14-0519.

[103] ICDD. V2C PDF#73-1320.

[104] Jeitschko W, Nowotny H, Benesovsky F. Ternary Compounds Containing Carbon (V-Ge-C, Nb-Ga-C, Ta-Ga-C, Ta-Ge-C, Cr- Ga-C, AND Cr-Ge-C). Monatsh. Chem. 1963;94:844.

[105] Eckerlin P, Kandler H, Stegherr A. Structure Data of Elements and Intermetallic Phases: Springer-Verlag, 1971.

[106] P. Eckerlin HK, A. Stegherr. Structure Data of Elements and Intermetallic Phases: Springer-Verlag, 1971.

[107] ICDD. Tetragonal Cr5Ge3 PDF #15-0662.

[108] ICDD. Tetragonal V5Ge3 PDF#15-0661.

[109] ICDD. Hexagonal V5Ge3 PDF#15-0661.

[110] Parthe E, Norton JT. Crystal structures of Zr5Ge3, Ta5Ge3 and Cr5Ge3. Acta Crystallographica 1958;11:14.

[111] Amini S, Zhou A, Gupta S, DeVillier A, Finkel P, Barsoum MW. Synthesis and elastic mechanical properties of Cr2GeC. J. Mat. Res. 2008;23:2157.

[112] Scabarozi TH, Lofland SE, Hettinger JD, Barsoum MW, Amini S. Unpublished results.
[113] Lofland SE. Unpublished result.
[114] Wanga CP, Zhenga AQ, Liu XJ. Thermodynamic assessments of the V–Ge and V–Pt systems. Intermetallics 2008;16:544.
[115] Boller H. Kristallchemische Untersuchungen an Komplexcarbiden und-nitriden mit aufgefülltem Re3B-Typ. Monatshefte für Chemie 1971;102:431.
[116] ICDD. Cr23C6 PDF#35-0783.
[117] ICDD. VC PDF#73-0476.
[118] ICDD. V8C7 PDF#35-0786.
[119] Lofland SE. Unpublished result.
[120] Meikap AK, Jana AR, De SK, Chatterjee S. Low temperature transport properties of thin disordered vanadium oxide films. J. Low Temp. Phys. 1991;85:295.
[121] ICDD. Cr2GeC PDF#18-0384.
[122] ICDD. V2GeC PDF#18-0567.
[123] Phataka NA, Saxenaa SK, Feib Y, Hu J. Synthesis of a new MAX compound (Cr0.5V0.5)2GeC and its compressive behavior up to 49 GPa. J. Alloy. Compd. 2009;475:629.
[124] Finkel P, Seaman B, Harrell K, Hettinger JD, Lofland SE, Ganguly A, Barsoum MW, Sun Z, Li S, Ahuja R. Low Temperature Elastic, Electronic and Transport Properties of $Ti_3Si_{1-x}Ge_xC_2$ Solid Solutions. Phys. Rev. B, 2004;70:085104.
[125] Finkel P, Seaman B, Harrell K, Palma J, Hettinger JD, Lofland SE, Ganguly A, Barsoum MW, Sun Z, Li S, Ahuja R. Electronic, thermal, and elastic properties of Ti3 Si1-x Gex C2 solid solutions. Physical Review B 2004;70:085104.
[126] Emmerlich J, Palmquist J-P, Hogberg H, Molina-Aldareguia JM, Czigany Z, Persson PO, Jansson U, Hultman L. Growth of Ti3SiC2 thin films by elemental target magnetron sputtering. J. Appl. Phys. 2004;96:4817.
[127] Magnuson M, Palmquist JP, Mattesini M, Li S, Ahuja R, Eriksson O, Emmerlich J, Wilhelmsson O, Eklund P, Hogberg H, Hultman L, Jansson U. Electronic structure investigation of Ti[sub 3]AlC[sub 2], Ti[sub 3]SiC[sub 2], and Ti[sub 3]GeC[sub 2] by soft x-ray emission spectroscopy. Physical Review B (Condensed Matter and Materials Physics) 2005;72:245101.
[128] Zhang X-f, Lu A-x. Effects of titanium coating on property of diamond. T. Nonferr. Metal Soc 2007;17:715.
[129] Högberg H, Hultman L, Emmerlich J, Joelsson T, Eklund P, Molina-Aldareguia JM, Palmquist JP, Wilhelmsson O, Jansson U. Growth and characterization of MAX-phase thin films. Surf. Coat. Tech. 2005;193:6.
[130] Högberg H, Hultman L, Emmerlich J, Joelsson T, Eklund P, Molina-Aldareguia JM, Palmquist JP, Wilhelmsson O, Jansson U. Growth and characterization of MAX-phase thin films. Surface and Coatings Technology 2005;193:6.
[131] Eklund P, Beckers M, Frodelius J, Högberg H, Hultman L. Magnetron sputtering of Ti3SiC2 thin films from a Ti3SiC2 compound target. J. Vac. Sci. Technol. A 2007;25:1381.

Appendix A: Formation of Ti_2AlC by Solid State Reaction of TiC films on Al_2O_3

A.1. Introduction

For MAX phase film growth a seedlayer is usually required.[57-59] Even when a seedlayer is not deposited, a binary carbide seedlayer often forms at the interface anyway.[55, 65, 126] During this thesis numerous binary carbides were synthesized for use as buffer layers as well as properties characterization. Typically the MAX phases have a similar *a* lattice constant as their respective binary growing in the (111) orientation for cubic MX binaries or *a* lattice for the hexagonal M_2X binaries, thus making them excellent candidates for use as buffer layers.

A.2. Results and Discussion

Investigating the deposition of TiC on sapphire at various temperatures yielded an interesting result, Ti_2AlC was observed by XRD for deposit temperatures above 725 °C. Figure A.1 shows XRD patterns of TiC films deposited on Al_2O_3 at various temperatures. At 725 °C and below only TiC (111) and a very weak unknown peak around 34.5° were observed. Deposits at 800 °C and 900 °C resulted in phases of TiC, Ti_2AlC, Ti_8C_5, and Ti metal. Clearly, Ti_2AlC had its strongest diffraction and smallest FWHM at 900 °C indicating that it had the highest degree of ordering. Also notable was the peak around 18°, associated with ordered hexagonal Ti_8C_5. It has been shown Ti_8C_5 formed for deposits of Ti on diamond at room temperature, indicating that it is more stable at lower temperatures.[128] At 1000 °C only strong TiC and weak Ti_2AlC were easily resolvable, with possibly some Ti metal present. Figure A.2 shows the *c* lattice constant of Ti_8C_5 and

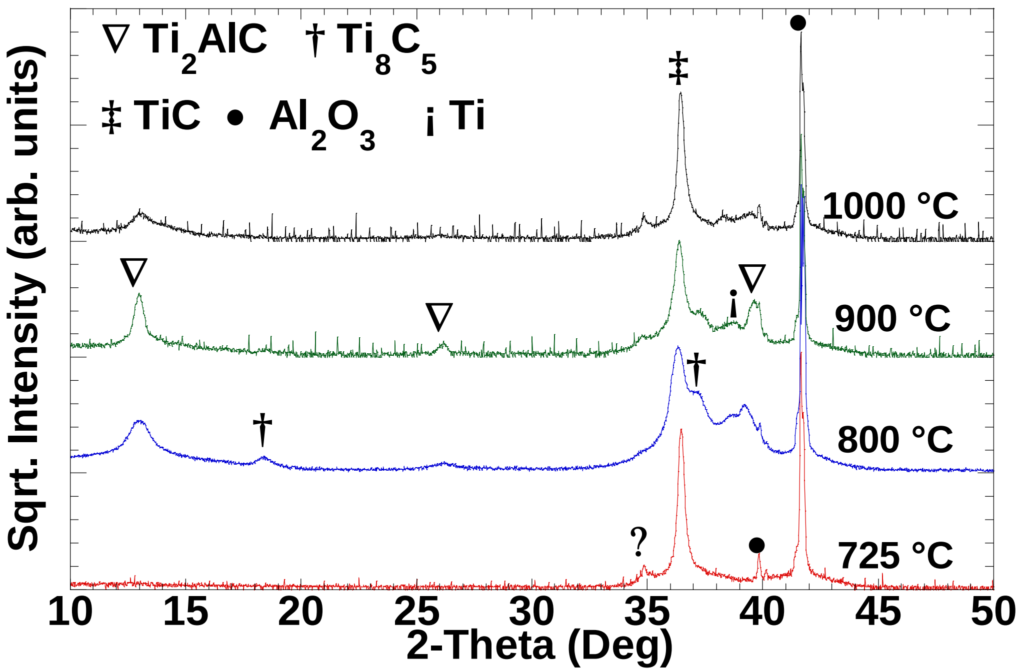

Figure A.1 XRD pattern of TiC deposited on Al_2O_3 at various temperatures. Above 725 °C Ti_2AlC (001) peaks emerge indicating a solid state reaction between the TiC film and substrate. Additional peaks from Ti_8C_5, Ti, and an unidentified peak around 35° were also observed.

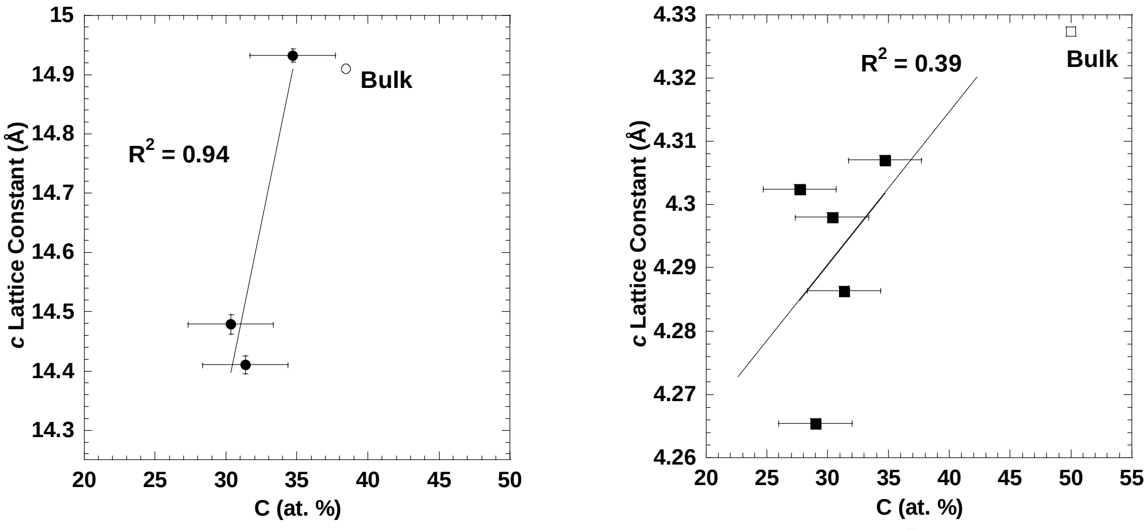

(a) **(b)**

Figure A.2 a) Calculated *c* lattice constant for ordered Ti_8C_5 phase observed in TiC films. b) Calculated *a* lattice constant for disordered TiC phase observed in TiC films. Lines represent linear fits of the data, open markers represent bulk lattice values.

a lattice constant of TiC as a function of C concentration. Linear fits of the data subtly showed the shift in lattice constant due to carbon content.

Under high vacuum and high temperature the oxygen present in the substrate must react with some of the depositing Ti to form a titanium oxide and evaporate from the film. It is not surprising that the Al becomes free to bind with the depositing species to form new phases. What was surprising was the distance to which Al migrated forming these other phases. Figure A.3 is a cross-section TEM image of a TiC film deposited on sapphire at 900 °C. The arrows indicate regions where Ti_2AlC formed. Most of the MAX phase observed was at the substrate-film interface, where an approximately 10 nm thick Ti_2AlC layer formed. However, there appeared to be regions where Ti_2AlC formed away from the interface, some near the surface of the film. Clearly the mobility of the Al was more than simple diffusion, possibly a more volatile liquid phase. SAED (not shown) confirmed the presence of Ti_2AlC, clearly showing the hexagonal six-fold symmetry.

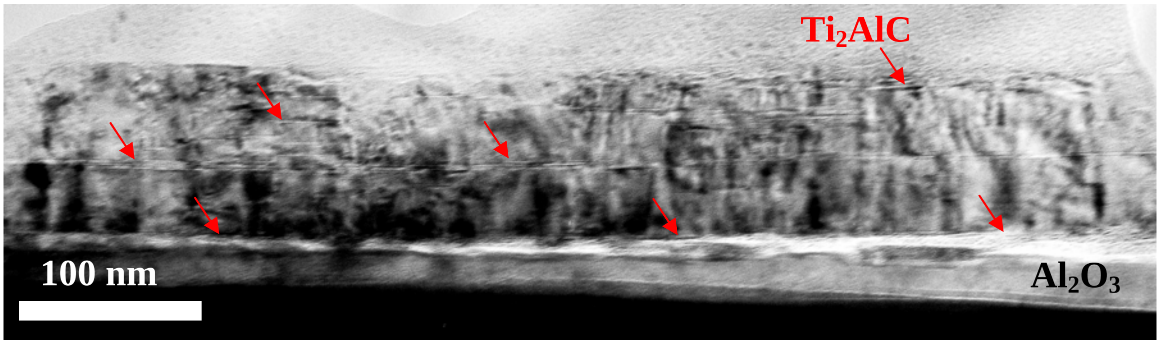

Figure A.3 Cross-section TEM of TiC deposited on Al_2O_3 at 900 °C. Arrows indicate regions where Ti_2AlC has grown, some far from the substrate interface.

Appendix B: Synthesis of Ti_3SiC_2 Thin Films from a Compound Target

B.1. Introduction

The first attempt at thin film synthesis of a MAX phase was deposition of Ti_3SiC_2 from a compound target made by 312 LLC (Vineland, NJ). The purpose was to verify the system's ability to synthesize a thin film of a previously synthesized phase.[57, 58, 126, 129] These studies indicated that phase formation occurs above 850 °C, either with or without the use of a seedlayer. Additional phases of $Ti_5Al_2C_3$ and $Ti_7Al_2C_5$ were also observed. Depositing from a compound target is a more favored means of coating materials limiting the amount of equipment (power supplies, cathodes, targets...) required.

B.2. Results and Discussion

XRD analysis of films synthesized at 900 °C (Fig. B.1a) were found to only contain TiC (111). Chemical analysis found the films to be Si-deficient with a Ti:Si molar ratio of ~4:1. This was most likely due scattering of the atoms during deposition and desorption from the surface due to the elevated temperature. In order to resolve the Si deficiency a second target containing Si was configured in the chamber. XRD of subsequent films (Fig B.1b) showed *c*-axis oriented Ti_3SiC_2 along with TiC (111). These results were somewhat in agreement with those reported by the group in Linköping.[58, 126, 130] The Si deficiency was unlike previous observations in deposits from compound targets of Ti_3SiC_2 and Ti_2AlC where carbon was found to be in excess in both studies.[55, 131] It was clear that depositing from a compound target did not allow control of composition, therefore it was concluded that deposits from elemental targets was the best approach as the flux could be controlled for each material.

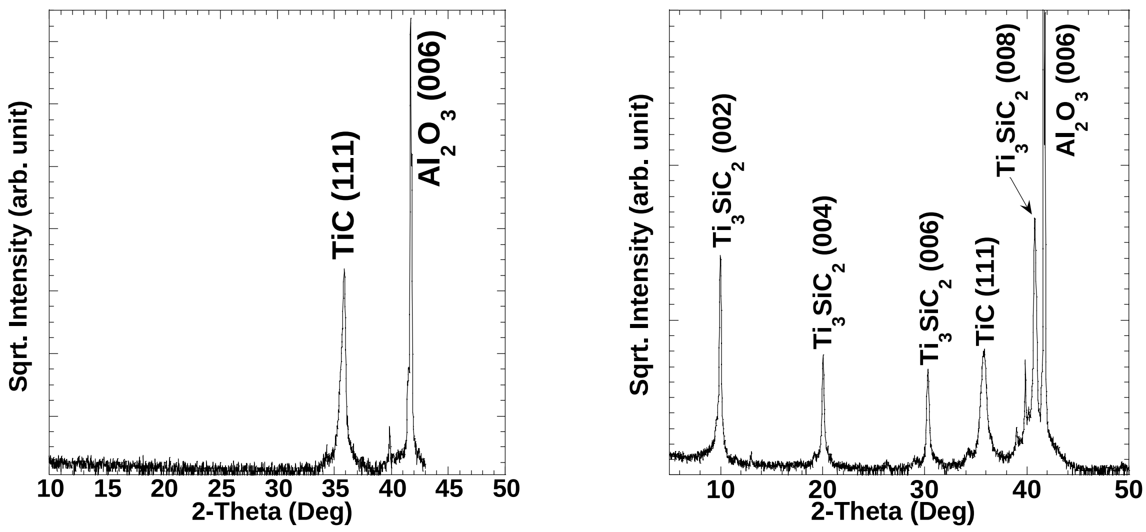

(a) **(b)**

Figure B.1 a) XRD pattern of a film deposited from a Ti_3SiC_2 compound target at 925 °C. Only TiC (111) was observed, subsequent analysis using EDS indicated that the film was deficient in Si. b) XRD pattern of a film co-deposited from a compound Ti_3SiC_2 target and Si target at 850 °C. Epitaxial Ti_3SiC_2 and TiC phases were present.

Ti_3SiC_2 film showed metal-like electrical conductivity behavior down to 2 K (Fig. B.2). The resistivity value was higher than that reported in bulk[31] and thin film[57]. The Hall coefficient as a function of temperature is shown in Figure B.3a. All films showed positive coefficients, in good agreement with previous results for bulk. Magnetoresistance (Fig. B.3b) revealed small values with slight temperature dependence. With low R_H values and positive quadratic, non-saturating magnetoresistances a two-band model is required to analyze experimental results as described in 4.3.4. Similar to what has been reported in previous studies of MAX phases the carrier concentration was found to be $n \approx p \approx 8.6 \times 10^{26}$ m^{-3}. [5, 27, 30, 31]

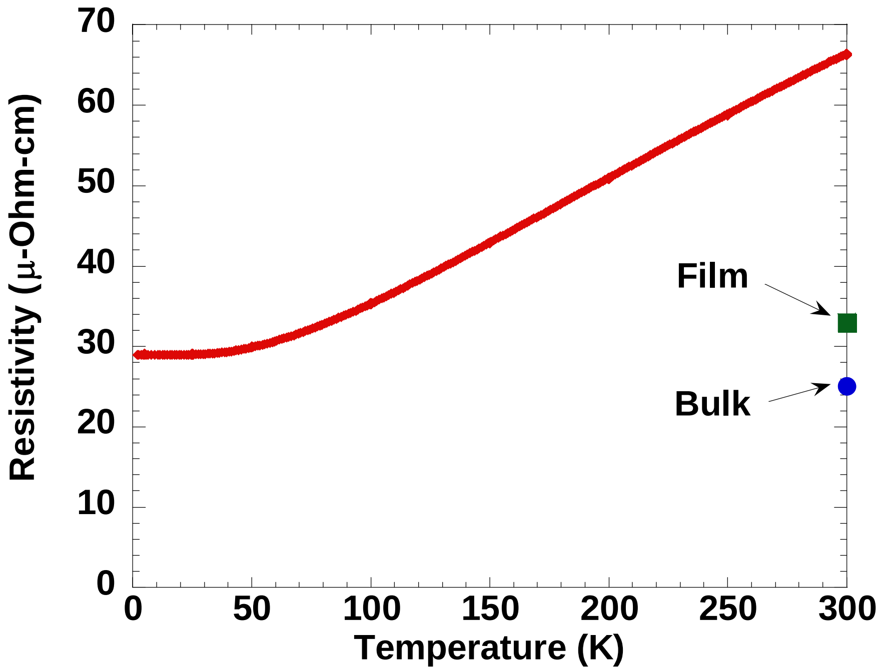

Figure B.2 Resistivity as a function temperature for Ti_3SiC_2 thin film deposited at 825 °C. Metal-like behavior was observed down to 2 K. Room-temperature resistivity was higher than that previously reported in bulk [31] and thin film [58].

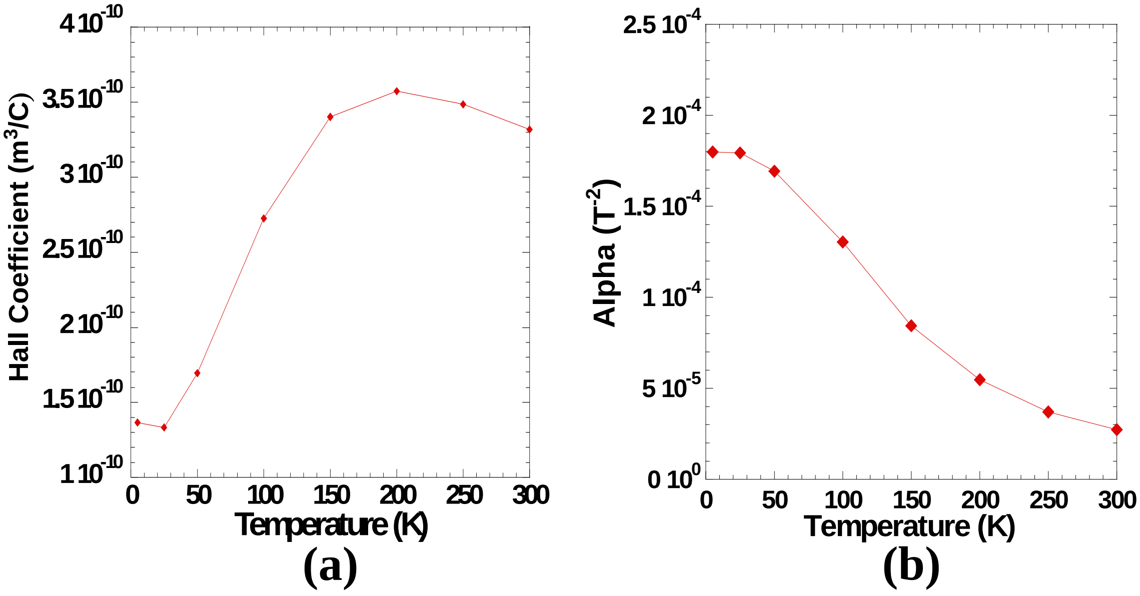

Figure B.3 a) Temperature dependence of Hall coefficient for Ti_3SiC_2 thin films. b) Magnetoresistance as a function of temperature.

Appendix C: Magnetotransport Measurement Analysis

C.1. Introduction

In this Appendix, a description of the measurement analysis for magnetotransport of MAX phase thin film is presented. The purpose is to show the quality of the measurements for sample to sample comparison along with showing the reason for no error bars in magnetoresistance and Hall coefficient figures.

C.2. Discussion

The technique used in measuring magnetotransport properties was shown in Section 4.3. Briefly, samples were positioned on a measurement puck such that the magnetic field would be perpendicular to the film. The sample was held at a temperature while the magnetic field was changed (sweeping) from maximum to minimum (or vice versa). Resistance measurements are taken at set intervals during the field sweeping. From the results plots of Volts vs. Field were generated. Figures C.1-C.3 shows the data for the samples measured in Chapters 5-7 at 5 and 300 K. As can be seen, the plots were parabolic in shape, associated to the magnetoresistance (MR), and were tilted, associated to the Hall coefficient (R_H). By fitting the plots with a second order polynomial, the MR and R_H can be extracted through the following equations:

$$MR = \frac{a}{c} \tag{C.1}$$

$$R_H = \frac{b t_f w_f}{I w_t} \tag{C.2}$$

where a, b, c, t_f, w_f, I, and w_t are the quadratic square term, the quadratic linear term, the quadratic y-intercept term, t_f the film thickness, w_f the film width, I the applied sample current, and w_t the transverse film width, respectively. The quality of quadratic fit (R^2) is also shown in Figures C.1-C.3. Most samples were fit extremely well (> 0.99) leading to minimal error through this calculation. Also note from Eqs. C.1 and C.2 is the MR is independent of sample tilt and dimensions, where as R_H is affected by them. The former alters the applied field (B) to B cos α, where α is the tilt angle and the latter, any dimension measurement error, will affect the overall R_H value. Since most of the quadratic fits were very good and the microbridges were well defined, error analysis was not performed on the MR and R_H results, thus the absence of error bars in the respective figures in Chapters 5-7.

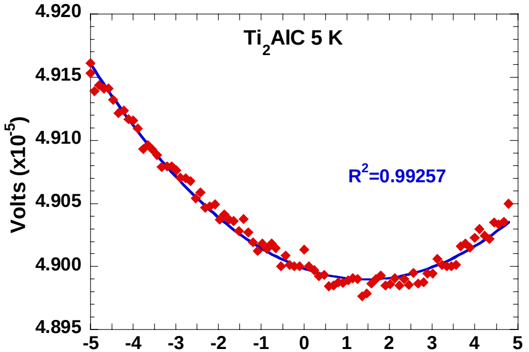

Ti$_2$AlC 5 K
R^2=0.99257
Volts (x10^{-5})
4.920
4.915
4.910
4.905
4.900
4.895
-5 -4 -3 -2 -1 0 1 2 3 4 5
Field (T)

(a)

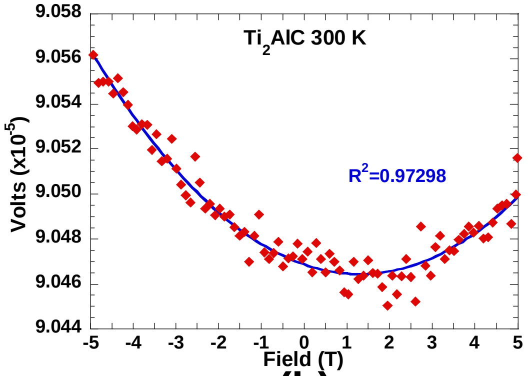

Ti$_2$AlC 300 K
R^2=0.97298
Volts (x10^{-5})
9.058
9.056
9.054
9.052
9.050
9.048
9.046
9.044
-5 -4 -3 -2 -1 0 1 2 3 4 5
Field (T)

(b)

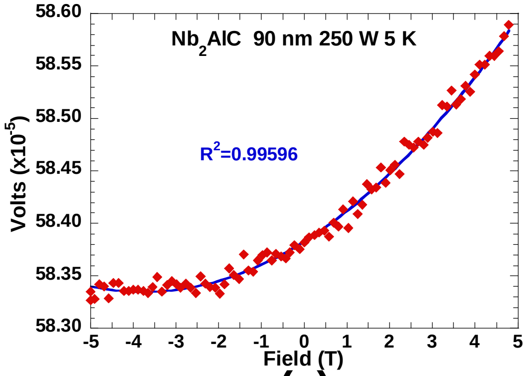

Nb$_2$AlC 90 nm 250 W 5 K
R^2=0.99596
Volts (x10^{-5})
58.60
58.55
58.50
58.45
58.40
58.35
58.30
-5 -4 -3 -2 -1 0 1 2 3 4 5
Field (T)

(c)

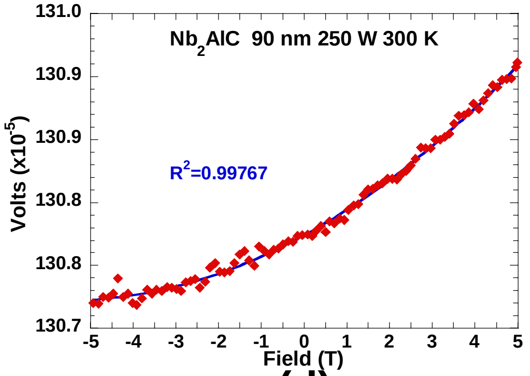

Nb$_2$AlC 90 nm 250 W 300 K
R^2=0.99767
Volts (x10^{-5})
131.0
130.9
130.9
130.8
130.8
130.7
-5 -4 -3 -2 -1 0 1 2 3 4 5
Field (T)

(d)

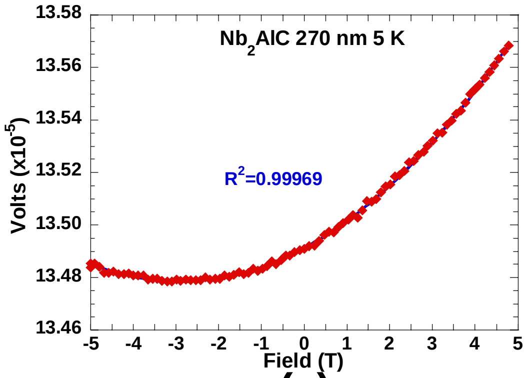

Nb$_2$AlC 270 nm 5 K
R^2=0.99969
Volts (x10^{-5})
13.58
13.56
13.54
13.52
13.50
13.48
13.46
-5 -4 -3 -2 -1 0 1 2 3 4 5
Field (T)

(e)

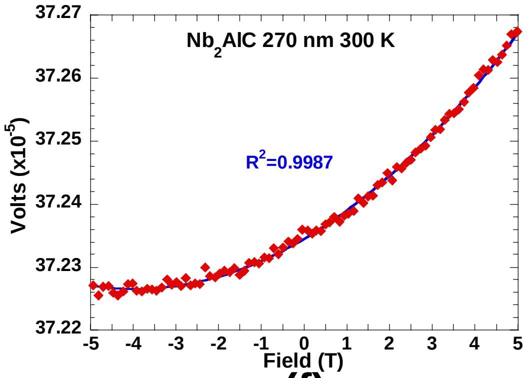

Nb$_2$AlC 270 nm 300 K
R^2=0.9987
Volts (x10^{-5})
37.27
37.26
37.25
37.24
37.23
37.22
-5 -4 -3 -2 -1 0 1 2 3 4 5
Field (T)

(f)

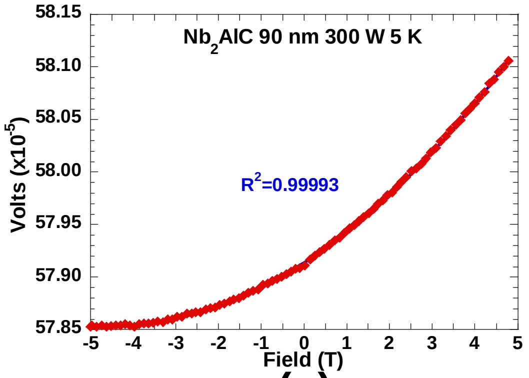

Nb$_2$AlC 90 nm 300 W 5 K
R^2=0.99993
Volts (x10^{-5})
58.15
58.10
58.05
58.00
57.95
57.90
57.85
-5 -4 -3 -2 -1 0 1 2 3 4 5
Field (T)

(g)

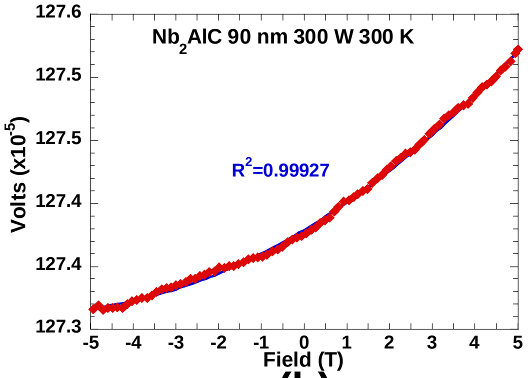

Nb$_2$AlC 90 nm 300 W 300 K
R^2=0.99927
Volts (x10^{-5})
127.6
127.5
127.5
127.4
127.4
127.3
-5 -4 -3 -2 -1 0 1 2 3 4 5
Field (T)

(h)

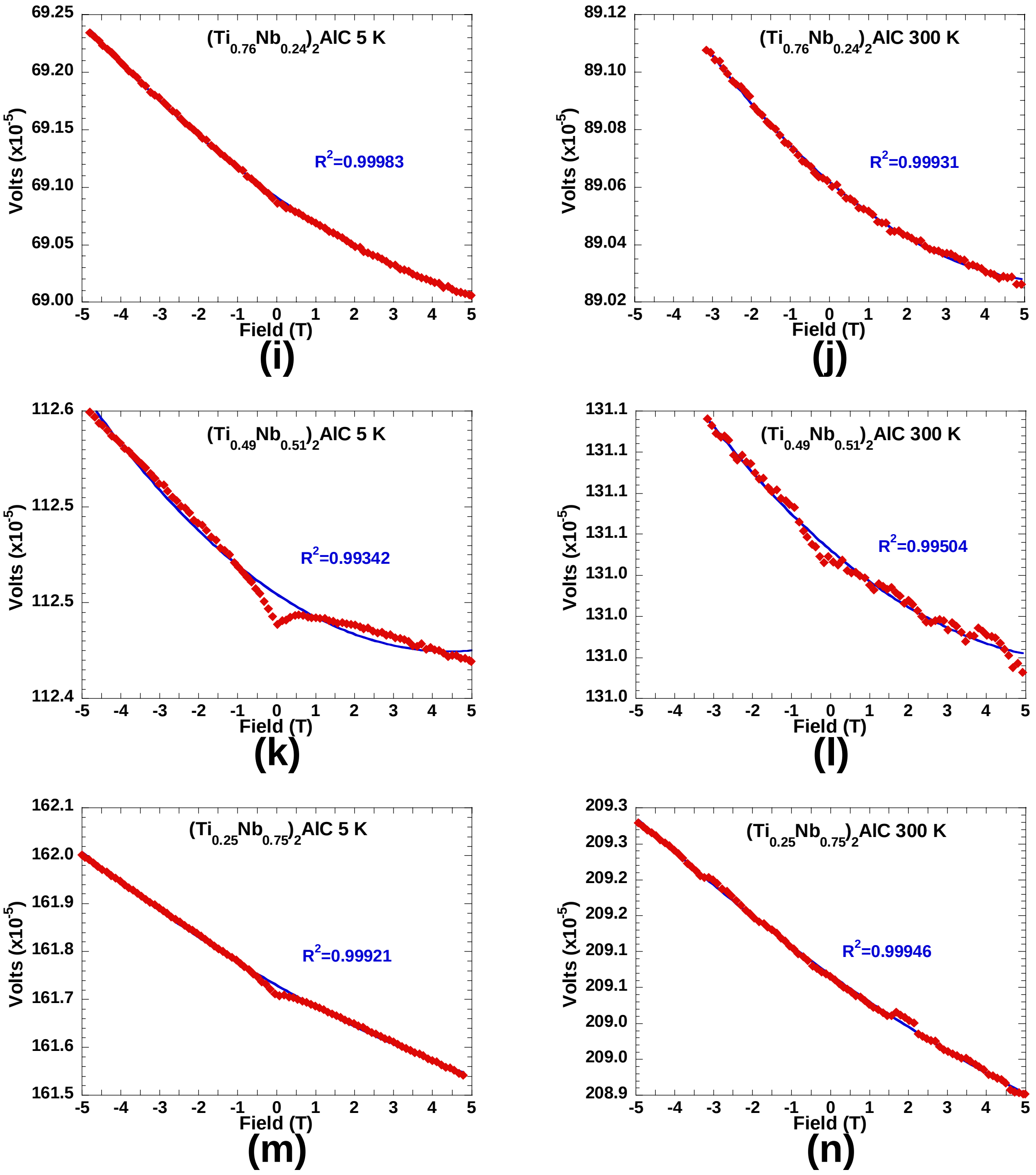

Figure C.1 Measured magnetotransport data showing quality of fit (R^2) to a second order polynomial for thin films of a) Ti_2AlC (875 °C) at 5 K, b) Ti_2AlC (875 °C) at 300 K, c) Nb_2AlC 90 nm 250 W carbon (900 °C) at 5 K, d) Nb_2AlC 90 nm 250 W carbon (900 °C) at 300 K, e) Nb_2AlC 270 nm (900 °C) at 5 K, f) Nb_2AlC 270 nm (900 °C) at 300 K, g) Nb_2AlC 90 nm 300 W carbon (900 °C) at 5 K, h) Nb_2AlC 90 nm 300 W carbon (900 °C) at 300 K, i) $(Ti_{0.76})Nb_{0.24})_2AlC$ (850 °C) at 5 K, j) $(Ti_{0.76})Nb_{0.24})_2AlC$ (850 °C) at 300 K, k) $(Ti_{0.49})Nb_{0.51})_2AlC$ (850 °C) at 5 K, l) $(Ti_{0.49})Nb_{0.51})_2AlC$ (850 °C) at 300 K, m) $(Ti_{0.25})Nb_{0.75})_2AlC$ (850 °C) at 5 K, n) $(Ti_{0.25})Nb_{0.75})_2AlC$ at 300 K. End-member films were deposited directly on Al_2O_3 while solid solutions were deposited on TiC, temperatures in parenthesis represent deposition temperature.

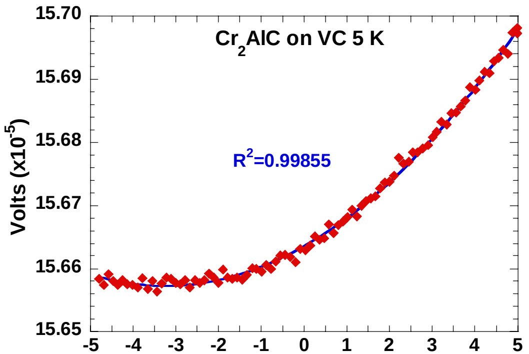
Cr$_2$AlC on VC 5 K
R^2=0.99855
Volts (x10^{-5})
15.70
15.69
15.68
15.67
15.66
15.65
-5 -4 -3 -2 -1 0 1 2 3 4 5
Field (T)

(a)

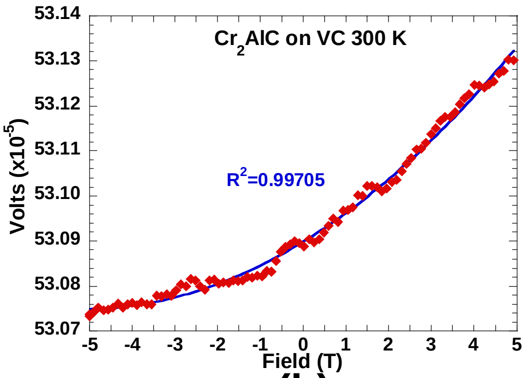
Cr$_2$AlC on VC 300 K
R^2=0.99705
Volts (x10^{-5})
53.14
53.13
53.12
53.11
53.10
53.09
53.08
53.07
-5 -4 -3 -2 -1 0 1 2 3 4 5
Field (T)

(b)

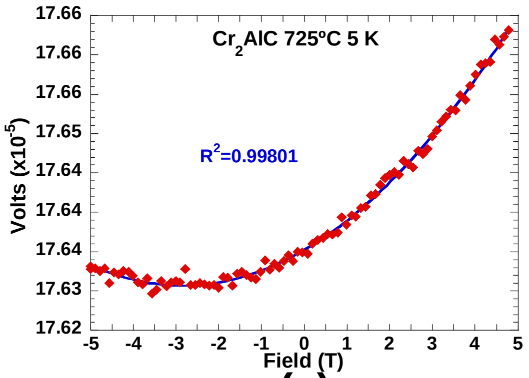
Cr$_2$AlC 725ºC 5 K
R^2=0.99801
Volts (x10^{-5})
17.66
17.66
17.66
17.65
17.64
17.64
17.64
17.63
17.62
-5 -4 -3 -2 -1 0 1 2 3 4 5
Field (T)

(c)

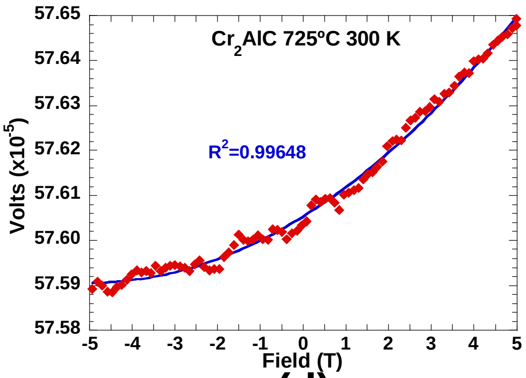
Cr$_2$AlC 725ºC 300 K
R^2=0.99648
Volts (x10^{-5})
57.65
57.64
57.63
57.62
57.61
57.60
57.59
57.58
-5 -4 -3 -2 -1 0 1 2 3 4 5
Field (T)

(d)

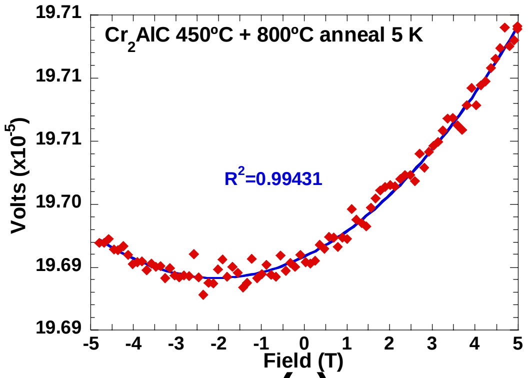
Cr$_2$AlC 450ºC + 800ºC anneal 5 K
R^2=0.99431
Volts (x10^{-5})
19.71
19.71
19.71
19.70
19.69
19.69
-5 -4 -3 -2 -1 0 1 2 3 4 5
Field (T)

(e)

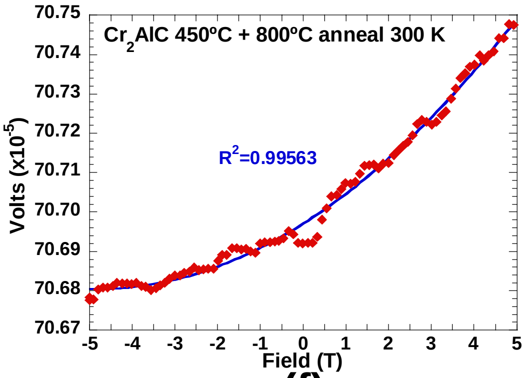
Cr$_2$AlC 450ºC + 800ºC anneal 300 K
R^2=0.99563
Volts (x10^{-5})
70.75
70.74
70.73
70.72
70.71
70.70
70.69
70.68
70.67
-5 -4 -3 -2 -1 0 1 2 3 4 5
Field (T)

(f)

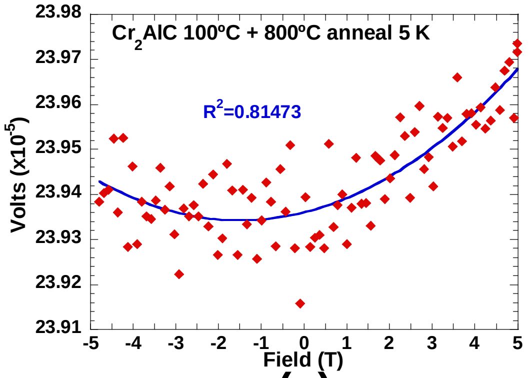
Cr$_2$AlC 100ºC + 800ºC anneal 5 K
R^2=0.81473
Volts (x10^{-5})
23.98
23.97
23.96
23.95
23.94
23.93
23.92
23.91
-5 -4 -3 -2 -1 0 1 2 3 4 5
Field (T)

(g)

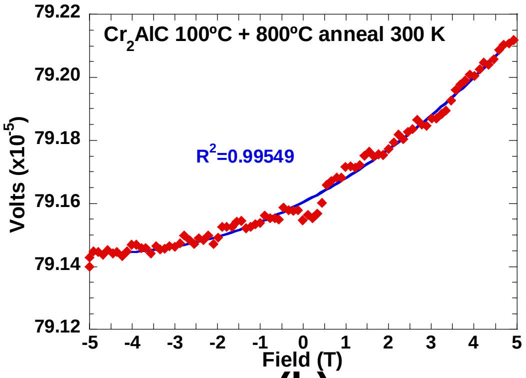
Cr$_2$AlC 100ºC + 800ºC anneal 300 K
R^2=0.99549
Volts (x10^{-5})
79.22
79.20
79.18
79.16
79.14
79.12
-5 -4 -3 -2 -1 0 1 2 3 4 5
Field (T)

(h)

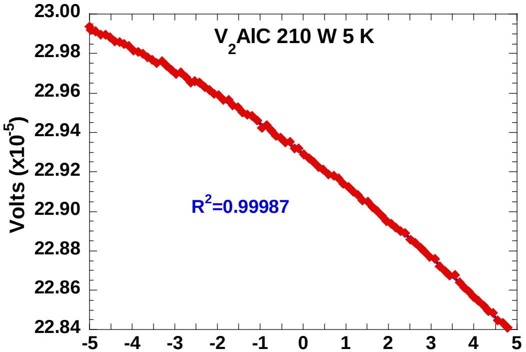
V_2AlC 210 W 5 K
R^2=0.99987
Volts (x10^{-5})
23.00
22.98
22.96
22.94
22.92
22.90
22.88
22.86
22.84
-5
-4
-3
-2
-1
0
1
2
3
4
5
Field (T)

(i)

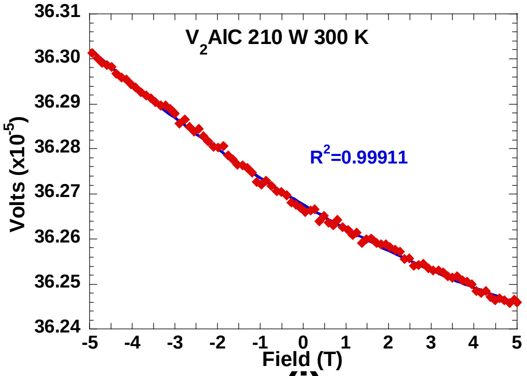
V_2AlC 210 W 300 K
R^2=0.99911
Volts (x10^{-5})
36.31
36.30
36.29
36.28
36.27
36.26
36.25
36.24
-5
-4
-3
-2
-1
0
1
2
3
4
5
Field (T)

(j)

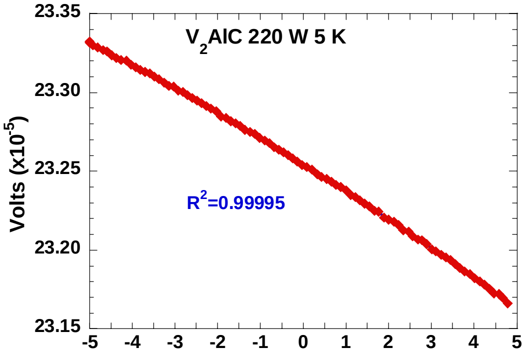
V_2AlC 220 W 5 K
R^2=0.99995
Volts (x10^{-5})
23.35
23.30
23.25
23.20
23.15
-5
-4
-3
-2
-1
0
1
2
3
4
5
Field (T)

(k)

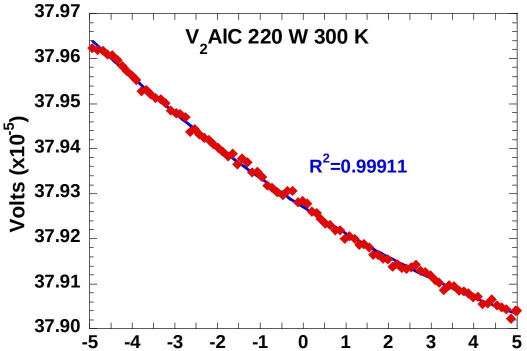
V_2AlC 220 W 300 K
R^2=0.99911
Volts (x10^{-5})
37.97
37.96
37.95
37.94
37.93
37.92
37.91
37.90
-5
-4
-3
-2
-1
0
1
2
3
4
5
Field (T)

(l)

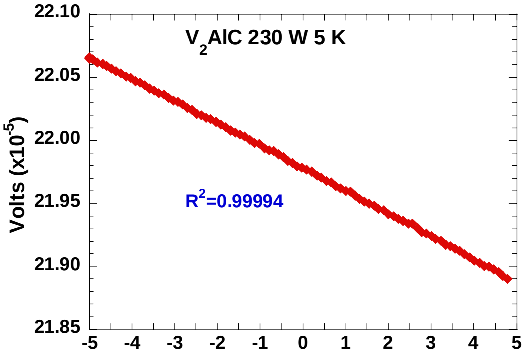
V_2AlC 230 W 5 K
R^2=0.99994
Volts (x10^{-5})
22.10
22.05
22.00
21.95
21.90
21.85
-5
-4
-3
-2
-1
0
1
2
3
4
5
Field (T)

(m)

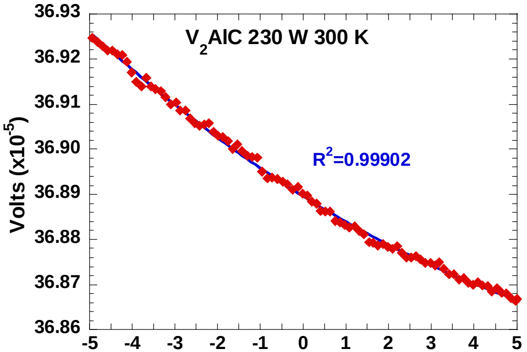
V_2AlC 230 W 300 K
R^2=0.99902
Volts (x10^{-5})
36.93
36.92
36.91
36.90
36.89
36.88
36.87
36.86
-5
-4
-3
-2
-1
0
1
2
3
4
5
Field (T)

(n)

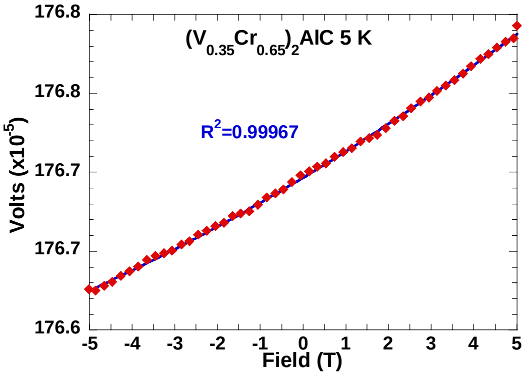
$(V_{0.35}Cr_{0.65})_2AlC$ 5 K
R^2=0.99967
Volts (x10^{-5})
176.8
176.8
176.7
176.7
176.6
-5
-4
-3
-2
-1
0
1
2
3
4
5
Field (T)

(o)

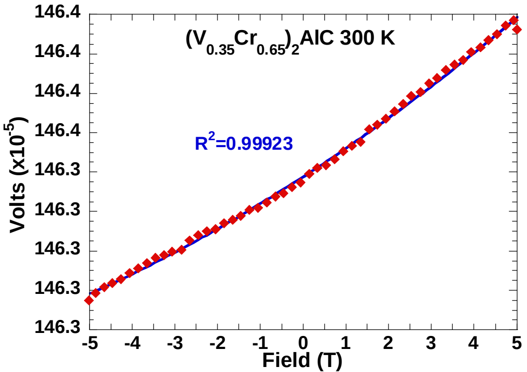
$(V_{0.35}Cr_{0.65})_2AlC$ 300 K
R^2=0.99923
Volts (x10^{-5})
146.4
146.4
146.4
146.4
146.3
146.3
146.3
146.3
146.3
-5
-4
-3
-2
-1
0
1
2
3
4
5
Field (T)

(p)

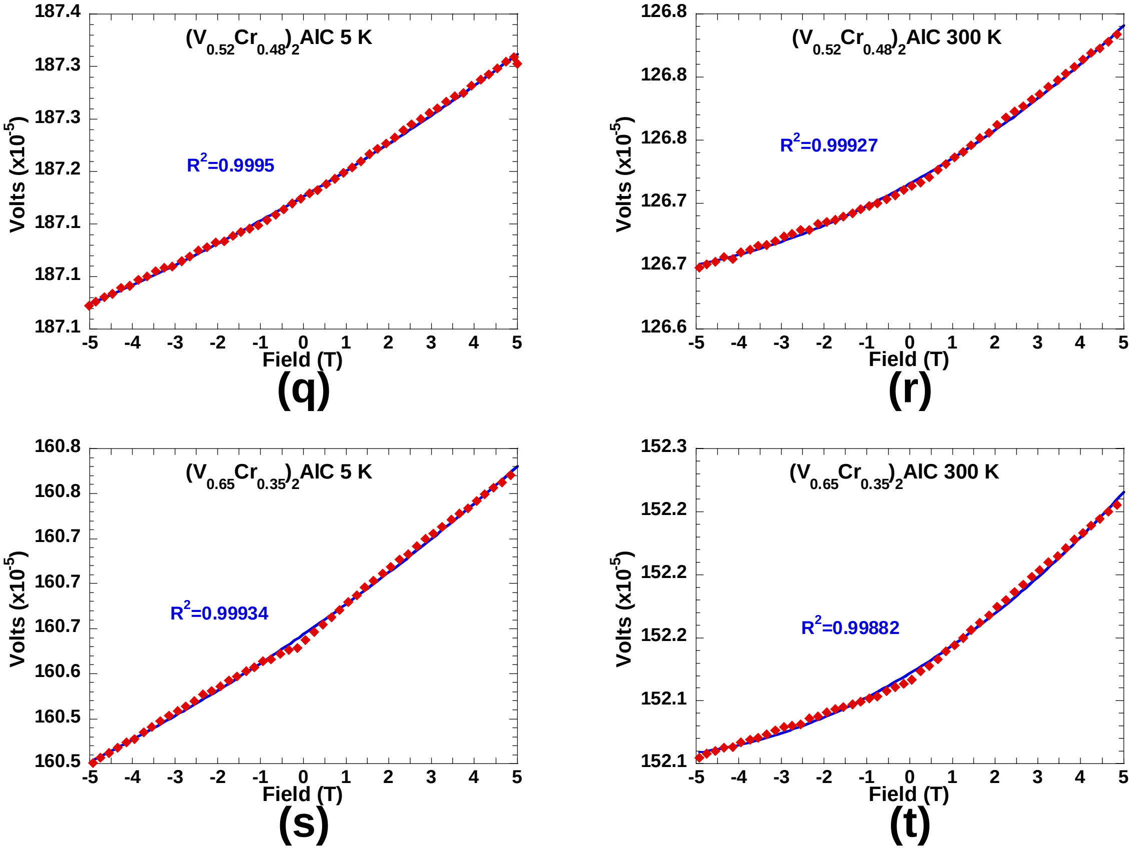

(q) (r)

(s) (t)

Figure C.2 Measured magnetotransport data showing quality of fit (R^2) to a second order polynomial for thin films of a) Cr_2AlC on VC (850 °C) at 5 K, b) Cr_2AlC on VC (850 °C) at 300 K, c) Cr_2AlC (725 °C) at 5 K, d) Cr_2AlC (725 °C) at 300 K, e) Cr_2AlC (450 °C annealed at 800 °C) at 5 K, f) Cr_2AlC (450 °C annealed at 800 °C) at 300 K, g) Cr_2AlC (100 °C annealed at 800 °C) at 5 K, h) Cr_2AlC (100 °C annealed at 800 °C) at 300 K, i) V_2AlC 210 W carbon (900 °C) at 5 K, j) V_2AlC 210 W carbon (900 °C) at 300 K, k) V_2AlC 220 W carbon (900 °C) at 5 K, l) V_2AlC 220 W carbon (900 °C) at 300 K, m) V_2AlC 230 W carbon (900 °C) at 5 K, n) V_2AlC 230 W carbon (900 °C) at 300 K, o) $(V_{0.35}Cr_{0.65})_2AlC$ (850 °C) at 5 K, p) $(V_{0.35}Cr_{0.65})_2AlC$ (850 °C) at 300 K, q) $(V_{0.52}Cr_{0.48})_2AlC$ (850 °C) at 5 K, r) $(V_{0.52}Cr_{0.48})_2AlC$ (850 °C) at 300 K, s) $(V_{0.65}Cr_{0.35})_2AlC$ (850 °C) at 5 K, t) $(V_{0.65}Cr_{0.35})_2AlC$ (850 °C) at 300 K. All films were deposited directly on Al_2O_3 unless specified otherwise, temperatures in parenthesis represent deposition temperature.

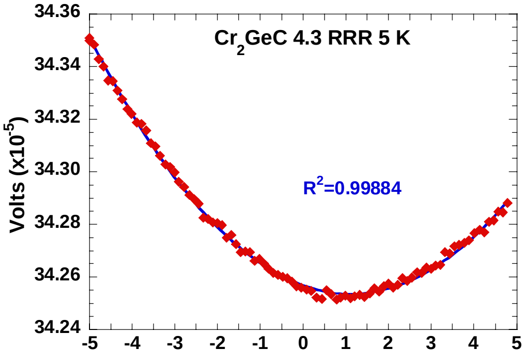
Cr$_2$GeC 4.3 RRR 5 K
R^2=0.99884
Volts (x10^{-5})
34.36
34.34
34.32
34.30
34.28
34.26
34.24
Field (T)
-5 -4 -3 -2 -1 0 1 2 3 4 5

(a)

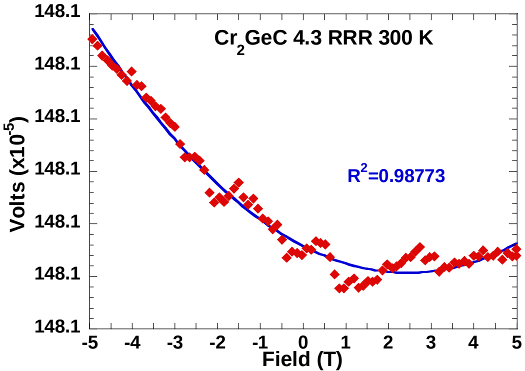
Cr$_2$GeC 4.3 RRR 300 K
R^2=0.98773
Volts (x10^{-5})
148.1
148.1
148.1
148.1
148.1
148.1
148.1
Field (T)
-5 -4 -3 -2 -1 0 1 2 3 4 5

(b)

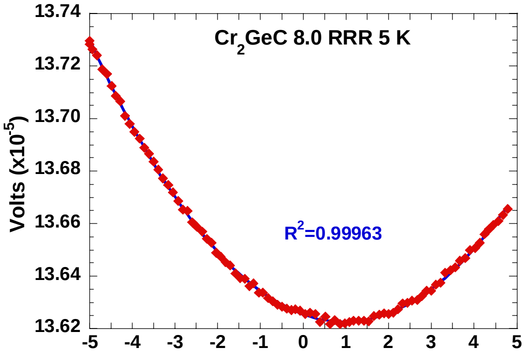
Cr$_2$GeC 8.0 RRR 5 K
R^2=0.99963
Volts (x10^{-5})
13.74
13.72
13.70
13.68
13.66
13.64
13.62
Field (T)
-5 -4 -3 -2 -1 0 1 2 3 4 5

(c)

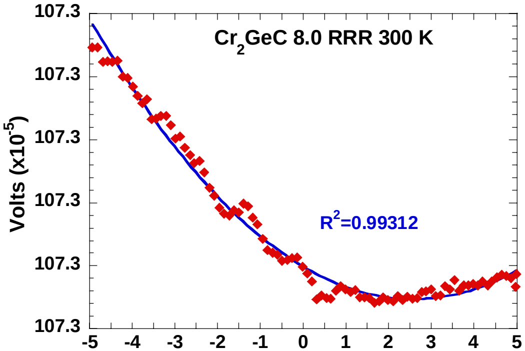
Cr$_2$GeC 8.0 RRR 300 K
R^2=0.99312
Volts (x10^{-5})
107.3
107.3
107.3
107.3
107.3
107.3
Field (T)
-5 -4 -3 -2 -1 0 1 2 3 4 5

(d)

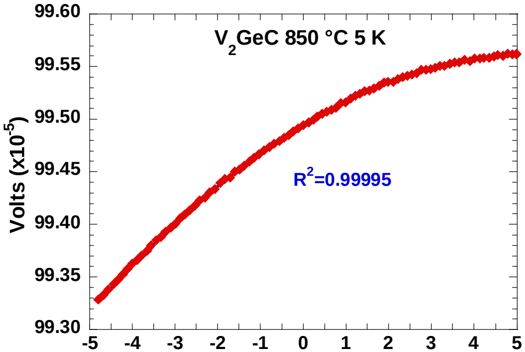
V$_2$GeC 850 °C 5 K
R^2=0.99995
Volts (x10^{-5})
99.60
99.55
99.50
99.45
99.40
99.35
99.30
Field (T)
-5 -4 -3 -2 -1 0 1 2 3 4 5

(e)

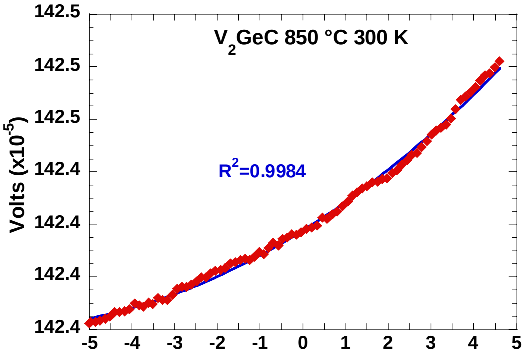
V$_2$GeC 850 °C 300 K
R^2=0.9984
Volts (x10^{-5})
142.5
142.5
142.5
142.4
142.4
142.4
142.4
Field (T)
-5 -4 -3 -2 -1 0 1 2 3 4 5

(f)

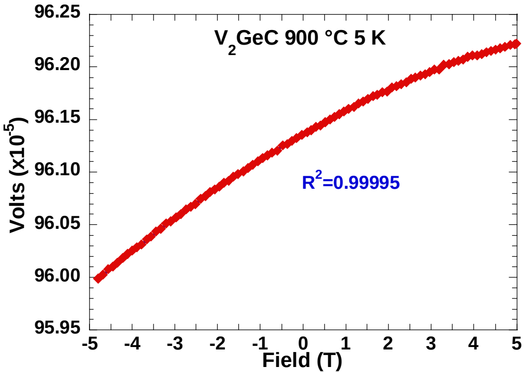
V$_2$GeC 900 °C 5 K
R^2=0.99995
Volts (x10^{-5})
96.25
96.20
96.15
96.10
96.05
96.00
95.95
Field (T)
-5 -4 -3 -2 -1 0 1 2 3 4 5

(g)

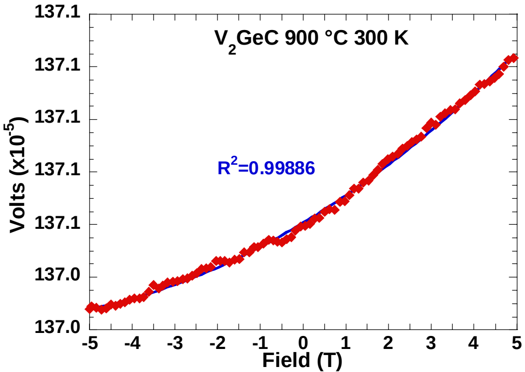
V$_2$GeC 900 °C 300 K
R^2=0.99886
Volts (x10^{-5})
137.1
137.1
137.1
137.1
137.1
137.0
137.0
Field (T)
-5 -4 -3 -2 -1 0 1 2 3 4 5

(h)

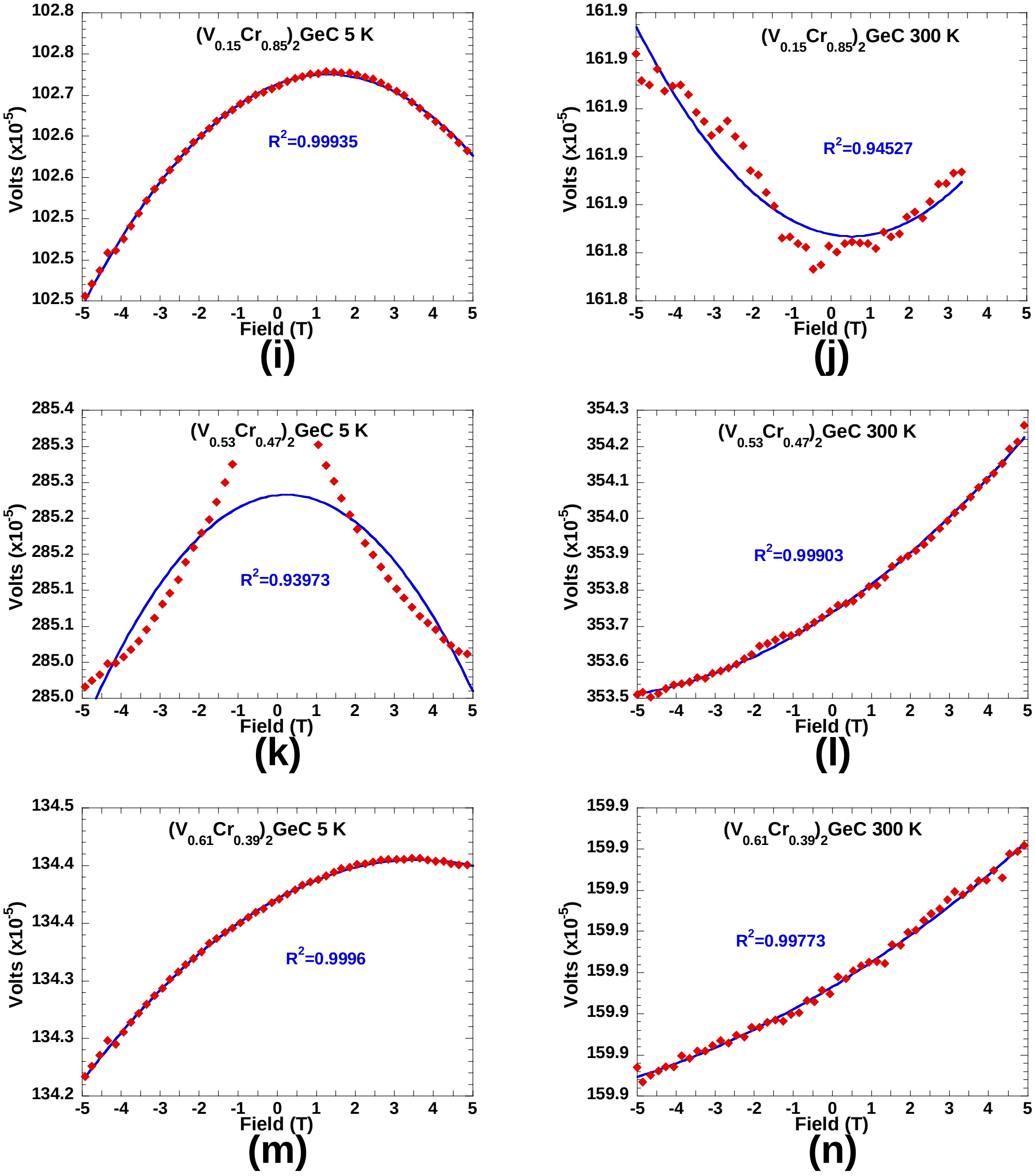

Figure C.3 Measured magnetotransport data showing quality of fit (R^2) to a second order polynomial for thin films of a) Cr_2GeC 4.3 RRR (900 °C) at 5 K, b) Cr_2GeC 4.3 RRR (900 °C) at 300 K, c) Cr_2GeC 8.0 RRR (900 °C) at 5 K, d) Cr_2GeC 8.0 RRR (900 °C) at 300 K, e) V_2GeC (850 °C) at 5 K, f) V_2GeC (850 °C) at 300 K, g) V_2GeC (900 °C) at 5 K, h) V_2GeC (900 °C) at 300 K, i) $(V_{0.15}Cr_{0.85})_2GeC$ (850 °C) at 5 K, j) $(V_{0.15}Cr_{0.85})_2GeC$ (850 °C) at 300 K, k) $(V_{0.53}Cr_{0.47})_2GeC$ (850 °C) at 5 K, l) $(V_{0.53}Cr_{0.47})_2GeC$ (850 °C) at 300 K, m) $(V_{0.61}Cr_{0.39})_2GeC$ (850 °C) at 5 K, n) $(V_{0.61}Cr_{0.39})_2GeC$ (850 °C) at 300 K. All films were deposited directly on Al_2O_3 unless specified otherwise, temperatures in parenthesis represent deposition temperature.

APPLIED PHYSICS LETTERS **95**, 101907 (2009)

Combinatorial investigation of $(Ti_{1-x}Nb_x)_2AlC$

T. H. Scabarozi,[1,2] C. Gennaoui,[1] J. Roche,[1] T. Flemming,[1] K. Wittenberger,[1] P. Hann,[1]
B. Adamson,[1] A. Rosenfeld,[1] M. W. Barsoum,[2] J. D. Hettinger,[1] and S. E. Lofland[1,a)]
[1]*Department of Physics and Astronomy, Rowan University, Glassboro, New Jersey 08028, USA*
[2]*Department of Materials Science and Engineering, Drexel University, Philadelphia 19104, USA*

(Received 27 May 2009; accepted 29 July 2009; published online 9 September 2009)

We have synthesized thin films of $(Ti_{1-x}Nb_x)_2AlC$ by combinatorial method on TiC (111) seed layers grown on *c*-axis sapphire (Al_2O_3) substrates at 900 °C using magnetron sputter. X-ray diffraction showed the films to be *c*-axis oriented and epitaxial, and films contained a minor secondary phase of (Ti,Nb)C, irrespective of stoichiometry. Most notably, Raman spectroscopy suggest a sizable increase in the elastic modulus in the Nb-rich region as compared to either of the end members. *© 2009 American Institute of Physics*. [doi:10.1063/1.3207748]

MAX phases are a group of ternary compounds with a general composition of $M_{n+1}AX_n$ ($n=1$, 2, or 3), where M is a transition metal, A is an A-group element, and X is carbon or nitrogen. There currently are more than 50 distinct *MAX* phases synthesized in bulk,[1] with much of the interest in these refractory compounds due to their machinability and reasonably large stiffness.[2–4] With low friction and oxidation resistance,[1] these materials are possible candidates for protective coatings. However, much remains unknown about these materials in regards to the properties of solid solutions. Thus far, studies in bulk have been limited to $(Nb_{0.5}Ti_{0.5})AlC$,[5] $(V_{0.5}Ti_{0.5})AlC$,[6] $(Ti_{0.5}Hf_{0.5})InC$,[5] $(Ti_{0.5}Zr_{0.5})InC$,[7] $Ti_2Al(C_{0.5}N_{0.5})$,[8] $Ti_3Al(C_{0.5}N_{0.5})$,[9] $Ti_3(Si,Ge)C_2$,[10] $Ti_3(Si,Al)C_2$,[11] $Ti_3Al_{0.8}Sn_{0.2}C_2$,[9] and Cr–V–Al–C.[12] There has been no report on solid solutions of *MAX* phase thin films, especially since only a few of the phases have ever been made into thin films. Only one combinatorial study has been reported so far, that being in the Cr–Al–C system.[13] In that study the authors determined the compositional range for the formation of Cr_2AlC. In this paper we report on a pseudoternary combinatorial investigation of $(Ti,Nb)_2AlC$ thin films and identify a region with enhanced elastic stiffness.

Thin films of $(Ti_{1-x}Nb_x)_2AlC$ were deposited in a custom-built ultrahigh vacuum magnetron sputtering chamber. The system has a rotating table with two 2 in. cathodes positioned directly over the substrate and two offset 1 in. cathodes to create a compositional gradient. The substrate rotation rate was approximately 18 rpm with a substrate-cathode distance of 10 cm. The substrate temperature was determined by optical pyrometer which was calibrated with a thermocouple. All depositions were performed on ∅50.8 mm (0001) oriented epi-polished sapphire (Al_2O_3) wafers and Si wafers of approximately 1×5 cm^2. Prior to deposition, a base pressure of 5×10^{-8} Torr was obtained. In order to facilitate growth, 20 nm buffer layers of TiC (111) were deposited at a substrate temperature of 700 °C in high-purity argon (99.999%) at 50 SCCM (SCCM denotes standard cubic centimeter per minute) and 10 mTorr. Following deposition of the buffer layer, the substrate temperature was ramped to 900 °C at 25 °C/min and held for 15 min. Ti–Nb–Al–C depositions were then performed for 60 min with an average deposition rate of 200 nm/h.

X-ray diffraction (XRD) was performed on a Scintag X_2 configured in standard θ-θ Bragg–Bretano geometry utilizing Cu $K\alpha$ radiation ϕ scans were measured with a Bruker D8 4-circle diffractometer utilizing Cu $K\alpha$ radiation. Electron microscopy and chemical composition were performed with a LEO 1530VP scanning electron microscope, equipped with an EDAX energy dispersive spectrometer (EDS) operating with an accelerating voltage of 11 kV. The films grown on Si were used to measure the $M:A$ ratio. The carbon content was determined via a process described earlier[14] and checked with a Rigaku Primus ZSX2 wavelength dispersive x-ray fluorescence spectrometer using bulk ternary carbide standards. Atomic force microscopy (AFM) was performed with a JEOL 5200 scanning probe microscope in both contact and noncontact modes. Friction was measured with a spherical tip (10 μm radius) on a Hysitron Triboscope used with the JEOL 5200. For each sample, measurements were performed in multiple locations under loads of up to 1000 μN.

Raman spectra were taken at room temperature with a Renishaw 2000 spectrometer with either an Ar-ion laser (514.5 nm) or HeNe laser (633 nm). Spectra were collected in static mode over five accumulations with a 60 s exposure time. Experimental peak positions were calculated through Lorentzian fitting with a system resolution of 2 cm^{-1}.

EDS measurements showed that $(Ti_{1-x}Nb_x)_2AlC$ was deposited for x ranging from 0.03–0.96 while the $M:A$ ratio was maintained between 1.9 and 2.1. XRD results (Fig. 1) clearly show (00*l*) *MAX* phase peaks along with the initial TiC buffer layer and a secondary phase of (Ti,Nb)C (111). It is well established that Ti-based *MAX* phase films usually require a buffer layer to facilitate growth,[15–18] although other materials in the family like Nb_2AlC (Ref. 14) and V_2GeC (Ref. 18) grow better directly on sapphire. However, it is to be noted that Nb_2AlC (Ref. 14) and V_2GeC (Ref. 18) films always showed secondary phases regardless of film chemistry, similar to the pseudobinary carbide (Ti,Nb)C found in the present films. It is interesting that the introduction of Ti in Nb_2AlC leads to the formation of the pseudobinary carbide over the $Nb_5Al_3C_x$ found in the parent phase.[14] This is presumably related to the fact that $Nb_5Al_3C_x$ is a metastable phase.

ϕ scans, not shown, confirmed that the films were epitaxial. Figure 2 shows the *c*-axis lattice constant as a function

---

[a)]Electronic mail: lofland@rowan.edu.

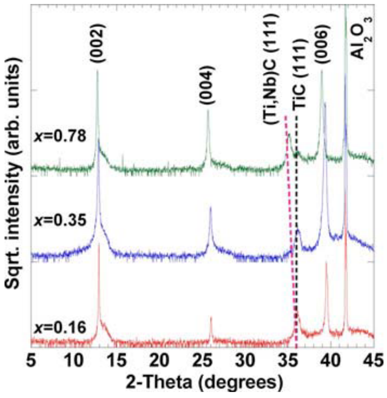

FIG. 1. (Color online) XRD patterns for different compositions of $(Ti,Nb)_2AlC$ thin films grown on TiC (111) seed layers show textured growth in the (001) orientation. A minor secondary phase of (Ti,Nb)C was observed in most films.

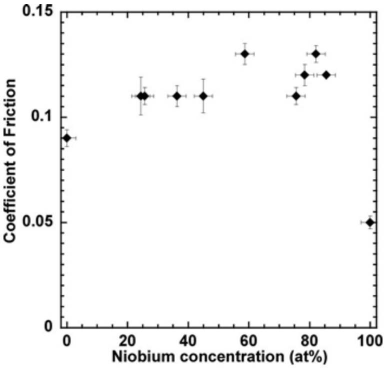

FIG. 3. Coefficient of friction as a function of Nb concentration. Overall the friction does not appear to be affected by substitution.

of x and the observed linear relation agrees with Vegard's law and confirms solubility across the entire range. A slight increase in lattice constant over the bulk value results from the compressive stress of the substrate based on the surface reconstruction of sapphire.[19]

AFM results indicated that the films were relatively rough, with root mean square roughness of up to 50 nm; however, the grain size was effectively independent of composition, averaging around 500 nm. Results of friction testing are shown in Fig. 3. The friction coefficients are all reasonably small (<0.14) with an average value of ~ 0.1, although Nb_2AlC clearly had the lowest friction. In all cases, the coefficients were independent of load. Not surprisingly, the friction was largest for the roughest samples. The present values are significantly larger than those reported for the basal plane of bulk Ti_3SiC_2 (Ref. 20) but are commensurate with the value of 0.1 found by Emmerlich *et al.*[21] in films of Ti_3SiC_2.

Selected Raman spectra are shown in Fig. 4. There are four first order modes in the M_2AX family,[22] three of which were generally observed in the present films. The lower and middle modes, ω_A and ω_B, have been attributed to longitudinal modes in the basal plane and the upper mode, ω_C, to a longitudinal mode along the c axis. The disappearance of the modes is likely directly attributable to increased Raman linewidth, indicative of mixing at the M site. Surprisingly, the observed modes did not show monotonic changes with x, but actually ω_C had a maximum near $x \sim 0.75$.

At a very simple level the elastic modulus $E \sim M\omega^2/V^{1/3}$, where M is the reduced mass of the mode, ω a characteristic phonon frequency, and V the unit cell volume. In each of the four Raman modes, the C atoms do not participate so $M = 1/2(M_A + 2M_M)$, where M_A is the mass of the A-group atom and M_M that of the transition metal. The change in cell volume is only a few percent between the two end members,[23] and this approximation yields the modulus of $Nb_2AlC \sim$ that of Ti_2AlC, as expected. For the solid solution, this approximation leads to hardening, with E for $x = 0.75$ nearly twice that of the end members. The present results are in contrast to substitution on the A-group which led to some softening[10,24,25] and X which had some hardening.[26,27]

In conclusion, solid solutions of $(Ti_{1-x}Nb_x)_2AlC$ thin films were synthesized by combinatorial methods by magnetron sputtering. XRD showed that solid solution mixing took place and that films were c-axis oriented and epitaxial to the substrate, although all films contained a minor secondary phase of (Ti,Nb)C. Raman spectroscopy suggests significant solid solution hardening, indicating that for refractory structural applications, $Ti_{0.25}Nb_{0.75}Al_2C$ is a better choice than either parent compound.

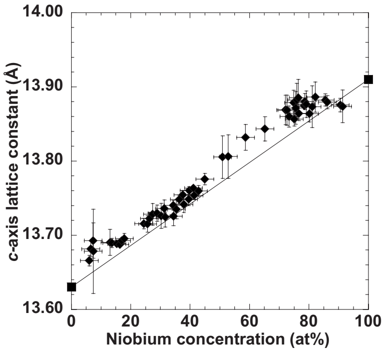

FIG. 2. c-axis lattice constant of $(Ti,Nb)_2AlC$ as a function of Nb concentration. The end points are the bulk values. No miscibility gap is observed.

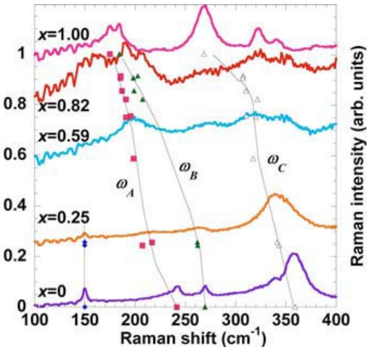

FIG. 4. (Color online) Raman spectra for various thin films of $(Ti,Nb)_2AlC$. Markers indicate the positions of vibrational modes as a function of Nb concentration. The lines serve as a guide for the eye.

This work was supported by NSF Grant No. DMR 0503711 and MRI Grant No. 082416.

[1] M. W. Barsoum, Prog. Solid State Chem. **28**, 201 (2000).

[2] S. E. Lofland, J. D. Hettinger, K. Harrell, P. Finkel, S. Gupta, M. W. Barsoum, and G. Hug, Appl. Phys. Lett. **84**, 508 (2004).

[3] B. Manoun, S. Saxena, and M. Barsoum, Appl. Phys. Lett. **86**, 101906 (2005).

[4] B. Manoun, S. Saxena, T. El-Raghy, and M. Barsoum, Appl. Phys. Lett. **88**, 201902 (2006).

[5] M. W. Barsoum, I. Salama, T. El-Raghy, J. Golczewski, W. D. Porter, H. Wang, H. J. Seifert, and F. Aldinger, Metall. Mater. Trans. A **33**, 2775 (2002).

[6] S. Gupta and M. W. Barsoum, J. Electrochem. Soc. **151**, D24 (2004).

[7] S. Gupta, E. N. Hoffman, and M. W. Barsoum, J. Alloys Compd. **426**, 168 (2006).

[8] M. W. Barsoum, M. Ali, and T. El-Raghy, Metall. Mater. Trans. A **31A**, 1857 (2000).

[9] B. Manoun, S. K. Saxena, G. Hug, A. Ganguly, E. N. Hoffman, and M. W. Barsoum, J. Appl. Phys. **101**, 113523 (2007).

[10] A. Ganguly, T. Zhen, and M. W. Barsoum, J. Alloys Compd. **376**, 287 (2004).

[11] M. Radovic, A. Ganguly, M. W. Barsoum, T. Zhen, P. Finkel, S. R. Kalidindi, and E. Lara-Curzio, Acta Mater. **54**, 2757 (2006).

[12] Y. Zhou, F. Meng, and J. Zhang, J. Am. Ceram. Soc. **91**, 1357 (2008).

[13] R. Mertens, Z. Sun, D. Music, and J. M. Schneider, Adv. Eng. Mater. **6**, 903 (2004).

[14] T. H. Scabarozi, S. E. Lofland, J. D. Hettinger, J. Roche, A. Rosenfeld, S. H. Lim, L. Salamanca-Riba, and M. W. Barsoum, Thin Solid Films **517**, 2920 (2009).

[15] J. P. Palmquist, U. Jansson, T. Seppanen, P. O. A. Persson, J. Birch, L. Hultman, and P. Isberg, Appl. Phys. Lett. **81**, 835 (2002).

[16] H. Högberg, L. Hultman, J. Emmerlich, T. Joelsson, P. Eklund, J. M. Molina-Aldareguia, J. P. Palmquist, O. Wilhelmsson, and U. Jansson, Surf. Coat. Technol. **193**, 6 (2005).

[17] J. Emmerlich, J.-P. Palmquist, H. Hogberg, J. M. Molina-Aldareguia, Z. Czigany, P. O. Persson, U. Jansson, and L. Hultman, J. Appl. Phys. **96**, 4817 (2004).

[18] O. Wilhelmsson, P. Eklund, H. Högberg, L. Hultman, and U. Jansson, Acta Mater. **56**, 2563 (2008).

[19] G. Renaud, Surf. Sci. Rep. **32**, 5 (1998).

[20] S. Myhra, J. W. B. Summers, and E. H. Kisi, Mater. Lett. **39**, 6 (1999).

[21] J. Emmerlich, G. Gassner, P. Eklund, H. Hogberg, and L. Hultman, Wear **264**, 914 (2008).

[22] J. E. Spanier, S. Gupta, M. Am, and M. W. Barsoum, Phys. Rev. B **71**, 012103 (2005).

[23] T. H. Scabarozi, S. Amini, O. D. Leaffer, A. Ganguly, S. Gupta, W. Tambussi, S. Clipper, J. E. Spanier, M. W. Barsoum, J. D. Hettinger, and S. E. Lofland, J. Appl. Phys. **105**, 013543 (2009).

[24] P. Finkel, B. Seaman, K. Harrell, J. Palma, J. D. Hettinger, S. E. Lofland, A. Ganguly, M. W. Barsoum, Z. Sun, L. Sa, and R. Ahuja, Phys. Rev. B **70**, 085104 (2004).

[25] B. Manoun, H. P. Liermann, R. P. Gulve, S. K. Saxena, A. Ganguly, M. W. Barsoum, and C. S. Zha, Appl. Phys. Lett. **84**, 2799 (2004).

[26] M. Radovic, A. Ganguly, and M. W. Barsoum, J. Mater. Res. **23**, 1517 (2008).

[27] T. Scabarozi, A. Ganguly, J. D. Hettinger, S. E. Lofland, S. Amini, P. Finkel, T. El-Raghy, and M. W. Barsoum, J. Appl. Phys. **104**, 073713 (2008).

Thin Solid Films 517 (2009) 2920–2923

Contents lists available at ScienceDirect

Thin Solid Films

journal homepage: www.elsevier.com/locate/tsf

Synthesis and characterization of Nb_2AlC thin films

T.H. Scabarozi [a,b], J. Roche [a], A. Rosenfeld [a], S.H. Lim [c], L. Salamanca-Riba [c], G. Yong [d], I. Takeuchi [c], M.W. Barsoum [b], J.D. Hettinger [a], S.E. Lofland [a,*]

[a] *Department of Physics and Astronomy, Rowan University, Glassboro, NJ 08028, USA*
[b] *Department of Materials Science and Engineering, Drexel University, Philadelphia, PA 19104, USA*
[c] *Department of Materials Science and Engineering, University of Maryland, College Park, MD 20742, USA*
[d] *Department of Physics and Astronomy, Towson University,Towson, MD 21252, USA*

ARTICLE INFO

Article history:
Received 6 June 2008
Received in revised form 6 December 2008
Accepted 17 December 2008
Available online 31 December 2008

Keywords:
Carbides
Sputtering
Superconductivity

ABSTRACT

We report on the synthesis and characterization of epitaxial *c*-axis oriented Nb_2AlC thin films deposited on *c*-axis sapphire (Al_2O_3) substrates by magnetron sputtering. Selected area electron diffraction reveal that independent of substrate temperature or film stoichiometry, there is the growth of a secondary phase not found in bulk, $Nb_5Al_3C_x$ with *a*- and *c*-axis lattice constants of 7.746 Å and 5.246 Å, respectively. Scanning electron micrographs reveal large surface features, many with hexagonal shape and faceted texture. Atomic force microscopy topographical measurements indicate a surface roughness of approximately 15% of the total film thickness. Electrical transport measurements show typical metal-like conduction with a room temperature resistivity of ≈0.9 μΩ-m and a residual resistivity ratio of 2.5. A superconducting transition was found at ≈440 mK.

1. Introduction

Ternary carbides and nitrides that follow the $M_{n+1}AX_n$ chemistry ($n=1$, 2 or 3), where M is a transition metal, A is an A-group element, and X is carbon and/or nitrogen, have drawn recent interest because of their unusual and sometimes unique properties [1–3]. These include high electrical and thermal conductivities and low coefficients of friction. The hexagonal structure consists of $M_{n+1}X_n$ layers interleaved by layers of the A-group element. The unusual combination of properties of these materials makes them candidates for applications, such as electronic contacts and protective coatings that require synthesis in thin-film form.

Growth of epitaxial MAX-phase films is becoming a mature area of research as demonstrated by the numerous publications on the synthesis and characterization of these films [4–9]. Oriented thin films should also provide insight to anisotropic properties of the material when compared directly to their bulk polycrystalline counterparts. Recent results have demonstrated that the anisotropy in the physical properties is not as large as expected and that low defect-concentration films have high charge mobilities that sometimes reveal new physics [10].

2. Experimental

Thin films were deposited in a custom built ultra-high vacuum magnetron sputtering chamber. Three magnetron cathodes housed individual two-inch elemental targets, which were about ~7 cm above the substrate. At deposition temperature, a base pressure of 5×10^{-8} Torr was achieved prior to each deposition. Films were deposited by radio-frequency sputtering in a sputtering grade Ar (99.9995%) atmosphere (50 sccm) at pressures ranging from 4–18 mTorr.

Substrates of MgO (111), Si (100), *c*- (00 l) and *r*-plane (012) sapphire (Al_2O_3), and polycrystalline Al_2O_3, were cleaned in acetone and methanol in an ultrasonic cleaner for 5 min prior to their placement in the chamber. Films were deposited in the temperature range of 700–1000 °C as determined by optical pyrometry. The substrate temperature was ramped at a rate of 35 °C/min to the desired temperature, where it was held for a minimum of 0.5 h prior to deposition. Films were deposited for 10–80 min at a deposition rate of ~7 nm/min.

Two-theta X-ray diffraction (XRD) was carried out with a Scintag X_2 diffractometer utilizing Cu-Kα radiation. 4-circle XRD was performed on a Bruker D8 Discover diffractometer utilizing Cu-Kα radiation. A JEOL JEM-2100F high-resolution field-emission transmission electron microscope (HRTEM) operating at 200 kV was used to investigate the interfaces and microstructure. Surface morphology and topography was investigated by scanning electron microscopy (SEM) with a LEO 1530VP field-emission microscope operating at 11 kV and by atomic force microscopy (AFM) with a JEOL SPM-5200 using a 10 nm diameter tip in both contact and non-contact modes with resonant frequencies of 25 and 300 kHz, respectively. Chemical analysis was performed by energy dispersive X-ray spectroscopy (EDS) with an EDAX Genesis detector on the SEM. Due to limitations of EDS only the Nb and Al elements were quantifiable.

Raman spectra were taken at room temperature with a Renishaw 2000 spectrometer with either an Ar-ion laser (514.5 nm) or HeNe laser

---

[*] Corresponding author.
E-mail address: lofland@rowan.edu (S.E. Lofland).

0040-6090/$ – see front matter © 2009 Elsevier B.V. All rights reserved.
doi:10.1016/j.tsf.2008.12.047

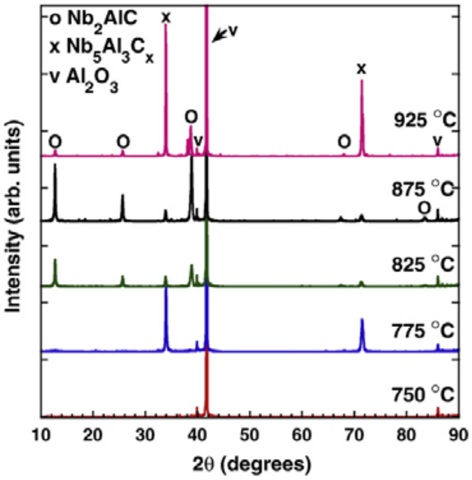

Fig. 1. X-ray diffraction pattern of Nb–Al–C films grown at various temperatures on *c*-axis sapphire. Curves are offset for clarity.

(633 nm). Spectra were collected in static mode over five accumulations with a 60-s exposure time for each accumulation. Experimental peak positions were calculated through Lorentzian fitting with a system resolution of 2 cm^{-1}.

Electrical transport measurements were carried out on 400-μm wide by 1.6-mm long microbridges that were defined by standard photolithographic techniques, followed by acid wet etch in $1HF+1HNO_3+1H_2O$. The resistivity was measured as a function of temperature T for $0.4\ K \leq T \leq 300\ K$ range with a Quantum Design Physical Properties Measurement System by a four-probe technique. The details of this experimental procedure can be found elsewhere [10–14].

3. Results and discussion

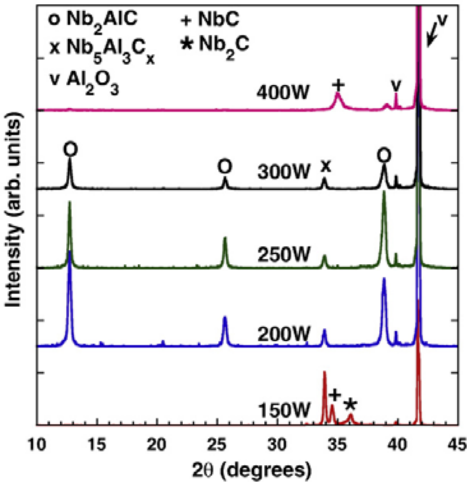

Fig. 2. X-ray diffraction patterns of films deposited at various carbon powers. Curves are offset for clarity.

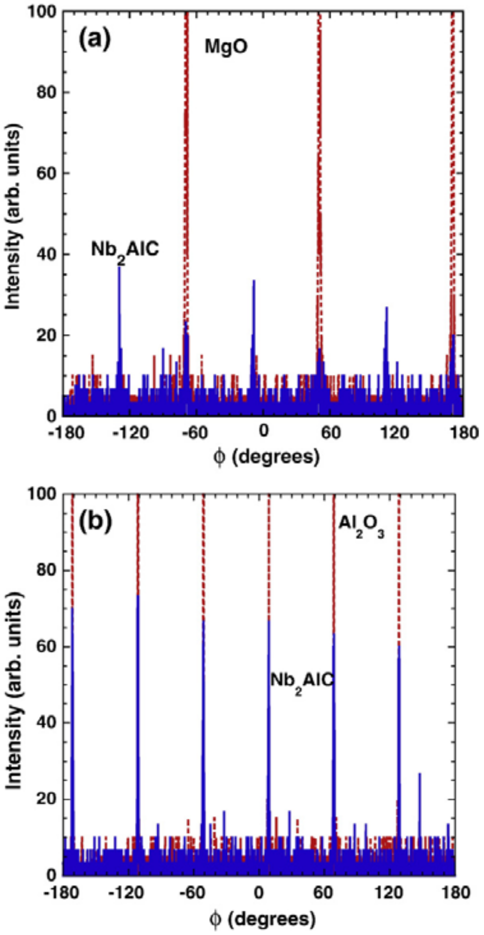

Fig. 3. ϕ scan of (103) peak of Nb_2AlC grown at 900 °C and a) (200) peak of MgO and b (116) peak of sapphire indicating that the films are epitaxial.

Since carbon content can only be qualitatively determined by EDS, carbon content was initially estimated by optimizing films of (111) NbC and (001) Nb_2C grown on *c*-plane sapphire at 850 °C. The power settings for Nb, C, and Al were 100, 200, and 90 W, respectively, fo depositions between 700 and 1000 °C (Fig. 1). At 750 °C only smal amounts of Nb_2C and $Nb_5Al_3C_x$ (discussed below) were detected b XRD. Formation of *c*-axis textured Nb_2AlC was observed for depositio temperatures above 800 °C up to 950 °C along with a secondary phas of $Nb_5Al_3C_x$ with the strongest MAX phase XRD peaks at 875–900 °

Subsequently, a set of films were grown at 900 °C with varyin carbon content with the goal of making single phase Nb_2AlC. Fig. shows the XRD results for films deposited with various carbon powe settings. As expected from our investigation of carbon stoichiometr of NbC and Nb_2C, the strongest diffraction peaks due to Nb_2AlC wer observed at a power setting of 200 W; however, $Nb_5Al_3C_x$ wa generally observed whenever Nb_2AlC was present. At the highes carbon concentration, the only instance where Nb_2AlC was foun without $Nb_5Al_3C_x$, the MAX phase was the minority phase and the fil was predominately Nb_2C. At low carbon concentration only th $Nb_5Al_3C_x$, NbC, and Nb_2C phases were present. Varying the depositio pressure between 5–18 mTorr had no discernable effect on th resulting films.

We were also able to grow Nb_2AlC films on (111) MgO substrates a 6 mTorr and 900 °C without a buffer layer. Despite repeated attempts, w were not able to grow Nb_2AlC films on substrates of Si, R-plane sapphire

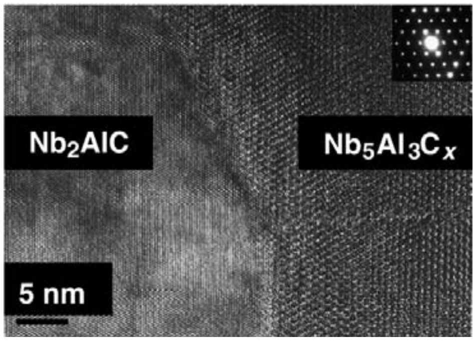

Fig. 4. Plan-view HRTEM micrograph of 270-nm thick Nb_2AlC film grown at 900 °C on *c*-axis sapphire. Two clearly different sized hexagonal structures are observed. The inset shows diffraction of the $Nb_5Al_3C_x$ phase.

or polycrystalline Al_2O_3 substrates. The lattice mismatches between Nb_2AlC and (001) α-Al_2O_3 and (111) MgO are 2.1% and 4.1%, with the films experiencing tensile and compressive strains, respectively. The former is calculated from the surface reconstruction of Al_2O_3 [15]. Both sets of films grew epitaxially, as seen from the XRD ϕ scans (Fig. 3) with in-plane relationships of $[1\bar{1}0]_{Al_2O3}||[100]_{Nb_2AlC}$ and $[101]_{MgO}||[100]_{Nb_2AlC}$.

For MAX-phase film growth a seed-layer is usually required [4,6–8]. Even when a seed layer is not deposited, a binary carbide seed layer often forms at the interface anyway [6]. In addition, (111) NbC and (001) Nb_2C have relatively small lattice mismatches of 1.8% and 0.2%, respectively. The deposition of buffer layers of (111) TiC, (111) NbC, or (001) Nb_2C on any substrates did not improve results. In fact, the quality of the films grown on *c*-axis sapphire with buffer layers, as determined from XRD, was substantially less even though both the lattice mismatch and surface roughness were minimal.

Plan-view HRTEM image of an optimized film grown on *c*-axis sapphire (Fig. 4) shows two different hexagonal structures — the one on the left is Nb_2AlC and the other has a large *a*-axis lattice parameter. Selected area electron diffraction (SAED) shown in Fig. 5 confirms that this phase (top layer) grows epitaxially *c*-axis oriented with *a*- and *c*-axis lattice constants of 7.746 Å and 5.246 Å, respectively, the latter of which gives rise to the (002) diffraction peak observed at 33.9°. While $Nb_5Al_3C_x$ does not exist in bulk [16], these lattice constants are clearly consistent with those of other $M_5A_3C_x$ compounds [5,8]. As can be seen from Fig. 5, $[110]_{Al_2O3}||[100]_{Nb_2AlC}||[110]_{Nb_5Al_3C_x}$. We speculate that since $Nb_5Al_3C_x$ forms at lower temperature as compared to that of the MAX phase, it is the more stable phase due to the presence of lattice strain. This behavior may be similar to what happens with epitaxial films of V_2GeC which always have intergrowths of V_8C_7 [17].

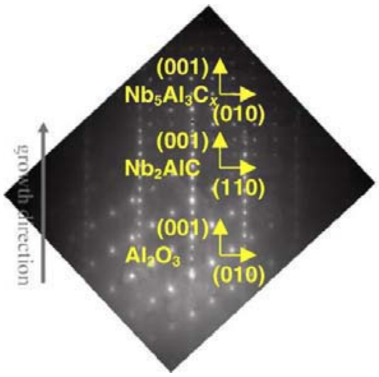

Fig. 5. Selected area electron diffraction pattern of a cross section of a 270-nm thick Nb_2AlC film grown on sapphire. There are clear the epitaxial relations among the Al_2O_3, Nb_2AlC and $Nb_5Al_3C_x$ layers.

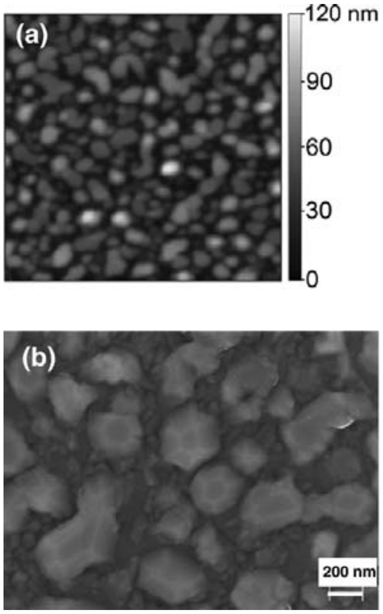

Fig. 6. a) Atomic force micrograph of a 90-nm thick Nb_2AlC (90 nm) thin film grown on sapphire. b) SEM image of the same film in which ~300 nm hexagonal features which are more clearly seen.

Fig. 6 shows the topography of a 90-nm film grown on *c*-axis sapphire. The average surface roughness values were generally ≈15% of the total film thickness for all films. The inset of Fig. 6 shows an SEM image, which highlights the hexagonal facets ~350 nm in size and the concomitant voids of ≈175 nm. As a result of the complex surface morphology, nanoindentation and lateral force scratch testing were difficult and did not lead to reproducible results.

All first-order Raman active phonon modes associated with Nb_2AlC were observed (Table 1). There is reasonable agreement between the values found for the thin films and the calculated and measured values for bulk [18,19]. The largest difference between the bulk and film occurs for the ω_2 mode, which is a longitudinal mode in the basal plane where the atoms are some constrained due to lattice strain. There is also often a peak near 350 cm^{-1} which we attribute to $Nb_5Al_3C_x$.

The electrical resistivity ρ of all films was metal-like down to 2 K (Fig. 7). The room-temperature value of ρ in the stoichiometric films was about twice that of the bulk [11] even though the residual resistivity ratios [ρ(300 K)/ρ(4 K)] were about the same at ~2.5. This suggests that unlike the Ti_2GeC system [10], there is measurable anisotropy in the conductivity. The lower right inset in Fig. 7 shows the very low-temperature resistivity of the film with a superconducting transition at a critical temperature T_c of 440 mK. In our previous

Table 1
Measured and calculated energies of the first order Raman modes of Nb_2AlC

	Raman shift (cm^{-1})				
	ω_1	ω_2	ω_3	ω_4	References
Film	148	198	184	270	This work
Bulk	149.4	~211	~190	262.8	[18]
Calculated	148	197.7	181.5	268.3	[18]
Calculated	144	211	193	251	[19]

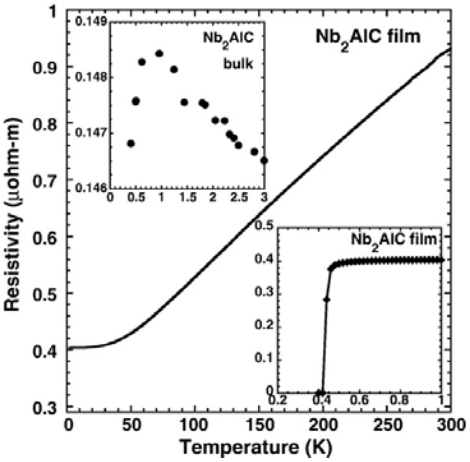

Fig. 7. Electrical resistivity of Nb$_2$AlC thin film showing metal-like conduction. The lower right inset shows a superconducting transition of 440 mK for the thin film. The upper left inset shows a partial superconducting transition estimated to be 430 mK for the bulk.

study [11], transport measurements were performed down only to 5 K; re-measuring the same Nb$_2$AlC bulk sample to lowest temperatures revealed the onset of superconductivity (upper left), with an estimated critical temperature of ≈430 mK. This suggests that the carbon stoichiometry of the films was rather close to that of the bulk, since it is well known that the T_c of niobium carbide depends rather sensitively on the carbon content [20].

4. Conclusions

In summary, we grew epitaxial thin films of Nb$_2$AlC on (001) sapphire and (111) MgO with and without binary carbide buffer layers. The best results were obtained on c-axis sapphire at 900 °C without the use of buffer layers. All films contained intergrowths of a new epitaxial phase Nb$_5$Al$_3$C$_x$. Film roughness was approximately 15% the film thickness. The resistivity was metal-like and appears to have weak anisotropy. A superconducting transition was found at 440 mK

Acknowledgement

This work was funded by the National Science Foundation grants DMR-0503711 and MRSEC 0520471.

References

[1] M.W. Barsoum, Prog. Solid State Chem. 28 (2000) 201.
[2] M.W. Barsoum, M. Radovic, in: F. Buschow, Kramer, Mahajan, Veyssiere (Eds.) Encyclopedia of Materials Science and Technology, Elsevier, 2006, p. 16.
[3] M.W. Barsoum, M. Radovic, in: F. Buschow, Kramer, Mahajan, Veyssiere (Eds.) Encyclopedia of Materials Science and Technology, Elsevier, 2006, p. 11.
[4] J.P. Palmquist, U. Jansson, T. Seppanen, P.O.A. Persson, J. Birch, L. Hultman, P. Isberg Appl. Phys. Lett. 81 (2002) 835.
[5] J.P. Palmquist, S. Li, P.O.A. Persson, J. Emmerlich, O. Wilhemsson, H. Högberg, M.I Katsnelson, B. Johansson, R. Ahujia, O. Eriksson, L. Hultman, U. Jansson, Phys. Rev. I 70 (2004) 165401.
[6] J. Emmerlich, J.-P. Palmquist, H. Hogberg, J.M. Molina-Aldareguia, Z. Czigany, P.O. Persson U. Jansson, L. Hultman, J. Appl. Phys. 96 (2004) 4817.
[7] O. Wilhelmsson, J.-P. Palmquist, T. Nyberg, U. Jansson, Appl. Phys. Lett. 85 (2004 1066.
[8] H. Högberg, P. Eklund, J. Emmerlich, J. Birch, L. Hultman, J. Mater. Res. 20 (2005 779.
[9] H. Högberg, L. Hultman, J. Emmerlich, T. Joelsson, P. Eklund, J.M. Molina-Aldareguia, J.P. Palmquist, O. Wilhelmsson, U. Jansson, Surf. Coat. Technol. 193 (2005) 6.
[10] T.H. Scabarozi, P. Eklund, J. Emmerlich, H. Högberg, T. Meehan, P. Finkel, M.W. Barsoum J.D. Hettinger, L. Hultman, S.E. Lofland, Solid State Commun. 146 (2008) 498.
[11] J.D. Hettinger, S.E. Lofland, P. Finkel, T. Meehan, J. Palma, K. Harrell, S. Gupta, A. Ganguly T. El-Raghy, M.W. Barsoum, Phys. Rev. B 72 (2005) 115120.
[12] P. Finkel, B. Seaman, K. Harrell, J. Palma, J.D. Hettinger, S.E. Lofland, A. Ganguly M.W. Barsoum, Z. Sun, S. Li, R. Ahuja, Phys. Rev. B 70 (2004) 085104.
[13] P. Finkel, M.W. Barsoum, J.D. Hettinger, S.E. Lofland, H.I. Yoo, Phys. Rev. B 67 (2003 235108.
[14] S.E. Lofland, J.D. Hettinger, T. Meehan, A. Bryan, P. Finkel, S. Gupta, M.W. Barsoum G. Hug, Phys. Rev. B 74 (2006) 1.
[15] G. Renaud, Surf. Sci. Rep. 32 (1998) 1.
[16] A.I. Gusev, Russ. Chem. Rev. 95 (1996) 379.
[17] O. Wilhelmsson, P. Eklund, H. Högberg, L. Hultman, U. Jansson, Acta Mater. 56 (2008) 2563.
[18] J.E. Spanier, S. Gupta, M. Amer, M.W. Barsoum, Phys. Rev. B 71 (2005) 012103.
[19] O.D. Leaffer, S. Gupta, M.W. Barsoum, J.E. Spanier, J. Mater. Res. 22 (2007) 2651.
[20] A.L. Giorgi, E.G. Szklarz, E.K. Storms, A.L. Bowman, B.T. Matthias, Phys. Rev. 125 (1962) 837.

JOURNAL OF APPLIED PHYSICS **105**, 013543 (2009)

Thermal expansion of select $M_{n+1}AX_n$ (M=early transition metal, A=A group element, X=C or N) phases measured by high temperature x-ray diffraction and dilatometry

T. H. Scabarozi,[1,2] S. Amini,[2] O. Leaffer,[2] A. Ganguly,[2] S. Gupta,[2] W. Tambussi,[1]
S. Clipper,[1] J. E. Spanier,[2] M. W. Barsoum,[2] J. D. Hettinger,[1] and S. E. Lofland[1,a)]
[1]*Department of Physics and Astronomy, Rowan University, Glassboro, New Jersey 08028, USA*
[2]*Department of Materials Science and Engineering, Drexel University, Philadelphia, Pennsylvania 19104, USA*

(Received 18 July 2008; accepted 4 October 2008; published online 14 January 2009)

Herein we report on a systematic investigation of the thermal expansion of select $M_{n+1}AX_n$ phases. The bulk dilatometric thermal expansion coefficient α_{dil} was measured in the 25–1200 °C temperature range and the thermal expansion of more than 15 of these phases was studied by x-ray diffraction in the 25–800 °C temperature range. The coefficient of thermal expansion for the *a* axis α_a ranged between $(2.9\pm0.1)\times10^{-6}$ °C^{-1} (Nb_2AsC) and $(12.9\pm0.1)\times10^{-6}$ °C^{-1} (Cr_2GeC) while the coefficient for the *c* axis (α_c) ranged between $(6.4\pm0.2)\times10^{-6}$ °C^{-1} (Ta_2AlC) and $(17.6\pm0.2)\times10^{-6}$ °C^{-1} (Cr_2GeC). Weak anisotropy in the thermal expansion was seen in most phases, with the largest value of α_c/α_a belonging to Nb_2AsC. The Grüneisen parameters along the *a* and *c* directions were calculated from *ab initio* values for the elastic compliances and were relatively isotropic. A good correlation was found between the thermal expansion anisotropy and the elastic constant c_{13} and we conclude that the anisotropy in thermal expansion is related to the bonding between the $M-A$ elements. © *2009 American Institute of Physics*.
[DOI: 10.1063/1.3021465]

I. INTRODUCTION

The $M_{n+1}AX_n$ (MAX) phases ($n=1-3$) are layered hexagonal compounds, in which near close-packed layers of M (early transition metals) are interleaved with layers of group A element (mostly IIIA and IVA), with the X-atoms (C and/or N) filling the octahedral sites between the M layers. Most of these phases were synthesized in powder form in the 1960s by Nowotny.[1] At this time it is fairly well established that these phases have an unusual and sometimes unique combination of properties.[2–16] They are elastically stiff, have relatively low thermal expansion coefficients, and have good thermal and electrical conductivities.[2,17] They are relatively soft, with Vickers hardness values of 2–8 GPa, easily machinable, thermal shock, and damage tolerant. Some are fatigue, creep, and oxidation resistant.[18] At higher temperatures, they can undergo a brittle-to-plastic transition.[12] Some, such as Ti_2AlC, are exceptionally oxidation resistant and are candidate materials for high temperature structural industrial applications.[19]

Elastic measurements indicate that these materials are stiff, particularly in shear. In particular, some M_2AX (211) materials, such as Ti_2SC (Ref. 20), show enhanced elastic properties although they are not as readily machinable as other MAX-phase materials. It is believed that the origin of the increased modulus in this material is due to stronger $M-A$ bonds. A similar study done on Nb_2AsC showed higher compressibility in the *a*-direction than the *c*-direction, which can be associated with the position of Nb being closer to the As.[21]

In the M_3AX_2 (312) materials, increased stiffness is a result of a higher fraction of the stronger $M-X$ bonds. The most studied MAX phase, Ti_3SiC_2, exhibits weak elastic anisotropy associated with two different Ti–C bonds and Si vibrating preferentially along the *a* axis.[22,23] Compressibility studies[24] of $Ti_3Si_{1-x}Ge_xC_2$ found solid-solution softening occurred while investigations of Ti_3AlCN and $Ti_2AlC_{0.5}N_{0.5}$ suggest the formation of vacancies on both the Al and N sites leading to the decrease in bulk moduli.[25] In M_4AX_3 compounds, there are even less weaker $M-A$ bonds and the $M-X$ bonds are shorter and stiffer, as reported for Ti_4AlN_3.[26] An exception is seen in Ta_4AlC_3 where high-pressure diffraction studies reveal little anisotropy in compressibility attributed to lattice softening due to differences in atomic packing.[27] The purpose of this paper is to further investigate the role of bonding anisotropies in the MAX phases by measuring the thermal expansion of a large number of these phases by high temperature x-ray diffraction (XRD).

II. EXPERIMENTAL DETAILS

All samples were synthesized by either hot isostatic pressing or hot pressing, providing fully dense and predominantly single phase microstructures. Details of processing of Cr_2AlC and Ta_2AlC can be found in Ref. 18, $Ti_2Al(C_{0.5}N_{0.5})$ in Ref. 28, $Ti_3Al(C_{0.5}N_{0.5})_2$ in Ref. 29, Ti_3SiC_2 in Ref. 4, Ti_3GeC_2 and $Ti_3Si_{0.25}Ge_{0.75}C_2$ in Ref. 30, V_2AlC, V_2AsC, Nb_2AlC, Nb_2SnC, Ti_2AlC, and Hf_2InC in Ref. 31, Ti_3AlC_2 and Ti_4AlN_3 in Ref. 32, Nb_2AsC in Ref. 33, Cr_2GeC in Ref. 34, Ti_2AlN in Ref. 35, and Ti_2SC in Ref. 36.

To synthesize the V_2GeC samples, V and C powders (Alfa Aesar, Ward Hill, MA) and Ge powder (Cerac Inc.,

---

[a)] Electronic mail: lofland@rowan.edu.

Milwaukee, WI) were mixed in stoichiometric proportions, ball milled for 12 h, and dried at 150 °C for 24 h. The powder mixtures were sealed in graphite foil, placed in a graphite die, heated at 10 °C/min in a graphite-heated vacuum atmosphere hot press (Series 3600, Centorr Vacuum Industries, Somerville, MA), annealed at 875 °C for 3 h, and then hot pressed at 1350 °C for 6 h under a load that corresponded to a stress of 45 MPa.

The bulk thermal expansion measurements were performed with a dilatometer (model 1161, Anter Corporation Unitherm, Pittsburgh, PA) on electric-discharge machined bar-shaped specimens with dimensions of $\sim 3 \times \sim 3 \times \sim 20$ mm^3. The heating and cooling rates were set at 3 K/min. To avoid oxidation, the dilatometric experiments were carried out under an atmosphere of ultrahigh pure Ar gas.

The high-temperature XRD diffractometer (Scintag X_2) was configured with a furnace (Edmund Bühler HDK-2.3). The diffractometer utilized Cu $K\alpha$ radiation (40 mA and 45 kV) and a Si(Li) Peltier-cooled solid-state detector. Data were taken from $5°-100°$ in steps of 0.02° with hold times of 1 or 2 s/step. MAX phase powders were mixed together with Si and Cu powders at ratios such that the intensity values of the strongest diffraction lines of the various materials were roughly equal at room temperature. The Si powder was mixed with the MAX phase to serve as a standard for alignment. The Cu powder was used to measure the mixture temperature via knowledge of its thermal expansion. From a slurry mixture, a 50–75 μm coating was applied either on a substrate (Zr, Mo, or sapphire) or directly on the Pt/Rh-10% heating element. A Pt/Rh-30% thermocouple was bonded to the back of the heater for temperature control. To minimize possible oxidation, the measurements were carried out either under vacuum (10^{-4} Torr) or in a He atmosphere from room temperature to 1000 °C. The heating rate was 20 °C/min with a 15 min hold time prior to each scan. Spectra were fit to a Pearson7 line shape by Scintag software DMSNT 1.36b. Lattice refinements were done with XLAT.[37] The thermal expansion for Si was taken from Ref. 38 and that of Cu from NIST.[39]

Ab initio density functional calculations were conducted with the Vienna *ab initio* simulation package (VASP) (Ref. 40) and the MEDEA (Ref. 41) interface. All calculations were carried out using the projector augmented wave[42,43] and the generalized gradient approximation.[44] Relaxed structures were calculated and energies were converged with respect to the k-mesh with MEDEA's convergence method. Subsequent calculations were carried out with the k-mesh resulting from the convergence. Elastic properties were calculated with MEDEA's mechanical and thermomechanical module,[45] which calculates the stress tensor from changes in energy when the unit cell is strained. Strains of 0.005, 0.01, and 0.02 were simulated. The reported elastic constants are from a least-squares fitting of the values calculated for each strain.

III. RESULTS AND DISCUSSION

Figure 1 shows the dilatometric thermal expansion α_{dila} as a function of temperature T for select compositions. The curves are shifted vertically for clarity. The α_{dila} values, reported in column 9 of Table I, were calculated by a least-squares fit of both the heating and cooling curves in the temperature range mentioned therein. Also included in the table are previously reported values.

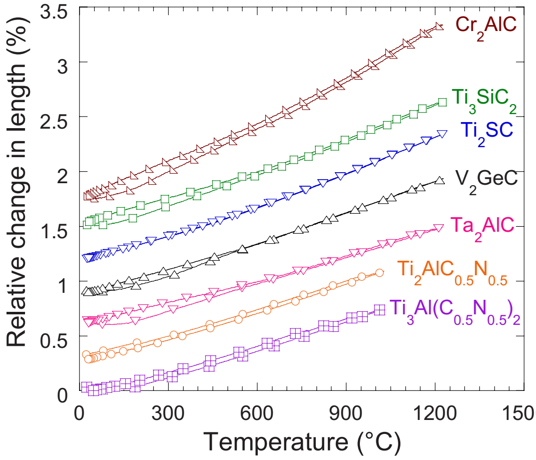

FIG. 1. (Color online) Thermal expansion as a function of temperature for selected MAX phases from dilatometer measurements. Curves have been shifted vertically for clarity.

Figure 2 shows several XRD patterns of Cr_2GeC at different temperatures. It is clearly seen the Cr_2GeC and Cu peaks noticeably shift to the left with increasing temperature. The shift for Si is much less indicating that, (i) its thermal expansion is smaller and, (ii) more importantly, that the sample height remains effectively constant, minimizing corrections due to focus.

Figure 3 shows the temperature dependencies and estimated errors of the lattice constants of more than 15 MAX

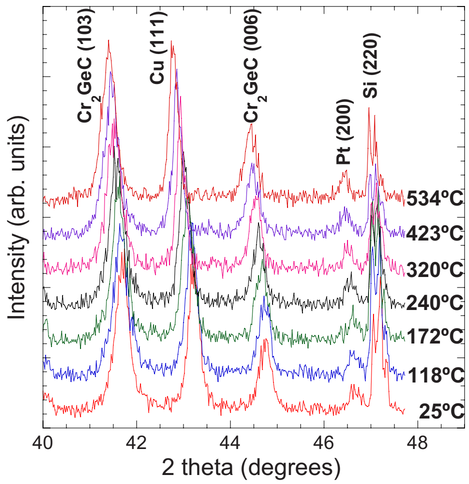

FIG. 2. (Color online) High temperature XRD of Cr_2GeC. Shifting peaks can be seen due to atomic spacing increasing as a function of temperature. Silicon and copper are used as internal standards for alignment and temperature determination, respectively. The Pt peak is associated with the heater strip.

TABLE I. Lattice parameters and thermal expansions for the MAX-phases studied by XRD (numbers in parentheses are estimated standard deviations in the last significant figure of the refined parameter).

									Other work			
Compound	a (Å)	c (Å)	α_a (10^{-6} °C^{-1})	α_c (10^{-6} °C^{-1})	Anisotropy (α_c/α_a)	c/a	α_{av} (10^{-6} °C^{-1})	α_{dila} (10^{-6} °C^{-1})	α_a (10^{-6} °C^{-1})	α_c (10^{-6} °C^{-1})	α_{av} (10^{-6} °C^{-1})	Ref.
Ti_4AlN_3	2.9884(1)	23.3810(35)	8.3(2)	8.3(9)	1.00(1)	7.824	8.3(5)	9.7(2)[a]	9.6(1)[b]	8.8(1)[b]	9.4(1)[b]	46
								9.1(5)				
								9.1(2)[c]	8.4(1)[d]	9.3(10)[d]	8.6(4)[d]	22
Ti_3SiC_2	3.0663(1)	17.6510(18)	8.9(1)	10.0(2)	1.12(2)	5.756	9.3(2)	9.1(2)[e]	8.6(1)[b]	9.7(1)[b]	9.1(2)[b]	23
Ti_3AlCN	3.0442(2)	18.3890(11)	6.0(2)	11.3(2)	1.89(2)	6.041	7.8(2)	7.5(5)				
Ti_3GeC_2	3.0873(2)	17.8071(10)	8.1(2)	9.7(2)	1.20(3)	5.768	8.6(2)	7.8(2)				
$Ti_3Si_{0.25}Ge_{0.75}C_2$	3.0855(5)	17.7960(18)	8.8(6)	11.1(3)	1.27(6)	5.768	9.6(5)					
Ti_3AlC_2	3.0698(1)	18.4998(2)	8.3(1)	11.1(1)	1.33(1)	6.026	9.2(1)	9.0(2)[f]				
								7.9(5)				
Ti_2AlCN	3.0247(1)	13.6046(5)	8.4(1)	8.8(1)	1.05(2)	4.498	8.5(1)	10.5(2)[a]				
								8.2(2)[g]				
Ti_2AlN	2.9872(2)	13.6108(6)	10.6(2)	9.75(2)	0.92(3)	4.556	10.3(2)	8.8(2)[a]	8.6(2)[d]	7.0(5)[d]	8.1(5)[d]	28
Ti_2SC	3.2046(1)	11.2092(3)	8.6(1)	8.7(2)	1.01(2)	3.498	8.7(1)	9.3(6)	8.5(5)[d]	8.8(2)[d]	8.6(6)[d]	47
V_2AlC	2.9176(3)	13.1281(9)	9.1(2)	10.0(7)	1.10(16)	4.500	9.4(10)	9.4(5)	9.34(5)[d]	9.48(4)[d]	9.39(5)[d]	48
V_2GeC	3.0034(1)	12.2527(9)	6.9(1)	15.8(3)	2.27(1)	4.080	9.9 (2)	9.4(6)				
V_2AsC	3.1127(1)	11.3884(4)	7.2(1)	14.0(1)	1.92(1)	3.659	9.5(1)					
Cr_2GeC	2.9500(2)	12.1010(10)	12.9(1)	17.6(2)	1.37(1)	4.102	14.5(2)	9.5(5)				
Cr_2AlC	2.8571(2)	12.8208(6)	12.8(3)	12.1(1)	0.94(3)	4.487	12.6(2)	12.8(5)				
Nb_2SnC	3.2376(2)	13.8135(4)	6.6(4)	14.5(2)	2.17(2)	4.267	9.3(3)	7.8(2)[h]				
								7.5(2)[g]				
Nb_2AlC	3.1063(1)	13.8783(11)	8.8(2)	6.8(3)	0.78(6)	4.468	8.1(2)	8.7(2)[i]				
Nb_2AsC	3.3235(1)	11.9036(3)	2.9(1)	10.6(1)	2.57(1)	3.582	5.5(1)	7.3(5)				
Hf_2InC	3.3085(1)	14.7351(10)	7.2(1)	7.6(2)	1.05(3)	4.454	7.3(2)	7.6(2)[j]				
Ta_2AlC	3.0804(2)	13.8630(7)	9.2(2)	6.4(2)	1.43(3)	4.5	8.3(2)	7.2(6)				
								8.8(2)[g]				
Ti_2AlC								8.2(2)[a]	7.1(3)[d]	10.0(5)[d]	8.1(5)[d]	28

[a] Reference 28.

[b] Neutron diffraction.

[c] Reference 22.

[d] XRD.

[e] Reference 23.

[f] Reference 49.

[g] Reference 2.

[h] Reference 50.

[i] Reference 51.

[j] Reference 52.

phases measured in this work. Table I lists the values of α_a and α_c, as well as previously reported high-temperature XRD or neutron diffraction results. The values obtained from diffraction (column 8) are compared with the dilatometric values (column 9) by assuming the average coefficient of thermal expansion, $\alpha_{av}=(2/3\ \alpha_a+1/3\ \alpha_c)$. In most cases, the results agree reasonably well with those of other measurements. For example, the presently reported values for α_a and α_c for Ti_3SiC_2, $(8.9\pm0.1)\times10^{-6}$ and $(10.0\pm0.2)\times10^{-6}$ °C^{-1}, respectively, are in excellent agreement with previous results.[22,23] The same is true for V_2AlC and Ti_2SC.[53,54] The agreement is not as good for Ti_2AlN,[28] which may reflect variations in stoichiometry.[35,55]

Figure 4(a) compares α_{av} of the MAX phases (solid circles) with those of their corresponding MX (open squares). From this plot it is reasonable to conclude that a relationship exists between the two. With the notable exception of Nb_2AsC, which is unusual, as noted above, the α values of the binaries are indeed lower than those of the corresponding MAX phase, suggesting that, on the average, the $M-X$ bonds are stronger than the $M-A$ bonds, a not too surprising conclusion.

The anisotropy ratio (α_c/α_a), listed in column 6 of Table I, for the most part, is >1, as might be anticipated since the c direction involves the relatively weaker $M-A$ bonds. However, as seen in Fig. 5(a), the anisotropy is mostly a function of the A-group element.

In an isotropic system, the volume thermal expansion α_V is given by

$$\alpha_V=\gamma\frac{c_v}{BV} \tag{1}$$

where γ is the Grüneisen parameter, a measure of the anharmonicity, which gives rise to thermal expansion, B is the bulk modulus, V is the molar volume, and c_V is the molar specific heat at constant volume. In Table II are the lattice constants a, B, and γ for the cubic binary carbides, assuming that the Dulong–Petit law applies, i.e., $c_V=3mR$, where m is

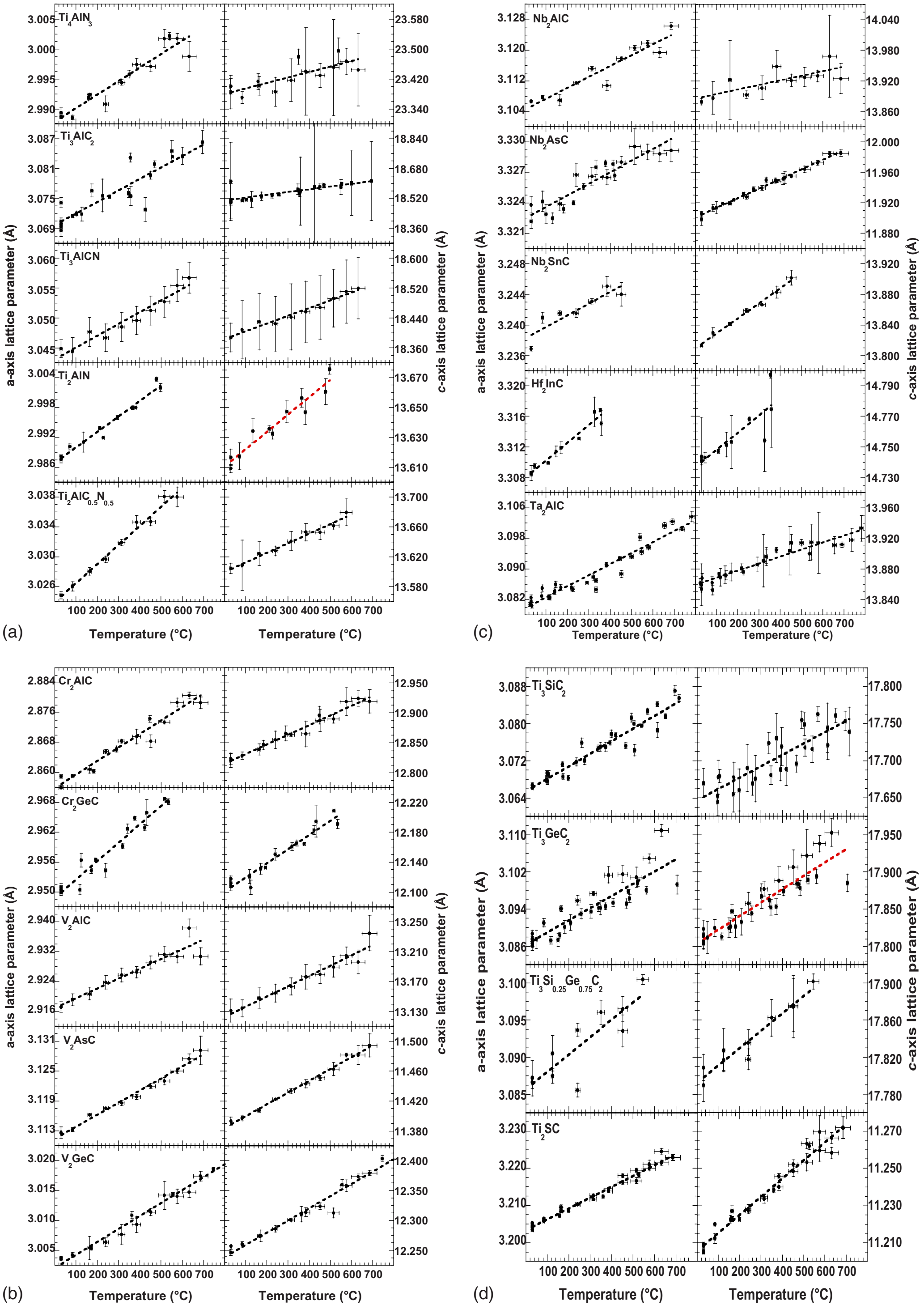

FIG. 3. (Color online) Temperature dependence of the lattice constants for (a) various Ti–Al–*X* phases, (b) various M_2AC (M=Cr or V, A=Al, As, or Ge) phases, (c) various M_2AC (M=Nb, Hf, or Ta, A=Al, As, In, or Sn) phases, and (d) various Ti–A–C (A=Si, Ge, or S) phases.

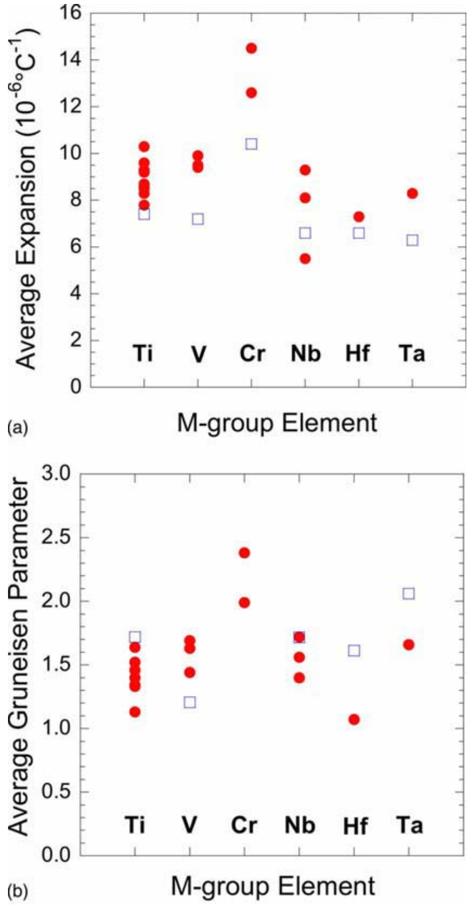

FIG. 4. (Color online) (a) Average thermal expansion as a function of the M-group element for MAX phase materials (solid markers). (b) Average Grüneisen parameter as a function of M-group element for MAX phase materials (solid markers). In both figures, open markers represent the values for the respective binary carbide.

the number of atoms per unit cell and R is the ideal gas constant. Where possible, we used XRD data for the thermal expansion and diamond anvil cell measurements of the bulk moduli. For the most part, the values are between 1.5 and 2, as expected for metallic compounds. The outlier is VC, which is always substoichiometric.[63]

When the average Grüneisen parameters of the ternaries and binaries are plotted on the same figure [Fig. 4(b)], there is little correlation between the two, which indirectly implicates the A-group element in the thermal expansion anisotropies observed. This notion can be tested further. In a system with axial symmetry (i.e., hexagonal, tetragonal, or rhombohedral), one can write down the Grüneisen parameters for the a and c directions, as γ_a and γ_c, respectively, as

$$\gamma_a = \frac{V}{C_v}[(c_{11}+c_{12})\alpha_a + c_{13}\alpha_c], \tag{2a}$$

TABLE II. Lattice parameter and properties for binary carbides.

Binary carbide	a (Å)	α (10^{-6} °C^{-1})	B (GPa)	γ
TiC	4.328	9.44[a]	248[b]	1.72
VC	4.153	7.3[c]	258[d]	1.20
ZrC	4.698	7.37[a]	195[e]	1.35
NbC	4.47	7.74[f]	274[g]	1.71
HfC	4.639	7.37[f]	242[h]	1.61
TaC	4.456	7.45[f]	345[e]	2.06
Cr_3C_2		10.4[c]		

[a] Reference 56.
[b] Reference 57.
[c] Reference 58.
[d] Reference 59.
[e] Reference 27.
[f] Reference 60.
[g] Reference 61.
[h] Reference 62.

$$\gamma_c = \frac{V}{C_v}(2c_{13}\alpha_a + c_{33}\alpha_c), \tag{2b}$$

where c_{ij} are the elastic stiffness constants.[64]

Since MAX phase single crystals large enough for the measurement of the various elastic constants do not exist to date, one must rely on *ab initio* calculations for those constants to proceed with the analysis. Nonetheless, one can check the validity of the calculated numbers by comparing them with the measured values for B, the shear modulus G, and the compressibilities along the a and c directions, κ_a and κ_c, respectively. The Voigt averages, which provide a method of connecting the calculated elastic constants to the measured parameters, yield

$$B = \frac{2(c_{11}+c_{12}) + 4c_{13} + c_{33}}{9}, \tag{3a}$$

$$G = \tfrac{1}{30}(7c_{11} - 5c_{12} + 2c_{33} - 4c_{13} + 12c_{44}). \tag{3b}$$

For hydrostatic compression, one finds

$$\kappa_a = \frac{c_{33} - c_{13}}{c_{33}(c_{11}+c_{12}) - 2c_{13}^2}, \tag{4a}$$

$$\kappa_c = \frac{c_{11} + c_{12} - 2c_{13}}{c_{33}(c_{11}+c_{12}) - 2c_{13}^2}. \tag{4b}$$

The calculated elastic constants, as well as the measured values, are listed in Table III.

While the agreement between the calculated and measured values for B, G, κ_a, and κ_c is not exact,[16,17,24–26,49,66–68] they are generally close except for the latter two, which are particularly sensitive to the value of c_{13}. It is to be noted that there has been, in general, excellent agreement between the calculated and observed Raman spectra,[69] further evidence that the calculated elastic constants are quite reasonable.

As seen in Table IV, the calculated γ values from $c_V = 3mR$, where $m = 4(n+1)$ for the MAX phases, range between 1.5 and 2.5, as expected for metallic compounds. Figure 4(b) shows that the average Grüneisen parameter is ef-

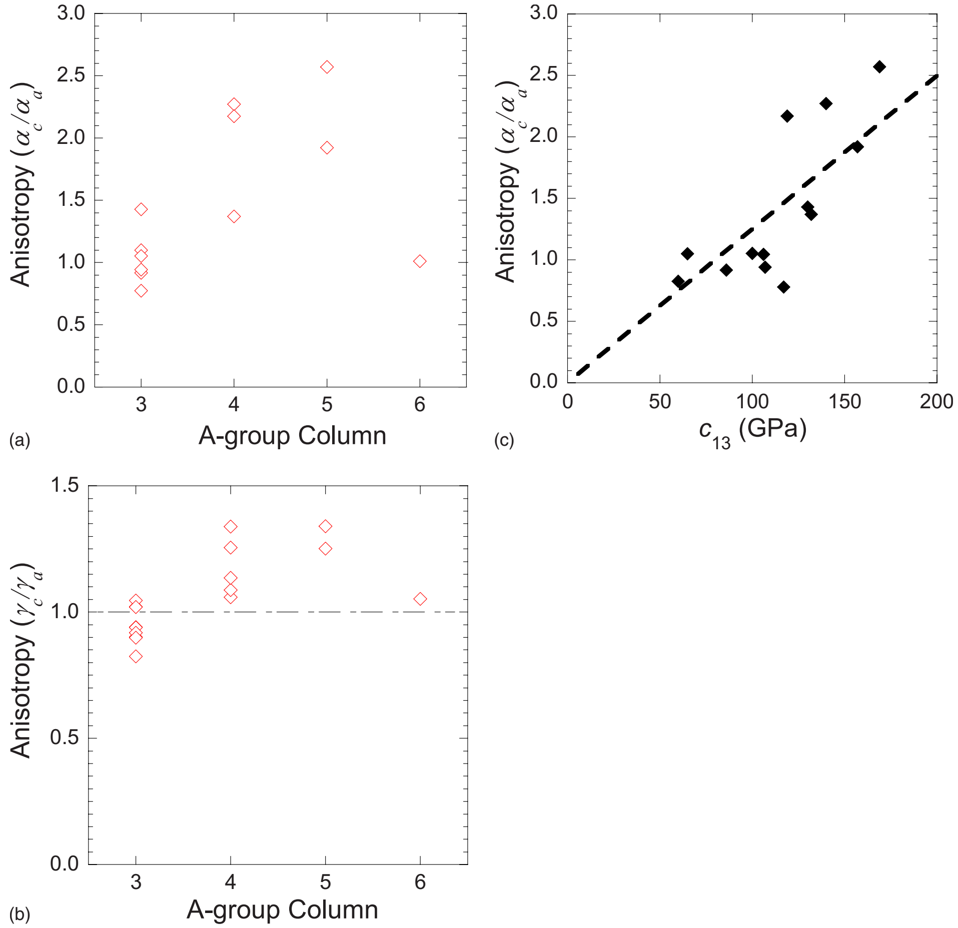

FIG. 5. (Color online) (a) Anisotropy in thermal expansion vs *A*-group elements. (b) Anisotropy in the Grüneisen parameter vs *A*-group column. (c) The compliance tensor element c_{13} vs the *A*-group column.

fectively constant for a given *M*-group element but does not obviously relate to that of the corresponding binary carbide.

Comparing Figs. 4(a) and 4(b), one notices a direct correlation between α and γ. From Eq. (1), $\alpha \propto \gamma / BV$ and, thus, BV is effectively constant for all MAX phases of any given family. This relationship has been found in a variety of other class of solids such as halides,[70] oxides,[70] and chalcogenides,[71] as well as for binary carbides.[53] The correlation for the latter, however, has not been nearly as good as the results shown here for the ternaries. The discrepancies for the binary carbides have been partly attributed to stoichiometry and microstructure.[72]

Note that the anisotropies in the calculated γ values [Fig. 5(b)] are small compared to those of the corresponding α values [Fig. 5(a)]. This reflects the fact that the anharmonicity is relatively isotropic and suggests that the anisotropy in thermal expansion is related predominantly to the anisotropy in the elastic constants, which must be a consequence of the bonding of the *M* element to the A group. Confirming this notion is the fact that the anisotropy in α of the 211 phases correlates well with c_{13} [Fig. 5(c)]. This is not too surprising since c_{13} compares the bonding strengths in the *a* and *c* planes of hexagonal crystals. In Fig. 5(c) Nb_2AlC is an outlier, most probably a direct result of the exceptionally strong Nb–Al bonds.[73] Nb_2SnC is also an outlier, but in the opposite sense, in that α_c is considerably larger than α_a. Using the same logic, it is reasonable to conclude that the Nb–Sn bonds are weaker than average, which is not reflected in c_{13}. Lastly we note that the good correlation found in Fig. 5(c) indirectly confirms the validity of both the thermal expansion measurements and *ab initio* calculations, which are in good agreement with other similar calculations on the MAX phases given in the literature.[74–81]

IV. CONCLUSIONS

We measured the thermal expansion of a number of MAX phases. Overall, anisotropy between the *a* and *c* axes was mild for most of them, the largest belonging to Nb_2AsC. The Grüneisen parameters determined from *ab initio* calculated elastic constants are consistent with expectations for metals and are relatively isotropic. The anisotropy in thermal

TABLE III. Elastic properties of the measured MAX-phases in this study.

	Calculated elastic parameters										Measured elastic parameters				
Compound	c_{11} (GPa)	c_{12} (GPa)	c_{13} (GPa)	c_{33} (GPa)	c_{44} (GPa)	B (GPa)	G (GPa)	$10^3\kappa_a$ (GPa^{-1})	$10^3\kappa_c$ (GPa^{-1})	Ref.	B^* (GPa)	$10^3\kappa_a$ [a] (GPa^{-1})	$10^3\kappa_c$ [a] (GPa^{-1})	Ref.	G [b] (GPa)
Ti_4AlN_3	405	94	102	361	160	196	153	1.63	1.85	[c]	216(2)	1.30	1.60	26	127[d]
Ti_3SiC_2	365	125	120	375	122	204	122	1.65	1.61	[c]	206(6)	0.92	2.02	52	138[e]
Ti_3GeC_2	355	143	80	404	172	191	144	1.72	1.79	[c]	197(4)	1.60	1.60	24	141[e]
Ti_3AlC_2	361	75	70	299	124	161	132	1.90	2.46	65	226(3)	0.80	2.10	25	124[f]
Ti_2AlN	312	69	86	283	127	154	120	2.12	2.25	[c]	169(3)	1.80	1.90	51	120[g]
Ti_2SC	339	90	100	354	162	179	139	1.93	1.74	[c]	191(3)	1.42	2.20	46	125[h]
V_2AlC	346	71	106	314	151	175	136	1.92	1.89	65	201(3)	1.00	2.20	16	116[i]
V_2GeC	311	122	140	291	158	191	116	1.74	1.76	[c]					
V_2AsC	334	109	157	321	170	204	128	1.77	1.39	[c]					
Cr_2GeC	315	145	132	339	91	199	91	1.71	1.62	[c]					80[j]
Cr_2AlC	384	79	107	382	147	193	146	1.79	1.62	65	165(2)	2.10	1.70	16	105[i]
Nb_2SnC	268	86	119	267	98	161	89	2.24	1.75	[c]					
Nb_2AlC	341	94	117	310	150	183	129	1.80	1.87	65	209(2)	1.40	1.40	16	117[i]
Nb_2AsC	334	104	169	331	167	209	127	1.84	1.14	[c]	224(2)	1.30	0.70	21	
Hf_2InC	284	69	65	243	91	134	99	2.30	2.88	[c]					
Ta_2AlC	339	113	130	326	154	194	126	1.73	1.69	[c]					
Ti_2AlC	308	55	60	270	111	137	117	2.31	2.68	65	186(2)	1.10	2.40	16	118[i]

[a] Determined from diamond-anvil cell XRD studies.
[b] Determined from velocity of sound measurements.
[c] Present work.
[d] Reference 66.
[e] Reference 30.
[f] Reference 49.
[g] Reference 27.
[h] Reference 36.
[i] Reference 17.
[j] Reference 34.

expansion is related to the bonding between $M-A$, while the magnitude of the thermal expansion is controlled by $M-X$ bonding. The bulk modulus of any given family of compounds is inversely related to the unit cell volumes.

ACKNOWLEDGMENTS

We gratefully acknowledge the support of the National Science Foundation through Grant No. DMR-0503711. The authors acknowledge the support of C. Lunk for assistance with the XRD equipment.

TABLE IV. Calculated Grüneisen parameters of MAX phase materials.

Compound	γ_a	γ_c	$\langle\gamma\rangle$	Anisotropy (γ_c/γ_a)
Ti_4AlN_3	1.36	1.28	1.33	0.94
Ti_3SiC_2	1.61	1.70	1.64	1.06
Ti_3GeC_2	1.42	1.54	1.46	1.09
Ti_3AlC_2	1.33	1.36	1.34	1.02
Ti_2AlN	1.55	1.46	1.52	0.94
Ti_2SC	1.38	1.45	1.40	1.05
V_2AlC	1.41	1.48	1.44	1.05
V_2GeC	1.51	1.89	1.63	1.25
V_2AsC	1.56	1.95	1.69	1.25
Cr_2GeC	2.27	2.58	2.38	1.14
Cr_2AlC	1.98	2.01	1.99	1.02
Nb_2SnC	1.54	2.06	1.72	1.34
Nb_2AlC	1.62	1.46	1.56	0.90
Nb_2AsC	1.26	1.69	1.40	1.34
Hf_2InC	1.10	1.01	1.07	0.92
Ta_2AlC	1.71	1.54	1.66	0.90
Ti_2AlC	2.41	1.99	2.27	0.83

[1] G. Nowotny, Prog. Solid State Chem. **2**, 27 (1970).
[2] M. W. Barsoum, Prog. Solid State Chem. **28**, 201 (2000).
[3] M. W. Barsoum, D. Brodkin, and T. El-Raghy, Scr. Mater. **36**, 535 (1997).
[4] M. W. Barsoum and T. El-Raghy, J. Am. Ceram. Soc. **79**, 1953 (1996).
[5] M. W. Barsoum and T. El-Raghy, J. Mater. Synth. Process. **5**, 197 (1997).
[6] M. W. Barsoum and T. El-Raghy, Metall. Mater. Trans. A **30**, 363 (1999).
[7] M. W. Barsoum, T. El-Raghy, C. J. Rawn, W. D. Porter, H. Wang, A. Payzant, and C. Hubbard, J. Phys. Chem. Solids **60**, 429 (1999).
[8] M. W. Barsoum, L. Farber, T. El-Raghy, and I. Levin, Metall. Mater. Trans. A **30**, 1727 (1999).
[9] M. W. Barsoum, G. Yaroschuck, and S. Tyagi, Scr. Mater. **37**, 1583 (1997).
[10] T. El-Raghy and M. W. Barsoum, J. Am. Ceram. Soc. **82**, 2849 (1999).
[11] M. W. Barsoum, T. El-Raghy, and L. Ogbuji, J. Electrochem. Soc. **144**, 2508 (1997).
[12] T. El-Raghy, M. W. Barsoum, A. Zavaliangos, and S. R. Kalidindi, J. Am. Ceram. Soc. **82**, 2855 (1999).
[13] T. El-Raghy, A. Zavaliangos, M. W. Barsoum, and S. R. Kalidindi, J. Am. Ceram. Soc. **80**, 513 (1997).
[14] L. Farber, M. W. Barsoum, A. Zavaliangos, T. El-Raghy, and I. Levin, J.

Am. Ceram. Soc. **81**, 1677 (1998).

[15] I. M. Low, S. K. Lee, B. Lawn, and M. W. Barsoum, J. Am. Ceram. Soc. **81**, 225 (1998).

[16] B. Manoun, R. P. Gulve, S. K. Saxena, S. Gupta, M. W. Barsoum, and C. S. Zha, Phys. Rev. B **73**, 024110 (2006).

[17] J. D. Hettinger, S. E. Lofland, P. Finkel, T. Meehan, J. Palma, K. Harrell, S. Gupta, A. Ganguly, T. El-Raghy, and M. W. Barsoum, Phys. Rev. B **72**, 115120 (2005).

[18] M. W. Barsoum and M. Radovic, *Encyclopedia of Materials: Science and Technology*, edited by K. H. J. Buschow (Elsevier, Amsterdam, 2004).

[19] M. W. Barsoum, N. Tzenov, A. Procopio, T. El-Raghy, and M. Ali, J. Electrochem. Soc. **148**, C551 (2001).

[20] T. H. Scabarozi, S. Amini, P. Finkel, O. D. Leaffer, J. E. Spanier, M. W. Barsoum, M. Drulis, H. Drulis, W. M. Tambussi, J. D. Hettinger, and S. E. Lofland, J. Appl. Phys. **104**, 033502 (2008).

[21] R. S. Kumar, S. Rekhi, A. L. Cornelius, and M. W. Barsoum, Appl. Phys. Lett. **86**, 111904 (2005).

[22] B. Manoun, S. K. Saxena, H. P. Liermann, and M. W. Barsoum, J. Am. Ceram. Soc. **88**, 3489 (2005).

[23] M. W. Barsoum, T. El-Raghy, C. J. Rawn, W. D. Porter, H. Wang, E. A. Payzant, and C. R. Hubbard, J. Phys. Chem. Solids **60**, 429 (1999).

[24] B. Manoun, H. Yang, S. K. Saxena, A. Ganguly, M. W. Barsoum, B. E. Bali, Z. X. Liu, and M. Lachkar, J. Alloys Compd. **433**, 265 (2007).

[25] B. Manoun, S. K. Saxena, G. Hug, A. Ganguly, E. N. Hoffman, and M. W. Barsoum, J. Appl. Phys. **101**, 113523 (2007).

[26] B. Manoun, S. K. Saxena, and M. W. Barsoum, Appl. Phys. Lett. **86**, 101906 (2005).

[27] B. Manoun, S. K. Saxena, T. El-Raghy, and M. W. Barsoum, Appl. Phys. Lett. **88**, 201902 (2006).

[28] T. El-Raghy, M. Ali, and M. W. Barsoum, Metall. Mater. Trans. A **31A**, 1857 (2000).

[29] M. Radovic, A. Ganguly, M. W. Barsoum, T. Zhen, P. Finkel, S. R. Kalidindi, and E. Lara-Curzio, Acta Mater. **54**, 2757 (2006).

[30] P. Finkel, B. Seaman, K. Harrell, J. Palma, J. D. Hettinger, S. E. Lofland, A. Ganguly, M. W. Barsoum, Z. Sun, S. Li, and R. Ahuja, Phys. Rev. B **70**, 085104 (2004).

[31] S. E. Lofland, J. D. Hettinger, K. Harrell, P. Finkel, S. Gupta, M. W. Barsoum, and G. Hug, Appl. Phys. Lett. **84**, 508 (2004).

[32] P. Finkel, M. W. Barsoum, J. D. Hettinger, S. E. Lofland, and H. I. Yoo, Phys. Rev. B **67**, 235108 (2003).

[33] S. E. Lofland, J. D. Hettinger, T. Meehan, A. Bryan, P. Finkel, S. Gupta, M. W. Barsoum, and G. Hug, Phys. Rev. B **74**, 174501 (2006).

[34] S. Amini, A. Zhou, S. Gupta, A. DeVillier, P. Finkel, and M. W. Barsoum, J. Mater. Res. **23**, 2157 (2008).

[35] T. H. Scabarozi, A. Ganguly, J. D. Hettinger, S. E. Lofland, S. Amini, P. Finkel, T. El-Raghy, and M. W. Barsoum, J. Appl. Phys. **104**, 073713 (2008).

[36] S. Amini, M. W. Barsoum, and T. El-Raghy, J. Am. Ceram. Soc. **90**, 3953 (2007).

[37] B. Rupp, Scr. Metall. **22**, 69 (1988).

[38] C. A. Swenson, J. Phys. Chem. Ref. Data **12**, 179 (1983).

[39] NIST Standard Reference Material No. 736.

[40] G. Kresse and J. Furthmuller, Phys. Rev. B **54**, 11169 (1996).

[41] MedeA, 2.2.1 ed. (Materials Design, Angel Fire, NM).

[42] G. Kresse and D. Jouber, Phys. Rev. B **59**, 1758 (1999).

[43] P. E. Blöchl, Phys. Rev. B **50**, 17953 (1994).

[44] J. P. Perdew, K. Burke, and M. Ernzerhof, Phys. Rev. Lett. **77**, 3865 (1996).

[45] Y. Le Page and P. Saxe, Phys. Rev. B **65**, 104104 (2002).

[46] M. W. Barsoum, C. J. Rawn, T. El-Raghy, A. T. Procopio, W. D. Porter, H. Wang, and C. R. Hubbard, J. Appl. Phys. **87**, 8407 (2000).

[47] S. R. Kulkarni, M. Merlini, N. Phatak, S. K. Saxena, G. Artioli, S. Amini, and M. W. Barsoum, J. Alloys Compd. (in press).

[48] S. R. Kulkarni, M. Marco, N. Phatak, S. K. Saxena, G. Artioli, S. Gupta, and M. W. Barsoum, J. Am. Ceram. Soc. **90**, 3013 (2007).

[49] N. V. Tzenov and M. W. Barsoum, J. Am. Ceram. Soc. **83**, 825 (2000).

[50] T. El-Raghy, S. Chakraborty, and M. W. Barsoum, J. Eur. Ceram. Soc. **20**, 2619 (2000).

[51] M. W. Barsoum, I. Salama, T. El-Raghy, J. Golczewski, W. D. Porter, H. Wang, H. J. Seifert, and F. Aldinger, Metall. Mater. Trans. A **33A**, 2775 (2000).

[52] M. W. Barsoum, J. Golczewski, H. J. Seifert, and F. Aldinger, J. Alloys Compd. **340**, 173 (2002).

[53] A. Krajewski, L. D'Alessio, and G. D. Maria, Cryst. Res. Technol. **33**, 341 (1998).

[54] S. R. Kulkarni, R. S. Vennila, N. A. Phatak, S. K. Saxena, C. S. Zha, T. El-Raghy, M. W. Barsoum, W. Luo, and R. Ahuja, J. Alloys Compd. **448**, L1 (2008).

[55] M. Radovic, A. Ganguly, and M. W. Barsoum, J. Mater. Res. **23**, 1517 (2008).

[56] C. R. Houska, J. Phys. Chem. Solids **25**, 359 (1964).

[57] N. A. Dubrovinskaia, L. S. Dubrovinsky, S. K. Saxena, R. Ahuja, and B. Johansson, J. Alloys Compd. **289**, 24 (1999).

[58] H. O. Pierson, *Handbook of Refractory Carbides and Nitrides* (Noyes, Westwood, NJ, 1996).

[59] H. P. Liermann, A. K. Singh, B. Manoun, S. K. Saxena, V. B. Prakapenka, and G. Shen, Int. J. Refract. Met. Hard Mater. **22**, 129 (2004).

[60] C. R. Hquska, J. Am. Ceram. Soc. **47**, 310 (1964).

[61] H. P. Liermann, A. K. Singh, M. Somayazulu, and S. K. Saxena, Int. J. Refract. Met. Hard Mater. **25**, 386 (2007).

[62] H. L. Brown, P. E. Armstrong, and C. P. Kempter, J. Chem. Phys. **45**, 547 (1966).

[63] A. I. Gusev, A. A. Rempel, and A. J. Magerl, *Disorder and Order in Strongly Nonstoichiometric Compounds: Transition Metal Carbides, Nitrides, and Oxides* (Springer, New York, 2001).

[64] T. H. K. Barron, J. G. Collins, and G. K. White, Adv. Phys. **29**, 609 (1980).

[65] J. Wang and Y. Zhou, Phys. Rev. B **69**, 214111 (2004).

[66] A. T. Procopio, M. W. Barsoum, and T. El-Raghy, Metall. Mater. Trans. A **31A**, 333 (2000).

[67] B. Manoun, F. X. Zhang, S. K. Saxena, M. W. Barsoum, and T. El-Raghy, J. Phys. Chem. Solids **67**, 2091 (2006).

[68] A. Onodera, H. Hirano, T. Yuasa, N. F. Gao, and Y. Miyamoto, Appl. Phys. Lett. **74**, 3782 (1999).

[69] J. E. Spanier, S. Gupta, M. Amer, and M. W. Barsoum, Phys. Rev. B **71**, 012103 (2005).

[70] D. L. Anderson and O. L. Anderson, J. Geophys. Res. **75**, 3494 (1970).

[71] A. Jayaraman, B. Batlogg, R. G. Maines, and H. Bach, Phys. Rev. B **26**, 3347 (1982).

[72] L. Lopez-de-la-Torre, B. Winkler, J. Schreuer, K. Knorr, and M. Avalos-Borja, Solid State Commun. **134**, 245 (2005).

[73] G. Hug, M. Jaoun, and M. W. Barsoum, Phys. Rev. B **71**, 024105 (2005).

[74] Z. M. Sun and Y. C. Zhou, Phys. Rev. B **60**, 1441 (1999).

[75] Z. Sun, S. Li, R. Ahuja, and J. M. Schneider Solid State Commun. **129**, 589 (2004).

[76] B. Holm, R. Ahuja, and B. Johansson, Appl. Phys. Lett. **79**, 1450 (2001).

[77] Y. C. Zhou, Z. M. Sun, X. H. Wang, and S. Q. Chen, J. Phys. Condens. Matter **13**, 10001 (2001).

[78] J. M. Schneider, Z. Sun, R. Mertens, F. Uestel, and R. Ahuja Solid State Commun. **130**, 445 (2004).

[79] J. Y. Wang and Y. C. Zhou, Phys. Rev. B **69**, 144108 (2004).

[80] J. Y. Wang and Y. C. Zhou, J. Phys. Condens. Matter **16**, 2819 (2004).

[81] Z. M. Sun, D. Music, R. Ahuja, and J. M. Schneider, J. Phys. Condens. Matter **17**, 7169 (2005).

Solid State Communications 146 (2008) 498–501

Contents lists available at ScienceDirect

Solid State Communications

journal homepage: www.elsevier.com/locate/ssc

Weak electronic anisotropy in the layered nanolaminate Ti_2GeC

T.H. Scabarozi [a,b], P. Eklund [c], J. Emmerlich [c], H. Högberg [c], T. Meehan [b], P. Finkel [b], M.W. Barsoum [a], J.D. Hettinger [b], L. Hultman [c], S.E. Lofland [b,*]

[a] *Department of Materials Engineering, Drexel University, Philadelphia, PA 19104, United States*
[b] *Department of Physics and Astronomy, Rowan University, Glassboro, NJ 08028, United States*
[c] *Thin Film Physics Division, Department of Physics, Chemistry, and Biology, IFM, Linköping University, S-581 83 Linköping, Sweden*

ARTICLE INFO

Article history:
Received 2 January 2008
Received in revised form
14 March 2008
Accepted 17 March 2008 by A. Pinczuk
Available online 25 March 2008

PACS:
72.15.Eb
73.50.Jt
72.15.Gd

Keywords:
A. MAX phase
B. Thin films
D. Anisotropy
D. Electronic transport

ABSTRACT

We have investigated the anisotropy in electronic transport of the layered ternary Ti_2GeC by comparing the results of measurements on *c*-axis oriented epitaxial thin-film and polycrystalline bulk samples. The electrical conductivities, Hall coefficients, and magnetoresistances were analyzed within a multi-band framework. An adequate description of the magnetotransport data on the film with the highest mobility required the use of the explicit field-dependent conductivity tensor with three conduction bands. The analysis indicated that $n \approx p$, although with $n \approx 3.5 \times 10^{27}$ m^{-3}. The ratio of the *a*- to *c*-axis conductivities is small and contrary to theoretical predictions.

The layered machinable ternary carbides and nitrides with the general formula, $M_{n+1}AX_n$ (where M is an early transition metal, A is an A-group element and X is C or N) represent a new class of solids with unusual and sometimes unique combinations of mechanical, electrical, and thermal properties [1–3]. In a series of studies, magnetron sputtering has been shown to be a powerful method for synthesis of high-quality epitaxial MAX-phase thin films [4–7]. In addition to their potential technological importance in a number of applications, such as electrical-contacts and power-technology [8,9], measurements of epitaxial thin films allows an investigation of anisotropic electrical transport.

The MAX phases are known to be highly anisotropic with respect to plastic deformation (order-of-magnitude differences between dislocations motion along the *c* and *a* directions), while the difference in elastic moduli for different orientations is much smaller. For example, the calculated values of the elastic moduli in different directions of Ti_3SiC_2 differ by less than ∼15% [1,3,10,11]. However, there have been theoretical papers that have predicted significant anisotropies in electrical-transport properties [12,13].

The main purpose of the present work is to further improve our understanding of the electronic transport properties of the MAX phases in general and to investigate transport anisotropy for the model system Ti_2GeC in particular. To achieve this goal, we measured the electrical resistivity ρ, magnetoresistance MR, and Hall coefficient R_H of Ti_2GeC epitaxial thin films and compared the results to those of a polycrystalline bulk sample.

Epitaxial thin-film synthesis and microstructure details can be found elsewhere [5,14]. In general, *c*-axis oriented epitaxial films were grown on single-crystal *c*-axis sapphire substrates by dc magnetron sputtering at 900 °C. Deposition was performed in an ultra-high vacuum chamber from elemental targets operated in constant-current mode. As-deposited films were characterized by a combination of X-ray diffraction (XRD) and transmission electron microscopy (TEM) and were found to be predominantly single-phase epitaxial Ti_2GeC. All films were deposited on a TiC (111) seed layer, ≈20 nm thick, to facilitate epitaxial MAX-phase growth. The total film thickness was ≈200 nm.

Two different Ti_2GeC samples were investigated. One - henceforth referred to as sample A – was synthesized at a slightly higher Ge flux than the other (henceforth referred to as sample B), which was deposited with the nominal 2:1:1 (Ti:Ge:C) composition. As evidenced by XRD and TEM [14], sample A had a higher crystalline quality (2θ XRD-peak full width at half maximum

---

[*] Corresponding author. Tel.: +1 856 256 4382; fax: +1 856 256 4478.
E-mail address: lofland@rowan.edu (S.E. Lofland).

0038-1098/$ – see front matter © 2008 Elsevier Ltd. All rights reserved.
doi:10.1016/j.ssc.2008.03.026

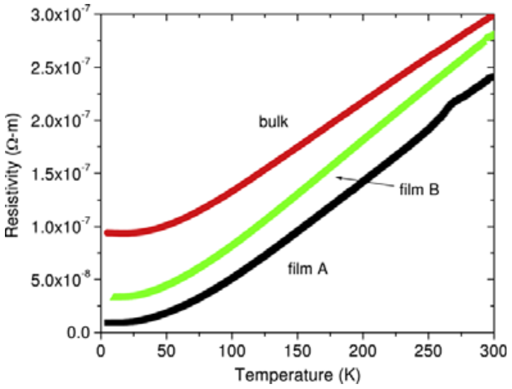

Fig. 1. Resistivity as a function of temperature for bulk and thin films of Ti_2GeC.

~0.4° and threading dislocation density ~ 10^9 cm^{-2}) than that of sample B. Sample A, however, contained Ge surface islands due to Ge segregation during growth; this does not affect the measured resistivity values [14].

Electrical transport measurements were carried out on the thin film specimens. R_H, ρ and MR were measured as a function of temperature T in the 1.8 K $\leq T \leq$ 300 K range and in magnetic fields B up to 9 T using a Quantum Design Physical Properties Measurement System (PPMS) using four and/or five probes. The details of the experimental procedures can be found elsewhere [15–17].

In our previous work [15–17], the small R_H values and the positive quadratic, non-saturating MR

$$\frac{\Delta\rho}{\rho(B=0)} = \alpha B^2 \tag{1}$$

where $\Delta\rho$ is the change in ρ with B and α the MR coefficient (see below) required a two-band model to analyze the experimental results. In the low-field limit of the two-band model, the following applies:

$$\sigma = \frac{1}{\rho} = e(n\mu_n + p\mu_p) \tag{2}$$

$$\alpha = \frac{\mu_n\mu_p np(\mu_n+\mu_p)^2}{(\mu_n n + \mu_p p)^2} \tag{3}$$

$$R_H = \frac{(\mu_p^2 p - \mu_n^2 n)}{e(\mu_p p + \mu_n n)^2} \tag{4}$$

where n and p are the electron and hole carrier densities, respectively; μ_n and μ_p their respective mobilities; e the electronic charge; σ the electrical conductivity; and α the MR coefficient defined in Eq. (1).

Fig. 1 compares the ρ values for the films and bulk sample. All samples show typical metallic-like conduction down to the lowest temperatures. The ρ values of both films are lower than that of the bulk sample. The room-temperature ρ values, $d\rho/dT$ for $T > 70$ K, and the residual resistivity ratios (RRR) are listed in Table 1.

In Fig. 2, the low-field R_H values are plotted as a function of T. The R_H values are mostly positive and small (1–2 orders of magnitude smaller) in comparison to those of typical transition-metal carbides like TiC [18]. The MR of film B and bulk sample were positive, quadratic and non-saturating. The low-field 5-K α value for film A (Fig. 3) is the highest ever recorded for a MAX phase to date. It is important to note that at lower temperatures (<150 K) and high magnetic fields, the MR of film A was *not* quadratic as is required for the application of Eqs. (2)–(4).

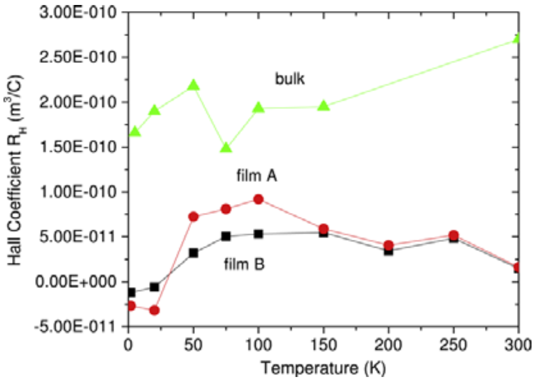

Fig. 2. Temperature dependence of R_H of bulk and thin film samples of Ti_2GeC.

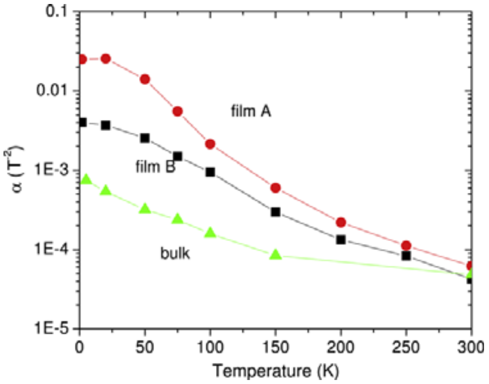

Fig. 3. Temperature dependence of the MR coefficient α.

With three equations (Eqs. (2)–(4)) but four unknowns, one can either solve for p as a function of n, or alternatively assume that $n \approx p$ (see below) [15–17,19,20]. Due to the small values of R_H, the positive quadratic, non-saturating MR, and to remain consistent with previous studies on bulk samples, we make the latter assumption and solve for $n(=p)$, μ_n and μ_p. The results are listed in Table 1. Despite the very different natures of the films as compared to the bulk sample, within the two-band framework, the results for the bulk samples and film B yielded $n \approx p \approx 1.6 \times 10^{27}$ m^{-3}.

However, for sample A at low temperatures (<150 K) the conditions for the low-field limit are not met for the full range of B used; i.e. ρ_{xx} is not quadratic and ρ_{xy} is not linear in B. It is thus necessary to use the general magnetotransport expressions [21]:

$$\sigma_{xx} = e\sum\frac{n_i\mu_i}{1+(\mu_i B)^2} \tag{5}$$

$$\sigma_{xy} = e\sum\frac{\mathrm{sgn}(n_i)n_i B\mu_i^2}{1+(\mu_i B)^2} \tag{6}$$

where $\sigma_{xx} = \rho_{xx}/(\rho_{xx}^2+\rho_{xy}^2)$, $\sigma_{xy} = \rho_{xy}/(\rho_{xx}^2+\rho_{xy}^2)$ and $\rho_{xy} = R_H B$. This inversion of the resistivity tensor is allowed since the measurements were taken in the isotropic *ab* plane of the sample. The inverted σ_{xx} and σ_{xy} are shown in Fig. 4a,b respectively. Also shown as dashed lines are the expectations for these conductivities in the low field limit. From fits to the data with Eqs. (5) and (6), it is clear that at least three conduction bands are required to achieve reasonable agreement to both σ_{xx} and σ_{xy} simultaneously

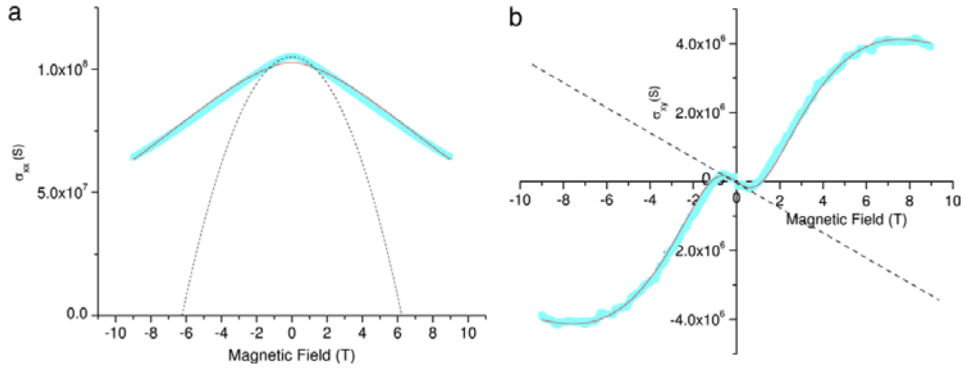

Fig. 4. Field dependence of (a) σ_{xx} and, (b) σ_{xy} of the Ti_2GeC film A at 1.8 K. The solid lines represent fits to Eqs. (3) and (4). The dotted black lines are extrapolated from the low-field results, viz. Eqs. (2) and (4).

Table 1
Summary of electronic parameters

Sample	ρ_{RT} (μΩ m)	dρ/dT (μΩ m/K)	RRR	$n \approx p$ (10^{27} m^{-3})	μ_n (5 K) (m^2/Vs)	μ_p (5 K) (m^2/Vs)
Ti_2GeC bulk[b]	0.30	0.00084	3.2	1.6 ± 0.3	0.027	0.027
Ti_2GeC- A	0.24	0.00097	25.3	3.7 ± 0.5[a]	0.088[a]	0.090[a]
				1.6 ± 0.3[b]	0.10[b]	0.098[b]
Ti_2GeC – B[b]	0.27	0.00100	8.6	1.6 ± 0.3	0.055	0.055

Note the averaging in carrier density is over the 5–300 K temperature range.

[a] Assuming three bands, an electron-like with a carrier density of $4 \pm 2 \times 10^{25}$ m^{-3} and a mobility at 5 K of 0.5 m^2/V s.

[b] Assuming two bands (see text).

(solid lines in Fig. 4). From a three-band fit, the feature at ≈ 0.5 T in σ_{xy} can be attributed to an electron-like band with high mobility ($\mu_1 = 0.5 \pm 0.1\,\mathrm{m^2/V\,s}$) yet small carrier concentration ($n_1 = 4 \pm 2 \times 10^{25}\,\mathrm{m^{-3}}$), and as a result that band actually has minimal contribution to the total conductivity. The majority of the conductivity can be described by two bands, one electron-like ($\mu_2 = 0.08 \pm 0.01\,\mathrm{m^2/V\,s}$, $n_2 = 3.7 \pm 0.5 \times 10^{27}\,\mathrm{m^{-3}}$) and one hole-like ($\mu_3 = 0.09 \pm 0.01\,\mathrm{m^2/V\,s}$, $n_3 = 3.7 \pm 0.5 \times 10^{27}\,\mathrm{m^{-3}}$).

It is important to note that while the n and p of the dominant bands from the three-band model are different from those extracted from the two-band model, the measurements are consistent between samples A, B, and bulk. Using only the low-field data for sample A, the two-band model yields an $n \approx p \approx 1.6 \times 10^{27}\,\mathrm{m^{-3}}$ (see Table 1) in accord with the other Ti_2GeC samples. The higher quality sample reveals the additional band. The bulk sample and film B have a third band but the manifestation of this band is not noticeable due to the lower non-intrinsic mobility of the carriers in this low concentration in these dirtier samples. The use of more than two bands to describe the data is unjustified as long as the results can be described by the low-field approximations (R_H linear and α quadratic in B), which was the case for the bulk and B samples.

However, had the mobility for sample A actually been as large as predicted by the two-band model, the change in conductivity with field (Eq. (5)) would have been much greater than that observed in Fig. 4a. The difference between the results obtained using Eqs. (5) and (6) and the low-field results (i.e. Eqs. (2) and (4)) is due to the large mobility of band 1. In the low-field limit $\sigma_{xx} \approx e\sum n_i\mu_i[1-(\mu_i B)^2] = \sigma_{xx}(B=0) - e\sum n_i\mu_i^3B^2$ and $\sigma_{xy} = e\sum \mathrm{sgn}(n_i)n_iB\mu_i^2$; i.e. the magneto-conductance and Hall conductivity are proportional to μ^3 and μ^2, respectively, and the mobilities have a significantly greater impact on the magnetotransport as compared to the carrier densities. Therefore, the results on sample A, although different than on samples that can be described by a two-band model, suggest that the assumption that $n \approx p$ is robust and that using only the low-field results provides, at worst, approximate values. Note that it is unlikely that there are additional significant conduction bands in Ti_2GeC since σ_{xx} at 9 T decreased about 40% from the zero-field value. That is, most of the conduction can be accounted for by just those three bands since Eq. (3) allows for a large decrease in conductivity of a band when $B > 1/\mu_i$.

The curves for the intrinsic resistivity (not shown), $\rho_{\mathrm{in}} = \rho - \rho_0$, where ρ_0 is the low-temperature residual resistivity are quite similar for the bulk and the epitaxial thin-film samples, suggesting that the resistivity is nearly isotropic. To estimate, we use an effective medium approximation for the intrinsic conductivity ($= 1/\rho_{\mathrm{in}}$) of the bulk sample, assuming spherical grains [22]. This yields

$$\frac{2(\sigma-\sigma_a)}{\frac{2}{3}\sigma+\frac{1}{3}\sigma_a}+\frac{(\sigma-\sigma_c)}{\frac{2}{3}\sigma+\frac{1}{3}\sigma_c}=0 \tag{7}$$

where σ_a and σ_c represent the intrinsic in-plane and out-of-plane conductivities, respectively, and σ is the average conductivity of the bulk sample. Using σ_a values from the films yields $\sigma_c/\sigma_a = 1.6 \approx 1$. Thus, the present results suggest nearly isotropic intrinsic mobilities, $\mu_{\mathrm{in}} \approx e\tau/m^*$, where τ is the scattering time and m^* the effective mass of the charge carriers.

It is worthwhile to put these observations in the context of the published band structure of Ti_2GeC [13]. The experimental observations that there is conduction by both holes and electrons and that the electronic transport is isotropic in that compound are in contrast to the expectations from the band structure calculation [13]. These results indicate that for all bands crossing the Fermi energy, E_F, with wave vector **k**, going from the Γ point to either the K or M point (i.e. in the ab plane), $1/m^* \propto (\partial^2\varepsilon/\partial k^2)_{\varepsilon=E_F} < 0$, where ε is the energy, indicating that conduction is solely by holes. Also, the calculation predicts that along the c direction, viz. **k** going from the Γ point to the A point, there are no bands crossing E_F, suggesting that the conductivity along the *c* direction should be rather small, i.e. $\sigma_c/\sigma_a \ll 1$, which is in contrast to these experimental observations.

Previously we have shown that the electrical transport can be described by electron-phonon interactions [23]. The magnitude of the resistivity, along the *c* axis and in the basal plane suggests that in both cases the process is dominated by scattering from the narrow *d* bands of Ti. In other words, the scattering time, both in and out of the basal planes, is dominated by the interaction of carriers in the *d* band with phonons. Estimates of the electron-phonon coupling constant λ taken by comparing calculated band structure density of states to the low-temperature linear term of the heat capacity indicate that the effective mass enhancement of the present materials is not more than 20%. This may be an indication that the effective mass does not have large anisotropy. This leads one to the surprising result that the scattering must be nearly isotropic, in spite of the obvious orientation dependence of the carrier bands. This gives credence to treating the electronic properties in the isotropic approximation [23].

In conclusion, the electronic transport in epitaxial thin films of Ti_2GeC was compared with that of bulk samples. For the film with the highest conductivity, the full expression for the magneto-transport was required, and the data indicated the need for a three-band model. The two dominant bands yielded $n = p \approx 3.5 \times 10^{27}$ m^3, somewhat higher but similar to that found in the bulk. The observed isotropic behavior in transport $(\sigma_c/\sigma_a) = 1.6 \approx 1$ is in contrast to the *ab initio* calculations.

Acknowledgments

This work was funded by the National Science Foundation (DMR-0503711), the Swedish Research Council (VR), the Swedish Agency for Innovation Systems (VINNOVA), and the Swedish Foundation for Strategic Research (SSF).

References

[1] M.W. Barsoum, Prog. Solid State Chem. 28 (2000) 201.
[2] M.W. Barsoum, in: R.W.C.K.H.J. Buschow, M.C. Flemings, E.J. Kramer, S. Mahajan, P. Veyssiere (Eds.), Encyclopedia of Materials Science and Technology, Elsevier, Amsterdam, 2006.
[3] M.W. Barsoum, M. Radovic, in: R.W.C.K.H.J. Buschow, M.C. Flemings, E.J. Kramer, S. Mahajan, P. Veyssiere (Eds.), Encyclopedia of Materials Science and Technology, Elsevier, Amsterdam, 2004.
[4] J. Emmerlich, H. Högberg, S. Sasvari, et al., J. Appl. Phys. 96 (2004) 4817.
[5] H. Högberg, P. Eklund, J. Emmerlich, et al., J. Mater. Res. 20 (2005) 779.
[6] H. Högberg, L. Hultman, J. Emmerlich, et al., Surface Coatings Tech. 193 (2005) 6.
[7] J.-P. Palmquist, S. Li, P.O.Å Persson, et al., Phys. Rev. B 70 (2004) 165401.
[8] P. Isberg, J.-P. Palmquist, U. Jansson, et al. International Patent WO03/046247 April 14, 2005.
[9] H.L. Tuller, M.A. Spears, R. Mlcak, US Patent 6544674, June 6, 2002.
[10] B. Holm, R. Ahuja, B. Johansson, Appl. Phys. Lett. 79 (2001) 1450.
[11] R. Yu, X.F. Zhang, X.F. He, et al., J. Mater. Res. 20 (2005) 1180.
[12] Y.C. Zhou, Z.M. Sun, Phys. Rev. B 61 (2000) 12570.
[13] Y.C. Zhou, H.Y. Dong, X.H. Wang, S.Q. Chen, J. Phys. Condens. Matt. 12 (2000) 9617.
[14] J. Emmerlich, P. Eklund, D. Rittrich, H. Högberg, L. Hultman, J. Mater. Res. 12 (2007) 2279.
[15] J.D. Hettinger, S.E. Lofland, P. Finkel, et al., Phys. Rev. B 72 (2005) 115120.
[16] P. Finkel, B. Seaman, K. Harrell, et al., Phys. Rev. B 70 (2004) 085104.
[17] P. Finkel, M.W. Barsoum, J.D. Hettinger, et al., Phys. Rev. B 67 (2003) 235108.
[18] F.A. Modine, M.D. Foegelle, C.B. Finch, et al., Phys. Rev. B. 40 (1989) 9558.
[19] H.I. Yoo, M.W. Barsoum, T. El-Raghy, Nature 407 (2000) 581.
[20] M.W. Barsoum, H.I. Yoo, T. El-Raghy, Phys. Rev. B 62 (2000) 10194.
[21] J.W. McClure, Phys. Rev. 112 (1958) 715.
[22] Z.D. Genchev, Supercond. Sci. Technol. 6 (1993) 532.
[23] S.E. Lofland, J.D. Hettinger, T. Meehan, A. Bryan, P Finkel, M.W. Barsoum, Phys. Rev. B 74 (2006) 174501.

JOURNAL OF APPLIED PHYSICS **104**, 033502 (2008)

Electrical, thermal, and elastic properties of the *MAX*-phase Ti_2SC

T. H. Scabarozi,[1] S. Amini,[1] P. Finkel,[1] O. D. Leaffer,[1] J. E. Spanier,[1] M. W. Barsoum,[1]
M. Drulis,[2] H. Drulis,[2] W. M. Tambussi,[3] J. D. Hettinger,[3] and S. E. Lofland[3,a)]
[1]*Department of Materials Science and Engineering, Drexel University, Philadelphia, Pennsylvania 19104, USA*
[2]*Polish Academy of Sciences, Trzebiatowski Institute of Low Temperature and Structure Research, P.O. Box 1410, 50-950 Wroclaw 2, Poland*
[3]*Department of Physics and Astronomy, Rowan University, Glassboro, New Jersey 08028, USA*

(Received 2 January 2008; accepted 20 May 2008; published online 1 August 2008)

We report on the electronic, thermal, and elastic properties of the layered ternary, Ti_2SC. Resistivity, Hall effect, and magnetoresistance were measured as a function of temperature between 2 and 300 K and at fields up to 9 T. The Hall coefficient is negative and roughly temperature independent. The transport results were analyzed within a two-band framework, with electrons as the dominant charge carrier. The room-temperature thermal conductivity (≈ 60 W/m K) is the highest of any *MAX* phase measured to date, with a substantial phonon contribution. The specific heat was measured from 2 to 300 K, yielding a Debye temperature of 765 K and in agreement with the Debye temperature of 745 K found from ultrasonic time-of-flight measurements. Young's, shear, and bulk moduli from the latter measurements were 290, 125, and 145 GPa, respectively. The calculated values of the lattice parameters ($a=3.2051$ Å and $c=11.2636$ Å), and Young's, shear, and bulk moduli (329, 138, and 179 GPa, respectively), based on the results of density functional theoretical simulations, compare favorably with measurements. © *2008 American Institute of Physics*. [DOI: 10.1063/1.2959738]

I. INTRODUCTION

Machinable ternary carbides and nitrides with the general formula, $M_{n+1}AX_n$ (where M is an early transition metal, A is an A-group element, and X is C or N) represent a class of solids with an unusual combinations of properties.[1–3] Two independent basal slip systems render them exceedingly damage tolerant, thermal shock resistant, and relatively tough.[3] Their most characteristic attribute, however, has to be the ease by which most materials within this family can be machined.

Studies on bulk materials have shown that most of the carbon-based *MAX* phases—especially the Ti-containing ones—are compensated conductors in that the concentrations of electrons and holes are nearly equal.[4–8] Their electron and hole mobilities are also quite comparable. Consistent with their compensated nature, many *MAX*-phase compounds exhibit a thermopower near zero over a wide range of temperatures.[5–8]

Original synthesis of Ti_2SC powder was achieved by Kudielka and Rhode,[9] followed by Nowotny.[10] Sulfur containing ternaries, as well as P and As, have a considerably shorter c-axis lattice parameter than those of all other *MAX* compounds. This results in the lowest c/a ratio of the M_2AX (211) compounds and is thus expected to exhibit different transport properties. For instance, Nb_2SC is a known superconductor, with a transition temperature of 3–5 K depending on C concentration.[11]

This paper examines the physical properties of Ti_2SC to gain insight into its elastic, electronic, thermal, and magnetic transport properties. To achieve this goal, we measured the electrical resistivity ρ, magnetoresistance coefficient α, Hall coefficient R_H, thermal conductivity κ, Seebeck coefficient, and heat capacity c_p, of fully dense Ti_2SC, and compared the measurements to results of density functional theoretical simulations.

II. EXPERIMENTAL AND ANALYSIS DETAILS

The sample fabrication details are described elsewhere.[12] In general, samples were hot pressed in a vacuum atmosphere hot press starting with—325 mesh Ti_2SC powder (3-ONE-2 LLC, Voorhees, NJ). The powder was wrapped in graphite foil, placed in a graphite die and heated up at 10 °C/min to 1500 °C and held at that temperature for 5 h. The chamber was pressurized at 500 °C to a maximum pressure of ~45 MPa that was maintained throughout the process.

Electrical and thermal transport measurements were carried out on samples with dimensions $1\times1\times10$ mm^3. R_H, ρ, and the magnetoresistance MR, were measured as a function of temperature in the 2–300 K range and in magnetic fields up to 9 T. Thermopower and thermal conductivity were measured between 2 and 400 K. All measurements were performed on a Quantum Design Physical Properties Measurement System with a four-probe technique. The details of the experimental procedures can be found elsewhere.[4,7,8]

Ultrasonic echo-pulse measurement of longitudinal v_l and shear v_s sound velocities were carried out at room temperature on polished $8\times8\times8$ mm^3 cubes cut from the same batch used for the transport and thermal measurements. For room temperature, Salol® was used as a bonding compound for the lithium niobate ultrasonic transducer tuned at its fundamental frequency of 15 MHz. Both sound velocity measurements were performed on a RAM 10000 from Ritec which has a resolution of 10 ppm time-of-flight resolution.

[a)] Electronic mail: lofland@rowan.edu.

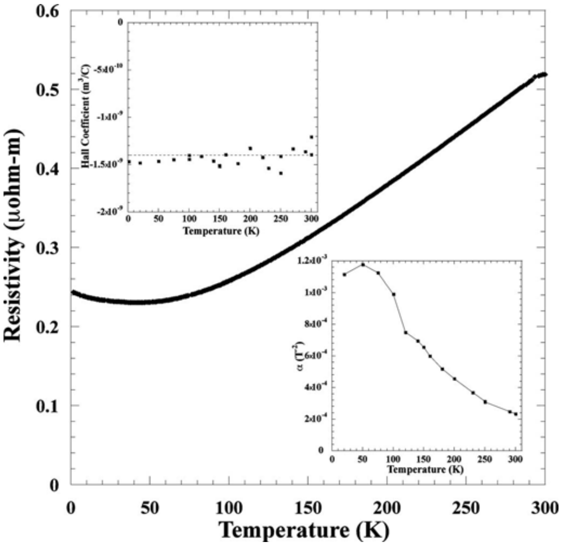

FIG. 1. Temperature dependence of resistivity. Note the linear temperature dependence at high temperatures and the slightly increasing value of resistivity at temperatures below 40 K. The upper-left inset shows the nearly temperature independent Hall coefficient, R_H. The dashed line in this inset is the average of R_H over that temperature range. The lower-right inset is the temperature dependence of the parabolic magnetic field dependence of the resistivity $\{\alpha B^2 = \rho(B) - \rho(0)/[\rho(0)]\}$.

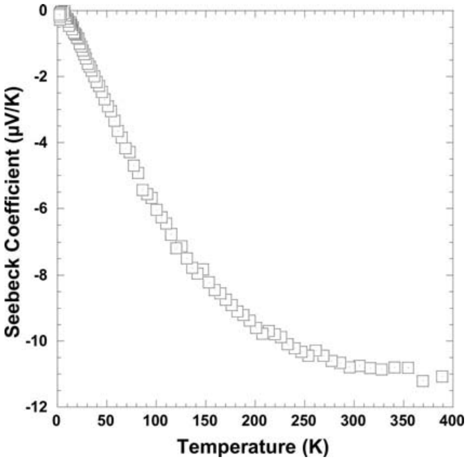

FIG. 2. Plot of the Seebeck coefficient as a function of temperature.

Other experimental details on this technique are discussed elsewhere.[8]

Raman spectra were taken at room temperature with a Renishaw 2000 spectrometer using Ar ion laser excitation (514.5 nm). Spectra were collected in static mode with ten accumulations with a 60 s exposure time. Experimental peak positions were calculated through Lorentzian fitting with a system resolution of 2 cm^{-1}.

Density functional theoretical (DFT) calculations of total energy, of interatomic forces, and of the stiffness tensor components were performed with the Vienna *ab initio* simulation package[13] (VASP) as implemented in MedeA (Materials Design, Angel Fire, NM), which has been used previously to predict energy-optimized structures in other *MAX* phases.[14] The relaxed lattice parameters and atomic positions were calculated by using the automated energy convergence in MedeA. Phonon and mechanical property calculations were started with the relaxed cell as the initial configuration. All calculations were done with a first-order Methfessel–Paxton smearing[15] with a width of 0.2 eV, and the generalized gradient approximation-Perdew, Burke and Ernzerhof/projector augmented-wave (GGA-PBE/PAW) (Refs. 16 and 17) pseudopotentials implemented by VASP (Ref. 18) using a 400 eV plane wave cutoff. These were chosen because of the metal-like electronic properties of the *MAX* phases. A $9\times 9\times 3$ *k*-point grid evenly spaced in the first Brillouin zone was used, chosen to be the same as the final *k*-point grid from the automated convergence, which was constrained to choose odd-sized grids. The moduli were calculated from the stiffness matrix which was calculated by perturbing the unit cell in five directions (necessitated by the hexagonal symmetry) to strains of 0.005, 0.01, and 0.02, calculating the energy after relaxing the atomic positions, and then using a least-squares fitting to determine the constants in the matrix.[19,20] The residual of the least-squares fitting was 3.7%.

Phonon modes were calculated from MedeA's implementation of PHONON,[21] using the direct approach with two-point displacements where select atom positions were perturbed according to the symmetry of the cell giving partial derivatives for the energy. Modes were determined from the eigenvectors of the force matrix computed. The same optimized unit cell was used rather than a supercell because our interest was limited to the gamma point energies. Raman modes were identified based on their symmetry following Ref. 14.

III. RESULTS

Figure 1 displays the electrical resistivity as a function of temperature. The linearly decreasing temperature dependence of this material shows metallic-like conduction down

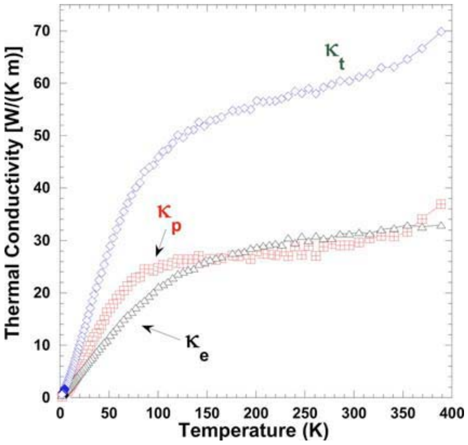

FIG. 3. (Color online) Temperature dependence of thermal conductivity. The solid squares represent the measured thermal conductivity, κ. Open triangles represent L_0T/ρ; solid triangles represent $k_p^{\min}$ determined by subtracting L_0T/ρ from κ.

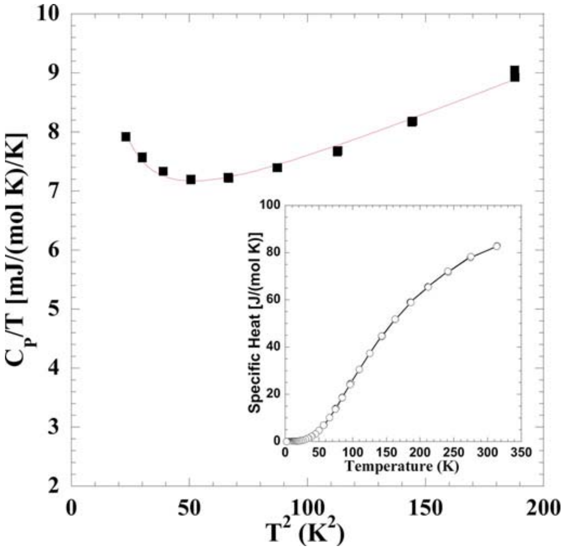

FIG. 4. (Color online) Plot of c_p/T vs T^2 at low temperatures. The increase at $T<7$ K is likely from a Schottky anomaly. The inset shows the c_p over the full temperature range measured.

to ~50 K. R_H, plotted as function of temperature, T, in the upper-left inset of Fig. 1, is relatively large, negative, and generally temperature independent. The lower-right inset of Fig. 1 is a plot of the temperature dependence of the MR coefficient, α, which is defined as $\{[\rho(B)-\rho(0)]/\rho(0)=\alpha B^2\}$, where $\rho(B)$ is the field-dependent resistivity. In general, the MR is positive, quadratic, and nonsaturating for all measured temperatures and magnetic fields up to 9 T.

The Seebeck coefficient as a function of temperature is shown in Fig. 2. At higher temperatures the thermopower is negative at roughly -10 μV/K. The thermal conductivity,κ, monotonically increases with temperature up to 390 K (Fig. 3). In Fig. 4, we present the low-temperature specific heat c_p/T as a function of T^2. The overall temperature dependence of c_p is shown as an inset.

Figure 5 shows the Raman spectra for Ti_2SC, which has four peaks associated with it. Table I lists experimental and calculated Raman peak positions, which are in excellent agreement. The longitudinal and shear sound velocities are $v_l \approx 8200$ m/s and $v_s \approx 5200$ m/s, respectively. Table II lists experimental and calculated physical properties such as the lattice constants and elastic moduli.

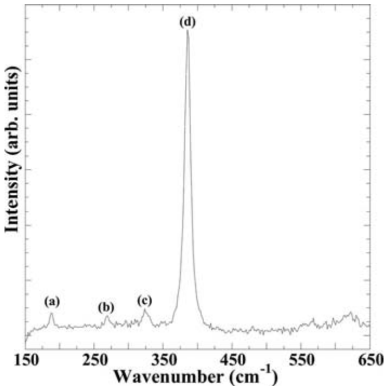

FIG. 5. Raman spectra at room temperature for Ti_2SC. Lorentzian fitted peaks are approximately (a) 188.1, (b) 269.9, (c) 325.4, and (d) 385.8 cm^{-1}.

TABLE I. Experimental and calculated Raman peak positions for Ti_2SC.

Measured positions (cm^{-1})	188	270	325	386
Calculated positions (cm^{-1})	185	264	315	381

IV. DISCUSSION

A large negative Seebeck coefficient and relatively large and roughly temperature independent negative R_H indicates a single-band, n-type, conductor. In the low-field limit of the single-band model, the following apply:

$$\sigma = \frac{1}{\rho} = en\mu_n, \tag{1}$$

$$R_H = \frac{1}{en}, \tag{2}$$

$$\alpha = \mu_n^2, \tag{3}$$

where n is the electron carrier density, μ_n is the electron mobility, e is the charge of an electron, and σ the electrical conductivity. This simple set of expressions allows a check for consistency between the temperature dependence of ρ and the transport data that can be extracted through the application of a magnetic field. For example, the magnitude and temperature dependence of ρ can be estimated from R_H and α. However, when these values are used, we find a temperature dependent ρ that is a factor of five *smaller* than the measured ρ.

Thus in order to properly analyze this system, a two-band model, used on most *MAX* phases studied to date, is required. In the low-field limit of the two-band model, the following apply:

$$\sigma = \frac{1}{\rho} = e(n\mu_n + p\mu_p), \tag{4}$$

$$\alpha \frac{\mu_n\mu_p np(\mu_n + \mu_p)^2}{(\mu_n + \mu_p p)^2}, \tag{5}$$

TABLE II. Comparison of experimental and calculated properties of Ti_2SC.

Parameter	Experimental value	Calculated value
a (nm)	0.3204	0.3205
c (nm)	1.1211	1.1264
v_l (m/s)	8200	8836
v_s (m/s)	5200	5446
E (GPa)	290	329
B (GPa)	145	179
μ (GPa)	125	138
ν	0.16	0.19
Θ_D (K)	765 ± 15, 745	735

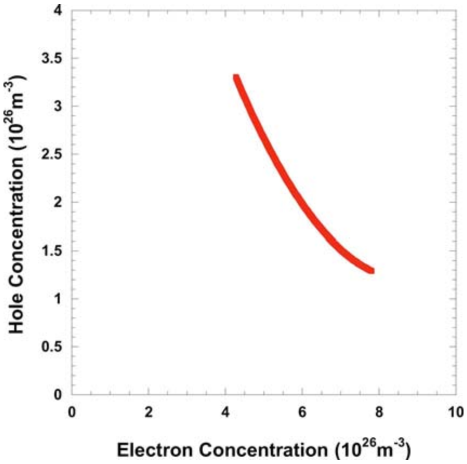

FIG. 6. (Color online) Allowed values for n and p, calculated from a two-band model.

$$R_H = \frac{(\mu_p^2 p - \mu_n^2 n)}{e(\mu_p p + \mu_n n)^2}, \tag{6}$$

where p is the hole carrier density; μ_p is the respective mobility. As there are four unknowns and three equations, a unique solution is not possible; however, it must be kept in mind that for all measurements at all fields and temperatures, there was no deviation from low-field behavior, implying that the scattering criterion of $\mu_n B$, $\mu_p B \ll 1$ is satisfied. Assuming $\mu B = 0.5$ and a maximum field of 10 T, this puts an upper limit on μ_n and μ_p of 0.05 $\mathrm{m^2/V\ s}$. Note that the selected criterion is not very restrictive since deviations from the low-field model would be expected in this case. Since n and p are independent of temperature for metal-like conductors which has been confirmed for most *MAX* phases examined to date,[4,7,8] the low-temperature results, where the mobility is highest, yield the graph shown in Fig. 6 for the allowed n and p values. Since the Seebeck is negative, we anticipate that $n > p$; i.e., $4 \times 10^{26}\ \mathrm{m^{-3}} < n < 8 \times 10^{26}\ \mathrm{m^{-3}}$ and $1.5 \times 10^{26}\ \mathrm{m^{-3}} < p < 3.5 \times 10^{26}\ \mathrm{m^{-3}}$. These values are about an order of magnitude smaller than those of other carbide *MAX* phases.[22]

The room-temperature value for κ (≈ 60 W/m K) is the largest measured in any *MAX*-phase material to date. Charge carriers and phonon transport entropy so, $\kappa = \kappa_e + \kappa_p$, where κ_e is the thermal conductivity due to the charge carriers and κ_p that due to the phonons. According the Wiedemann–Franz law

$$\frac{\kappa_e \rho}{T} = 2.45 \times 10^{-8} = L_0, \tag{7}$$

where L_0 is the Lorenz number. It is known that the value of L_0 is only correct at temperatures or much lower or higher than Debye temperature. Using L_0 at all temperatures provides an upper limit on the thermal conductivity due to charge motion and a minimum contribution from the phonon channel which will be designated as $\kappa_p^{\min}$. Application of this expression allows an extraction of $\kappa_p^{\min}$ from κ using the following:

$$\kappa = \kappa_p + \kappa_e = \kappa_p^{\min} + \frac{L_0 T}{\rho}. \tag{8}$$

After performing this manipulation of the data, we find that $L_0 T/\rho$ and $\kappa_p^{\min}$ are nearly equal over most of the temperature range measured (Fig. 3). This indicates that the enhanced thermal conductivity is a result of a large contribution from the phonon channel in comparison to that of other *MAX*-phase materials. A large phonon contribution to κ suggests a stiff material. This conclusion is consistent with the A-group element not rattling in the structure, as typical for all other A-group elements except Al, which is also relatively well bound.[2]

For most metal-like conductors, including the *MAX* phases, c_p is given as

$$c_p = \gamma T + \beta T^3 \tag{9}$$

at low temperature T, where γ is related to the electronic density of states, $N(E_F)$, and β relates to the phonon excitations. The data shown in Fig. 4 cannot be fit with Eq. (9) because of the increase in c_p at $T < 7$ K. This increase is most likely due to a Schottky anomaly. At temperatures where $k_B T >> \varepsilon$, where k_B is Boltzmann's constant and ε the energy difference between the two low-lying levels, c_p from a Schottky anomaly depends on temperature as AT^{-2}. Fitting the data with the sum of the three contributions yields a reasonably good fit with the fitting parameters γ, β, and A per unit cell being 11.2 $\mathrm{mJ/mole\ K^2}$, 0.034 $\mathrm{mJ/mole\ K^4}$, and 480 mJ/mole, respectively.

The γ term for Ti_2SC is in agreement with that found for other Ti-based 211 *MAX* phases and is given by

$$\gamma = \frac{(1 + \lambda)\pi^2 k_B^2 N(E_F)}{3}, \tag{10}$$

where λ is the electron-phonon coupling. Setting $\lambda = 0.2$ (an approximate value for other Ti-based carbide *MAX* phases),[22] one finds $N(E_F) \sim 5.7\ \mathrm{eV^{-1}/unit\ cell}$.

For the phonon contribution to c_p, the characteristic parameter is the Debye temperature Θ_D, which is related to β by

$$\Theta_D^3 = \frac{12\pi^4 Rx}{5\beta}, \tag{11}$$

where x is the number of atoms per formula unit and R is the gas constant. The values derived from the experimentally determined β are $\Theta_D = 765 \pm 15$ K. This is the largest value measured to date for a 211 material[23] and is commensurate with the values determined for the typically stiffer 312 *MAX*-phase materials and also consistent with the large phonon contribution to the thermal conductivity.

The Schottky-like anomaly probably arises from lattice defects. Such defects would be consistent with the upturn in the low-temperature resistivity and may be related with Fe impurities introduced during grinding of the powders since long collection time energy dispersive spectroscopy indicate about 2 wt % Fe. To test this, we synthesized Ti_2SC with 5 and 15 wt % Fe. Performing low-temperature c_p measurements and the analysis outlined above, we find a 10% and a 6% variation in γ and Θ_D, respectively, but a 400% increase in the strength of the *A* term with increasing Fe content. This suggests that while the presence of Fe may produce lattice defects of an unknown type, which manifest in the presence of a Schottky anomaly, they have minimal impact on the intrinsic elastic and electronic properties; i.e., γ and Θ_D.

The elastic Debye temperature, Θ_s, is given by

$$\Theta_s = \frac{h}{k_B}\left[\frac{N v_l^3 v_s^3}{4\pi(v_s^3 + 2v_l^3)}\right]^{1/3}, \tag{12}$$

where h is Planck's constant and N is the number of atoms per unit volume. Using this expression, we find that Θ_s is 745 K, which is comparable to that determined from c_p.

The Poisson ratio

$$\nu = \frac{v_l^2 - 2v_s^2}{(2v_l^2 - 2v_s^2)} \tag{13}$$

of the $M_{n+1}AX_n$ phases generally lies between 0.19 and 0.22.[2] The present measurements yield $\nu=0.16$, suggesting a weaker bonding anisotropy that of most *MAX* phases. The elastic moduli are defined by

$$E = v_s^2 \rho_M \frac{(3v_l^2 - 4v_s^2)}{(v_l^2 - v_s^2)},$$

$$\mu = \rho_M v_s^2,$$

$$B = \frac{\rho_M v_s^2}{3(1-2\nu)} \frac{3v_l^2 - 4v_s^2}{v_l^2 - v_s^2}, \tag{14}$$

where E, μ, and B are Young's, shear, and bulk moduli, respectively, and ρ_M the density of the material. Using these expressions, we find that E, μ, and B are 290, 125, and 145 GPa, respectively. In general, like other *ab initio* work on the *MAX* phases,[24–29] the agreement between theory and experiment is quite good. This coupled with the agreement between calculated and measured Raman spectra indicates a good understanding of the bonding in this material. We note in passing that while E and B are commensurate with those of most other 211 materials, the shear modulus is somewhat larger; approaching those in the 312 compounds.[2] We believe this, in part, explains the higher hardness of this material relative to the other *MAX* phases.[12]

This analysis suggests that Ti_2SC is unusual among *MAX*-phase family: the electronic carrier concentration is rather small, while elastic measurements indicate that this material is stiff, particularly in shear. This work relates to measurements on a material with A group from the VIA column of the Periodic Table which contains elements with high electron affinities. Enhanced bonding between S and the Ti-C units is consistent with all elastic and mechanical observations and with the observation that this material is not as readily machinable as other *MAX*-phase materials. We suspect that the origin of the increased modulus in this material is through a stronger bonding to the A-group planes, while in the 312 materials it is a result of a higher fraction of *M*-*X* bonds.

V. SUMMARY

The layered ternary, Ti_2SC, is an unusual *MAX* phase. The electrical conductivities, Hall coefficients, and magnetoresistances were analyzed within the low-field limit of a two-band framework, with electrons as the dominant charge carriers. Thermal transport results suggest that the phonon contribution to the thermal conductivity was as important as the electronic contribution. This suggests a stiff material, which agrees with ultrasonic time-of-flight measurements, yielding Young's, shear, and bulk moduli of 290, 125, and 145 GPa, respectively. Finally, the results of DFT simulations of lattice parameters, moduli, and zone-center phonon energies are in good agreement with experimental results.

ACKNOWLEDGMENTS

This work was supported by the NSF under Grant No. DMR 0503711. O.D.L gratefully acknowledges support from the U.S. Department of Education GAANN Fellowship under Award No. P200A060117.

[1] M. W. Barsoum, Prog. Solid State Chem. **28**, 201 (2000).
[2] M. W. Barsoum, in *Encyclopedia of Materials Science and Technology*, edited by R. W. C. K. H. J. Buschow, M. C. Flemings, E. J. Kramer, S. Mahajan, and P. Veyssiere (Elsevier, Amsterdam, 2006).
[3] M. W. Barsoum and M. Radovic, in *Encyclopedia of Materials Science and Technology*, edited by R. W. C. K. H. J. Buschow, M. C. Flemings, E. J. Kramer, S. Mahajan, and P. Veyssiere (Elsevier, Amsterdam, 2004).
[4] J. D. Hettinger, S. E. Lofland, P. Finkel, J. Palma, K. Harrell, S. Gupta, A. Gunguly, T. El-Raghy, and M. W. Barsoum, Phys. Rev. B **72**, 115120 (2005).
[5] H. I. Yoo, M. W. Barsoum, and T. El-Raghy, Nature (London) **407**, 581 (2000).
[6] M. W. Barsoum, H. I. Yoo, I. K. Polushina, V. Y. Rud, Y. V. Rud, and T. El-Raghy, Phys. Rev. B **62**, 10194 (2000).
[7] P. Finkel, B. Seaman, K. Harrell, J. D. Hettinger, S. E. Lofland, A. Ganguly, M. W. Barsoum, Z. Sun, S. Li, and R. Ahuja, Phys. Rev. B **70**, 085104 (2004).
[8] P. Finkel, M. W. Barsoum, J. D. Hettinger, S. E. Lofland, and H. I. Yoo, Phys. Rev. B **67**, 235108 (2003).
[9] H. Kudielka and H. Rhode, Z. Kristallogr. **114**, 447 (1960).
[10] H. Nowotny, Prog. Solid State Chem. **5**, 27 (1971).
[11] K. Sakamaki, W. Wada, H. Nozaki, Y. Onuki, and M. Kawai, Solid State Commun. **112**, 323 (1999).
[12] S. Amini, M. W. Barsoum, and T. El-Raghy, J. Am. Ceram. Soc. **90**, 3953 (2007).
[13] G. Kresse and J. Furthmuller, Phys. Rev. B **54**, 11169 (1996).
[14] J. E. Spanier, S. Gupta, S. Amer, and M. W. Barsoum, Phys. Rev. B **71**, 012103 (2005).
[15] M. Methfessel and A. T. Paxton, Phys. Rev. B **40**, 3616 (1989).
[16] J. P. Perdew, K. Burke, and M. Ernzerhof, Phys. Rev. Lett. **77**, 3865 (1996).
[17] P. E. Blöchl, Phys. Rev. B **50**, 17953 (1994).
[18] G. Kresse and J. Joubert, Phys. Rev. B **59**, 1758 (1999).
[19] Y. Le Page and P. Saxe, Phys. Rev. B **63**, 174103 (2001).
[20] Y. Le Page and P. Saxe, Phys. Rev. B **65**, 104104 (2002).
[21] K. Parlinski, Z. Q. Li, and Y. Kawazoe, Phys. Rev. Lett. **78**, 4063 (1997).
[22] S. E. Lofland, J. D. Hettinger, T. Meehan, A. Bryan, P. Finkel, S. Gupta, M. W. Barsoum, and G. Hug, Phys. Rev. B **74**, 174501 (2006).
[23] S. E. Lofland, J. D. Hettinger, K. Harrell, P. Finkel, S. Gupta, M. W. Barsoum, and G. Hug, Appl. Phys. Lett. **84**, 508 (2004).
[24] B. Holm, R. Ahuja, and B. Johansson, Appl. Phys. Lett. **79**, 1450 (2001).
[25] G. Hug and E. Frie, Phys. Rev. B **65**, 113104 (2002).
[26] G. Hug, M. Jaouen, and M. W. Barsoum, Phys. Rev. B **71**, 024105 (2005).
[27] N. Medvedeva, D. Novikov, A. Ivanovsky, M. Kuznetsov, and A. Freeman, Phys. Rev. B **58**, 16042 (1998).
[28] Z. Sun, S. Li, R. Ahuja, and J. M. Schneider, Solid State Commun. **129**, 589 (2004).
[29] Z. M. Sun and Y. C. Zhou, Phys. Rev. B **60**, 1441 (1999).

JOURNAL OF APPLIED PHYSICS **104**, 073713 (2008)

Electronic and thermal properties of $Ti_3Al(C_{0.5},N_{0.5})_2$, $Ti_2Al(C_{0.5},N_{0.5})$ and Ti_2AlN

T. Scabarozi,[1,2] A. Ganguly,[2] J. D. Hettinger,[1] S. E. Lofland,[1] S. Amini,[2] P. Finkel,[1]
T. El-Raghy,[3] and M. W. Barsoum[2,a)]
[1]Department of Physics and Astronomy, Rowan University, Glassboro, New Jersey 08028, USA
[2]Department of Materials Science and Engineering, Drexel University, Philadelphia, Pennsylvania 19104, USA
[3]3ONE2, Voorhees, New Jersey 08043, USA

(Received 7 March 2008; accepted 17 July 2008; published online 3 October 2008)

In this paper we report on the electronic, magnetotransport, thermoelectric, and thermal properties of $Ti_3Al(C_{0.5},N_{0.5})_2$, $Ti_2Al(C_{0.5},N_{0.5})$, and Ti_2AlN. The electrical conductivities, Hall coefficients, and magnetoresistances are analyzed within a two-band framework and compared with the end members, Ti_2AlC and Ti_3AlC_2. The analysis shows that all compounds are compensated conductors with hole and electron carrier densities of about 1.5×10^{27} m^{-3}. The room temperature thermal conductivities of the carbonitrides are both over ≈50 W/mK, with the phonon contribution of $Ti_3Al(C_{0.5},N_{0.5})_2$ particularly large at over 35 W/mK. The low-temperature specific heat of $Ti_3Al(C_{0.5},N_{0.5})_2$ and $Ti_2Al(C_{0.5},N_{0.5})$ yield Debye temperatures of 685 and 724 K, respectively, comparable to those of the end members. © *2008 American Institute of Physics*.

[DOI: 10.1063/1.2979326]

I. INTRODUCTION

Recent interest in an unusual class of 50+ layered ternary carbides and nitrides [with the general chemical formula $M_{\nu+1}AX_\nu$ (MAX), where $\nu=1-3$, M is an early transition metal, A is an A element (mostly IIIA and IVA), and X is either C and or N][1,2] has intensified because of their potential use in a number of applications. As more is understood about these solids more applications are being identified. Their potential in applications results partially because of their physical structure, i.e., comprised of $M_{\nu+1}X_\nu$ layers interleaved with pure A-group layers; because of how they deform as a result of this layered structure they are readily machinable, despite the fact that some of them are elastically quite stiff, as well as lightweight.[3] They are also excellent electric and thermal conductors.[2] When combined with the low friction coefficients associated with their basal planes,[4] and the excellent oxidation resistances of some of them,[5,6] their potential in applications such as rotating contacts at room and elevated temperatures becomes obvious.

These materials fall into groups with $\nu=1$, 2, and 3. There are nearly 50 with $\nu=1$, 5 [Ti_3SiC_2,[1] Ti_3GeC_2,[1] Ti_3AlC_2,[1] Ti_3SnC_2,[7] and Ta_3AlC_2[8] with $\nu=2$, and 6 [Ti_4AlN_3,[2] Ta_4AlC_3,[9] Ti_4SiC_3,[10] Ti_4GeC_3,[11] Nb_4AlC_3,[12] and V_4AlC_3[13] with $\nu=3$. Much of the interesting physics leading to the properties of these materials can best be evaluated and understood through systematic investigations where the elemental constituents are varied, while maintaining the same crystallographic structure. For example, in a recent paper[14] we compared the electronic and thermal properties of M_2AlC phases, where M was Ti, V, Cr, and Nb in 5–300 K, and concluded that these compounds were nearly compensated conductors, viz., the densities and mobilities of electrons and holes were almost equal over the temperature regime explored. The same is true of Ti_3SiC_2, Ti_3GeC_2, and their solid solutions.[15]

In this paper—which is a continuation of our efforts in understanding the chemistry/physical property relationships in these compounds—we report on the effect of substitutions at the X-sites on the thermal and electrical properties. As far as we are aware—and with the exception of recent work,[16–18] in which we showed that the replacement of C by N in Ti_2AlC and $Ti_3Al(C_{0.5},N_{0.5})_2$, henceforth referred to as Ti_3AlCN, results in the continuous shrinking of the lattice parameters—this aspect has to date not been explored. Interestingly the monotonic decrease in unit cell volume was not always concomitant with increases in elastic properties, as one would expect. This discrepancy was attributed to the presence of vacancies on the N and/or Al sites as C was replaced by N.[16,17] Herein we further explore the effect of substitutions on the X-sites on properties by measuring the electrical resistivities, Hall and Seebeck voltages, magnetoresistances, and thermal properties of select $Ti_2AlC_{0.5}N_{0.5}$, Ti_3AlCN, and Ti_2AlN. We also compare these with previous results on Ti_2AlC,[14] Ti_3AlC_2, and $Ti_4AlN_{2.9}$.[19]

II. EXPERIMENTAL DETAILS

Polycrystalline bulk samples were fabricated by reactively hot isostatically pressing a stoichiometric mixture of powders of the constituent elements. The Ti_3AlCN and $Ti_2AlC_{0.5}N_{0.5}$ samples were made from stoichiometric mixtures of Ti, Al, AlN (−200 mesh, 99.0% Cerac Inc., WI), and graphite powders, ball milled overnight followed by cold pressing to ≈600 MPa. The green bodies were presintered in a vacuum furnace at 525 °C for 2 h then at 625 °C for 10 h. The presintered pellets were then sintered in a hot isostatic

---

[a)]Electronic mail: barsoumw@drexel.edu.

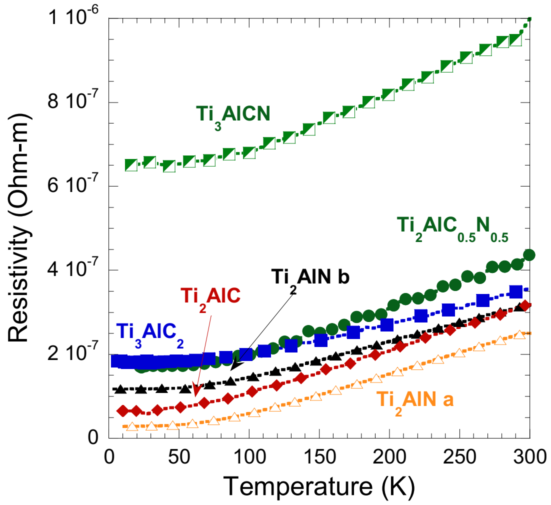

FIG. 1. (Color online) Temperature dependence of resistivity.

press at a temperature of 1400 °C and pressure of 100 MPa for 10 h. The processing and microstructural details for Ti_3AlCN can be found elsewhere.[16–18]

Two Ti_2AlN samples were studied. The first, henceforth labeled Ti_2AlN-a, was made by hot pressing Ti (99% pure, −325 mesh, Alfa Aesar, Ward Hill, MA) and AlN (99.0% pure, −200 mesh, Alfa Aesar, Ward Hill, MA) powders that were stoichiometrically weighed, ball milled for 12 h, and then dried in vacuum for 12 h at 150 °C. The powder mixture was then poured and wrapped in graphite foil, placed in a graphite die, and heated, under vacuum, at 10 °C/min—in a graphite-heated hot press (Series 3600, Centorr Vacuum Industries, Somerville, MA) up to 1400 °C and held at that temperature for 8 h. A load, corresponding to a stress of ~45 MPa, was applied when the temperature reached 500 °C and maintained throughout the run. The second, henceforth referred to as Ti_2AlN-b, was made by pressureless sintering of prereacted Ti_2AlN powders (3ONE2, Voorhees, NJ). All samples were at least 99% of their theoretical density.[18]

Parallelepiped-shaped specimens with approximate dimensions of $1\times1\times10$ mm^3 were cut from the bulk samples. The electrical resistivity ρ, Hall voltage V_H, and magnetoresistance were measured for temperatures T ranging between 5 and 300 K and magnetic field B, of up to 5 T with a quantum design physical property measurement system (PPMS). Details are given elsewhere.[14,15,19–21] The Seebeck coefficients, specific heat capacities c_p, and thermal conductivities κ were measured from 1.8 to 300 K in zero magnetic field, also with the PPMS.

III. RESULTS AND DISCUSSION

Results of the T dependences of the electrical transport parameters are shown in Figs. 1–3. Figure 1 demonstrates the linear dependence of ρ as a function of T as is typical of materials in this family and their metal-like conduction[14,15,20,21] resulting from the large density of states at the Fermi level $N(E_F)$.[22,23] The low-temperature residual resistivity and the residual resistivity ratio (RRR), defined as $\rho(300\ \text{K})/\rho(5\ \text{K})$, are measures of sample quality such as in metals High residual resistivity values and small RRRs suggest sizable scattering from impurities, vacancies, or other defects. As can be seen in Fig. 1, the residual resistivity is highest for Ti_3AlCN. In general, the materials containing both N and C have higher residual resistivities and lower RRRs than the materials containing only N or C (Table I). The RRR value of the Ti_2AlN-a sample was 8.6, which is not only significantly higher than that of Ti_2AlN-b, but it also has the highest RRR value measured in this work.

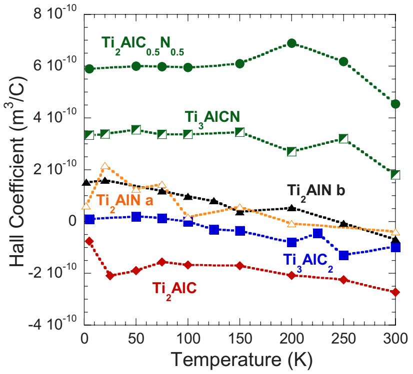

FIG. 2. (Color online) Temperature dependence of Hall coefficients.

Wet chemical analysis and electron dispersive spectroscopy of the Ti_2AlN-a and Ti_2AlN-b samples suggest that they have the following slightly different chemistries, respectively, $Ti_2Al_{1.04}N_{0.98}$ and $Ti_2AlN_{0.95}$, with an uncertainty of ±0.03 in the stoichiometric values. Interestingly, the Ti_2AlN-b sample was stoichiometric for the M:A ratio as compared to Ti_2AlN-a, but showed a larger nitrogen deficiency. Where the excess Al in Ti_2AlN-a is situated is not understood. More importantly, how that somehow enhances the conductivity is also not understood. Given that it is well established that vacancies in binary transition carbides and nitrides are potent electron scatterers,[24] their lower concentration in the a-sample could explain the difference. It would

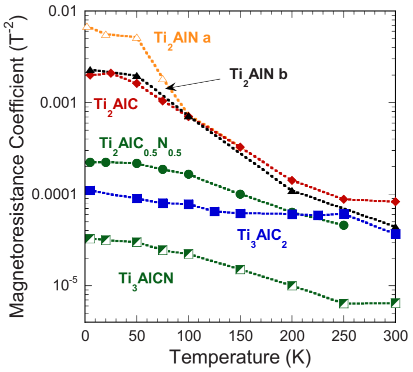

FIG. 3. (Color online) Temperature dependence of the magnetoresistance coefficient α, which correlates directly with the resistivity (Fig. 1).

TABLE I. Summary of electrical transport parameters as calculated from the room temperature and 4 K resistivity, R_H and α results for the X-site substituted solid solutions assuming $\mu_n=\mu_p=\sqrt{\alpha}$.

Composition	Temperature (K)	ρ ($\mu\Omega$ m)	RRR	R_H ($\times 10^{11}$) m^3/C	$\alpha(T^{-2})$ (m^4/V^2 s^2)	μ_n (m^2/V s)	μ_p (m^2/V s)	n (10^{27}/m^3)	p (10^{27}/m^3)	Ref.
Ti_3AlC_2	300	0.353	1.95	−1.2	3.7×10^{-5}	0.0063	0.006 3	1.41	1.4	This work
	4	1.81		1.0	1.1×10^{-4}	0.01	0.01	1.71	1.73	
	300	0.387	⋯	−1.2	4.0×10^{-5}	0.0046–0.0042	0.0054−0.003	1.5–1.6	2–4	19
Ti_3AlCN	300	0.40	1.5	17.4	6.5×10^{-6}	0.0025	0.0025	2.5	3.5	This work
	4	0.27		33	3.3×10^{-5}	0.0057	0.0057	1.8	2	
Ti_2AlC	300	0.36	4.9	−27	2.6×10^{-5}	0.0051	0.0051	1.39	1.2	This work
	4	0.073		−8	4.5×10^{-4}	0.021	0.021	2.1	1.9	
	300	0.36	4.8	−28	2.0×10^{-4}	0.009	0.0082	≈1	≈1	14[a]
$Ti_2Al(C_{0.5},N_{0.5})$	300	0.36	2.86	45.6	3.5×10^{-5}	0.0059	0.0059	1.1	1.8	This work
	4	0.126		60	2.2×10^{-4}	0.015	0.015	1.2	2.4	
Ti_2AlN-a	300	0.25	8.5	−3.9	1.7×10^{-4}	0.012	0.012	1.02	1.05	
	4	0.029		6.1	6.9×10^{-3}	0.083	0.083	1.24	1.3	
Ti_2AlN-b	300	0.343	2.8	−7	4.8×10^{-5}	0.0063	0.0063	1.46	1.4	
	4	0.123		16	2.0×10^{-4}	0.014	0.014	1.6	2.0	
$Ti_4AlN_{2.9}$	300	2.61	1.1	90	3.0×10^{-7}	0.000 55	0.000 55	0.8	3.51	This work
	300	2.61		90 ± 5	3.0×10^{-7}	⋯	0.000 34	⋯	7.0	19[b]

[a] Assuming $n=p$.

[b] Assuming a single band model.

also be consistent with the fact that $Ti_4AlN_{2.9}$, with its nitrogen deficiency, has the lowest mobility of all MAX phases measured to date (Table I). To further explore this facet we annealed the Ti_2AlN-b sample in Ar at 1200 °C for 6 h, before cooling it to room temperature in 20 h. This procedure increased the RRR value from 2.8 to 3.2, presumably due to the annealing out of some of the defects. These comments notwithstanding, more work is needed to better understand the relationship between stoichiometry and transport in these materials. A fruitful area of research would be to explore the effects of stoichiometry on the transport properties of the N-containing MAX phases.

The Hall coefficient R_H is plotted in Fig. 2 as a function of T. In all cases, the values are small. The carrier concentrations should be T independent since they are metals from an electronic conduction perspective. For the materials containing only N or C, the tendency is for R_H to become more holelike as the temperature is decreased, suggesting that the hole mobility increases faster with decreasing temperatures than the electron mobility. In the materials containing both C and N, the increased scattering due to defects removes or obscures this temperature dependent behavior.

Figure 3 plots the temperature dependence of the quadratic magnetoresistance coefficient α [see Eq. (2), below]. Comparing Figs. 1 and 3, it is clear that α scales inversely with the resistivity. In general, α scales with the mobility of the carriers (see below). The thermopower results, shown in Fig. 4, are small and consistent with the compensated nature of these materials.

To better understand the mechanisms of electronic conduction in these solids, it is useful to analyze the magnetotransport results. For internal consistency a multiband model is required to explain the results. Within a two-band framework, in the low-field limit (requiring $\mu_n B$ and $\mu_p B$ <0.25),[25] R_H is given by

$$R_H=\frac{(\mu_p^2 p-\mu_n^2 n)}{e(\mu_p p+\mu_n n)^2}, \tag{1}$$

where μ_p, μ_n, p, and n are the hole and electron mobilities and the hole and electron concentrations, respectively. In the two-band model the magnetoresistance $\Delta\rho/\rho$, defined as $\rho(B)-\rho(B=0)/\rho(B=0)$, and the electrical conductivity σ are described by

$$\frac{\Delta\rho}{\rho}=\alpha B^2=\frac{\mu_n\mu_p np(\mu_p+\mu_n)^2}{(n\mu_n+p\mu_p)^2}B^2, \tag{2}$$

$$\sigma=\frac{1}{\rho}=e(n\mu_n+p\mu_p). \tag{3}$$

In Eqs. (1)–(3) there are four unknowns; to solve the problem an additional equation is required for a unique solution. There is one additional constraint, since all magnetotransport

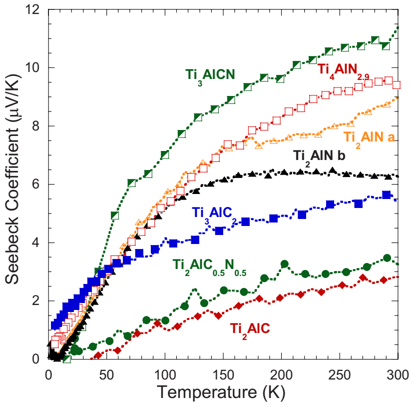

FIG. 4. (Color online) Plot of the Seebeck coefficients as a function of temperature.

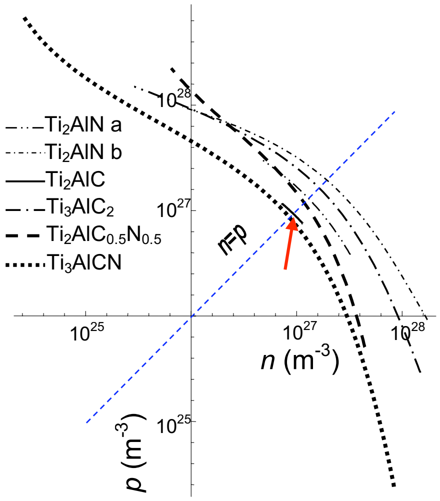

FIG. 5. (Color online) Allowed n and p values at 5 K from Eqs. (1)–(3). Note log-log nature of plot. Arrow points to quite narrow range of possible values for Ti$_2$AlC.

data were well fit by the low-field equations and our maximal applied field was 5 T, this requires that μ_n and μ_p < 0.05 m^2/V s.[25] Figure 5 shows the implicit dependence of p on n for various samples at 5 K along with the line for $n = p$. To obtain these results we simply solved for n in terms of p; no other assumptions were made. The 5 K analysis is shown since the mobilities are largest at low temperatures, where the most stringent limits are placed on the allowed n and p values, and, as stated earlier, n and p should not be functions of temperature, given the metallic-like conductivity of these compounds. In any case, the curves at higher temperatures effectively lie on top of the low-temperature ones, but with a larger range of allowed n and p values.

All samples can be fitted to $n=p$. In fact, Ti$_2$AlC must be very nearly compensated since the range of allowed n and p values denoted by an arrow in Fig. 5 is quite narrow. The range of n and p values allowed for the other compounds, including Ti$_2$AlC$_{0.5}$N$_{0.5}$ and Ti$_3$AlCN, is larger. However, since they bracket the Ti$_2$AlC values, it seems reasonable to conclude that that $n=p$ for all compounds investigated here, except Ti$_4$AlN$_{2.9}$. This is especially true since the vast majority of MAX phases, especially the Ti-based ones, have to date also been found to be compensated.[14,15,19–21] This important conclusion is bolstered by the fact that—except for Ti$_4$AlN$_3$, which should be a semimetal if stoichiometric[31]—the density of states of the Ti d bands dominate the electronic transport.[22,26–30,32]

In our previous work to obtain some sense of the ranges in the n, p, μ_n, and μ_p, we assumed that $n=p$ and solved for the mobilities. This procedure resulted in electron and hole mobility values that were quite close. Herein, to gain further insight, we use a slightly different approach that we believe sheds even more light on the matter. We assumed that $\mu_p = \mu_n$, at which time Eq. (2) degenerates to

$$\mu_p = \mu_n = \sqrt{\alpha}. \tag{4}$$

Once the mobilities are determined, their values are inserted in Eqs. (1) and (3) and n and p are solved for. A major advantage of this approach is its simplicity. It is also trivial to match the sign of R_H to the majority carrier. Before proceeding much further, it is vital to note that because for the most part $n \approx p$ and $\mu_p \approx \mu_n$, both this approach and our previous approach[14] yield quite comparable results. For example, assuming $n=p$, we find for Ti$_3$AlC$_2$ that $n=1.5-1.6 \times 10^{27}$ m^{-3} and $p=2.0-4.0\times 10^{27}$ m^{-3}, with μ_p and μ_n both of the order of 0.004 m^2/V s.[19] Similarly, the carrier concentrations for Ti$_2$AlC were estimated to be 1.0×10^{27} m^{-3}.[14] These values compare well with those listed in Table I for Ti$_3$AlC$_2$ and Ti$_2$AlC. In short, none of the conclusions reached in this work would change if the assumption that $n=p$ is made instead. In reality, it is more likely that neither assumption is exactly correct; the actual situation is most probably somewhere in between. With these caveats, a perusal of the results listed in Table I clearly indicates that despite wide variations $[(13\pm 20)\times 10^{-11}$ m^3/C$]$ in R_H values, α $[(1.5\pm 2)\times 10^{-7}]$, mobilities ($0.016\pm 0.02$ m^2/V s), and temperature (4–300 K), the average and standard deviations in n and p are, respectively, $(1.5\pm 0.4)\times 10^{27}$ and $(1.8\pm 0.7)\times 10^{27}$ m^{-3}. (In all cases, the first number denotes the average and the second the standard deviation. The values for Ti$_4$AlN$_{2.9}$ were not included in the average.) The small standard deviations in n and p observed is a *remarkable* result—especially given the different chemistries, solid solution scattering, etc.,—and one that cannot be easily dismissed. It is, however, a result that is totally consistent with the problem at hand; the only constant should be the density of carriers—determined by the electronic structure, specifically in this case the Ti–Ti d orbitals—as observed. The electronic conduction of Ti-containing MAX phases is believed to occur almost exclusively in the d-d orbitals of the Ti atoms.[22,26–30] The results presented here confirm this notion.

Like in previous work, the mobilities at 5 K are related to the quality of the samples as measured by the RRR (Table I).

The sign of the Seebeck voltage is often used to qualitatively determine the sign of the dominant charge carrier. With this in mind, it may be expected that the Seebeck voltages should roughly reflect the sign and shape of R_H as a function of temperature. Comparing the Hall (Fig. 2) and the Seebeck (Fig. 4) coefficients it is clear there are *no* obvious correlations between them. Three of the materials have clearly changing signs of the Seebeck voltage with no corresponding changes in R_H, again providing evidence that these compounds are nearly compensated.

Figure 6 shows the low-temperature heat capacity for the carbonitrides. Fitting c_p to

$$c_p = \gamma T + \beta T^3, \tag{5}$$

yields a γ value of 2.6 mJ/mol Ti K^2, for both Ti$_2$AlC$_{0.5}$N$_{0.5}$ and Ti$_3$AlCN γ is related to $N(E_F)$, renormalized by the electron-phonon coupling constant λ,

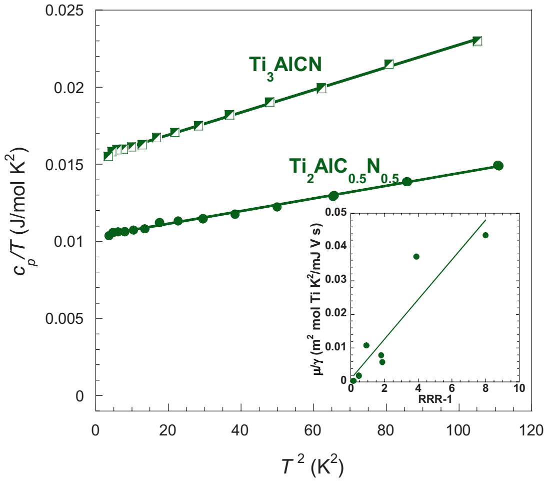

FIG. 6. (Color online) Low-temperature specific heat for the carbonitrides. The line represents a fit to Eqs. (4) and (5). Inset shows dependence of mobility at 5 K normalized by the specific heat electronic term γ and the RRR.

$$\gamma = \frac{(1+\lambda)\pi^2 k_B^2 N(E_F)}{3}, \tag{6}$$

where k_B is Boltzmann's constant. However, as shown earlier,[32] the λ values per Ti atom are not more than about 0.5, suggesting that the true $N(E_F)$ values for the carbonitrides are significantly larger than the related end members. The corresponding γ values of Ti_2AlN, Ti_2AlC, Ti_3AlC_2, and $Ti_4AlN_{2.9}$ are 1.5, 1.2, 0.8, and 1.0 mJ/mol Ti K^2, respectively.[22] Clearly, the substitution must shift the Ti d levels from those of the end members as reflected in the increased $N(E_F)$. As noted above, it is important to note that as previously shown,[22,33] there is no correlation between n and p and $N(E_F)$. As expected, the corresponding Debye temperatures 724 and 685 K for $Ti_2AlC_{0.5}N_{0.5}$ and Ti_3AlCN, respectively, are comparable to those of the end members Ti_2AlN, Ti_2AlC, and Ti_3AlC_2, viz., 690, 619, and 760, respectively.[22] The inset in Fig. 6 displays the dependence of the μ(at 5 K)/γ on RRR$-$1. The linear dependence again can be attributed to electronic conduction taking place primarily through the Ti d bands.[14,32]

As a rule, the MAX phases are good thermal conductors [Fig. 7(a)] because they are good electronic conductors. Figure 7(b) plots the minimum phonon conductivity κ_{ph}^{min} assuming the Wiedemann–Franz law,

$$\kappa_{ph}^{min} = \kappa - \frac{L_0 T}{\rho}, \tag{7}$$

where L_0 is the Lorenz number$=2.45\times10^{-8}$ W Ω/K^2. It is important to note the Wiedemann–Franz law is exact only at high and low temperatures, thus setting lower limits for the phonon conductivity. From Figs. 7(a) and 7(b), one finds that the total thermal conductivity κ has substantial contributions from both the electronic and phonon terms.

Since phonons are easily scattered by defects, especially in transition metal carbides and nitrides,[34] κ_{ph} should be—as shown previously[14]—sensitive to sample quality as measured by the RRR. Inset in Fig. 7(a) shows that such a correlation does exist. This correlation, however, appears to break down for Ti_3AlCN, which was not included in the data points used to fit the straight line shown in the inset of Fig. 7(a). This apparent outlier was discussed in a recent paper,[16] where it was suggested that the effect of stiffening of the bonds, due to the addition of N, more than compensates for the introduction of defects on the X-sites.

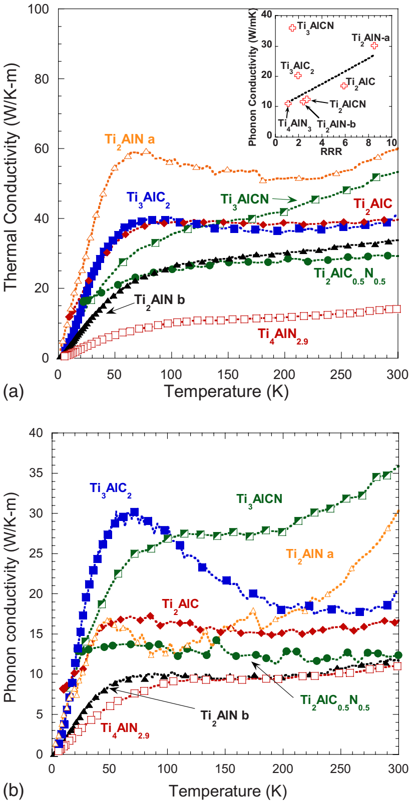

FIG. 7. (Color online) Temperature dependence of the (a) total thermal and the (b) minimum phonon conductivities. The correlation between RRR and κ_{ph} is good as long as the datum point for Ti_3AlCN is not included [(a) inset]. The R^2 value of the dashed line shown—that does not include the outlier—is 0.80.

IV. SUMMARY AND CONCLUSIONS

By measuring the electrical and thermal conductivities, magnetoresistances, Hall and Seebeck coefficients between 5 and 300 K of Ti_2AlN, Ti_3AlCN, and $Ti_2AlC_{0.5}N_{0.5}$, and comparing them with those of Ti_2AlC, Ti_3AlC_2, and $Ti_4AlN_{2.9}$ we show that, like other MAX phases, the electrical conductivities in these solids are compensated, with $n \approx p \approx 1.5-1.8\times10^{27}$ m^{-3}.

The values of $N(E_F)$ of the carbonitrides appear to be enhanced compared to those of the end members, although the electronic transport of all materials can be adequately described by the same model. The thermal conductivities of the carbonitrides are reasonably large and the phonon contribution to that of Ti_3AlCN is sizable.

ACKNOWLEDGMENTS

This work was funded by the National Science Foundation (Grant No. DMR 0503711). S.E.L. and J.D.H. also acknowledge support from the NSF (Grant No. DMR 0114073).

[1] H. Nowotony, Prog. Solid State Chem. **2**, 27 (1970).
[2] M. W. Barsoum, Prog. Solid State Chem. **28**, 201 (2000).
[3] M. W. Barsoum and T. El-Raghy, J. Am. Ceram. Soc. **79**, 1953 (1996).
[4] S. Myhra, J. W. B. Summers, and E. H. Kisi, Mater. Lett. **39**, 6 (1999).
[5] M. Sundberg, G. Malmqvist, A. Magnusson, and T. El-Raghy, Ceram. Int. **30**, 1899 (2004).
[6] M. W. Barsoum, L. H. Ho-Duc, M. Radovic, and T. El-Raghy, J. Electrochem. Soc. **150**, B166 (2003).
[7] S. Dubois, T. Cabioc'h, P. Chartier, V. Gauthier, and M. Jaouen, J. Am. Ceram. Soc. **90**, 2642 (2007).
[8] J. Etzkorn, M. Ade, and H. Hillebrecht, Inorg. Chem. **46**, 1410 (2007).
[9] B. Manoun, S. K. Saxena, T. El-Raghy, and M. W. Barsoum, Appl. Phys. Lett. **88**, 201902 (2006).
[10] J. P. Palmquist, S. Li, P. O. A. Persson, J. Emmerlich, O. Wilhemsson, H. Högberg, M. I. Katsnelson, B. Johansson, R. Ahujia, O. Eriksson, L. Hultman, and U. Jansson, Phys. Rev. B **70**, 165401 (2004).
[11] H. Högberg, P. Eklund, J. Emmerlich, J. Birch, and L. Hultman, J. Mater. Res. **20**, 779 (2005).
[12] C. Hu, F. Li, J. Zhang, J. Wang, J. Wang, and Y. Zhou, Scr. Mater. **57**, 893 (2007).
[13] J. Etzkorn, M. Ade, and H. Hillebrecht, Inorg. Chem. **46**, 7646 (2007).
[14] J. D. Hettinger, S. E. Lofland, P. Finkel, J. Palma, K. Harrell, S. Gupta, A. Ganguly, T. El-Raghy, and M. W. Barsoum, Phys. Rev. B **72**, 115120 (2005).
[15] P. Finkel, B. Seaman, K. Harrell, J. D. Hettinger, S. E. Lofland, A. Ganguly, M. W. Barsoum, Z. Sun, S. Li, and R. Ahuja, Phys. Rev. B **70**, 085104 (2004).
[16] M. Radovic, A. Ganguly, and M. W. Barsoum, J. Mater. Res. **23**, 1517 (2008).
[17] B. Manoun, S. K. Saxena, G. Hug, A. Ganguly, E. N. Hoffman, and M. W. Barsoum, J. Appl. Phys. **101**, 113523 (2007).
[18] A. Ganguly, M. Radovic, and M. W. Barsoum, Ph.D. thesis, Drexel University, 2006.
[19] P. Finkel, M. W. Barsoum, J. D. Hettinger, S. E. Lofland, and H. I. Yoo, Phys. Rev. B **67**, 235108 (2003).
[20] T. H. Scabarozi, S. Amini, P. Finkel,O. D. Leaffer, J. E. Spanier, M. W. Barsoum, M. Drulis, H. Drulis, W. M. Tambussi,J. D. Hettinger, and S. E. Lofland, J. Appl. Phys. **104**, 033502 (2008).
[21] P. Finkel, J. D. Hettinger, S. E. Lofland, M. W. Barsoum, and T. El-Raghy, Phys. Rev. B **65**, 035113 (2001).
[22] S. E. Lofland, J. D. Hettinger, K. Harrell, P. Finkel, S. Gupta, M. W. Barsoum, and G. Hug, Appl. Phys. Lett. **84**, 508 (2004).
[23] J. C. Ho, H. H. Hamdeh, M. W. Barsoum, and T. El-Raghy, J. Appl. Phys. **86**, 3609 (1999).
[24] W. S. Williams, MRS Symposia Proceedings No. 411 (Materials Research Society, Pittsburgh, 1996), p. 169.
[25] J. W. McClure, Phys. Rev. **112**, 715 (1958).
[26] N. Medvedeva, D. Novikov, A. Ivanovsky, M. Kuznetsov, and A. Freeman, Phys. Rev. B **58**, 16042 (1998).
[27] G. Hug, M. Jaoun, and M. W. Barsoum, Phys. Rev. B **71**, 024105 (2005).
[28] Z. M. Sun and Y. C. Zhou, Phys. Rev. B **60**, 1441 (1999).
[29] Y. C. Zhou, Z. Sun, X. Wang, and S. Chen, J. Phys.: Condens. Matter **13**, 10001 (2001).
[30] B. Holm, R. Ahuja, and B. Johansson, Appl. Phys. Lett. **79**, 1450 (2001).
[31] B. Holm, R. Ahuja, S. Li, and B. Johansson, J. Appl. Phys. **91**, 9874 (2002).
[32] S. E. Lofland, J. D. Hettinger, T. Meehan, A. Bryan, P. Finkel, S. Gupta, M. W. Barsoum, and G. Hug, Phys. Rev. B **74**, 174501 (2006).
[33] M. K. Drulis, H. Drulis, S. Gupta, T. El-Raghy, and M. W. Barsoum, J. Appl. Phys. **99**, 093502 (2006).
[34] W. S. Williams, Prog. Solid State Chem. **6**, 57 (1971).

CURRICULUM VITA
THEODORE H. SCABAROZI JR.

Education

Ph.D.	Drexel University, Philadelphia, PA Degree in Materials Science and Engineering	December 2009
B.Sc.	Rowan University, Glassboro, NJ Degree in Physics	May 2001
A.Sc.	Gloucester County College, Sewell, NJ Associate in Science	December 1999

Professional Experience

DuPont Electronic Technologies: Printed Circuit Materials Research and Development Technician	2002-2005
DuPont Holographics Research and Development Technician	2001-2002

Publications

2009

T. H. Scabarozi, C. Steinmetz , E. Pfeiffer , J. Applegate, C. Gennaoui, S. Benjamin, J. Roche, B. Adamson, M.W. Barsoum, J. D. Hettinger, S. E. Lofland, “Thin films in the Cr-V-Ge-C systems synthesized by combinatorial method”, In preparation

T. H. Scabarozi, J. Applegate, T. Flemming, C. Steinmetz , C. Gennaoui, S. Benjamin, J. Roche, B. Adamson, M.W. Barsoum, J. D. Hettinger, S. E. Lofland, “Combinatorial investigation of $(V_{1-x}Cr_x)_2AlC$”, In preparation

T. H. Scabarozi, C. Gennaoui, J. Roche, T. Flemming, K. Wittenberger, P. Hann, B. Adamson, A. Rosenfeld, M.W. Barsoum, J. D. Hettinger, S. E. Lofland, “Combinatorial investigation of $(Ti_{1-x}Nb_x)_2AlC$”, *App. Phys. Lett.* **95**, 1 (2009)

T.H. Scabarozi, S. Amini , O. Leaffer, A. Ganguly, S. Gupta, W. Tambussi, S. Clipper, J.E. Spanier, M.W. Barsoum , J.D. Hettinger, S.E. Lofland, “Thermal Expansion of Select $M_{n+1}AX_n$ (M=early transition metal, A=A-group element, X=C or N) Phases measured by high temperature x-ray diffraction and dilatometry”, *J. Appl. Phys.* **105**, 013543 (2009)

T.H. Scabarozi, J. Roche, A. Rosenfeld, S.H. Lim, L. Salamanca-Riba, G. Yong, I. Takeuchi, M.W. Barsoum, J.D. Hettinger, S.E. Lofland, "Synthesis and characterization of Nb_2AlC thin films", *Thin Solid Films* **517**, 2920-2923 (2009)

2008

T.H. Scabarozi, S. Amini, P. Finkel, O.D. Leaffer, J.E. Spanier, M.W. Barsoum , M. Drulis, H. Drulis, W.M. Tambussi, J.D. Hettinger, S.E. Lofland, "Electrical, thermal, and elastic properties of the MAX-phase Ti_2SC", *J. Appl. Phys.* **104**, 033502 (2008)

T. Scabarozi, A. Ganguly, J.D. Hettinger, S.E. Lofland, S. Amini, P. Finkel, T. El-Raghy, M.W. Barsoum, "Electronic and thermal properties of $Ti_3Al(C_{0.5}, N_{0.5})_2$, $Ti_2Al(C_{0.5}, N_{0.5})$ and Ti_2AlN", *J. Appl. Phys.* **104**, 073713 (2008)

T.H. Scabarozi, P. Eklund, J. Emmerlich, H. Högberg, T. Meehan, P. Finkel, M.W. Barsoum, J.D. Hettinger, L. Hultman, S.E. Lofland, "Weak electronic anisotropy in the layered nanolaminate Ti_2GeC", *Solid St. Comm.* **146**, 498-501 (2008)

2003

S.E. Lofland, **T. Scabarozi**, Y. Moritomo, Sh. Xu, et al, "Magnetism of the double perovskite Sr_2FeMoO_6,", *J. Magn. Magn. Mater* **260**, 181, (2003).

S.E. Lofland, **T. Scabarozi**, K.V. Ramanujachary and W.H. McCarroll, "Unusual magnetic ordering of $La_5Mo_4O_{16}$," , *J. Magn. Magn. Mater* **260**, 184, (2003).

2001

S. Kale, S.M. Bhagat, S.E. Lofland, **T. Scabarozi**, S.B. Ogale, A. Orozco, S.R. Shinde, T. Venkatesan, B. Hannoyer, B. Mercey, W. Prellier, "Film thickness and temperature dependence of the magnetic properties of pulsed laser deposited Fe_3O_4 films on different substrates," *Phys. Rev. B* **64**, 205413 (2001).

S.E. Lofland, **T. Scabarozi**, S. Kale, S.M. Bhagat, S.B. Ogale, T. Venkatesan, R.L. Greene, J. Gopalakrishnan, K. Ramesha, "Ferromagnetic resonance and magnetization studies on ferrimagnetic double perovskites A_2FeReO_6 (A= Ca, Sr, Ba)," *IEEE Trans. Magn.* **37**, 2153 (2001).

International Conference Presentations

Intl. Conf. of Metallurgical Coatings and Thin Films, San Diego, CA April 2008
"Thin Film Synthesis and Characterization of M-A-C (M=Cr, Nb, Ti, V; A=Al, Ge) Compounds"

Intl. Conf. of Metallurgical Coatings and Thin Films, San Diego, CA April 2007
"An Investigation of MAX-Phases by Thin Film Combinatorial Methods"

The American Physical Society Annual Meeting, Denver, CO March 2007
“Thin Film Synthesis and Characterization of MAX-Phase Compounds”

The American Physical Society Annual Meeting, Baltimore, MD March 2006
“Thermal Transport and Heat Capacity of Ti_3AlCN and $Ti_2AlC_{0.5}N_{0.5}$”

The American Physical Society Annual Meeting, Baltimore, MD March 2001
“Torque Magnetometry of $La_5Mo_4O_{16}$”